Spectral resource optimization for MU-MIMO systems with partial frequency bandwidth overlay

Hua Fu

Thèse

THESE INSA Rennes
sous le sceau de l'Université européenne de Bretagne
pour obtenir le titre de
DOCTEUR DE L'INSA DE RENNES
Spécialité : Electronique et Télécommunications

présentée par
Hua FU

ECOLE DOCTORALE : MATISSE
LABORATOIRE : IETR

Spectral Resource Optimization for MU-MIMO Systems with Partial Frequency Bandwidth Overlay

Thèse soutenue le 22.05.2015
devant le jury composé de :

Marie-Laure Boucheret
Professeur, ENSEEIHT, Toulouse / *Présidente du jury*
Emanuel Radoi
Professeur, UBO, Brest / *Rapporteur*
Didier Le Ruyet
Professeur, CNAM, Paris / *Rapporteur*
Guillaume Ferré
Maître de Conférences, ENSEIRB-MATMECA, Bordeaux / *Examinateur*
Matthieu Crussière
Maître de Conférences, INSA, Rennes / Co-Encadrant
Maryline Hélard
Professeur, INSA, Rennes / Directrice de thèse

Spectral Resource Optimization for MU-MIMO Systems with Partial Frequency Bandwidth Overlay

Hua FU

To my parents

ACKNOWLEDGEMENTS

It is my great pleasure to acknowledge the many people who have helped, encouraged and supported me to make this thesis possible.

Foremost, I am heartily thankful to my Ph.D. advisor, Prof. Maryline Hélard, for accepting me to pursue my thesis in laboratory IETR and for her invaluable guidance throughout the last three and half years. Thank you for giving me such an interesting topic and thank you for all the insightful advices and warm encouragements. I would like also to express my sincere gratitude to my co-advisor: Maître de conférences, Dr. Matthieu Crussière, for the inspiring discussions, the expert advices and the kind encouragements, which support me to complete this thesis.

I would like to express my sincere thanks to all the members of my thesis defense committee, Prof. Didier Le Ruyet, Prof. Emanuel Radoi, Prof. Marie-Laure Boucheret and Dr. Guillaume Ferré, for reading and evaluating my thesis. Their expert advices and comments have greatly helped me to improve my thesis.

I would like to thank my colleagues in the lab: Thierry Dubois, Hussein Kdouh, Philippe Tanguy, Roua Youssef, Yvan Kokar, Mohamad Maaz, Yaset Oliva, Jordane Lorandel, Hiba Bawab, Rida El Chall, Ali Cheaito, Sofiane Chabane, Mihai-Ionut Andries, Georges Da-Silva Abdou Khadir Fall, Thomas Larhzaoui, Tony Makdissy and Samar Sindian (too many names to mention). Thank you for the friendly working environment, the nice discussions and the interesting activities. I would like also to express my thanks to Laurent Guillaume, Jérémy Dossin, Pascal Richard and Aurore Gouin, for the always availability and expert supports.

I would like to thank my friends met at Rennes: Yang Yang, Hui Ji, Haifang Si, Jinglin Zhang, Weiyu Li, Weizhi Lu, Duo Wang, Han Yuan, Wei Liu, Yi Liu, Qingyuan Gu, Zhigang Yao, liang Tang, Yanping Wang, Jia Fu, Xu Zhang, Jiali Xu, Hengyang Wei and Zhaoxin Chen, for their kind help and all the fun we have shared. I am also thankful to Ming Liu and Tian Xia, for the daily accompaniment, the interesting discussions and all the kindly help.

Last but not least, I would like to express my deepest gratitude to my family, especially to my parents, for their infinite love, comprehension and support.

RÉSUMÉ EN FRANÇAIS

L'industrie des télécommunications a connu un développement très rapide depuis sa naissance. Une nouvelle génération de téléphonie mobile a vu le jour tous les dix ans environ depuis le premier système "1G", connu commercialement sous le nom de "Nordic Mobile Telephone", introduit en 1981. C'est à partir des années 1990 que les systèmes de téléphonie mobile ont véritablement commencé à s'imposer au sein de la vie quotidienne. En plus des services voix initiaux, d'autres services de type fax, transmission de données et messagerie instantanée ont également été progressivement lancés. Avec la mise en place des systèmes de 3e et 4e générations, chacun est aujourd'hui parfaitement habitué à obtenir des services toujours plus variés, tel que l'accès internet, la téléphonie sur IP, la télévision haute définition, les services de jeux en réseau ou encore et le cloud computing. On peut donc considérer que les réseaux de téléphonie mobile ont sans nul doute bouleversé nos modes de communication, et sont même devenus indispensables à la vie moderne.

Dans ce contexte, un défi important à chaque nouvelle génération de téléphonie est de pouvoir répondre à la demande sans cesse croissante d'augmentation des débits de transmission, alors même que la ressource spectrale reste limitée. Des progrès considérables dans le domaine du traitement du signal ont été réalisés ces vingt dernières années, pour tenter notamment de résoudre les problèmes de congestion du spectre. Parmi les technologies les plus récentes et les plus sophistiquées, les systèmes à antennes multiples (MIMO) permettent de mettre à disposition un degré de liberté supplémentaire grâce à l'exploitation de la dimension spatiale. Au cours de la dernière décennie, après de nombreuses études et expériences, les techniques MIMO sont devenues matures et sont aujourd'hui progressivement incorporées au sein des normes récentes de communication.

D'autre part, le développement massif des réseaux cellulaires a conduit à une expansion sans précédent des parcs de stations de base, conduisant à une augmentation tout aussi importante de la consommation énergétique induite par le fonctionnement de ces stations. Les opérateurs doivent alors faire face à des coûts opérationnels importants pour maintenir le fonctionnement de leur réseau. Du point de vue des utilisateurs également, l'autonomie des terminaux ne cesse de diminuer en raison de l'exécution de programme et d'algorithmes de traitement du signal de plus en plus complexes. Par conséquent, au-delà des critères de débit et de gestion du spectre évoqués précédemment, la prochaine génération de systèmes de télécommunications doit relever un défi supplémentaire relatif à la réduction de la consommation d'énergie des réseaux.

Une solution prometteuse à ce double défi consiste en la mise en oeuvre de techniques dites MIMO multi-utilisateur (MU-MIMO). Ces systèmes ont reçu une attention très forte ces dernières années et sont actuellement partiellement intégrés dans plusieurs normes de nouvelle génération de systèmes sans fil, comme par exemple le système LTE-Advanced ou le système 802.16m. Les systèmes MU-MIMO font référence à un topologie d'émission-réception dans laquelle la station de base est équipée de plusieurs antennes et effectue des transmissions simultanées vers un ensemble de terminaux équipés d'un nombre faible d'antennes (typiquement une seule). Le

multiplexage entre utilisateurs est assuré par le biais de la dimension spatiale. On parle alors d'accès multiple spatial (SDMA), réputé pour fournir un débit potentiellement plus élevé que les approches classiques à division temporelle ou fréquentielle (TDMA, FDMA). En suivant cette stratégie d'exploitation de la dimension spatiale, les systèmes dits MIMO massifs ont été introduits très récemment par Marzetta en 2010. Ces systèmes se basent sur l'utilisation d'un nombre d'antennes d'un ordre de grandeur largement supérieur, au moins d'un facteur 100, aux systèmes MIMO et MU-MIMO traditionnels. Les premières études théoriques montrent que ces systèmes peuvent espérer atteindre des niveaux de capacité 10 fois supérieurs aux systèmes classiques, tout en permettant d'améliorer l'efficacité énergétique d'un ordre 100. On comprend alors que l'approche MIMO massif est très prometteuse pour les systèmes "5G".

Toutefois, en prenant en compte des considérations pratiques, équiper une station de base de plus de 100 antennes n'est aujourd'hui pas une hypothèse réaliste. Or, réduire le nombre d'antennes à une grandeur plus acceptable, typiquement $4 \sim 64$ antennes, conduit nécessairement à une dégradation des performances attendues pour les systèmes MIMO massifs. L'objectif de cette thèse est d'étudier précisément le comportement des systèmes MU-MIMO avec un nombre fort mais modéré d'antennes sur la station de base. Notre but étant de nous intéresser en priorité aux systèmes à faible coût énergétique, nous avons étudié les techniques de précodage dérivées de l'approche du filtre adapté, telles que les précodages MRT (maximum ratio transmission), EGT (equal gain transmission) et TR (time reversal). Nous avons apporté une attention particulière à l'analyse des performances théoriques de ces techniques, et nous avons notamment cherché à établir des modèles de performance précis pour un nombre arbitraire d'antennes d'émission et pour différentes gammes de rapport signal sur bruit (SNR). Nos résultats ont été comparés avec ceux obtenus pour des systèmes MIMO massifs.

En outre, nos investigations sur les systèmes à nombre modéré d'antennes nous ont conduit à proposer un schéma de transmission basé sur un recouvrement partiel de la bande fréquentielle utilisée pour deux transmissions concurrentes au sein d'un même système. Ce principe, nommé PFBO (Partial Frequency Bandwidth Overlay), a pour but d'améliorer et d'adapter l'efficacité spectrale des systèmes MU-MIMO à nombre d'antennes modéré et transmis avec SNR relativement faible. Les techniques d'étalement de spectre ont également été combinées avec le schéma PFBO pour améliorer encore plus les performances de ce système. Le taux de recouvrement optimal est proposé permettant de maximiser l'efficacité spectrale du système en fonction du SNR.

Nous résumons dans les paragraphes suivants les résultats principaux obtenus dans cette thèse.

Chapitre 1 : Contexte et modèlisation du système

Systèmes MU-MIMO à échelle modérée

En dépit des nombreux avantages démontrés par les analyses théoriques présentes dans la littérature, le déploiement des systèmes MIMO massifs nécessite encore des recherches conséquentes devant prendre en compte les aspects pratiques de leur mise en oeuvre. Une question importante qui se pose est la suivante : "est-il possible d'atteindre des avantages similaires à ceux théoriquement formulés pour les systèmes MIMO massifs (faible coût des terminaux, faible consommation d'énergie, faible niveaux d'interférences) avec un nombre d'antennes modérement élevé ?"

Dans cette thèse, nous proposons un schéma de transmission à faible complexité et à haute efficacité énergétique basée sur un système MU-MIMO à échelle modérée. Les techniques de précodage dérivées du filtre adapté sont appliquées pour effectuer un accès multiple entre utilisateurs dans la dimension spatiale (SDMA). Contrairement à d'autres précodeurs de type Zero-Forcing

(ZF) par exemple, avec de tels précodeurs, le niveau d'interférence inter-utilisateur ne peut être considéré comme nul. Cependant, le niveau de puissance utile au sein de chaque récepteur est maximisé par le principe de filtrage adapté, ce qui rend ce type de précodeurs intéressant pour des gammes de SNR faible. Un système MU-MIMO précodé est présenté Fig. 1.

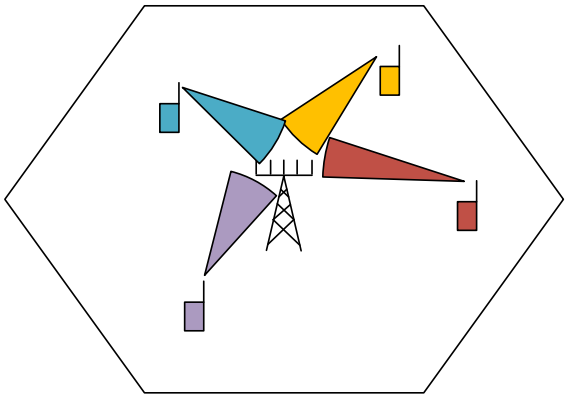

FIGURE 1 – Système MU-MIMO précodé

En supposant que le canal est connu à l'émission, les vecteurs de précodage sont directement déduits des réponses des canaux associés aux liens spatiaux entre chaque antennes d'émission et de réception. Dans le cas des précodeurs à filtrage adapté, le calcul des vecteurs de précodage est basé sur des opérations simples. Nous notons qu'avec ce type de précodage, une coopération entre des stations de base adjacentes est faisable simplement car aucun échange d'information n'est requis entre stations pour former les vecteurs de précodage. Ceci signifie qu'avec un tel système par exemple, des utilisateurs en position limite entre deux cellules adjacentes pourraient être servis par coopération entre les stations de base de ces cellules. En supposant une parfaite synchronisation entre les stations de base, un précodage distribué peut être appliqué sur les signaux transmis.

Schéma PFBO

Pour les systèmes MU-MIMO présentés précédemment, le multiplexage multi-utilisateur est réalisé grâce à des techniques de précodage non conçues pour annuler directement l'interférence entre utilisateurs. Si le nombre d'antennes d'émission est suffisamment grand, l'interférence entre utilisateur est réduite de façon naturelle et un multiplexage spatial de bonne qualité est obtenu entre les utilisateurs. En revanche, si le nombre d'antennes est trop faible, le niveau d'interférence entre utilisateurs devient important et vient fortement dégrader la séparation entre les flux. Une façon simple de minimiser cet effet est d'opérer une séparation partielle entre les utilisateurs selon l'axe fréquentiel. On obtient alors un système dans lequel on réalise un recouvrement partiel du spectre alloué à deux utilisateurs différents. Le schéma de recouvrement fréquentiel partiel, nommé PFBO (Partial Frequency Bandwidth Overlay) est présenté Fig. 2. Un tel système permet de contrôler le niveau d'interférence inter-utilisateur en fonction de la qualité de la composante SDMA, et donc du nombre d'antennes utilisé. Ce système peut être vu comme une solution mixte à multiplexage fréquentiel et spatial.

On comprend qu'en fonction du nombre d'antennes utilisé et de la gamme de SNR de fonctionnement, le niveau d'interférence inter-utilisateur sera variable et conduira à un niveau de recouvrement fréquentiel lui aussi variable. Ces principes nous motivent à analyser finement les

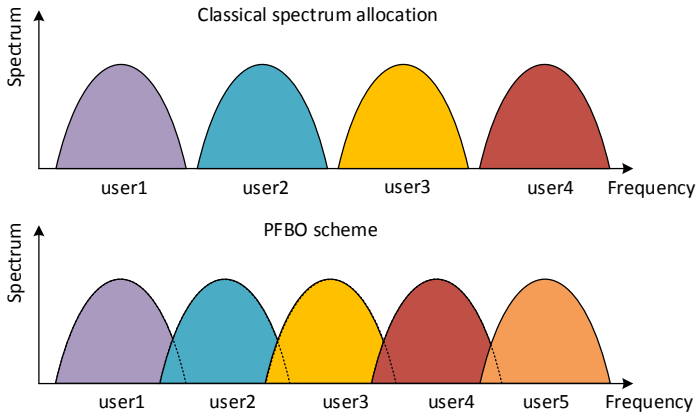

FIGURE 2 – Schéma PFBO

performances du système proposé en fonction du nombre d'antennes, pour différents niveaux du SNR et pour différents taux de recouvrement.

Chapitre 2 : Capacité système des schémas PFBO

Schéma PFBO associé aux systèmes mono-porteuse et multi-porteuse

L'utilisation d'un schéma PFBO pour des signaux de type mono-porteuse est présentée Fig. 3. La largeur de bande effectivement recouverte est notée Δf.

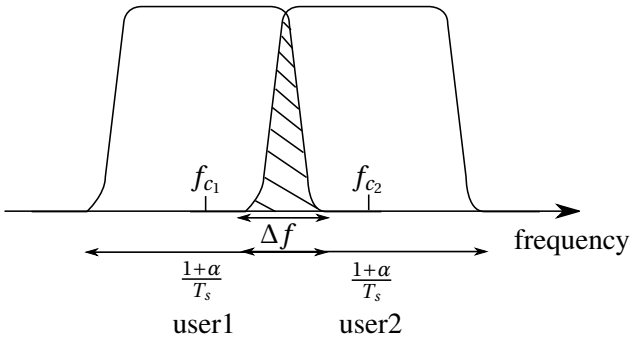

FIGURE 3 – Schéma PFBO appliqué aux signaux mono-porteuses

En notant $user1$ l'utilisateur d'intérêt et $user2$ l'utilisateur interférent, l'evolution de l'efficacité spectrale du $user1$ en fonction du taux de recouvrement est présenté Fig. 6 pour différentes techniques de précodage et pour un nombre variable M d'antennes de transmission. avec $\gamma = SNR, \gamma \in \{0, 5, 10, 15, 20\}\, dB$. On observe une légère amélioration de l'efficacité spectrale pour des taux de recouvrement faibles. Cette augmentation est obtenue lorsque le niveau d'interférence reste tolérable par rapport au niveau de bruit. Par contre, pour un taux de recouvrement important, l'interférence devient dominante et l'efficacité spectrale se dégrade rapidement. Cependant, grâce

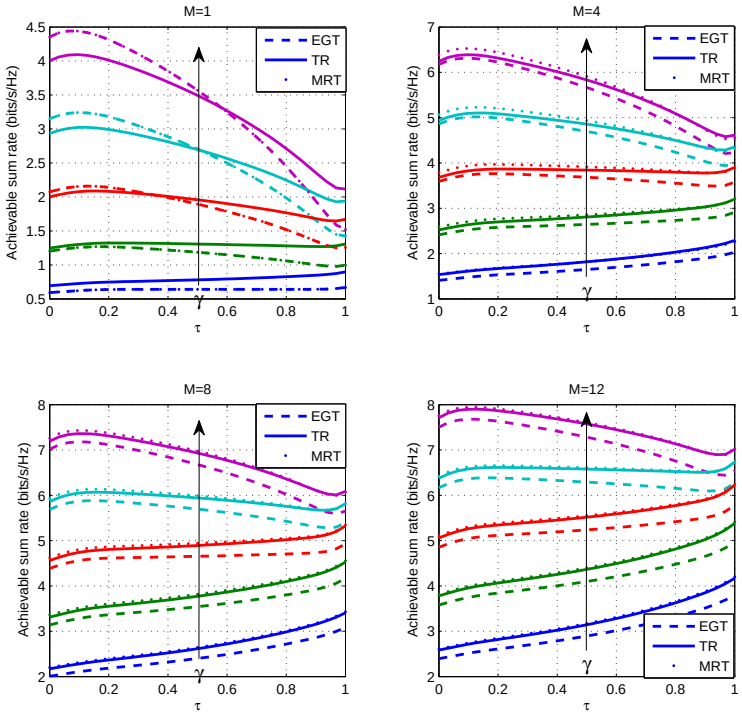

FIGURE 4 – Efficacité spectrale du système PFBO mono-porteuse en fonction du taux de recouvrement pour différents SNRs et M

aux techniques de précodage spatial MIMO, on observe que le schéma PFBO permet d'obtenir, selon la valeur de M, un gain d'efficacité spectrale à la fois pour des taux de recouvrement plus importants et pour des gammes de SNR plus élevées.

Pour les signaux OFDM à présent, la densité spectrale de puissance des signaux est modélisée comme une série de sous-bandes fréquentielles purement rectangulaires. Le schéma PFBO appliqué aux signaux OFDM est présenté Fig. 5.

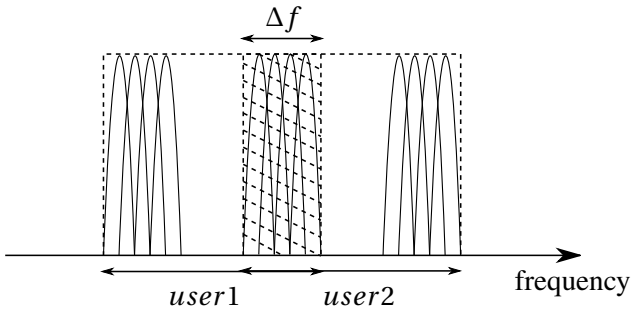

FIGURE 5 – PFBO schémas avec signaux OFDM

De part cette modélisation, on comprend que l'évolution de l'efficacité spectrale soit monotone comme présenté Fig. 6. A part cette différence, les mêmes conclusions que précédemment

peuvent être avancées sur le gain en efficacité spectrale que peut apporter le schéma PFBO selon le nombre d'antennes utilisées ou la gamme de SNR visée.

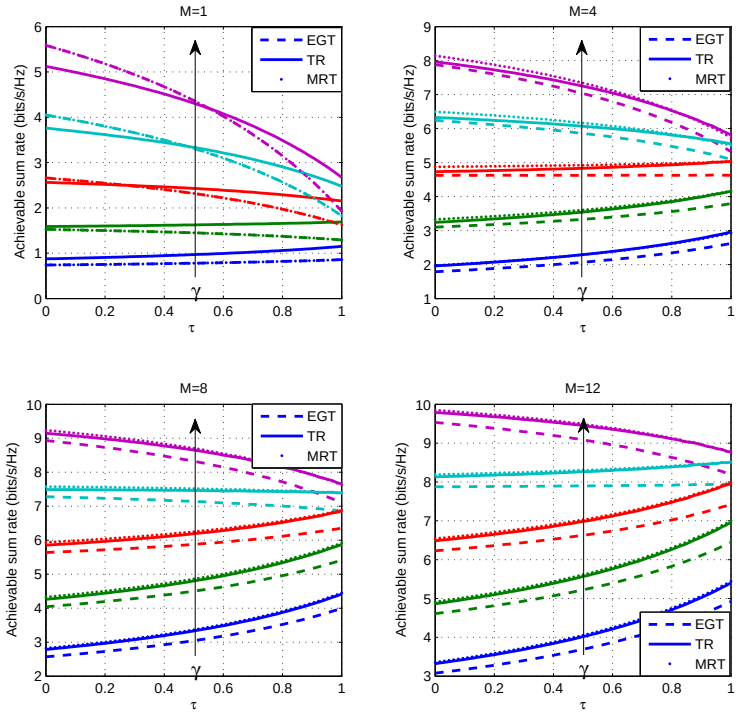

FIGURE 6 – Efficacité spectrale du système PFBO OFDM en fonction du taux de recouvrement pour différents SNRs et M

Pour aller plus loin dans l'analyse des performances du schéma PFBO, nous avons cherché à identifier l'évolution des taux de recouvrement optimaux τ_{max} en fonction de γ pour differentes configurations de systèmes. Les résultats synthétiques sont reportés Fig. 7. Pour les signaux mono-porteuses, nous observons qu'avec un faible SNR, comme le bruit est dominant, le choix optimal est de recouvrir complètement les spectres des deux utilisateurs concurrents. En revanche, quand le SNR augmente, nous observons un effet de seuil à partir duquel le recouvrement devient partiel pour garantir une capacité optimale. Pour la modulation multi-porteuse, l'évolution du taux optimal étant monotone, l'effet de seuil est plus brutal, avec une valeur $\tau_{max} \in \{0, 1\}$. En d'autres termes, pour les signaux multi-porteuses, le choix optimal est soit d'effectuer un recouvrement complet, soit de ne pas effectuer de recouvrement du tout, et ce en fonction de M et γ.

Outre l'étude système, les bornes de capacité des systèmes MU-MIMO OFDM sont développées dans ce chapitre pour un nombre arbitraire N_u d'utilisateurs concurrents. Une série importante de développements analytiques est présente dans ce chapitre, conduisant à des résultats nouveaux sur des bornes de capacités qui s'avèrent être plus précises que celles généralement utilisées dans la littérature sur le MIMO massif. A titre d'exemple, la borne supérieure de capacité pour un système EGT-MIMO est :

$$\tilde{\tilde{R}}_{EGT,mu} = \frac{\psi(M) + ln(\frac{1+\frac{\pi}{4}(M-1)}{M}) + e^{\frac{1}{N_u\gamma}} Ei(-\frac{1}{N_u\gamma}) + ln(\gamma)}{ln(2)} \tag{1}$$

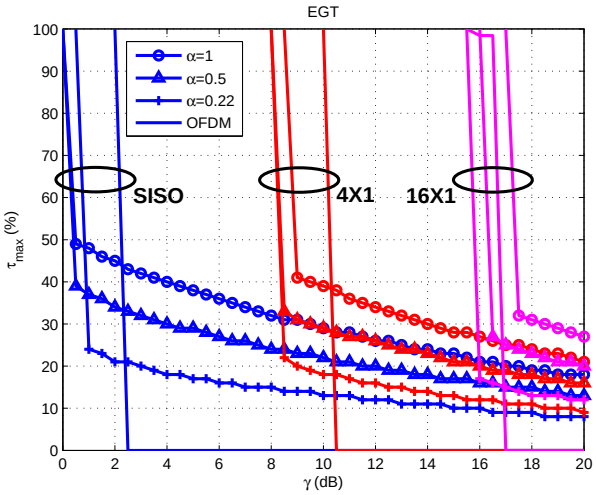

FIGURE 7 – Taux de recouvrement optimal τ_{max} en fonction du SNR pour les systèmes SISO et EGT-MIMO

avec $Ei(\cdot)$ la fonction exponential integral, et $\gamma = \frac{Eb}{N0}$. Des expressions similaires ont été trouvées pour les méthodes de précodage MRT et TR. L'ensemble de ces résultats ne sont pas présents dans la littérature et constituent une première contribution importante de ce travail de thèse.

Chapitre 3 : Taux d'erreurs binaires du schéma PFBO combinés aux systèmes EGT-MIMO-OFDM

Dans ce chapitre, on s'intéresse à développer de façon analytique les expressions de TEB des systèmes MIMO-OFDM utilisant le schéma PFBO. Le précodeur EGT a été choisi pour l'ensemble des développements, car il représente un bon compromis performance/complexité.

Calculs de taux d'erreurs sur canal plat en fréquence

Sous hypothèse de canal plat en fréquence, le signal reçu pour un système OFDM utilisant le schéma PFBO est :

$$\begin{cases} Y_p^{(1)} = a_p^{(1)} + N_p, \quad p \in \{1, \cdots, N_f - N_R\} \\ Y_p^{(1)} = a_p^{(1)} + a_{p'}^{(2)} + N_p, \quad p \in \{N_f - N_R + 1, \cdots, N_f\} \end{cases} \tag{2}$$

avec N_f le numbre total de sous-porteuses du spectre OFDM etN_p le bruit thermique sur la sous-porteuse p. L'indice p' définit l'indice de sous-porteuse de l'utilisateur interférent tel que $p' = p - N_f + N_R$. Le TEB pour l'ensemble des signaux transmis peut être calculé comme le TEB moyen sur l'ensemble des sous-porteuses. Après calculs, on trouve :

$$TEB_{\text{OFDM}} = \frac{N_R}{4N}\Big(1 + erfc\big(2\sqrt{\frac{E_b}{N_0}}\big)\Big) + \big(1 - \frac{N_R}{N_f}\big)\frac{1}{2}erfc\Big(\sqrt{\frac{E_b}{N_0}}\Big) \tag{3}$$

En raison de premier terme de l'équation, à savoir $\frac{N_R}{4N}$, on conclut que le TEB se dégrade fortement lorsque le nombre N_R de sous-porteuses touchées par le recouvrement de bande augmente. A fort SNR, ce terme sera dominant et sera responsable d'un plancher d'erreur dans les courbes de TEB.

Calculs de taux d'erreurs sur canal de Rayleigh

Toujours sous hypothèse de précodage EGT, le signal reçu sur la sous-porteuse p s'écrit à présent :

$$\begin{cases} Y^{(1)}_{p,EGT,nr} = \frac{1}{\sqrt{M}} \sum_{m=1}^{M} \left| H^{(1)}_{p,m} \right| a^{(1)}_p + N_p, \quad p \in \{1, \cdots, N_f - N_R\} \\ Y^{(1)}_{p,EGT,r} = \frac{1}{\sqrt{M}} \sum_{m=1}^{M} \left| H^{(1)}_{p,m} \right| a^{(1)}_p + \frac{1}{\sqrt{M}} \sum_{m=1}^{M} H^{(1)}_{p,m} e^{-j\Phi^{(2)}_{p',m}} a^{(2)}_{p'} + N_p, \quad p \in \{N_f - N_R + 1, \cdots, N_f\}. \end{cases} \tag{4}$$

L'analyse du taux d'erreurs doit se faire pour la partie non recouverte du spectre puis pour la partie recouverte. Pour la partie non recouverte, on propose d'utiliser une approximation de Nakagami *Nakagamki*$(M,1)$ pour modéliser le canal équivalent tenant compte du précodage EGT. Dans ce cas, les développements analytiques sont réalisables en utilisant des résultats d'intégrations tabulés. On obtient alors l'expression finale :

$$\begin{aligned} TEB_{EGT,nr}\left(\frac{Eb}{N0}, M\right) &= \int_0^\infty f(r|M) Q(r\sqrt{\frac{2Eb}{N0}}) dr \\ &= \frac{\Gamma\left(M + \frac{1}{2}\right)}{2\sqrt{\pi}\Gamma(M+1)} \cdot \frac{\left[M\frac{N_0}{E_b}\right]^M}{\left[1 + M\frac{N_0}{E_b}\right]^{M+\frac{1}{2}}} \times {}_2F_1\left(1, M+\frac{1}{2}, M+1, \frac{M}{M+\frac{Eb}{N0}}\right) \end{aligned} \tag{5}$$

avec $\Gamma(\cdot)$ présent la fonction Gamma, ${}_2F_1(\cdot)$ présent la fonction hypergéométrique.

Pour la partie recouverte partagée entre deux utilisateurs, il faut à la fois modéliser le canal équivalent avec précodage EGT, mais également tenir compte de l'interférence provenant du flux à destination de l'utilisateur concurrent. Là encore, la loi de Nakagami permet d'approcher de façon satisfaisante le comportement du canal équivalent. On propose alors le théorème suivant pour paramètrer correctement la loi de Nakagami :

Théoreme 1 : Pour un canal de Rayleigh, la composante en phase des symboles de transmission issus d'un système BPSK EGT-MIMO à deux utilisateurs avec un nombre suffisamment important d'antennes M subit une atténuation suivant une loi de m-Nakagami dont les paramètres peuvent directement être obtenus par :

$$\begin{cases} \bar{m} = \frac{\pi}{24-4\pi} M + \frac{1}{8} \\ \bar{w} = 1 \end{cases} \tag{6}$$

A partir de ce modèle, il est possible encore une fois de trouver une forme explicitée pour le TEB du système. On obtient après calculs :

$$\begin{aligned} TEB_{EGT,r}\left(\frac{E_b}{N_0}\right) &= \int_0^\infty Q\left(\Xi\sqrt{\frac{2E_b}{N_0}}\right) f(\Xi) d\Xi \\ &= \frac{\Gamma\left(\tilde{m} + \frac{1}{2}\right)}{2\sqrt{\pi}\Gamma(\tilde{m}+1)} \cdot \frac{\left[\frac{\tilde{m}}{\tilde{\omega}}\frac{N_0}{E_b}\right]^{\tilde{m}}}{\left[1 + \frac{\tilde{m}}{\tilde{\omega}}\frac{N_0}{E_b}\right]^{\tilde{m}+\frac{1}{2}}} \times {}_2F_1\left(1, \tilde{m}+\frac{1}{2}, \tilde{m}+1, \frac{\frac{\tilde{m}}{\tilde{\omega}}}{\frac{\tilde{m}}{\tilde{\omega}} + \frac{Eb}{N0}}\right) \end{aligned} \tag{7}$$

La figure suivante donne les courbes de TEB théoriques obtenus par les expressions analytiques proposées et ainsi que celles résultant des simulations. On observe que le modèle proposé présente une précision bien meilleure que celle de l'approximation Gaussienne couramment employée dans la littérature. Ce résultat représente une deuxième contribution importante de cette thèse.

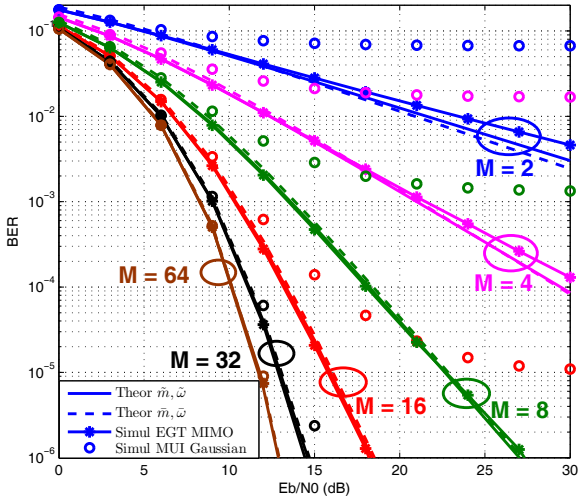

FIGURE 8 – TEB moyen du système EGT-OFDM MIMO à deux utilisateurs mettant en oeuvre le schéma PFBO, avec $N_f = 64$ et divers M. Comparaison entre les simulations, les approximations suivant le modèle de Nakagami et les approximations suivant le modèle Gaussien.

Chapitre 4 : Taux d'erreurs binaires du schéma PFBO combiné aux systèmes SS-OFDM

Dans ce dernier chapitre, on se propose d'ajouter une composante étalement de spectre, appliquée dans le domaine fréquentiel, aux systèmes étudiés précédemment. L'intérêt d'une telle composante est d'ajouter au système une capacité supplémentaire à rejeter l'interférence liée aux utilisateurs concurrents. On cherche alors à trouver les expressions analytique de TEB des systèmes ainsi formés. Une fois encore, c'est le précodeur EGT qui sera pris en référence dans les calculs.

Calculs de taux d'erreurs sur canal plat

On présente tout d'abord le schéma PFBO combiné avec un système SS-OFDM (spreading spectrum OFDM). Le recouvrement partiel des signaux concurrents entre deux utilisateurs concerne donc à la fois le domaine fréquentiel, mais aussi l'axe de codes d'étalement, comme presenté Fig. 9.

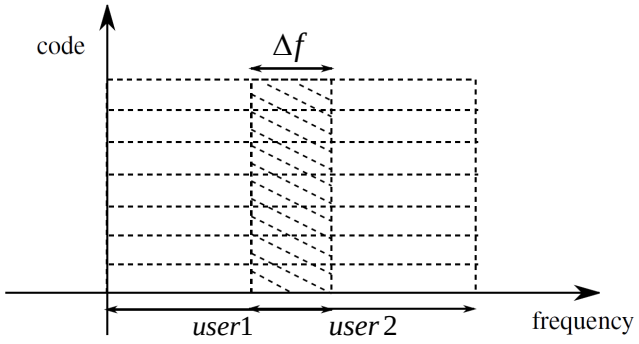

FIGURE 9 – PFBO schémas dans SS-OFDM système

Dans ce cas, le signal reçu devient :

$$\begin{cases} Y_p^{(1)} = \sum_{i=1}^{N_c=N_f} c_{p,i} a_i^{(1)} + N_p, & p \in \{1, \cdots, N_f - N_R\} \\ Y_p^{(1)} = \sum_{i=1}^{N_c=N_f} c_{p,i} a_i^{(1)} + \sum_{i=1}^{N_c=N_f} c_{p',i} a_i^{(2)} + N_p, & p \in \{N_f - N_R + 1, \cdots, N_f\} \end{cases} \tag{8}$$

Dans ces systèmes, les interférences ont différents comportements dépendant du taux de recouvrement, et donc du nombre de bribes de codes recouvertes. Cependant, on montre que dans la plupart des cas, la distribution des interférences s'approche d'une distribution Gaussienne. Dans ce cas le TEB s'écrit :

$$TEB_{\text{SS-OFDM}} = \int_0^{+\infty} p(x)(\frac{1}{2} erfc(\frac{x}{\sqrt{N_0}}))dx + \int_{-\infty}^{0} p(x)\big(1 - \frac{1}{2} erfc(\frac{-x}{\sqrt{N_0}})\big)dx, \tag{9}$$

avec $p(x)$ la PDF de loi normale telle que :

$$p(x) = \frac{1}{\sigma\sqrt{2\pi}} e^{\frac{(x-\mu)^2}{2\sigma^2}}, \tag{10}$$

avec les paramètres de moyenne $\mu = \sqrt{E_b}$ et d'écart type $\sigma = \sqrt{N_R / N_f}$.

Pour les cas particuliers où l'interférence ne peut pas être considérée comme Gaussienne, on utilise une distribution discrète de L valeurs possibles $R_L = \{r_1, r_2, \ldots, r_L\}$, la PDF de la lth valeur r_l étant :

$$p_l = \binom{L-1}{l-1} \frac{1}{2^{L-1}}, \tag{11}$$

Dans ce cas, l'expression du TEB est :

$$TEB_{\text{SS-OFDM}} = \sum_{l=1}^{L} p_l \ \frac{1}{2} erfc(r_l \sqrt{\frac{E_b}{N_0}}). \tag{12}$$

Les expressions théoriques précédentes sont vérifiées par simulations comme montré Fig. 10 :

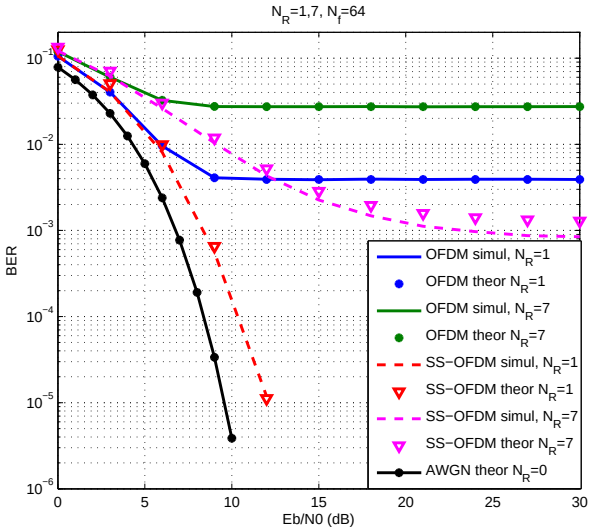

FIGURE 10 – Performances sur canal plat en fréquence des systèmes OFDM et SS-OFDM utilisant le schéma PFBO avec un nombre de sous-porteuse recouverte $N_R = 1,7$

Calculs de taux d'erreurs sur canal de Rayleigh

Dans le cas d'une transmission sur canal de Rayleigh, le signal reçu avec précodage EGT sur la sous-porteuse p s'écrit :

$$\begin{cases} Y_p^{(1)} = \dfrac{1}{\sqrt{M}} \displaystyle\sum_{m=1}^{M} \left| H_{p,m}^{(1)} \right| \sum_{i=1}^{N_c=N_f} c_{p,i} a_i^{(1)} + N_p, \quad p \in \{1, \cdots, N_f - N_R\} \\ Y_p^{(1)} = \dfrac{1}{\sqrt{M}} \displaystyle\sum_{m=1}^{M} \left| H_{p,m}^{(1)} \right| \sum_{i=1}^{N_c=N_f} c_{p,i} a_i^{(1)} + \dfrac{1}{\sqrt{M}} \sum_{m=1}^{M} H_{p,m}^{(1)} \Phi_{p,m}^{(2)} \sum_{i=1}^{N_c=N_f} c_{p',i} a_i^{(2)} + N_p, autrement \end{cases} \tag{13}$$

Pour les sous-bandes sans interférence, c'est-à-dire sans recouvrement spectral, on utilise un égaliseur MMSE (minimum d'erreur quadratique moyenne) classiquement calibré sur le niveau de bruit :

$$G_p = \frac{\frac{1}{\sqrt{M}} \sum_{m=1}^{M} \left| H_{p,m}^{(1)} \right|}{\frac{1}{M} \left(\sum_{m=1}^{M} \left| H_{p,m}^{(1)} \right| \right)^2 + N0}, \quad p \in \{1, \cdots, N_f - N_R\} \tag{14}$$

Pour les sous-bandes avec interférence, l'égaliseur MMSE doit tenir compte de la puissance d'interférence et sera calibré comme :

$$\begin{aligned} G_{p,R} &= \frac{\frac{1}{\sqrt{M}} \sum_{m=1}^{M} \left| H_{p,m}^{(1)} \right|}{\frac{1}{M} \left(\sum_{m=1}^{M} \left| H_{p,m}^{(1)} \right| \right)^2 + \frac{1}{M} \sum_{m=1}^{M} \left| H_{p,m}^{(1)} \Phi_{p,m}^{(2)*} \right|^2 + N0} \\ &\approx \frac{\frac{1}{\sqrt{M}} \sum_{m=1}^{M} \left| H_{p,m}^{(1)} \right|}{\frac{1}{M} \left(\sum_{m=1}^{M} \left| H_{p,m}^{(1)} \right| \right)^2 + \frac{1}{M} \sum_{m=1}^{M} \left| H_{p,m}^{(1)} \right|^2 + N0}, \quad \forall p \in \{N_f - N_R + 1, \cdots, N_f\} \end{aligned} \tag{15}$$

Grâce à l'étalement de spectre, chaque terme d'interférence est le résultat d'une moyenne des bribes d'interférence associées à chacune des sous-porteuses. Ainsi, les termes d'interférences après désétalement peuvent être considérés comme des processus Gaussiens. Suivant cette hypothèse, le TEB est alors approximé comme suit :

$$\mathrm{BER} = \frac{1}{2}\mathrm{erfc}\left(\frac{E[z]\sqrt{Eb}}{\sqrt{E\left[I^2\right] + E\left[J^2\right] + E\left[\left|G_p\right|^2\right] N_0}}\right) \tag{16}$$

avec z la réponse du canal équivalent, I^2 et J^2 respectivement la puissance d'interférence inter-code et l'interférence inter-canal. Ce résultat est la dernière contribution importante de cette thèse.

Conclusion et perspectives

Dans cette thèse, nous avons cherché à caractériser les performances théoriques des systèmes MU-MIMO avec un nombre d'antennes plus faible que dans les systèmes MIMO massifs très étudiés aujourd'hui. Nous avons donc travaillé la base d'un système MU-MIMO à échelle modérée qui peut être vu comme un intermédiaire, à la fois en terme de performance et de complexité, entre les systèmes MU-MIMO traditionnels et les systèmes MIMO massifs. Le faible nombre d'antennes conduisant à un gain de multiplexage relativement réduit et une interférence inter-utilisateur non négligeable, nous avons proposé d'adjoindre à ce système à échelle modéré, un principe de séparation partielle des utilisateurs en fréquence, appelé schéma PFBO. Les contributions de cette thèse ont alors été d'analyser les performances des systèmes MU-MIMO à échelle modérée, utilisant le schéma PFBO.

Nous avons en premier lieu analysé la capacité du schéma PFBO combiné à des modulations mono et multi-porteuses. En particulier, nous avons mis en évidence la présence d'un taux de recouvrement optimal permettant de maximiser l'efficacité spectrale pour les transmission mono et multiporteuses. Nous avons montré que ce taux de recouvrement était essentiellement dépendant du nombre d'antennes d'émission et de la gamme de SNR. En outre, nous avons effectué une recherche de bornes inférieures de capacité pour les systèmes MU-MIMO-OFDM utilisant les précodeurs EGT, TR et MRT. Ces bornes de capacité ont été calculées d'après une analyse statistique du comportement du canal, et s'avèrent bien plus précises que les bornes communément proposées dans la littérature pour les systèmes MIMO massifs.

En second lieu, nous nous sommes concentrés sur l'analyse des performances théoriques en terme de TEB des schémas PFBO pour les systèmes OFDM. Les expressions de TEB ont été établies pour des canaux plats en fréquence et pour des canaux de Rayleigh. En particulier, pour canal de Rayleigh, nous avons proposé d'utiliser l'équation de Nakagami pour modéliser la corrélation entre le signal utile et l'interférence multi-utilisateur pour les systèmes EGT-MIMO à deux utilisateurs et utilisant la modulation BPSK. Le choix du modèle statistique a été justifié et la dépendance linéaire entre les paramètres de Nakagami et le nombre d'antennes a été démontrée. Le modèle a été ensuite étendu au cas de la QPSK et pour un nombre d'utilisateurs concurrents quelconque.

Enfin, nous avons proposé d'ajouter une composante étalement de spectre aux systèmes étudiés afin d'améliorer encore leur capacité à rejeter les interférences issus des utilisateurs concurrents. Les expressions théoriques de TEB ont également été établies sur canal plat et de Rayleigh. En raison des techniques d'étalement de spectre, l'espérance de la réponse du canal s'est avérée suffisante pour donner des approximations de TEB précises. Ces approximations ont été vérifiées

par simulations. Il a finalement été montré que les techniques d'étalement de spectre permettent d'améliorer les performances des schémas PFBO.

En termes de perspectives à ce travail, l'analyse de TEB pour les systèmes MU-MIMO avec un ordre de modulation plus élevé tel que 8PSK ou 16QAM serait une poursuite du travail intéressante à court terme. Les résultats obtenus permettraient alors d'ajouter un paramètre supplémentaire (l'ordre de modulation) à utiliser au sein des systèmes MU-MIMO à échelle modérée. Notamment, on pourrait imaginer un seuil de décision dépendant du nombre d'antennes utilisées à partir duquel un ordre de modulations donné pourrait être exploitable, et ce en fonction du nombre d'utilisateurs concurrents. Ce genre de résultats serait tout aussi intéressant pour les systèmes MIMO massifs.

Plus largement, nous avons montré dans cette thèse que le modèle de Nakagami permettait de trouver une approximation souvent fiable aux phénomènes d'évanouissements observés sur les canaux équivalents après précodage. Cependant, ce modèle, uniquement défini pour des valeurs positives de la variable aléatoire ne permet pas toujours de modéliser finement le comportement des systèmes étudiés, notamment lorsque les interférences sont trop importantes. Une perspective importante serait donc de proposer une extension de la définition de Nakagami pour des échantillons à valeurs éventuellement négatives. Un tel modèle permettrait de traiter tous les cas de canaux équivalents rencontrés dans les systèmes MU-MIMO à échelle modérée.

Enfin, le PAPR des systèmes OFDM MU-MIMO précodés est un problème intéressant. Dans la littérature, des premiers résultats montrent que le PAPR des signaux SU-MIMO précodés par la technique EGT s'avère être de $1dB$ inférieur à celui de la technique MRT. Cependant, pour les systèmes MU-MIMO, les signaux émis sont différents de ceux des systèmes SU-MIMO. En outre, le PAPR des techniques TR n'a pas été évaluée dans aucun des systèmes. Il serait donc intéressant de se pencher de façon globale sur le problème du PAPR des systèmes MU-MIMO pour l'ensemble des précodeurs de la littérature et dans un contexte multi-utilisateur. Ce point est d'autant plus crucial que les systèmes à grand nombre d'antennes seront sans doute amenés à utiliser des composants à faible coût, y compris l'amplificateur de puissance dont les non-linéarités pourraient alors être particulièrement fortes.

CONTENTS

ABBREVIATIONS

AWGN Additive White Gaussian Noise
BER Bit Error Rate
BRAN Broadband Radio Access Networks
BS Base Station
CCI Cochannel Interference
CDMA Code Division Multiple Access
CDF Cumulative Distribution Function
CFO Carrier Frequency Offset
CFR Channel Frequency Response
CIR Channel Impulse Response
CP Cyclic Prefix
CSI Channel State Information
DFT Discrete Fourier Transform
DL Down-Link
DPC Dirty Paper Coding
EGT Equal Gain Transmission
ETSI European Telecommunications Standards Institute
FDD Frequency-Division Duplexing
FFT Fast Fourier Transform
GI Guard Interval
ICI Inter-Code Interference
IFFT Inverse Fast Fourier Transform
ISI Inter-Symbol Interference
ISM Industrial, Scientific and Medical
LoS Line-of-Sight
MAI Multiple Access Interference
MF Matched Filter
MIMO Multiple Input Multiple Output
MISO Multiple Input Single Output

MMSE Minimum Mean Squared Error
MRT Maximum Ratio Transmission
MUD Multi-User Detection
MUI Multiuser Interference
NLOS Non-Line-of-Sight
OFDM Orthogonal Frequency Division Multiplexing
PAPR Peak to Average Power Ratio
PBJ Partial Band Jamming
PDF Probability Density Function
PFBO Partial Frequency Bandwidth Overlay
PN Pseudo Noise
PSD Power Spectral Density
QAM Quadrature Amplitude Modulation
QPSK Quaternary Phase Shift Keying
RF Radio Frequency
RMS Root Mean Square
RMT Random Matrix Theory
RV Random Variable
SDMA Space-Division Multiple Access
SISO Single Input Single Output
SINR Signal to Interference and Noise Ratio
SS-OFDM Spread-Spectrum OFDM
SVD Singular Value Decomposition
SNR Signal to Noise Ratio
TDD Time-Division Duplexing
UWB Ultra-Wideband
WH Walsh-Hadamard
WLAN Wireless Local Area Network
ZF Zero Forcing

NOTATIONS

Nomenclature

x: scalar
$\mathbf{x}$: vector
$\underline{\mathbf{x}}$: matrix
$(\cdot)^*$: conjugate
$(\cdot)^T$: transpose
$(\cdot)^H$: hermitian
$\check{(\cdot)}$: lower bound
$\tilde{(\cdot)}$: approximate
$\mathrm{CN}(0,1)$: zero-mean, circularly-symmetric, unit-variance, complex Gaussian distributions

Mathematical notations

γ: SNR
τ: overlap ratio
k: user index
M: number of transmit antennas
N_c: number of spreading sequences N_f: number of subcarriers in OFDM systems
L_c: length of spreading sequences
p: subcarrier index

INTRODUCTION

THE telecommunication industry has been in rapid development since its birth. A new mobile generation appeared every decade since the first 1G system, Nordic Mobile Telephone, was introduced in 1981. From the beginning of the 1990s, mobile phone began to enter people's daily lives. In addition to the initial voice service, fax, data and SMS messaging services were gradually launched. Mobile phones have changed people's way of communications, and have become indispensable for modern life. Nowadays, with the 4G telecommunication systems, people is accustomed to get diverse services through smartphones, such as mobile web access, IP telephony, high-definition mobile TV, gaming services and cloud computing.

It is a big challenge to answer the explosively increasing demand of throughput with limited spectral resource. Considerable advances in digital signal processing have been realized for the last twenty years trying to solve spectrum congestion issues. Among recent advanced technologies, multiple input multiple output (MIMO) makes available an additional degree of freedom through the exploitation of the space dimension. During the last decade, after numerous studies and experiments, MIMO has become mature and is today beginning to be incorporated in emerging communication standards.

On the other hand, the rapid development of cellular network leads to the fast expansion of the base stations, which results in enormous energy consumption. The operators have to pay billions of dollars per year to maintain their network. For the user side, the autonomy of the devices keeps decreasing because of running the more and more complex programs and signal processing manipulations. Therefore, for the next generation of telecommunications systems, not only a higher throughput but also a lower energy consumption is expected.

In recent years, multi-user MIMO (MU-MIMO) systems received more and more attention and are now being introduced in several new-generation wireless standards (e.g., LTE Advanced, 802.16m). These systems refer to a base station (BS) with multiple antennas simultaneously serving a set of single (or more) antenna users. Multi-user multiplexing is assumed through the space-division multiple access (SDMA), which provides higher throughput than the traditional time-division multiple access (TDMA). More recently, massive MIMO systems were introduced by Marzetta in 2010, where an antenna array with an order of magnitude more elements, say 100 antennas or more, is considered. Such systems are expected to increase the capacity 10 times or more and simultaneously improve the radiated energy efficiency on the order of 100 times. Massive MIMO systems are promising candidates for 5G.

In fact, the deployment of large-scale antenna arrays makes the simple spatial precoding techniques to be efficient and optimal. The conjugate approach precoding techniques, such as the maximum ratio transmission (MRT), equal gain transmission (EGT) and time reversal (TR), use directly (or slightly modified) the conjugate of channel response as the precoder, to achieve an effect of matched filtering and lead to an energy focusing onto the target user. This kind of precoding techniques may perform sub-optimally in terms of interference cancellation compared to

the zero-forcing (ZF) approach, but provide a high energy efficiency and robustness in low SNR (signal-to-noise ratio) regime.

However, under practical constraints, not all the systems can be equipped with a very large-scale antenna array. In this thesis, we are interested in moderate-scale MU-MIMO systems, say $4 \sim 64$ antennas, which can be considered as an intermediate between the classical small-scale MIMO (≤ 10 antennas) and the massive MIMO systems. In this way, we can take advantage of the multi-antenna multiplexing gain while maintaining the implementation to a reasonable cost. However, with such a not-so-large scale, some results derived for massive MIMO systems, based on the random matrix theory (RMT), may lack of precision. The objective of this thesis is to optimize the throughput of moderate-scale MU-MIMO systems using conjugate approach spatial precoding. We are interested in the theoretical performance analysis of these precoding techniques. We look for establishing precise performance models for arbitrary number of transmit antenna and SNR level. The results will be compared with that obtained for massive MIMO systems.

In addition, for such moderate-scale MU-MIMO systems, the number of antennas may not sufficient to provide high energy focusing gain, hence, not able to assume perfect spatial division among the users. Consequently, the users can not use the same frequency bandwidth as in massive MIMO systems, and need to be separated in frequency. In this case, we propose a partial frequency bandwidth overlay (PFBO) transmission scheme to adapt the low-level energy focusing gain and to improve the system capacity. Such a system can be considered as a combination of the traditional frequency division multiple access (FDMA) and SDMA systems. The advantage of such a system is the high flexibility, such that the inter-channel interference can be controlled directly by the overlap ratio between the users. Therefore, for an arbitrary number of transmit antennas and SNR level, an optimal overlap ratio can be determined. The performance of the PFBO scheme is analyzed in this thesis with single-carrier and multi-carrier (known as orthogonal frequency division multiplexing, OFDM) waveforms. Moreover, spreading spectrum (SS) techniques are also proposed to be combined with the PFBO-OFDM scheme to further enhance the system performance.

Organization and Contributions

In the first chapter, we introduce the general techniques and concepts used in this thesis. We begin with a succinct overview on MIMO systems. Then classical MU-MIMO systems and the emerging massive MIMO systems are specified. Then the MU MIMO-OFDM transmissions system is presented. Various spatial precoding/beamforming techniques are introduced. We present in the third section the system model, including the moderate-scale MU-MIMO transmission scenario and the PFBO transmission scheme. In the last section, we present the propagation channel models, including the common AWGN channel model, the Rayleigh channel model and a set of indoor channel models decided at broadband radio access networks (BRAN) for HIPERLAN/2 simulations, called BRAN channel models.

In the second chapter, we analyze at first the spectral efficiency of the PFBO schemes with single carrier and multi-carrier signals. The optimal overlap ratios which provide the maximum achievable rate for two-user SIMO and MIMO systems are identified versus the SNR level and the scale of transmit antenna array. In the third section, we extend the capacity analysis to classical MU-MIMO systems with arbitrary number of users. Precise capacity approximations are derived with EGT, TR and MRT techniques, respectively. To that end, we introduce for each precoding

technique a statistical model for the non-flat fading channel and the interfering channel is Gaussian approximated. New closed-form capacity lower bounds are proposed in function of the number of transmit antennas. The obtained formula present higher accuracy than that derived for massive MIMO systems.

In the third chapter, the bit error rate (BER) performance of PFBO schemes is studied. The performance derivation is at first drawn with AWGN channel. Closed-form BER equation is obtained. Then we analyze the coherence bandwidth evolution of theoretical Rayleigh channels and Bran channels in function of the antenna array scale to demonstrate the difference of channel behavior between moderate-scale MU-MIMO systems and massive MIMO systems. In the last section, the BER performance derivation is drawn using theoretical Rayleigh channels. We propose a statistical model to approximate the non-flat fading channel and the correlated interference channel for two-user EGT MIMO systems using BPSK modulation. The analytical BER equations are confirmed through Monte-Carlo simulations. The study is then extended to QPSK and more users cases.

In the fourth chapter, the BER performance of PFBO schemes combined with SS-OFDM systems is studied. We begin by deriving the performance analysis using AWGN channel. Closed-form BER equation is obtained. Then we study the BER performance using Rayleigh channel model. Different interference components are identified and modeled. Accurate BER approximation is proposed. In the last section, we present the simulation results of OFDM and SS-OFDM systems with PFBO and MU-MIMO transmission schemes. The SS-OFDM systems are shown to be beneficial when combined with the PFBO scheme. However, with MU-MIMO schemes, the OFDM systems outperform the SS-OFDM systems.

At the end of thesis, we draw the conclusion and perspectives of our works.

Publications

Journal Paper

H. Fu, M. Crussière and M. Hélard, "BER Analysis for Downlink Multiuser MIMO-OFDM System using Equal Gain Transmission", accepted for publication in *IEEE wireless communications Letters*.

Communications Papers

H. Fu, M. Crussière and M. Hélard, "Partial channel overlay in moderate-scale MIMO systems using WH precoded OFDM", in *Proc. 21st International Conference on Telecommunications (ICT 2014)*, pp. 16-21, Lisbon, Portugal, May 2014.

H. Fu, M. Crussière and M. Hélard, "Spectral Efficiency Optimization in Overlapping Channels using TR-MISO Systems", in *Proc. IEEE Wireless Communications and Networking Conference (WCNC 2013)*, pp. 3770-3775, Shanghai, China, Apr. 2013.

National Communication

H. Fu, M. Crussière and M. Hélard, "Optimisation de la ressource spectrale pour les systèmes MU-MIMO avec recouvrement fréquentiel partiel", Réunion du GdR ISIS *L'Eco Radio*, Télécom ParisTech, May 2015.

CHAPTER 1

CONTEXT AND SYSTEM MODEL

In this first chapter, we present the main techniques and concepts used in this thesis. We begin by introducing the MIMO system model. The classical MU-MIMO systems and the emerging massive MIMO systems are presented in particular, which will be at the basis of our work. Then in the second section, we present the MIMO-OFDM transmission chain. Various linear precoding techniques are also specified for MU-MIMO OFDM context. In the third section, we introduce the system model of this thesis, which consists in a moderate-scale MU-MIMO transmission scenario. In addition, we propose the partial frequency bandwidth overlay (PFBO) transmission scheme which is intended to optimize the spectral resources sharing for MU-MIMO systems in the case where the number of transmit antennas are not sufficient to perform perfect SDMA. The propagation channel models are introduced in the fourth section, including the common AWGN channel model, the frequency Rayleigh channel model and the practical BRAN channel models.

1.1 MIMO systems

In the last two decades, MIMO techniques have raised great interests in the R&D activities on wireless communications systems. MIMO has been adopted as a key technology in various new generation wireless communications standards, such as LTE, WLAN, WIMAX, etc. Different from the traditional single-input single-output (SISO) system, MIMO system proceeds multiple antennas at transmitter and/or receiver sides, which provides an additional degree of freedom: the space dimension. According to the channel conditions and the system design, this new dimension promises two types of advantages, namely diversity gain and spatial multiplexing gain [1].

In this section, we first present a brief history of MIMO techniques and show the development of various MIMO algorithms. Then we remind the channel capacity of SISO and MIMO systems, revealing the potential capacity gain of MIMO techniques. The MU-MIMO and the innovative massive MIMO systems are particularly described in detail in the third part.

1.1.1 History of MIMO techniques

The MIMO technology is a breakthrough of the smart antenna technology in the domain of wireless communications. It has been intensely developed in the last two decades, various processing schemes have been proposed to exploit the spatial diversity gain as well as the spatial multiplexing gain.

In 1993, Wittneben has first introduced the diversity gain of MIMO systems [2]. He proposed to use multiple antennas to improve the system performance: the same message is transmitted through multiple antennas with different modulation parameters. The same year, Seshadri and Winters proposed two different transmission schemes by using multiple antennas at the transmitter [3]. The first scheme used channel coding, the coded symbols are transmitted through different transmit antennas. The diversity gain is observed when the transmission and reception antenna pairs are independent between each other (achieved by spacing the transmit or receive antennas several wavelengths apart). The second scheme introduces deliberate resolvable multipath distortion by transmitting on different antennas successfully delayed versions of the data symbols. At the receiver, a maximum likelihood sequence estimator resolves the multipath in an optimal manner to realize the diversity gain. This delay diversity scheme is considered as a first attempt to develop space-time codes (STC) [4].

In 1997, Paulraj described how space-time processing reduces the cochannel interference (CCI) while enhancing the diversity and antenna array gain, which can be used to improve the system capacity, coverage and transmission quality [5]. Tarokh et al. proposed in 1998 the space-time trellis codes (STCC) [4] and in 1999 the space-time block codes (STBC) [6] to achieve the maximum diversity order for a given number of transmit and receive antennas. Also in 1998, Alamouti proposed a scheme using two transmit antennas and N receive antennas to attain a diversity order of $2N$ [7]. In 1999, Narula explored several aspects of the design and optimization of coded multiple antenna transmission diversity methods for slow fading channels. The performance of optimized vector-coded systems and suboptimal scalar-coded systems are investigated. The achievable rates and associated outage characteristics of these systems are evaluated and compared, the complexity and implementation issues are also discussed [8].

Otherwise, it is possible to exploit the spatial diversity without channel state information (CSI) at neither the transmitter (CSIT) nor the receiver (CSIR), namely incoherent/differential detection, on the contrary to the coherent detection which uses CSI at the receiver to decode the data symbols. The first incoherent detection methods are proposed by Tarokh and Alamouti in 1998 [9]. The system provides the same diversity order as the coherent detection case but suffers from a $3dB$ penalty.

In addition, instead of exploiting the diversity gain to combat the multipath fading, another idea tends to use the multipath propagation as an advantage, turning the additional signal paths into additional channels to carry extra information. This leads to the spatial multiplexing gain of MIMO systems. In 1987, Winters studied the fundamental limits on the data rate of MIMO systems in Rayleigh fading environments [10]. He demonstrated that with M transmit and M receive antennas, up to M independent channels can be established in the same bandwidth. This results shows the large potential capacity gain of MIMO systems. In 1995, Telatar intestigated the use of multiple transmit and/or receive antennas for single user communications over the additive Gaussian channel with and without fading [11]. The capacity and error exponent formulas of such systems were derived. The results show that the potential capacity gains of MIMO systems is rather large when the fades and noises at different receive antennas are assumed independent. In 1996, Foschini began to analyze the MIMO systems with CSI available at the receiver. His

works show that for a $M \times M$ MIMO system, despite the M received waves interfering randomly, the system capacity grows linearly with M. He also invented a codec architecture called D-BLAST to approach the great capacity promised by MIMO systems [1]. In 1998, Foschini and Wolniansky proposed the V-BLAST architecture, which has been implemented in real-time in Bell labs. Using a laboratory prototype, the spectral efficiencies attain 20-40 bps/Hz in an indoor propagation environment at realistic SNRs and error rates. This is the first demonstration of spatial multiplexing transmission. The wireless spectral efficiencies of this magnitude are unprecedented and are furthermore unattainable using traditional SISO techniques [12].

The benefits of MIMO techniques can be further enhanced if both the transmitter and the receiver know CSI. In 1999, Telatar analyzed the capacity of a multiple-antenna system with perfect CSIR and CSIT [11]. The work of Skoglund and Jöngren in 2003 splitted the capacity-achieving encoder into separate fixed-codebook space-time encoding and beamforming based on the CSI feedback without capacity loss [13].

Apart from the conventional MIMO system where the transmission is carried out between one transmitter and one receiver (point-to-point) through M transmit antennas and N receive antennas (also called $M \times N$ single-user (SU) MIMO), the MU-MIMO system is developed and has received growing interests. MU-MIMO systems consist of a BS with M transmit antennas and N receive antennas employed by K users. Each user has one or more receive antennas, then $K \leq N$ [14]. The spatial multiplexing gain of SU-MIMO system is converted into a space division multiplexing gain which can be used as a novel multiple access method, namely SDMA. If the system only uses CSIR, in downlink (DL) transmission, it is possible to apply multi-user detection (MUD) for a given user to overcome the multiple access interference (MAI), but such techniques are often too costly to be used at the receivers [15]. Ideally, with CSIT and CSIR, it is preferable to mitigate the MAI at the transmitter side by intelligently designing the transmitted signal using MU-MIMO beamforming techniques or the coding techniques such as dirty paper coding (DPC) [16, 17].

Following this idea, more recently in 2010 [18], Marzetta introduced the massive MIMO concept, by using a large number of transmit antennas in MU-MIMO systems, the space division multiplexing gain being hereby substantially amplified. Both massive MIMO systems and MU-MIMO systems are described in 1.1.3.

MIMO is one of the fundamental element in the LTE system. In the most recent LTE-advanced (LTE-A, 3GPP Release 11) standard, a 8×8 MIMO is designed for DL transmission and 4×4 MIMO for uplink (UL) transmission. The LTE standard exploits the MIMO system with different operating modes, including spatial diversity, open and closed loop spatial multiplexing and closed loop MU-MIMO, and the system is able to switch between these modes to adapt the different operating circumstances. MIMO is also introduced in the IEEE 802.11n protocol for WLAN system and the standard IEEE 802.16, known as WiMAX, for up to 4×4 antenna chains.

1.1.2 SISO and MIMO system capacity

In this part, we present the channel capacity of SISO and MIMO systems. This helps to reveal the potential capacity gain of MIMO system and to understand the influence of various system parameters on the channel capacity.

1.1.2.1 SISO system capacity

According to Shannon [19], the capacity of a communication channel is the maximum bit rate for which arbitrarily small error probability can be achieved. The maximum achievable capacity of the additive white Gaussian noise (AWGN) channel in a SISO system is defined by the famous Shannon equation:

$$C_{awgn} = B_w \log_2 (1 + \text{SNR}) \tag{1.1}$$

where B_w is the frequency bandwidth, SNR is the received signal to noise ratio.

For fading channels, no single definition of capacity can be applicable in all scenarios. Several notions of capacity are developed to form a systematic view of performance limits of fading channels. These various capacity measures reveal the different resources available in fading channels: power, diversity and degrees of freedom [19].

With only CSIR, the transmitter sends the information data over all available frequency bandwidth including deep fading frequencies. In this case, two channel capacity definitions can be used, namely ergodic (Shannon) capacity and outage capacity [20, 21]. The ergodic capacity is defined as [20]:

$$C_{erg} = \int_0^{\infty} B_w log_2 (1+\gamma)\, p(\gamma)\, d\gamma \tag{1.2}$$

where γ is the instantaneous SNR at the receiver, $p(\gamma)$ is the probability density function (PDF) of γ. The ergodic capacity measures the average of the instantaneous capacity.

On the other hand, outage capacity applies to slow fading channels where the instantaneous SNR is assumed to be constant for a large number of symbols. Unlike the ergodic capacity scenario where the data needs to be correctly received over all fading states, the outage capacity fixes a higher transmission rate in admitting some data loss in deep fading frequencies. Specifically, the transmitter fixes a minimum received SNR γ_{min}. When the received SNR is below γ_{min}, the received symbols cannot be correctly decoded and the receiver declares an outage. The probability of outage is $p_{out} = p(\gamma < \gamma_{min})$. The average rate correctly received over many transmission bursts is:

$$C_{out} = (1 - p_{out})\, B_w log_2 (1 + \gamma_{min}) \tag{1.3}$$

We note that the value γ_{min} is typically a design parameter based on the required outage probability. The average rate correctly received C_{out} can be maximized by finding the optimal γ_{min}.

1.1.2.2 SU-MIMO system capacity

For SU-MIMO systems, the transmission is carried out between one transmitter and one receiver through M transmit antennas and N receive antennas. A $M \times N$ SU-MIMO system is presented in Fig. 1.1. Assuming flat fading channel, the channel response can be written as a matrix $\underline{\mathbf{h}} \in \mathbb{C}^{M \times N}$ with the element $h_{m,n}$ corresponding to the flat fading coefficient of the link between the mth transmit antenna and the nth receive antenna. We can, on one hand, exploit the antenna diversity when each transmit and receive antennas pair transmits the same information [22]. In this case, each antenna pair can be considered as an additional signal path. The receiver side receives multiple independently faded copies of the information, which helps to confront the channel fading and enhance the transmission quality.

Antenna diversity can be utilized at the transmitter and/or the receiver [23]. Receive antenna diversity systems intelligently combine the multiple received copies to achieve a higher average receive SNR [23]. A classical combing technique is maximum-ratio combining (MRC) [24], where

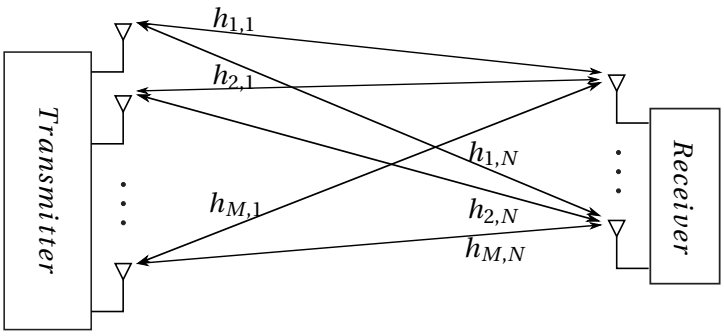

Figure 1.1: $M \times N$ SU-MIMO system

the signals from the received antenna elements are weighted such that the SNR of their sum is maximized. Transmit antenna diversity is more difficult to obtain, the channel-dependent beamforming techniques (with CSIT required) or the channel-independent space-time coding techniques can be used.

Particularly, for the case where CSIT and CSIR are both available, the maximum ratio transmission (MRT) is proposed by Lo [25] for SU-MIMO systems. It can be considered as the generalization of the maximum ratio algorithm for multiple transmitting antennas and multiple receiving antennas. It also provides a reference for the optimum performance that a system may obtain using both transmit and receive diversity [25]. Using the diversity expression of [25], the system capacity writes:

$$C = B_w \log_2 \left(1 + \frac{1}{N} \sum_{p=1}^{N} \sum_{q=1}^{N} \left| \sum_{m=1}^{M} h_{m,p} h_{m,q}^{*} \right| \mathrm{SNR} \right). \tag{1.4}$$

In the case where the transmission links are mutually orthogonal, i.e. $\forall p \neq q, \left| \sum_{m=1}^{M} h_{m,p} h_{m,q}^{*} \right| = 0$, the system capacity takes the smallest value:

$$C = B_w \log_2 \left(1 + \frac{1}{N} \sum_{n=1}^{N} \sum_{m=1}^{M} \left| h_{m,n} \right|^2 \mathrm{SNR} \right), \tag{1.5}$$

In the case where the transmission links are fully correlated, i.e. $\forall p \neq q, \left| \sum_{m=1}^{M} h_{m,p} h_{m,q}^{*} \right| = \sum_{m=1}^{M} \left| h_{m,q} \right|^2$, the system capacity takes on the largest value:

$$C = B_w \log_2 \left(1 + \frac{1}{N} \sum_{p=1}^{N} \sum_{q=1}^{N} \sum_{m=1}^{M} \left| h_{m,q} \right|^2 \mathrm{SNR} \right), \tag{1.6}$$

On the other hand, when the transmission links are considered independent from each other, they can be used to transmit different information, and form multiple parallel spatial channels [22]. In this case, the system capacity can be enhanced thanks to the spatial multiplexing gain. Foschini has shown in [1] that in high SNR regime, assuming CSIR and i.i.d. Rayleigh-faded gains between each antenna pair, the MIMO system channel capacity is:

$$C = \check{M} B_w \log_2(SNR) + O(1) \tag{1.7}$$

where $\check{M} = min\{M, N\}$. Hence the theoretical MIMO channel capacity is multiplied comparing to that of a SISO system.

In this case, if CSIT and CSIR are both available, *waterfilling* techniques can be performed to further improve the system capacity. *Waterfilling* techniques allow optimization of the MIMO system capacity by intelligently allocating power among the transmit antennas. The channel matrix $\underline{\mathbf{h}}$ is decomposed as $\underline{\mathbf{h}} = \underline{\mathbf{udv}}^H$ with $\underline{\mathbf{u}} \in \mathbb{C}^{M\times M}$ and $\underline{\mathbf{v}} \in \mathbb{C}^{N\times N}$ are unitary matrix, $\underline{\mathbf{d}} \in \mathbb{C}^{M\times N}$ is a rectangular diagonal matrix with non-negative real numbers $d_k, k \in \{1,\ldots,\check{M}\}$ on the diagonal. The "optimal power allocation" scheme is the solution to the well-known optimization problem [26]:

$$C_{opt} := \max_{P_1,\ldots,P_{\check{M}}} \sum_{k=1}^{\check{M}} B_w \log_2\left(1 + \frac{P_k d_k^2}{\sigma_b^2}\right), \tag{1.8}$$

$$\sum_{k=1}^{M} P_k = P_T, P_k \geq 0 \tag{1.9}$$

where P_T is the total transmit power constraint, σ_b^2 is the variance of the AWGN noise at the receiver.

By Lagrangian methods, the optimal power allocation converges to:

$$P_k^* = \left(\frac{1}{\lambda} - \frac{N_0}{d_k^2}\right)^+ \tag{1.10}$$

where λ is the Lagrange multiplier, $x^+ := max(x, 0)$. This solution can be considered as decomposing the MIMO channel as a set of parallel independent subchannels whose number equals the rank of matrix H ($\check{M}$), and their gains are the singular values d_k. *Waterfilling* scheme assigns more power to the subchannels with greater gain, and assigns less or no power to the subchannels with small gain. This scheme can be illustrated by a scenario of filling a vessel as shown in Fig. 1.2, therefore named as *waterfilling* strategy.

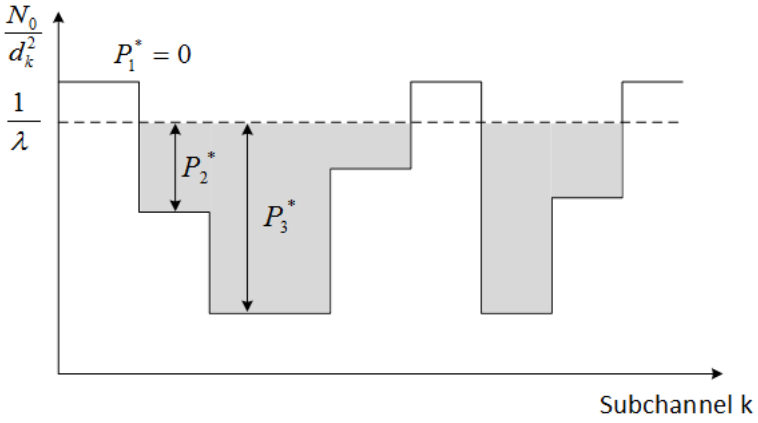

Figure 1.2: Waterfilling power allocation scheme

waterfilling techniques provide the optimal system capacity for SU-MIMO transmission scheme. However, these techniques require a high supplementary computation burden.

1.1.3 MU-MIMO and Massive MIMO systems

1.1.3.1 MU-MIMO system

Classical MU-MIMO systems assume a BS with M transmit antennas and in total N receive antennas employed by K users ($K \leq N$). The users are served simultaneously by the BS thanks to the SDMA. In this way, expensive equipment is only needed on the BS side and the user terminals can be relatively cheap single (or few) antenna devices [27]. Moreover, as time or frequency multiplexing is omitted, the system possesses reduced latency [28], simplified MAC layer, and more robustness against intentional jamming. MU-MIMO systems are expected to attain similar capacity as $M \times N$ SU-MIMO systems [29] with the performance generally less sensitive to the propagation environment due to the multiuser diversity.

In general, assuming CSIT and CSIR, two different approaches are considered for MU-MIMO systems: linear processing and DPC. Linear processing techniques consist in mitigating the MAI through channel inversion [30]. These techniques are rather simple with small dimension antenna array, but it has been shown in [31] that they do not result in the linear capacity growth with $\min(M,N)$ as expected for MU-MIMO system. This is because under transmitted power constraint, an ill-conditioned channel matrix after inversion may require a large normalization factor which will dramatically reduce the SNR at the receivers. Another solution is DPC technique which is a nonlinear method based on the concept of "writing on dirty paper" [16]. The application of this concept to DL MU-MIMO transmission is proposed in [17]. Assuming CSIT, the transmitter knows how the signal destined to $user1$ will affect $user2$, hence the transmitter can design a signal for $user2$ that avoids the known interference. This concept has been used to characterize the sum-capacity of the MU-MIMO system and indicates that the linear capacity growth is achievable. DPC can be performed through a QR decomposition of the channel or directly by designing jointly all the transmit signals [31]. The classical MU-MIMO system is of great interest for its high capacity and interference suppression, however, due to the high level of complexity of the channel decomposition or coding and the strict central coordination constraint, such classical MU-MIMO approaches are limited to a decade of transmit antennas and users.

1.1.3.2 Massive MIMO system

Massive MIMO is an emerging technology intensively developed in the last years. First proposed by Marzetta in 2010 [18], the idea is to use a very large number of transmit antennas at the BS to achieve orders of magnitude improvement in spectral and energy efficiency compared to the traditional small-scale MIMO systems [18, 32, 33, 27]. Massive MIMO systems are usually conceived with a few hundred antenna arrays. Asymptotic arguments based on RMT [18] demonstrate that the effects of uncorrelated noise and small-scale fading are eliminated, the number of users per cell are independent of the size of the cell, and the required transmitted energy per bit vanishes as the number of transmit antenna grows to infinity [27]. Furthermore, thanks to the large number of degrees of freedom, very simple linear precoding process can be used in massive MIMO systems to achieve high spatial division multiplexing gain.

The large excess of transmit antennas in massive MIMO systems realize a high-precision energy focusing onto the target user. A ten times or more growth in capacity can be expected [33]. An example has been shown in [18] that under realistic propagation assumptions, non-cooperative massive MIMO systems using matched filter (MF) precoding could in principle achieve a data rate of 17 Mbps for each of 40 users in a 20 MHz channel in both the UL and DL transmissions, with an average throughput of 730 Mbps per cell and an overall spectral efficiency of 26.5 bps/Hz.

Massive MIMO systems also provide high energy efficiency. It is shown in [34] that each single-antenna user in a massive MIMO system can scale down its transmit power proportionally to the number of antennas at the BS with perfect CSI, or to the square root of the number of BS antennas with imperfect CSI, to achieve the same performance as a SISO system without interference and fast fading. This results is very important for the development of "Green Communications" for future wireless networks, which looks for reducing the energy consumption for both BS and user terminals.

However, as massive MIMO technology resolves many inherent problems of the traditional communications systems, it brings new challenges [33]. For example, how to make many low-cost low-precision components to work together correctly? How to acquire and synchronize the users? How to reduce the internal power consumption to achieve a total energy saving? There are still many crucial challenges, as summarized hereafter.

- Channel estimation

To achieve high spatial division multiplexing gain, the BS should have good CSI for both the UL and the DL transmissions [33]. In general, frequency-division duplex (FDD) and time-division duplexing (TDD) modes are used to separate the UL and DL resource. For FDD, UL and DL use different frequency bands, which leads to different CSI. Channel estimation for the UL is done at the BS using the pilot sequences sent by the users. The time required for UL pilot transmission is independent of the number of antennas at the BS. However, channel estimation for the DL is more complex. The BS first transmits pilot symbols to all users, then the users feed back the estimated CSI of DL channel to the BS. The time required to transmit the DL pilot symbols is proportional to the number of antennas at the BS, which makes FDD infeasible for large-scale MIMO systems. Nevertheless, FDD mode can be used by designing precoding methods using partial CSI [35] or even no CSI or by exploiting potential frequency channel reciprocity with frequency correction algorithms [36].

Therefore, TDD mode is usually assumed for massive MIMO systems [37, 33, 27]. The BS uses directly the CSI obtained during the UL transmission to perform the DL precoding processing. The feasibility of this solution depends on the reciprocity between the UL and the DL channels, which we will discuss in the following. A TDD protocol is proposed in [37] and shows that it is always advantageous to increase the number of base stations, even when the UL SINR is low and the channel estimate poor. However, due to the limited channel coherence time, the same pilot sequences are reused among the neighboring cells [18], leading to the pilot contamination problem which is later presented.

- Channel reciprocity

The TDD mode allows both UL and DL signals to benefit from the whole frequency bandwidth of the channel. The reliability of TDD depends on the channel reciprocity. When the terminals are not moving very fast, e.g. indoor environment, the propagation channel can be considered as reciprocal. However, considering the imperfection of the materials, the hardware level chains between the BS and the terminals are not reciprocal. In practical, some calibration-based solutions have been tested [38, 39]. Specifically, [38] has discussed the reciprocity calibration in some details and obtained the successful experiment results with a 64-antenna system namely *Argos*. In fact, if the BS equipment is properly calibrated, the antenna array is still able to transmit a coherent beam to the terminal. While at the terminal side, the mismatch can be handled with some low-cost overheads [33].

- Pilot contamination

In a multi-cell context, the gain of massive MIMO can be limited by the pilot contamination. In fact, the maximum number of orthogonal pilot sequences is upper-bounded by the duration of the coherence interval divided by the channel delay spread [18]. Hence the same pilot sequence can be reused by the users in adjacent cells as shown in the left part of Fig. 1.3. Then at the BS, the result of channel estimation contains also the information from the users of other cells (dotted line). As a consequence, when the BS performs signal precoding with the contaminated channel estimation, a part of signal will be addressed to the undesired users (dotted line in the right part of Fig. 1.3) and acts as inter-cell interference.

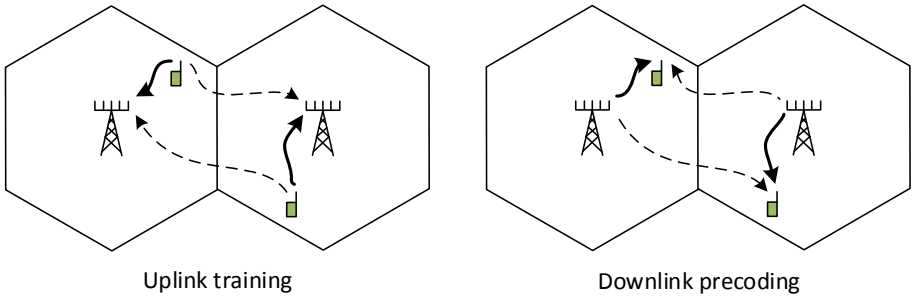

Figure 1.3: Pilot contamination problem

The interference caused by pilot contamination increases with the number of transmit antennas at the same rate as the desired signal [18]. As a consequence, the system performance is limited even when the number of transmit antennas tends to infinite. Many papers have dealt with this problem: constructing a coordination scheme between the BSs to optimize the pilot allocation [40, 41] or even estimating the channel directly from the received data thanks to the asymptotic orthogonality within massive MIMO channels [42].

1.2 Precoded MU-MIMO OFDM systems

In this section, the precoded MU-MIMO OFDM system is introduced, which is the transmission scenario of our works. The OFDM is applied to divide the frequency bandwidth into a set of parallel flat fading subbands which enables to perform the linear precoding techniques. We present at first the principles of OFDM modulation, then we explain how the MIMO techniques are combined with OFDM systems. At the end, the diverse linear precoding techniques are specified and adapted to the MIMO-OFDM context.

1.2.1 OFDM technique

The multicarrier modulation, also known as OFDM, has become a key technique in many communications systems, both for wired and wireless systems such as asymmetric digital subscriber line (ADSL), digital video broadcasting (DVB-C, DVB-T, DVB-H), power line communication (PLC), WLAN, and 4G cellular networks and mobile broadband standards, etc. The con-

cept of frequency multiplexing has been first proposed by Doeltz in 1957 [43], but until 1980s, with the development of the digital modulators, the OFDM technique finally became popular.

The general idea of OFDM consists in diving a common wideband frequency-selective channel into a set of individual subchannels. The bandwidth of subchannels is assumed narrow enough such that the fading is considered frequency-flat in each subchannel. As a consequence, the equalization process reduces to divide each received symbol by the corresponding fading coefficient, which also called one-tap equalization. In addition, as the subcarriers fade independently, diverse resource allocation schemes can be applied to approach the ideal water-filling capacity of the channel. Moreover, multiple access can be easily achieved by assigning subsets of subcarriers to different users, namely OFDMA system.

OFDM is a block modulation scheme as presented in Fig. 1.4. After mapping, a set of N_f symbols $[a_1, a_2, \ldots, a_{N_f}]$ is allocated in parallel to N_f subcarriers. The time duration of an OFDM symbol is N_f times longer than that of a single-carrier system, as one subcarrier bandwidth is N_f time smaller than that of the single-carrier bandwidth. The OFDM modulation is performed through an inverse fast Fourier transform (IFFT) [44]. The OFDM symbol is expressed as:

$$x_n = \frac{1}{\sqrt{N_f}} \sum_{p=1}^{N_f} a_p e^{j\frac{2\pi pn}{N_f}}, \quad n \in \{1, \ldots, N_f\} \tag{1.11}$$

Then a guard interval (GI) is added at the head of OFDM symbol to combat the ISI caused by the channel multipath spreading. The length of GI l_{GI} should be superior or equal to the channel spreading length. Then the OFDM symbol is rearranged in series and transformed in analogical signal through the analog-to-digital converter (ADC). In Fig. 1.4, only the baseband transmission scheme is presented.

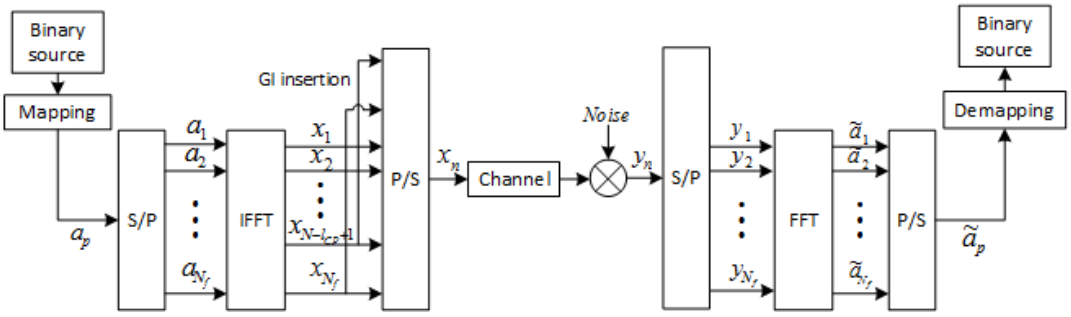

Figure 1.4: OFDM modulation and demodulation scheme

At the reception side, after similar RF and analog components as the transmitter, we reconstruct the received baseband signal y_n. The GI part is then removed. Thanks to the GI, the linear convolution of the transmitted sequence and the channel is converted to a circular convolution. With the fast Fourier transform (FFT), the temporal circular convolution is presented as a scalar multiplication in frequency domain. The received symbol after FFT is:

$$\tilde{a}_p = \frac{1}{\sqrt{N_f}} \sum_{n=1}^{N_f} y_n e^{-j\frac{2\pi pn}{N_f}}, \quad p \in \{1, \ldots, N_f\} \tag{1.12}$$

Then, as necessary, the frequency equalization is processed to correct the distortion comes from channel fading.

We note that the OFDM system is sensitive to the carrier frequency offset (CFO) as well as time and frequency synchronization error, hence the training sequences are required. Moreover, as the OFDM signal consists in a superposition of various tones of signal, the signal envelope is far from constant. The peak-to-average-power ratio (PAPR) is used to measure the fluctuation of the signal. As a consequence, OFDM signal requires high linearity RF components, which are poor energy efficiency. The PAPR reduction is a popular topic in the research of OFDM system.

1.2.2 MIMO-OFDM systems

MIMO technique can be combined with the OFDM systems by using in parallel OFDM modulator on each transmit antenna as shown in Fig. 1.5, while the OFDM demodulator is also applied on each receive antenna of the user. In this way, a MIMO frequency-selective channel is transformed into a MIMO flat-fading channel for each OFDM subcarrier [45]. The spatial precoding techniques can then be performed via each OFDM subcarrier.

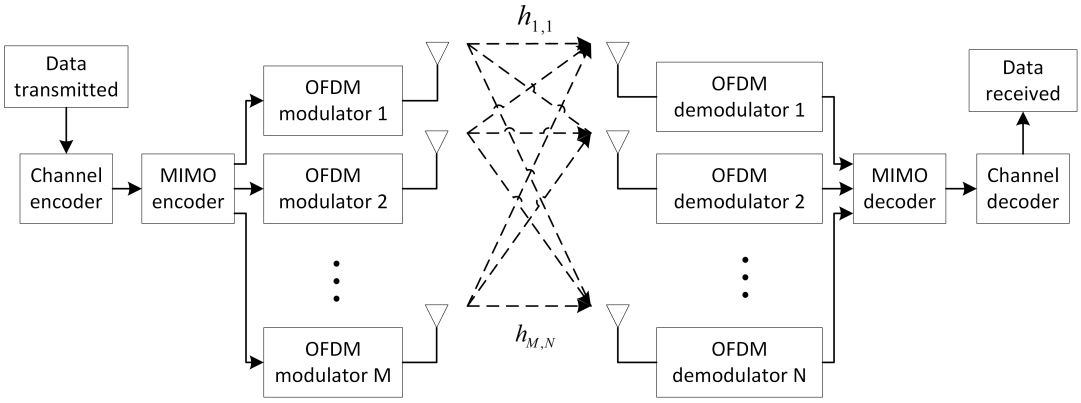

Figure 1.5: $M \times N$ MIMO OFDM system

1.2.3 Linear precoding techniques in MU-MIMO OFDM systems

The linear precoding techniques, also sometimes called beamforming, have been extensively developed in the last decades. It is considered as an advantageous way to exploit the full diversity of the channel. For MU-MIMO systems, assuming flat fading channel, the precoding techniques are used to form a beam signal via the target user while reducing the interference to the other users. In general, besides the capacity optimizing singular value decomposition (SVD) methods, the linear precoding methods can be classed by two approaches: zero-forcing (ZF) approach such as ZF and regularized ZF (RZF)/minimum mean square error (MMSE). This approach seeks to minimize the MAI among the users and leads to a centralized architecture where the BS collects the channel response of all the users to form the precoder matrix. The conjugate precoding approach is based on the maximum ratio algorithm, in the propose of maximizing the useful signal power at the reception side. This approach in general uses the conjugate of the channel response as the precoders, to enable the precoded signals transmitted from different antennas add ”in-phase” at the location of receiver, this phenomena is also known as spatial focusing. The common conjugate precoding approach includes maximum ratio transmission (MRT), equal gain transmission (EGT) and time reversal (TR)/matched filter (MF) [46]. The conjugate precoding approach often

leads to a de-centralized architecture where per-antenna processing is feasible. The computation complexity is widely reduced comparing to the ZF approach.

In this part, the different precoding techniques are presented in the context of MU-MIMO OFDM system where each OFDM subcarrier is considered as a flat fading sub-channel. A transmission scenario of a BS with M transmit antennas and K single-antenna users is considered. Perfect synchronization is assumed between the BS and the users.

1.2.3.1 SVD

The precoding techniques based on SVD are considered as the optimal methods to maximize the system performances [47, 48]. In fact, the MIMO channel can be resulted as a set of independent and parallel links, with the maximum number of links equals the minimum of transmit and receive antennas number [48].

For the pth OFDM subcarrier , the channel response can be expressed by a $M \times K$ matrix:

$$\underline{\mathbf{H}}_p = \left[\mathbf{H}_p^{(1)}\ \mathbf{H}_p^{(2)} \ldots \mathbf{H}_p^{(K)}\right] \in \mathbb{C}^{M\times K} \tag{1.13}$$

each column $\mathbf{H}_p^{(k)} \in \mathbb{C}^{M\times 1}$ refers to the channel frequency response (CFR) of $user k$ on the pth OFDM subcarrier via the M transmit antennas.

With perfect CSIT, the parallel channels are established by applying SVD to the channel matrix:

$$\underline{\mathbf{H}}_p = \underline{\mathbf{U}}_p \underline{\mathbf{D}}_p \underline{\mathbf{V}}_p^H \tag{1.14}$$

Then $\underline{\mathbf{U}}_p \in \mathbb{C}^{M\times M}$ is used at the transmitter as the precoding matrix, $\underline{\mathbf{V}}_p \in \mathbb{C}^{K\times K}$ is multiplied to the signal at the receiver as the postcoding matrix. In this way, the signals are transmitted through independent beams, which are, indeed, the eigenvectors of the channel correlation matrix $\underline{\mathbf{H}}_p^H \underline{\mathbf{H}}_p$. The beam power loadings are the squared singular values $\underline{\mathbf{D}}_p^2$.

The drawback of the SVD method is the high computing complexity. For a $M \times K$ channel matrix, SVD takes $O(MK^2)$ operations [49]. Moreover, the postcoding matrix need to be communicated to the users to decode the received signal. However, for MISO link, the SVD method reduces to the well known maximum ratio transmission (MRT) scheme [50].

1.2.3.2 ZF

ZF precoding techniques has received a lot of attention for classical MU-MIMO and massive-MIMO systems [51, 52, 53]. The idea is to completely annul the MAI through channel inversion. Taking the channel response $\underline{\mathbf{H}}_p$ described for SVD method, the ZF precoding matrix corresponding to the pth OFDM subcarrier writes [46]:

$$\underline{\mathbf{V}}_p = c_p \left(\underline{\mathbf{H}}_p \underline{\mathbf{H}}_p^H\right)^{-1} \underline{\mathbf{H}}_p \in \mathbb{C}^{M\times K}, \tag{1.15}$$

with c_p is the power normalization scalar, $c_p = \frac{1}{\sqrt{tr\left(\underline{\mathbf{H}}_p \underline{\mathbf{H}}_p^H\right)^{-1}}}$. If $\underline{\mathbf{H}}_p \sim CN(0,1)_{M\times K}$, $\mathbb{E}\left[c_p\right] = \frac{M-K}{K}$, with CN$(0,1)$ presents zero-mean, circularly-symmetric, unit-variance, complex Gaussian distributions.

The symbols transmitted on the M antennas are:

$$\mathbf{X}_p = \underline{\mathbf{V}}_p \left[a_{1,p}\ a_{2,p}\ \ldots\ a_{K,p}\right]^T \in \mathbb{C}^{M\times 1}, \tag{1.16}$$

$a_{k,p}$ presents the data symbol transmitted to user k on the pth subcarrier.

Hence, the symbols received by the K users are:

$$\mathbf{Y}_p = \underline{\mathbf{H}}_p^H \mathbf{X}_p = c_p \left[a_{1,p} \; a_{2,p} \; \dots \; a_{K,p} \right]^T \in \mathbb{C}^{K \times 1}. \tag{1.17}$$

The users receive on pth subcarrier the data symbol with power c_p^2.

ZF is simpler than SVD method since no postcoding processing is required for the users. For a $M \times K$ channel matrix, ZF takes $3K^2M + 2KM + \frac{2}{3}K^3$ operations (due to LU-based matrix inversion) [52] which is in the same scale as the SVD method. Interestingly, as the number of transmit antennas M grows, $(\underline{\mathbf{H}}_p \underline{\mathbf{H}}_p^H)/M$ tends to the identity matrix [32]. Consequently, the ZF precoder tends to the simple MF precoder. However, for practical values of $M << +\infty$, as we have mentioned for MU-MIMO system in 1.1.3.1, an ill-conditioned channel matrix after inversion may require a large normalization factor which will dramatically reduce the SNR at the receivers. Hence, ZF is highly suboptimal at low SNR regime.

1.2.3.3 RZF/MMSE

For classical MU-MIMO systems, an ill-conditioned channel matrix after inversion may requires a too higher transmit power to preserve the SNR at the receiver. Ultimately, allowing a limited amount of interference at each receiver potentially allows to provide higher capacity for a given transmit power level, or a lower transmit power for a given rate point [15]. The solutions which maximize sum capacity often allow some level of MAI at each receiver [31, 30]. This concept leads to the RZF/MMSE precoding schemes, where some level of MAI is admitted to attain better energy efficiency [31, 30]. Moreover, for multi-cell MU-MIMO systems, the RZF/MMSE precoding can be used to deal with the pilot contamination as described in [54]. For the pth frequency subband or subcarrier, the precoding matrix writes [55]:

$$\underline{\mathbf{V}}_p = \left[\underline{\mathbf{H}}_p \underline{\mathbf{H}}_p^H + \underline{\mathbf{Z}}_p + M\varphi \underline{\mathbf{I}}_M \right]^{-1} \underline{\mathbf{H}}_p \in \mathbb{C}^{M \times K}, \tag{1.18}$$

where $\underline{\mathbf{Z}}_p \in \mathbb{C}^M$ dealing with the interference caused by pilot contamination, $\varphi > 0$ is a regularization parameter contenting the AWGN and other residue interference. We note that RZF has similar complexity as the ZF precoding [52].

1.2.3.4 MRT

The conjugate precoding approach is based on the maximum ratio algorithm, in the purpose of maximizing the channel diversity. In 1999, Lo introduced MRT precoding scheme which relies on applying the matched filter at the transmitter [25]. For the pth OFDM subcarrier, the MRT precoding vector for user k is [45]:

$$\mathbf{V}_p^{(k)} = \frac{\mathbf{H}_p^{(k)*}}{\sqrt{\lambda_p^{(k)}}} \in \mathbb{C}^{M \times 1}, \tag{1.19}$$

with $\sqrt{\lambda_p^{(k)}} = \sqrt{\sum_{m=1}^{M} \left| H_{p,m}^{(k)} \right|^2}$ is the singular value of the channel vector $\mathbf{H}_p^{(k)} = \left[H_{p,1}^{(k)} \; H_{p,2}^{(k)} \; \dots \; H_{p,M}^{(k)} \right]^T$. We note that the precoding vector of user k is independent with the channel responses of the other users. However, the channel responses of different transmit-receive antenna pairs need to be centralized to compute the normalization factor λ. λ is required for each subcarrier of each user.

Then the received symbol for user k on pth OFDM subcarrier writes:

$$\begin{aligned} Y_{k,p} &= \sum_{m=1}^{M} \frac{\left|H_{p,m}^{(k)}\right|^2}{\sqrt{\lambda_p^{(k)}}} a_{k,p} \\ &= \sqrt{\sum_{m=1}^{M} \left|H_{p,m}^{(k)}\right|^2} a_{k,p} \end{aligned} \tag{1.20}$$

As MRT is equivalent to SVD method in MISO link, it is the optimal solution for MISO precoding. However, when the user number $K > 1$, MRT method is limited by residual MAI. The computation complexity is $2KM$ (due to the estimation of the normalization factor λ) [52] which is much smaller than that of ZF techniques. [34] and [46] have compared the energy and spectral efficiency of MRT and ZF methods in very large scale ($M = 100$ or 400) MU-MIMO system for UL and DL transmission, respectively. As the conclusion, ZF outperforms MRT at high SNR regime and vice versa at low SNR regime. MMSE always performs the best across the entire SNR range. It is important to note that in multicell environments with strong pilot contamination, MRC achieves a better performance than ZF [34]. Conjugate approach precoders are simpler and more robust to additional interference comparing to the ZF approach precoders.

1.2.3.5 EGT

EGT scheme is introduced in [23] in 2003. It is more simple than MRT techniques for it uses only the phase of the channel response, which simplifies the channel estimation and reduces the system overhead. Moreover, the peak to average power ratio (PAPR) of EGT signal is also lower than that of MRT signal [56]. In [57], the theoretical performance of EGT is found at most 1.049dB lower than the MRT scheme with arbitrary number of transmit antenna in SU-MISO transmission scheme. Similar results is extended to SU-MIMO system in [58]. However, both EGT and MRT systems exploit the full diversity order of the MIMO channel [23]. Considering the various advantages, EGT is a promising precoding technique for MIMO system.

The EGT precoding vector for user k on the pth OFDM subcarrier is [59]:

$$\mathbf{V}_p^{(k)} = \frac{1}{\sqrt{M}} \left[e^{-j\Phi_{p,1}^{(k)}} \; e^{-j\Phi_{p,2}^{(k)}} \; \dots \; e^{-j\Phi_{p,M}^{(k)}} \right]^T \tag{1.21}$$

where $\Phi_{p,m}^{(k)}$ is the argument of the CFR $H_{p,m}^{(k)}$ on the mth transmit antenna, $\sqrt{M}$ is used for power normalization over M transmit antennas. As EGT is a phase-only operation, it offers a unitary gain on every link [23], hence avoid any power imbalance among the transmit antennas. Moreover, the precoding factor of each antenna only depends on the CFR between this antenna and the user, which enables the implementation of distributed per-antenna transmission scheme, i.e. for UL, each antenna multiplies the received signals with the conjugate argument of the channel without sending the entire baseband signal to the BS for processing [34], for DL, each antenna directly use the conjugate argument of the channel as the precoder which is independent with the channel information of other antennas, hence avoiding centralized precoder processing at the BS.

The received symbol for user k on pth OFDM subcarrier is:

$$\begin{aligned} Y_{k,p} &= \frac{1}{\sqrt{M}} \sum_{m=1}^{M} H_{p,m}^{(k)} e^{-j\Phi_{p,m}^{(k)}} a_{k,p} \\ &= \frac{1}{\sqrt{M}} \sum_{m=1}^{M} \left|H_{p,m}^{(k)}\right| a_{k,p} \end{aligned} \tag{1.22}$$

Some implementation problems have been discussed in detail for EGT SU-MIMO systems. The performance loss due to scalar quantization of EGT precoder has been theoretically analyzed in [57], the performance loss via the number of feedback bits is presented. Once the total feedback bits number is fixed, the bit allocation scheme can be used in feedback bits to improve the system performance [60]. Moreover, [58] propose an antenna selection scheme for power allocation. Using the antennas with good conditions instead of all transmit antennas is proved has better power efficiency.

1.2.3.6 TR/MF

TR benefits from both spatial and temporal focusing properties which firstly demonstrated in the ultrasound and underwater acoustics [61] and later experimented with electromagnetic waves in the context of wireless communications [62, 63, 64]. TR consists in using the time reversed version of CIR to perform temporal pre-filtering at the transmitter. TR is an ideal paradigm for "Green communications" because of its inherent nature to fully harvest energy from the surrounding environment by exploiting the multi-path propagation [65]. [66] shows that the time and spatial focusing gain increases with the richness of the scattering environment. Hence TR is first developed in ultra-wideband (UWB) system. Performing over very large frequency bandwidths (>500 MHz) with pulse amplitude modulation, the focusing effect of TR is highlighted [67, 68].

TR is recently considered as interesting for narrow band communications systems, where the channel conditions is however less rich. The so-called rate back-off or oversampling strategies can be used to enhance the focusing gain in this context [69, 70, 65, 71]. Interestingly, based on the rate back-off factor and MIMO, [71] proposed a novel multiple access solution called time-reversal division multiple access (TRDMA). A number of system performance metrics, such as the effective SINR, the achievable sum rate and the outage achievable rate have been defined and evaluated. An interesting alternative for TR-MIMO system is rather to exploit the spatial richness of the propagation environment which increases with the number of transmit antennas [66]. The spatial and temporal focusing gains grow rapidly with the number of transmit antenna.

TR also can be performed in frequency with OFDM system, which equivalents to perform MF at the transmitter. TR-OFDM systems have been studied in [72, 73], and have been proven to allow designing of simple and efficient SU MISO-OFDM systems. In MU-MIMO systems, the TR precoding vector for user k on the pth OFDM subcarrier is [59]:

$$\mathbf{V}_p^{(k)} = \frac{\mathbf{H}_p^{(k)*}}{\sqrt{M}} \tag{1.23}$$

Noting that with the normalization factor $\sqrt{M}$, the transmit signal power after precoding process remains to be unitary.

The received symbol for user k on pth OFDM subcarrier is:

$$\begin{aligned} Y_{k,p} &= \frac{1}{\sqrt{M}} \sum_{m=1}^{M} H_{p,m}^{(k)} H_{p,m}^{(k)*} a_{k,p} \\ &= \frac{1}{\sqrt{M}} \sum_{m=1}^{M} \left| H_{p,m}^{(k)} \right|^2 a_{k,p} \end{aligned} \tag{1.24}$$

We observe a square on the received channel coefficient which is different from that of the MRT and EGT precoding techniques. This will exhibit as some special characters in system performance.

1.3 System model

In this section, we present the system model. We are interested in a not-so-large scale antenna array MU-MIMO system for the simplicity of implementation. The spatial focusing gain of such systems may not sufficient to assume perfect SDMA. Therefore, in the second part, we propose the PFBO transmission scheme which is a hybrid of SDMA and FDMA transmission while controlling the MAI.

1.3.1 Moderate-scale MU-MIMO systems

As seen in the massive MIMO systems, in spite of the numerous advantages demonstrated by theoretical derivations, still require more practical researches. For instance, in the actual LTE standard, only at most eight transmit antennas have been considered. Therefore, a more realistic vision is: Is that possible to attain same advantages of massive MIMO system, such as low cost terminals, low energy consumption at the user side and reduced radiated interference, with a not-so-large antenna array? Such context has been developed in [74, 51, 75], where a cellular layout with tens of antennas at each BS and one single antenna at each terminal is constructed. The system splits the users in one cell geographically in multiple user sets (called user bin) Fig. 1.6. Each bin is assigned with a subband of the available frequency bandwidth of the cell. Then the classical ZF precoding is applied to serve all the users within the same bin. The BS clustering issue is also considerable to enhance the performance of the bins at the border of the cell.

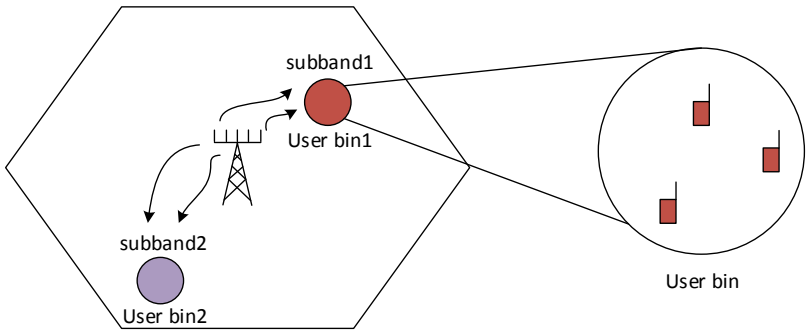

Figure 1.6: Cellular layout and user scheduling

The ZF precoding approach is a good solution for low-noise or high-power situations [15, 34, 46]. However, the computation burden exponentially increases with the number of transmit antennas and users, which makes the implementation with large scale antenna arrays too costly. Moreover, a strict central coordination is required, the CSI of each transmit/receive antenna pair needs to be collected and operated by the same BS, no co-located transmitter is applicable.

Particularly, as we mentioned in 1.2.3.2, ZF precoding approach is less energy efficient than conjugate precoding approach. Therefore, in low SNR regime or with strong additional interferences, conjugate precoding approach is preferable for its high energy efficiency and robustness [34]. In fact, a wide variety of digital communication systems operate at low power where both spectral efficiency and the energy-per-bit can be very low. Examples include wireless sensor networks which prefer to use low power and energy-efficient devices. For cellular networks, due to frequency reuse, users often operate at low SNR regime to avoid causing interference to other

users. It has been shown in [76, 77] that 40% of the geographical locations experience receiver SNR levels below 0dB [78].

The system capacity with ZF and MRT precoding schemes are presented in Fig. 1.7 for $M = 8$ and in Fig. 1.8 for $M = 64$. From Fig. 1.7, we observed that the MRT scheme outperforms the ZF scheme in low SNR regime. ZF scheme is efficient when $M >> K$, MRT scheme is preferable when $K \rightarrow M$. It is interesting to note that MRT can serve a number of users $K \geq M$ if the antenna diversity is rich enough. This propriety is beneficial for the multiple access systems with not-so-large number of antennas. Similar proprieties are observed for $M = 64$ in Fig. 1.8.

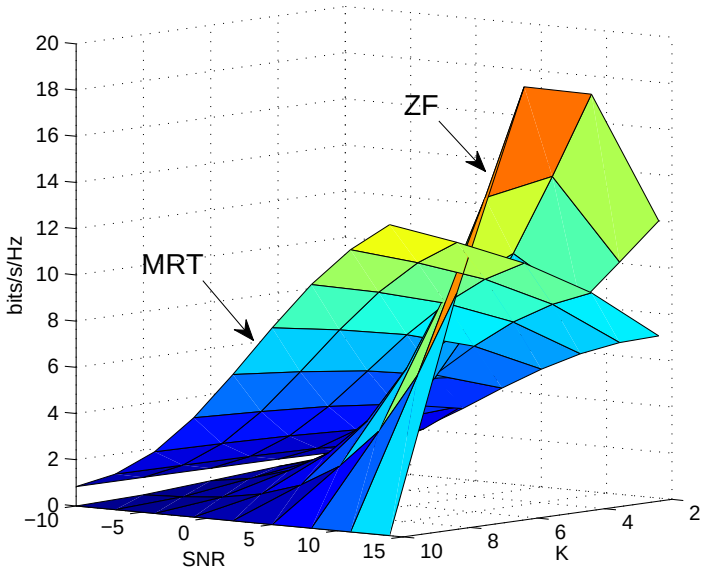

Figure 1.7: System capacity with ZF and MRT precoding schemes, tansmit antennas number $M = 8$

In this thesis, we propose a low-complexity and high energy-efficiency transmission scheme for moderate-scale MU-MIMO systems. The system is in low power consumption and robust in low SNR regime. Conjugate precoding approach is performed as the multiple access scheme. Although some level of MAI is residue, with high noise level, the system is less sensitive to the impact of interference. A single cell precoded MU-MIMO system is presented in Fig. 1.9. The space division multiplexing gain ensures the multi-user multiplexing and the MAI remains tolerable. Assuming CSIT, the precoding vectors are directly resulted from the channel information through simple operations. We note that with conjugate precoding approach, a cooperation between adjacent BSs is feasible. For exemple, the edge users can be served by the BSs from adjacent cells. Assuming perfect synchronization among the BSs, the useful signals can be added constructively at the target user.

We note that the precoding techniques are used here to exploit the space division multiplexing gain of MU-MIMO system, different from that in conventional SU-MIMO case, which is used to exploit the full diversity of MIMO channel.

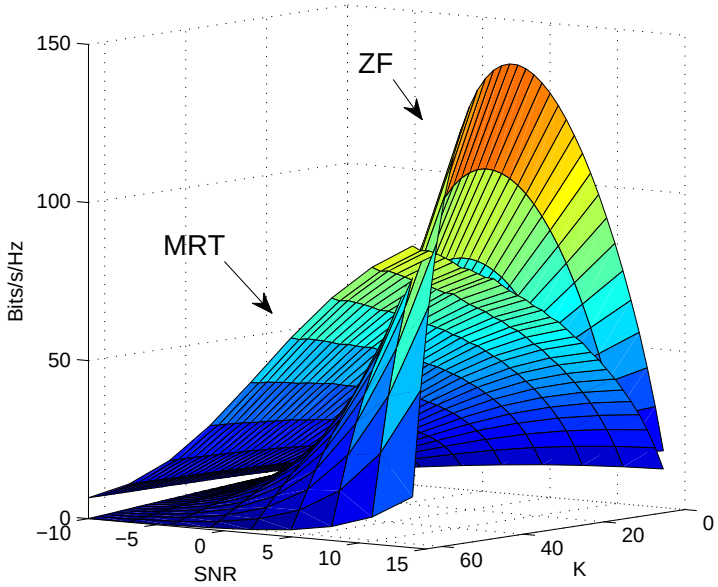

Figure 1.8: System capacity with ZF and MRT precoding schemes, tansmit antennas number $M = 64$

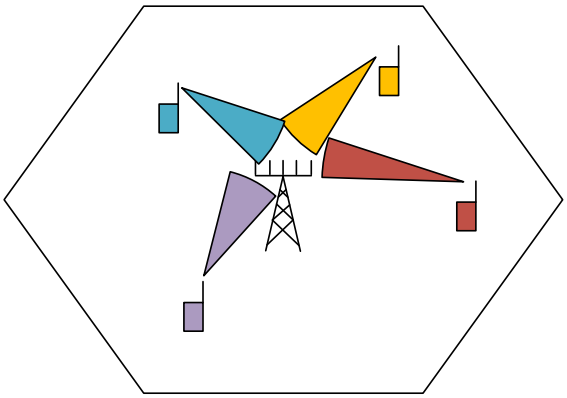

Figure 1.9: Precoded MU-MIMO system

1.3.2 PFBO transmission schemes

For the proposed moderate scale MU-MIMO systems, the multiuser multiplexing is achieved through conjugate precoding approach. The number of transmit antennas may not sufficient to provide high spacial focusing gain to assume perfect SDMA while ignoring the MAI. In this case, we propose a flexible SDMA-FDMA hybrid transmission scheme, namely partial spectrum frequency overlay (PFBO) scheme, in the purpose of enhancing the system spectral efficiency while controlling the MAI. The PFBO schemes is presented in Fig. 1.10.

Although in classical resource allocation approaches, the users are clearly divided in one or more dimensions to minimize the MAI. However, in low SNR regime, the system is not at the same degree of sensitivity as in high SNR regime, the impact of additional interference is less visible. This motivates us to analyze the performance of PFBO schemes with different SNR levels and system configurations.

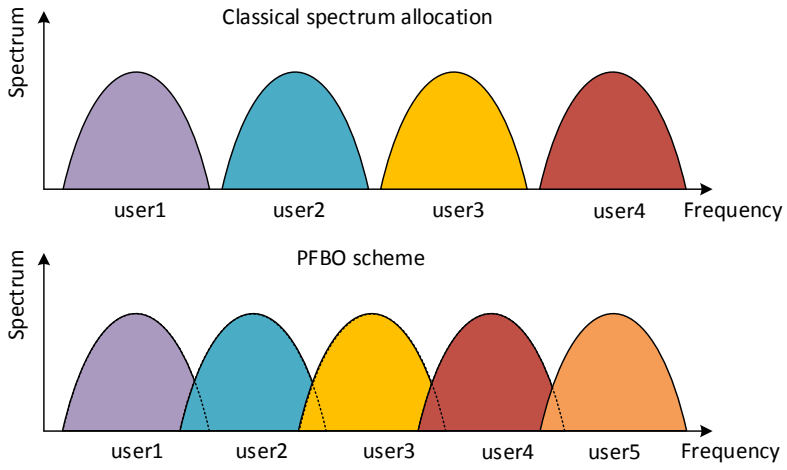

Figure 1.10: Classical spectrum allocation scheme and PFBO scheme

More precisely, we consider as the first step a two-user PFBO scheme. Assuming a common FDMA system in which the available frequency bandwidth is divided into independent subbands/channels as shown in Fig. 1.11. The $channel k$, denoted as h_k, is assigned to $user k$. A spectrum mask is specified for each channel in order to limit the egress power. The PFBO is performed between $user1$ and $user2$ as shown in 1.12.

We will analyze the spectrum efficiency of such two-user PFBO scheme with single carrier and OFDM signals in chapter 2. Both SISO and precoded MU-MIMO systems are concerned. The precoding techniques help to enhance the useful signal quality while mitigating the impact of inter-channel interference. While in chapter 3 and chapter 4, the BER performance of this two-user PFBO scheme is derived for OFDM and SS-OFDM systems, respectively.

It is interesting to note that for traditional SISO system, many literature studied the scenario where another channel use the same frequencies as the desired channel, which results in the cochannel interference (CCI). Many previous works have analyzed the impact of CCI. The performance of single-carrier system in presence of the CCI has been studied in [79, 80, 81]. In

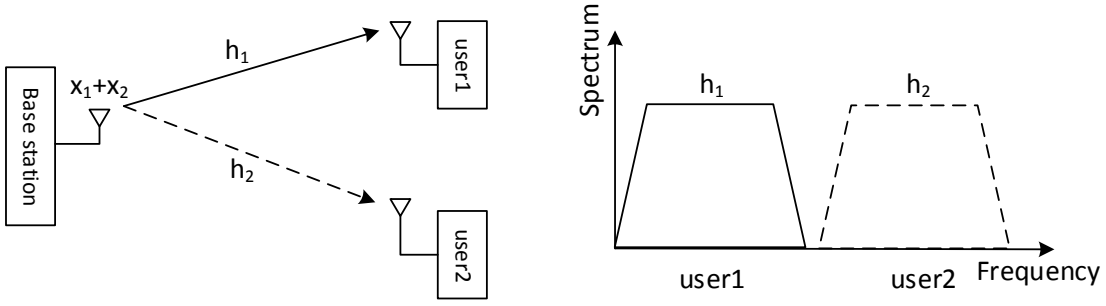

Figure 1.11: Common frequency bandwidth sharing model for SISO system

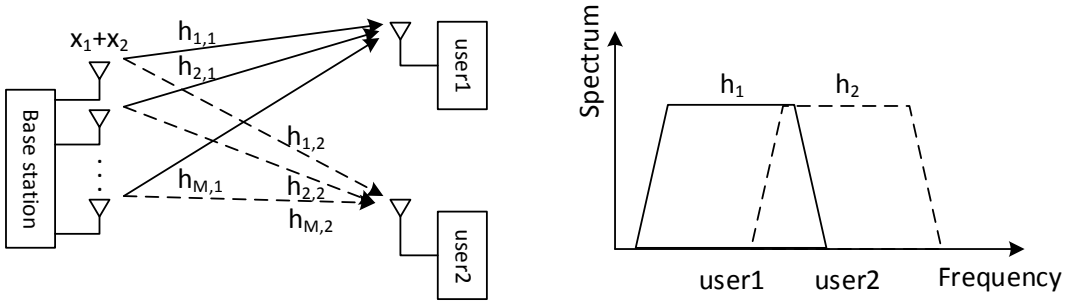

Figure 1.12: Two-user PFBO scheme

these works, the CCI is modeled as an AWGN noise because it is considered as an unexpected interference without disposable information. For OFDM system, authors in [82] have analyzed the impact of unintentional interference comes from adjacent cells which use a channel not sufficiently separated from the desired channel in the context of WLAN system. An upper bound of bit error rate (BER) performance has been provided according to the effective SNR level. Such interfering effect can also be seen as partial band jamming (PBJ). In [83], the BER analysis is derived with different jamming types in OFDM system. However, in SISO systems, CCI or jamming signal largely degrades the system performance unless their power is much lower then the desired signal.

1.4 Channel models

In the wireless communications systems, the transmitted signals suffer from various reflection and diffraction phenomenons due to the surrounding objects as shown in Fig. 1.13. Hence at the reception side, the received signal is not the same as the transmitted signal, but a superposition of divers copies of the transmitted signal traversing from different propagation paths. Such channel

is called multipath fading channel, described by the channel impulse response (CIR) as:

$$h(t) = \sum_{l} a_l \delta(t - \tau_l) \tag{1.25}$$

where a_l and τ_l are respectively the attenuation and delay of the l^{th} propagation path. They are dependent on the distance of the l^{th} path as well as the nature of reflectors. $\delta(.)$ is the unit impulse function, also called Dirac delta function.

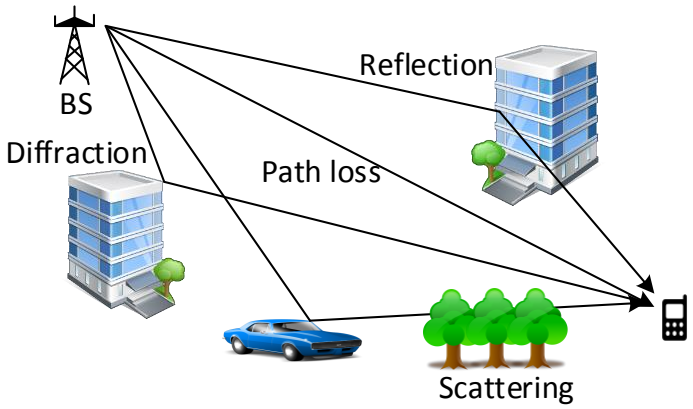

Figure 1.13: Multipath channel

1.4.1 Slow and fast fading

The distinction between slow and fast fading is important for fading channel modeling and performance evaluation of the systems. It indicates how rapidly the channel varies in time. In fact, the relative motion of the transmitter and/or the receiver causes a variation in the carrier frequency which is called the Doppler frequency shift. The notion of coherence time T_c is used to measure the time interval during which the CIR is considered as stationary. The coherence time is related to the maximum Doppler frequency shift f_{max} as:

$$T_c \approx \frac{1}{f_{max}} \tag{1.26}$$

The fading is considered to be slow if the symbol time duration T_s is inferior to the channel coherence time T_c ; otherwise it is considered to be fast. In slow fading channel, one particular fade level affects many successive symbols, whereas in fast fading channel, the channel changes during the symbol transmission, which also called temporal selective channel. In this thesis, we work with slow fading channel model as in the indoor environment, the movement of users is relatively slow.

1.4.2 Frequency selective fading

Frequency selectivity is another important character of fading channels, it describes the fluctuation in frequency of the channel. If all the spectral components of the transmitted signal are

affected in a similar manner (similar degradation level), the fading is said to be frequency non selective or equivalently frequency-flat [84]. Otherwise, the fading is called frequency selective. The notion coherence bandwidth f_c is used to measures the frequency range over which the fading process is correlated and is defined numerically as the frequency bandwidth over which the correlation function of two samples of the channel response taken at the same time but different frequencies falls below a suitable threshold. In this thesis, we have taken 0.9 as the threshold [85].

In the wireless multipath channel, we note the maximum delay spread τ_{max} as the difference between the shortest and the longest delay. Then the coherence bandwidth of the channel is related to the maximum delay spread τ_{max} as:

$$f_c \approx \frac{1}{\tau_{max}} \tag{1.27}$$

In an indoor environment, many objects are presented in the space, which create lots of paths and make the channel very frequency selective. The multi-carrier modulation (OFDM) is invented to combat the frequency fluctuation of the channel, where a wideband channel is divided into multiple independent narrow bands. Then the channel can be considered as flat fading in each narrow band.

1.4.3 Channel models

We present here the channel models that we have used in this thesis for system performance analysis.

1.4.3.1 AWGN channel

The additive white Gaussian noise (AWGN) channel is the most fundamental channel model. It is often used to derive the theoretical performance thresholds of a system. AWGN channel is a memoryless channel without interference, dispersion and fading, the only source is the thermal noise at the receiver. Hence the CIR is modeled by a Dirac delta function in addition with a Gaussian-distributed random noise. The AWGN is assumed to be statistically independent of the channel fading amplitude, and is characterized by a one-sided power spectral density (PSD) N_0 Watts/Hertz. The AWGN channel is the most ideal and simple channel model for no time and frequency selectivity has been considered.

1.4.3.2 Frequency Rayleigh fading channel

The Rayleigh distribution is frequently used to model the multipath fading channel with no direct line-of-sight (LOS) path [84]. The received carrier amplitude is modulated by the fading coefficients ξ which follows Rayleigh distribution. In this thesis, we use a theoretical frequency domain Rayleigh channel model, for which the fading coefficients for each OFDM subcarrier is independent with the others. Assuming the whole channel contains N_f subcarriers, the CFR is expressed as:

$$H(f) = \sum_{p=0}^{N_f-1} \xi_p \Pi\left(\frac{f - \frac{f_p + f_{p+1}}{2}}{f_{p+1} - f_p}\right) \tag{1.28}$$

With $\Pi(\cdot)$ denotes the rectangular function. $H(f)$ is displayed in Fig. 1.14.

The frequency Rayleigh channel model is also an idealist model which assumes an extremely rich frequency selectivity. It is very useful to derive theoretical performance limits of the systems.

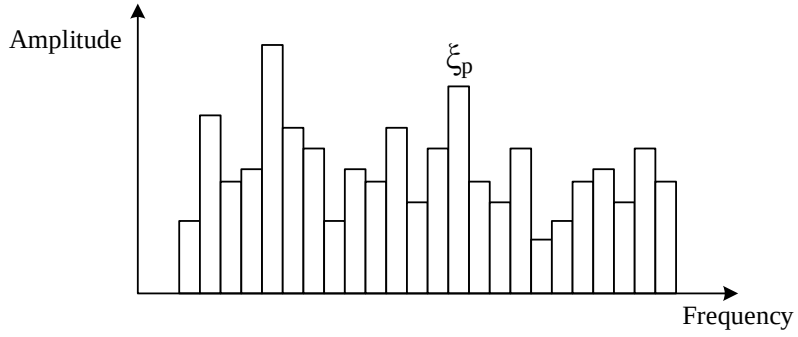

Figure 1.14: Frequency rayleigh channel model $H(f)$

To adapt the practical channel conditions, we introduce a Rayleigh channel model with larger coherence bandwidth. Assuming the whole frequency bandwidth B_w contains N_{coh} ($N_{coh} < N$) independent coherence bandwidths of equal size B_c, the CFR becomes:

$$H_{B_c}(f) = \sum_{n_c=1}^{N_{coh}} \xi_{n_c} \Pi \left(\frac{f - \left(f_{n_c-1} + \frac{B_c}{2} \right)}{B_c} \right) \tag{1.29}$$

with ξ_{n_c} is the frequency domain channel coefficients of the n_cth coherence bandwidth and $\left|\xi_{n_c}\right|$ follows independent Rayleigh distributions. $H_{B_c}(f)$ is displayed in Fig. 1.15.

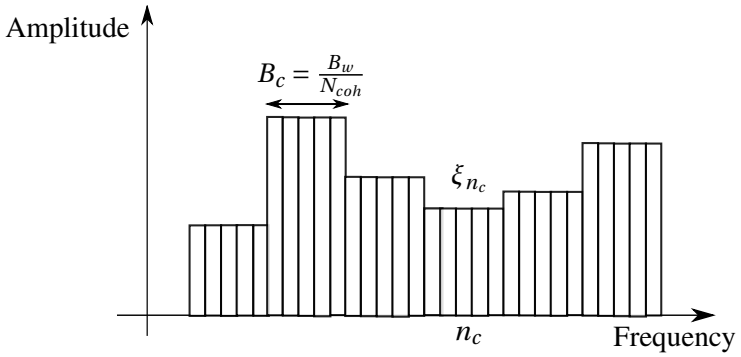

Figure 1.15: Frequency rayleigh channel model with coherence bandwidth B_c

Noting that when $N_{coh} = 1,\ B_c = B_w$, the channel is a flat fading channel (AWGN channel); when $N_{coh} = N_f,\ B_c = \frac{B_w}{N_f}$, the channel is a classical frequency Rayleigh channel where the coherence bandwidth is equal to the subcarrier spacing.

1.4.3.3 Bran channel model

Broadband Radio Access Network (BRAN) project is established in 1997 by European Telecommunications Standards Institute (ETSI) to define a Wireless LAN (WLAN) standard, namely HiperLAN (High Performance Radio LAN), as an alternative for the IEEE 802.11 standards.

The last version, HIPERLAN/2 [86], is designed as a fast wireless connection for many kinds of networks, as UMTS back bone network, ATM, IP networks. HiperLAN/2 uses the 5 GHz band and up to 54 Mbit/s data rate.

BRAN has decided a set of indoor channel models for HIPERLAN/2 simulations. A tapped delay line type of model, which is basically described in [87], has been chosen. In this model, in order to reduce the number of taps needed, the time spacing is non uniform, and for shorter delays, a more dense spacing is used. The average power fades exponentially with time. A Ricean K factor of 10 is set to the first tap if the channel contains a line-of-sight (LOS) path, all the other taps have Rayleigh fading statistics ($K = 0$). A classical (Jake's) Doppler spectrum corresponding to a terminal speed of 3 m/s is assumed for all taps.

Five channel models, A, B, C, D and E, have been designed. Model A corresponds to a typical office environment for non-line-of-sight (NLOS) conditions and $50ns$ average RMS delay spread. Model B corresponds to a typical large open space environment with NLOS conditions or an office environment with large delay spread. Models C and E correspond to typical large open space indoor and outdoor environments with large delay spread. Model D corresponds to LOS conditions in a large open space indoor or an outdoor environment.

The examples of normalized CIR and CFR of BRAN-A channel are presented in Fig. 1.16 and Fig. 1.17, respectively.

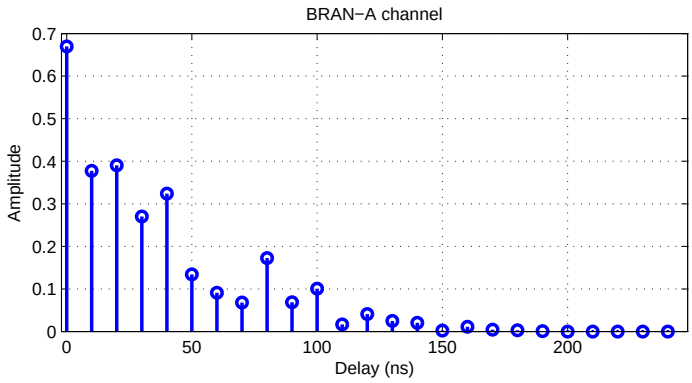

Figure 1.16: The CIR of BRAN-A channel

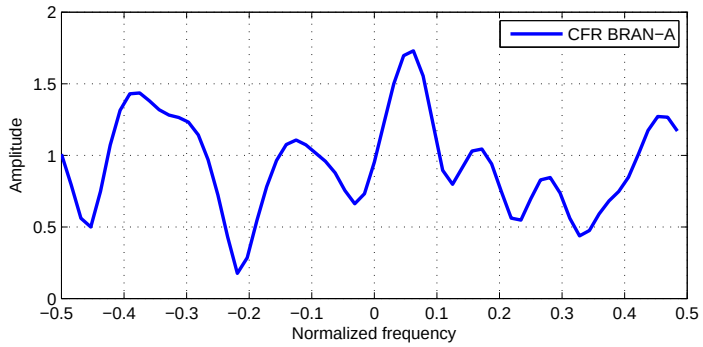

Figure 1.17: The CFR of BRAN-A channel

We note that the BRAN-A channel is relatively frequency-selective, because an office environment is rich of paths.

1.5 Conclusion

In this first chapter, we reminded the classical MU-MIMO and the innovative massive MIMO systems, from which we chose the moderate-scale MIMO as an intermediate to take advantages of both the SDMA capabilities and the reasonable implementation cost. To combat the residual MAI, a PFBO scheme, which consists in partial spectrum sharing among the FDMA users, has been proposed for the case where the number of transmit antennas is not sufficient to assume pure SDMA transmission. The performance of the PFBO scheme combined with various waveforms will be studied in the following chapters.

CHAPTER 2

CAPACITY ANALYSIS FOR BANDWIDTH OVERLAY SYSTEMS

As presented in 1.3.2, the partial frequency bandwidth overlay (PFBO) scheme is expected to improve the system capacity by intentionally overlapping the users from adjacent frequency bandwidths. Hence, in this chapter, we analyze the achievable sum rate of the PFBO scheme to identifier the potential capacity gain. We evaluate the system capacity in function of the overlap ratio, the number of transmit antennas and the SNR level. The objective is to establish the relationship between the system capacity and the different configuration parameters, and to identifier the optimal overlap ratio which corresponds to the maximal system capacity.

The rest of the chapter is organized as follows. In the first part, the spectrum models of PFBO scheme are introduced using both single carrier and multi-carrier waveforms. We present the equations of the useful signal component and the inter-channel interference. Then in the second part, we present the capacity evolution of the systems in function of different configuration parameters. Hereby, we identify the optimal overlap ratio τ_{max} that maximizes the achievable sum rate. At the end, new capacity lower bounds are derived using EGT, TR and MRT precoding techniques for general MU-MIMO systems.

2.1 Spectrum bandwidth overlapping models

In this first part we present the spectrum model of the PFBO scheme for both single carrier and multi-carrier waveforms. We begin with the SISO systems, then move on to the MU-MIMO systems by increasing the number of transmit antennas.

2.1.1 Bandwidth overlapping for SISO system with single carrier signals

With single carrier modulations, the transmit signal is shaped by a root-raised-cosine filter for the purpose of limiting the spectrum occupancy of the transmitted signal while preventing from

ISI. Hence the normalized transmitted PSD on baseband for the k^{th} user is:

$$G_{X_k}(f) = \begin{cases} T_s & |f| \le \frac{1-\alpha}{2T_s}, \\ \frac{T_s}{2}(1+\sin(\frac{\pi}{2\alpha} - \frac{\pi T_s}{\alpha}|f|)) & \frac{1-\alpha}{2T_s} \le |f| \le \frac{1+\alpha}{2T_s}, \\ 0 & |f| \ge \frac{1+\alpha}{2T_s}. \end{cases} \tag{2.1}$$

where T_s is the sample time, α is the roll-off parameter with $\alpha \in [0,1]$. Consequently, the effective spectrum occupancy B_w for such a signal writes $B_w = \frac{1+\alpha}{T_s}$.

Fig. 2.1 shows the PSD of a two-user PFBO model, where f_{c_1} and f_{c_2} indicate the central frequency of channels h_1 and h_2, respectively. Δf denotes the reused bandwidth, such as $f_{c_2} = f_{c_1} + B_w - \Delta f$. The striped area represents the inter-channel interference.

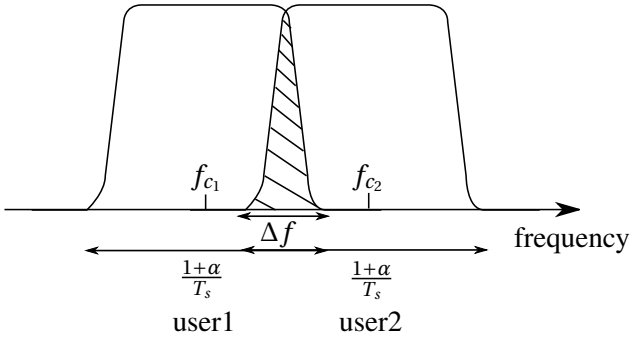

Figure 2.1: Spectrum overlapping using single carrier signal

Without loss of generality, assuming $user1$ is the user of interest while $user2$ is the interfering user. After perfect matched-filtering and synchronization, the PSD of the received stream is:

$$\begin{aligned} G_{Y_1}(f) &= \left|W(f)H^{(1)}(f)\right|^2 \left(P_{Use}G_{X_1}(f) + P_{Inf}G_{X_2}(f-(B_w-\Delta f))\right) + \left|W(f)\right|^2 N_0 \\ &= \left|H^{(1)}(f)\right|^2 \left|W(f)\right|^2 P_{Use}G_{X_1}(f) + \left|H^{(1)}(f)\right|^2 \left|W(f)\right|^2 P_{Inf}G_{X_2}(f-(B_w-\Delta f)) + \left|W(f)\right|^2 N_0 \\ &= \left|H^{(1)}(f)\right|^2 P_{Use}G_X^2(f) + \left|H^{(1)}(f)\right|^2 P_{Inf}G_X(f)G_X(f-(B_w-\Delta f)) + G_X(f)N_0 \end{aligned} \tag{2.2}$$

where $W(f)$ is the frequency response of the matched filter used at the receiver which is also a root-raised-cosine filter, $H_1(f)$ is the CFR of h_1, N_0 is the PSD of a complex zero-mean AWGN. P_{Use} and P_{Inf} are the useful signal power level and the interference signal power level, respectively.

The PSD of the useful signal component is:

$$G_X^2(f) = \begin{cases} T_s^2 & |f| \le \frac{1-\alpha}{2T_s}, \\ \frac{T_s^2}{4}(1+\sin(\frac{\pi}{2\alpha} - \frac{\pi T_s}{\alpha}|f|))^2 & \frac{1-\alpha}{2T_s} \le |f| \le \frac{1+\alpha}{2T_s}, \\ 0 & |f| \ge \frac{1+\alpha}{2T_s}. \end{cases} \tag{2.3}$$

The PSD of the inter-channel interference depends on the reused bandwidth Δf:

$$\begin{aligned} G_{Inf}(f) &= G_X(f)G_X(f-(B_w-\Delta f)) \\ &= \begin{cases} G_X(f)T_s & \frac{1+3\alpha}{2T_s} - \Delta f \le f \le \frac{3-\alpha}{2T_s} - \Delta f, \\ G_X(f)G_X(f-\frac{1+\alpha}{T_s}+\Delta f) & \frac{1+\alpha}{2T_s} - \Delta f \le f \le \frac{1+3\alpha}{2T_s} - \Delta f \ or \ \frac{3-\alpha}{2T_s} - \Delta f \le f \le \frac{3+3\alpha}{2T_s} - \Delta f \\ 0 & f \le \frac{1+\alpha}{2T_s} - \Delta f \ or \ f \ge \frac{3+3\alpha}{2T_s} - \Delta f. \end{cases} \end{aligned} \tag{2.4}$$

$G_{Inf}(f)$ is presented in Fig. 2.2 for different overlap ratios $\tau = \frac{\Delta f}{B_w}$.

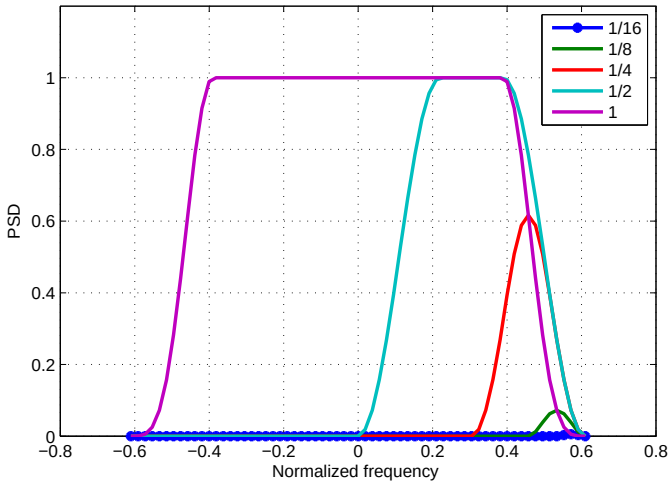

Figure 2.2: The PSD of interference signal for different overlap ratio values $\tau \in \{\frac{1}{16}, \frac{1}{8}, \frac{1}{4}, \frac{1}{2}, 1\}$

2.1.2 Bandwidth overlapping for SISO system with multi-carrier signals

In multi-carrier/OFDM system standards, we commonly turn off some subcarriers at the band edges to avoid the power egress out of the spectrum mask. Analytical expressions for the PSD of OFDM signal has been derived in [88]. We observed that the PSD of OFDM signal has a form approaching to a rectangle, especially when the null subcarriers are presented. Hence, for simplicity, we model the OFDM PSD as a bank of rectangles:

$$G_{X_i}(f) = \frac{1}{B_w} \sum_{p=0}^{N_f-1} \Pi\left(\frac{f - \frac{f_p + f_{p+1}}{2}}{\delta_f}\right) \tag{2.5}$$

where $\Pi(\cdot)$ denotes the rectangular function, p is the subcarrier index, the pth subcarrier occupies the subband $[f_p, f_{p+1}]$ and the subcarrier spacing is $\delta_f = f_{p+1} - f_p$. As defined in the single carrier case, B_w denotes the total bandwidth. With this model, we consider that the spectrum mask of the multi-carrier signal is strictly limited to N_f sub-bands without any excess bandwidth due to secondary lobes. This constitutes an ideal case that will be considered as a reference in the sequel. Accordingly, Fig. 2.3 presents the PSD of the two-user PFBO model in the multi-carrier case. Assuming perfect matched-filtering and synchronization at the receiver, as in section 2.1.1, it is straightforward to obtain the PSD of the inter-channel interference as a function of the overlapped bandwidth Δf:

$$G_{Inf}(f) = \frac{1}{B_w} \Pi\left(\frac{f - \left(f_{N_f} - \frac{\Delta f}{2}\right)}{\Delta f}\right) \tag{2.6}$$

2.1.3 Bandwidth overlapping in precoded MU-MIMO systems

A MU-MIMO system with two users is introduced in Fig. 2.4 in which M antennas are used at the transmitter and one single antenna per user at the receiver. We assume these antennas

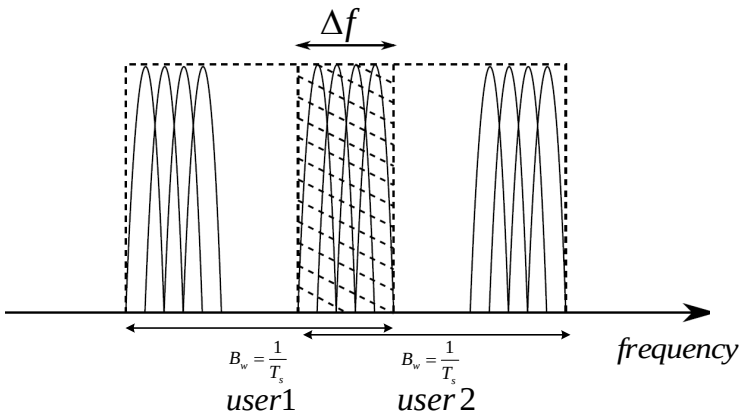

Figure 2.3: OFDM overlapped system

are placed sufficiently far apart (typically several wavelengths from real life experimental results [65, 89]), hence they are perfectly decorrelated. $x_m^{(1)}(t)$ and $x_m^{(2)}(t)$ denote the useful signal and the interfering signal transmitted on the mth antenna.

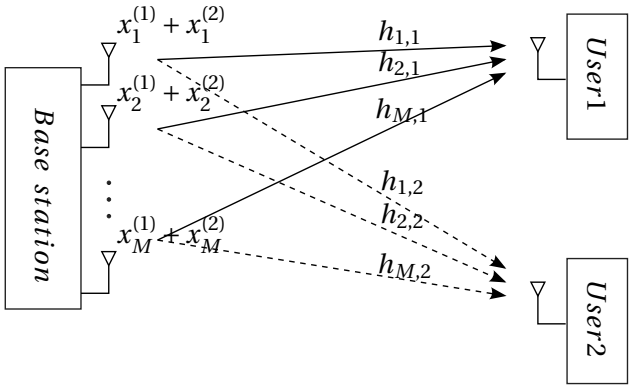

Figure 2.4: MU-MIMO system model with two users

The received signal for $user1$ is:

$$y^{(1)}(t) = w(t) * (\sum_{m=1}^{M} h_m^{(1)}(t) * (x_m^{(1)}(t) + x_m^{(2)}(t)) + n(t)) \tag{2.7}$$

where $w(t)$ and $n(t)$ are the time domain descriptions of the matched filter and the noise term, respectively. In the frequency domain, the convolution is converted to multiplication operator, the PSD of the received signal is thus:

$$G_{Y^{(1)}}(f) = \left|W(f)\right|^2 \left|\sum_{m=1}^{M} H_m^{(1)}(f) X_m^{(1)}(f)\right|^2 + \left|W(f)\right|^2 \left|\sum_{m=1}^{M} H_m^{(1)}(f) X_m^{(2)}(f)\right|^2 + \left|W(f)\right|^2 N_0 \tag{2.8}$$

2.2 Capacity analysis through simulations

2.2.1 Capacity analysis for single carrier signals in SISO systems

For single carrier system, the inter-channel interference affects the overlapped bandwidth as a colored noise (c.f. Fig. 2.1). In this case, the Shannon capacity is obtained by treating the channel as many narrow, independent Gaussian channels in parallel [90]:

$$C = \int_0^{B_w} \log_2\left(1 + \mathrm{SINR}(f)\right) df \tag{2.9}$$

Adapting to our channel model (c.f. 1.4.3.2) where the whole frequency bandwidth B_w contain N_{coh} coherence bandwidths of equal size B_c, the capacity equation rewrites as:

$$C_{sc} = \sum_{n_c=1}^{N_{coh}} \int_{B_c(n_c-1)}^{B_c n_c} \log_2\left(1 + \mathrm{SINR}(f)\right) df \tag{2.10}$$

Assuming P_{Use} and P_{Inf} are respectively the useful signal power level and the interference signal power level, γ is defined as the SNR density such as $\gamma = \frac{P_{Use}}{N_0}$. For any instantaneous realization of the channel, one can obtain the corresponding instantaneous effective $\mathrm{SINR}_{ins}(f)$:

$$\begin{aligned} SINR_{ins}(f) &= \frac{P_{Use} G_X^2(f) \left|H^{(1)}(f)\right|^2}{P_{Inf} G_{Inf}(f) \left|H^{(1)}(f)\right|^2 + G_X(f) N_0} \\ &= \frac{\gamma G_X(f) \left|H^{(1)}(f)\right|^2}{\frac{P_{Inf}}{P_{Use}} \gamma \frac{G_{Inf}(f)}{G_X(f)} \left|H^{(1)}(f)\right|^2 + 1} \end{aligned} \tag{2.11}$$

With the instantaneous effective $\mathrm{SINR}_{ins}(f)$, the instantaneous achievable rate of the system [71] can be deduced as $R_{ins} = \log_2\left(1 + \mathrm{SINR}_{ins}(f)\right)$. The achievable sum rate is an important efficiency metric for wireless downlink schemes. It measures the total amount of information that can be effectively delivered given the total transmit power constraint P [71].

The instantaneous achievable rate of the single carrier system is:

$$R_{sc,ins} = \frac{1}{B_w - \frac{\Delta f}{2}} \sum_{n_c=1}^{N_{coh}} \int_{B_c(n_c-1)}^{B_c n_c} \log_2\left(1 + \mathrm{SINR}_{ins}(f)\right) df \tag{2.12}$$

Averaging the instantaneous achievable rate over a set of random ergodic channels, the expected value is a good reference of the long-term system performance [71]:

$$\begin{aligned} R_{sc,avg} &= \mathbb{E}_{H^{(1)}}\left[R_{sc,ins}\right] \\ &= \frac{1}{B_w - \frac{\Delta f}{2}} \sum_{n_c=1}^{N_{coh}} \int_{B_c(n_c-1)}^{B_c n_c} \int_0^{\infty} \log_2\left(1 + \frac{\gamma G_X(f) \left|\xi_{n_c}\right|^2}{\frac{P_{Inf}}{P_{Use}} \gamma \frac{G_{Inf}(f)}{G_X(f)} \left|\xi_{n_c}\right|^2 + 1}\right) p(\xi_{n_c}) d\xi_{n_c} df \end{aligned} \tag{2.13}$$

Admitting the overlap ratio $\tau = \frac{\Delta f}{B_w}$, then $B_w - \frac{\Delta f}{2} = B_w(1 - \frac{\tau}{2})$. The numerical evaluation of the average achievable rate as a function of τ is presented in Fig. 2.5 for different values of γ and a roll-off factor $\alpha = 0.22$.

We observe that when $N_{coh} = 1$, i.e. Gaussian AWGN channel, the achievable rate is always maximal. As the value of N_{coh} increases, i.e. the frequency selectivity increases, the achievable

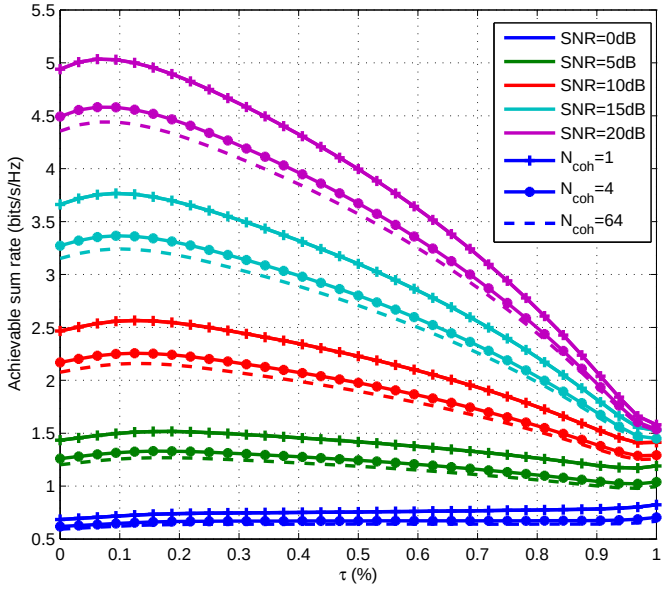

Figure 2.5: Achievable sum rate versus overlap ratio τ with single carrier modulation for different γ values

rate degrades. However, the differences between the curves corresponding to $N_{coh} = 4,\ 64$ are very small, especially at low SNR regime.

Moreover, when $SNR \geq 5dB$, the achievable rate slightly increases with the overlap ratio τ. This increase is obtained when the sub-band overlap is such that the interference level remains tolerable comparing to the noise level. In contrast to that, for larger overlap ratios, the interference becomes dominant and the spectral efficiency fast decreases. For low SNR regime, i.e. $SNR = 0dB$, the spectral efficiency remains almost constant or even keeps increasing. This is explained by the fact that the interference level never exceeds the AWGN noise level in that case. As a conclusion, a moderate sub-band overlapping helps to improve the average capacity of single carrier signal in SISO system.

2.2.2 Capacity analysis for multi-carrier signals in SISO systems

In the multi-carrier modulation (OFDM) case, due to the orthogonality properties, each sub-band is flat and independent with the others. Hence the system capacity over the whole band can be written as the sum of the capacity of each subcarrier:

$$C_{ofdm} = \sum_{p=0}^{N_f-1} \frac{B_w}{N_f} \log_2\left(1 + \mathrm{SNR}_p\right) \tag{2.14}$$

with SNR_p the SNR value of the pth subband.

For non-overlapped sub-bands, one has:

$$\mathrm{SNR}_{p,ins} = \frac{\left|H_p^{(1)}\right|^2 P_{Use}}{N_0} = \left|H_p^{(1)}\right|^2 \gamma \tag{2.15}$$

For overlapped sub-bands, one has:

$$\mathrm{SINR}_{p,ins} = \frac{\left|H_p^{(1)}\right|^2 P_{Use}}{\left|H_p^{(1)}\right|^2 P_{Inf} + N_0} = \frac{\gamma\left|H_p^{(1)}\right|^2}{\frac{P_{Inf}}{P_{Use}}\gamma\left|H_p^{(1)}\right|^2 + 1} \tag{2.16}$$

Then the instantaneous achievable rate is:

$$R_{ofdm,ins} = \frac{1}{B_w - \frac{\Delta f}{2}}\frac{B_w}{N_f}\left(\sum_{p=0}^{N_f-1-\frac{\Delta f}{B_w}N_f}\log_2\left(1+\mathrm{SNR}_{p,ins}\right) + \sum_{p'=N_f-\frac{\Delta f}{B_w}N_f}^{N_f-1}\log_2\left(1+\mathrm{SINR}_{p',ins}\right)\right) \tag{2.17}$$

The average achievable rate over random ergodic channels is:

$$\begin{aligned} R_{ofdm,avg} &= \mathbb{E}_{H^{(1)}}\left[R_{ofdm,ins}\right] \\ &= \frac{1}{N_f\left(1-\frac{\tau}{2}\right)}\left(\mathbb{E}_{H^{(1)}}\left[\sum_{p=0}^{N_f-1-\tau N_f}\log_2\left(1+\mathrm{SNR}_{p,ins}\right)\right] + \mathbb{E}_{H^{(1)}}\left[\sum_{p'=N_f-\tau N_f}^{N_f-1}\log_2\left(1+\mathrm{SINR}_{p',ins}\right)\right]\right) \end{aligned} \tag{2.18}$$

The average achievable rate as a function of τ for different values of SNR γ is depicted in Fig. 2.6. We observed that the curves uniformly decreases in high SNR regime and slightly increases in very low SNR regime, i.e. $0dB$, which indicates that the interference has more dramatic impact than in the single carrier case. This is mainly due to the ideal model taken here for the multi-carrier systems in which no side lobes effects are considered. Hence channel overlay directly affects useful subcarriers which translates into strong signal degradation as similarly shown in [82]. In fact, the ideal model used for OFDM corresponds to the single carrier case with $\alpha = 0$, hence, as shown in Fig. 2.5 and Fig. 2.6, $R_{ofdm,avg}$ is always higher than $R_{sc,avg}$.

On the other hand, same as in the single carrier case, the capacity is higher over AWGN channel (i.e. $N_{coh} = 1$). In order to propose a lower bound of the system capacity, in the following studies, we will take the worst case, i.e. $N_{coh} = N_f$, which means that each subband fades independently with the others. Therefore, (2.13) can be rewritten as:

$$R_{sc,avg} = \frac{1}{1-\frac{\tau}{2}}\frac{1}{B_w}\sum_{p=0}^{N_f-1}\int_{f_p}^{f_{p+1}}\mathbb{E}_\xi\left[\log_2\left(1+\frac{\gamma G_X(f)\left|\xi\right|^2}{\frac{P_{Inf}}{P_{Use}}\gamma\frac{G_{Inf}(f)}{G_X(f)}\left|\xi\right|^2+1}\right)\right]df, \tag{2.19}$$

and (2.18) can be rewritten as:

$$R_{ofdm,avg} = \frac{1-\tau}{1-\frac{\tau}{2}}\mathbb{E}_\xi\left[\log_2\left(1+\left|\xi\right|^2\gamma\right)\right] + \frac{\tau}{1-\frac{\tau}{2}}\mathbb{E}_\xi\left[\log_2\left(1+\frac{\gamma\left|\xi\right|^2}{\frac{P_{Inf}}{P_{Use}}\gamma\left|\xi\right|^2+1}\right)\right]. \tag{2.20}$$

From the previous analysis, we note that the maximum achievable rate is not always obtained at $\tau = 0$, which means that the channel overlapping can improve the system capacity, especially at low SNR regime. However, the improvement remains very limited due to the inter-channel interference. In the next part, we will investigate the influence of the choice precoded MU-MIMO systems with the impact of inter-channel interference.

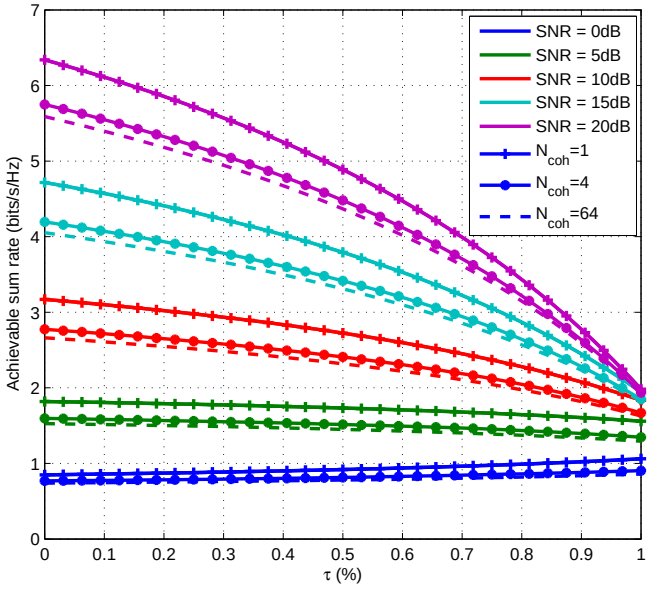

Figure 2.6: Achievable sum rate versus overlap ratio τ with multicarrier modulation for different γ values

2.2.3 Capacity analysis for precoded MU-MIMO systems

In this part, we analyze the system capacity for precoded MU-MIMO systems: EGT, TR and MRT precoding techniques have been considered and the performance has been compared.

For single carrier systems, the instantaneous SINR using EGT precoding is:

$$\mathrm{SINR}_{EGT,ins}(f) = \frac{\frac{1}{M}\left|\sum_{m=1}^{M}\left|\xi_m^{(1)}\right|\right|^2 \gamma G_X(f)}{\frac{1}{M}\left|\sum_{m=1}^{M}\xi_m^{(1)} e^{-j\Phi_m^{(2)}}\right|^2 \frac{P_{Inf}}{P_{Use}}\gamma\frac{G_{Inf}(f)}{G_X(f)} + 1} \tag{2.21}$$

with $\Phi_m^{(2)}$ is the phase of interfering channel. γ denotes the SNR which is the same as in SISO case. We recall that in our context, the MU-MIMO systems transmit the same power as the SISO systems, the capacity improvement is due to the energy focusing gain of spatial precoding techniques. Particularly, when $M = 1$, $R_{EGT,avg} = R_{ofdm,avg}$, we obtain exact the same average achievable rate as in the SISO system without precoding, which means that the EGT precoding technique can not improve the capacity of SISO system.

With TR precoding technique, the instantaneous SINR is:

$$\mathrm{SINR}_{TR,ins}(f) = \frac{\frac{1}{M}\left|\sum_{m=1}^{M}\left|\xi_m^{(1)}\right|^2\right|^2 \gamma G_X(f)}{\frac{1}{M}\left|\sum_{m=1}^{M}\xi_m^{(1)}\xi_m^{(2)*}\right|^2 \frac{P_{Inf}}{P_{Use}}\gamma\frac{G_{Inf}(f)}{G_X(f)} + 1} \tag{2.22}$$

With MRT precoding technique, the instantaneous SINR is:

$$\mathrm{SINR}_{MRT,ins}(f) = \frac{\sum_{m=1}^{M}\left|\xi_m^{(1)}\right|^2 \gamma G_X(f)}{\frac{\left|\sum_{m=1}^{M}\xi_m^{(1)}\xi_m^{(2)*}\right|^2}{\sum_{m=1}^{M}\left|\xi_m^{(2)}\right|^2}\frac{P_{Inf}}{P_{Use}}\gamma\frac{G_{Inf}(f)}{G_X(f)} + 1} \tag{2.23}$$

Replacing the SINR part of (2.19) with the above SINR expressions, the achievable sum rates are displayed in Fig. 2.2.3 with different antenna number M. We observed also a slight increase for small values of τ as in SISO case. However, with the increased scale of the transmit antenna array, a complete channel overlay becomes considerable for high SNR regime. We also note that when the antenna number M increases, the capacity of TR tends to that of MRT. The capacity of EGT keeps a gap with that of MRT which progressively increases with τ. This gap shows that the focusing gain of EGT method is smaller than that of MRT and TR methods, hence EGT systems are more sensitive to the inter-channel interference.

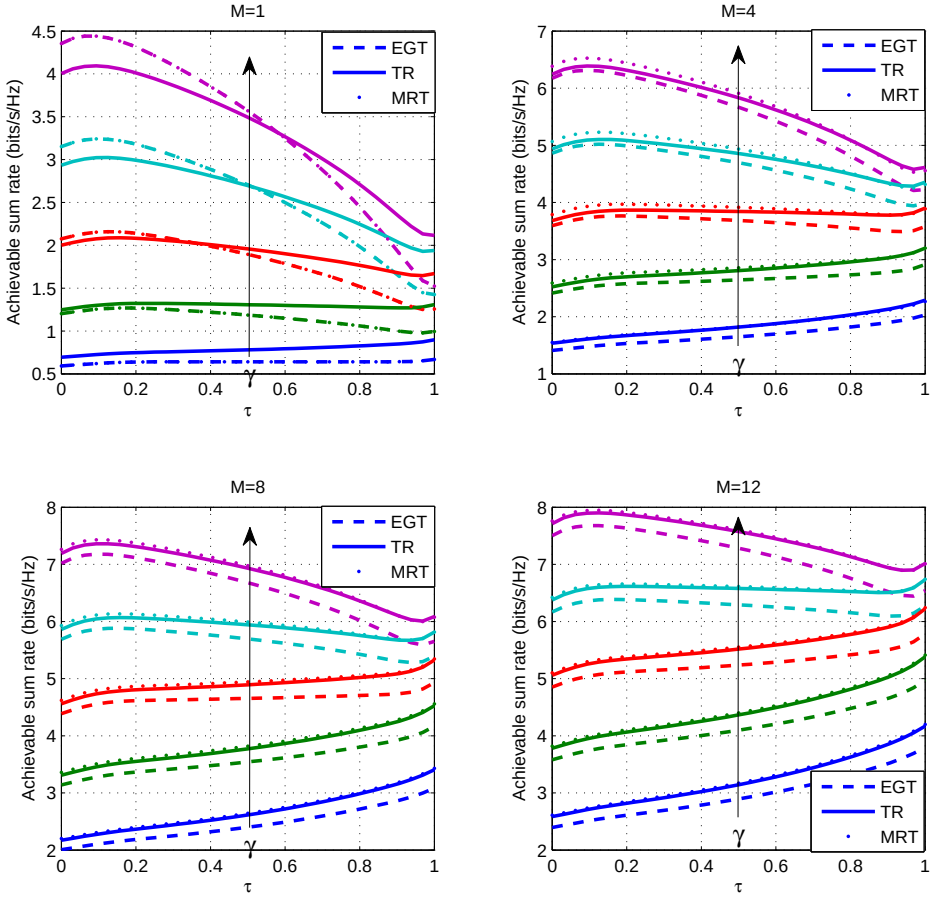

Figure 2.7: Achievable rate in function of the overlap ratio τ with single carrier modulation for $M \in \{1,4,8,12\}$ and $\gamma \in \{0,5,10,15,20\}\,dB$

For multi-carrier systems, the instantaneous SINR using EGT precoding is:

$$\mathrm{SINR}_{EGT,ins} = \frac{\frac{1}{M}\left|\sum_{m=1}^{M}\left|\xi_m^{(1)}\right|\right|^2 \gamma}{\frac{1}{M}\left|\sum_{m=1}^{M}\xi_m^{(1)} e^{-j\Phi_m^{(2)}}\right|^2 \frac{P_{Inf}}{P_{Use}}\gamma + 1} \tag{2.24}$$

With TR precoding technique, the instantaneous SINR is:

$$\mathrm{SINR}_{TR,ins} = \frac{\frac{1}{M}\left|\sum_{m=1}^{M}\left|\xi_m^{(1)}\right|^2\right|^2\gamma}{\frac{1}{M}\left|\sum_{m=1}^{M}\xi_m^{(1)}\xi_m^{(2)*}\right|^2\frac{P_{Inf}}{P_{Use}}\gamma+1} \tag{2.25}$$

With MRT precoding technique, the instantaneous SINR is:

$$\mathrm{SINR}_{MRT,ins}(f) = \frac{\sum_{m=1}^{M}\left|\xi_m^{(1)}\right|^2\gamma}{\frac{\left|\sum_{m=1}^{M}\xi_m^{(1)}\xi_m^{(2)*}\right|^2}{\sum_{m=1}^{M}\left|\xi_m^{(2)}\right|^2}\frac{P_{Inf}}{P_{Use}}\gamma+1} \tag{2.26}$$

Replacing the SINR part of (2.20) with the above SINR expressions, the achievable sum rates of OFDM systems are displayed in Fig. 2.8. We observed that the variation is monotonous as in SISO systems. However, with the increased scale of antenna array, the channel overlapping scheme becomes interesting for larger SNR range.

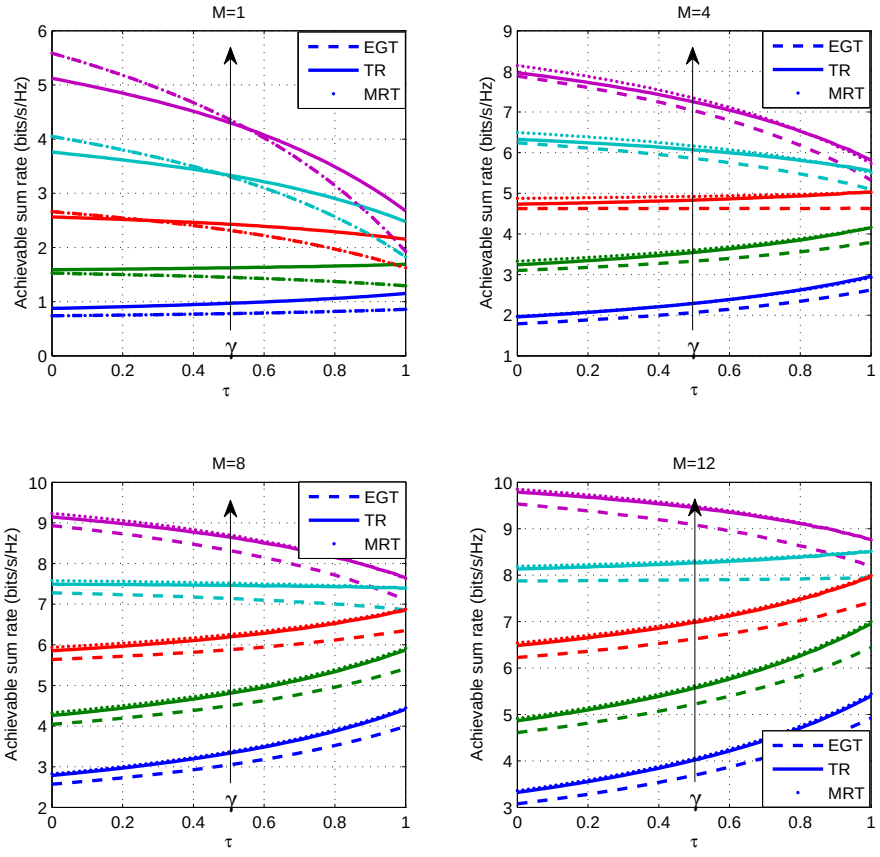

Figure 2.8: Achievable rate in function of the overlap ratio τ with OFDM for $M \in \{1,4,8,12\}$ and $\gamma \in \{0,5,10,15,20\}\,dB$

From the previous analysis, we noted that the achievable rate depends on the overlap ratio τ, the SNR γ and the antenna number M. In the next part, we would like to reveal the relationship between the optimal τ, corresponds to the maximal capacity and denoted as τ_{max}, and the parameters γ and M.

2.2.4 Optimal overlap ratio τ_{max}

For single carrier modulation, the achievable sum rates show quite complex variations with respect to τ. The τ_{max} evolution versus γ for different values of M and α is numerically evaluated as shown in Fig. 2.9, 2.10 and 2.11 for EGT, TR and MRT precoding systems, respectively. We observe that at low SNR regime, since the AWGN is dominant, the optimal choice is to completely overlap the signals of two users within a unique channel. Then as the SNR increases, we observe a kind of threshold effect at which the overlap becomes partial to guarantee the highest achievable sum rate and depends on α. Interestingly, the γ threshold value increases with M, which proves the multiplexing gain of multi-antenna system.

Another interesting point is that the thresholds of EGT systems are always smaller than that of TR and MRT systems, which proves again that EGT systems are more sensitive to the inter-channel interference.

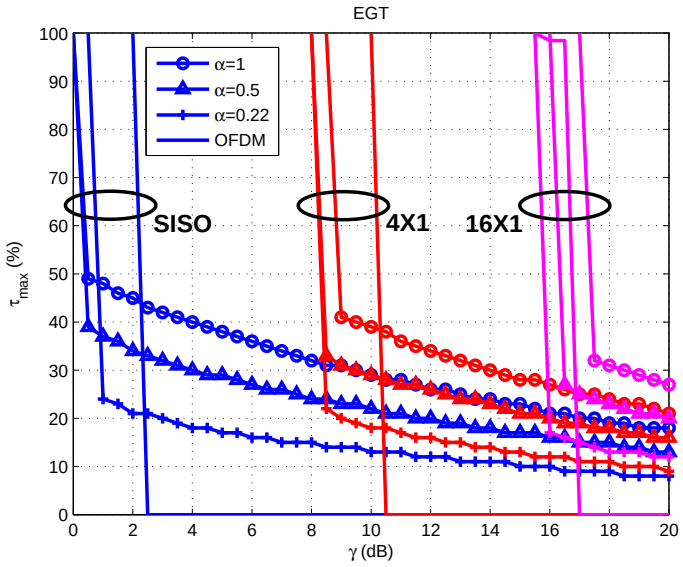

Figure 2.9: Optimal overlap ratio τ_{max} in function of γ for single carrier and multi-carrier systems using EGT precoding

For multicarrier modulation, the achievable rate evolution is monotonous (equivalent to the case of $\alpha = 0$). Consequently, $\tau_{max} \in \{0, 1\}$, which means that a partial overlapping may not maximize the system capacity. However, in practical cases, the overlapping can still be partial to adapt the constraint of bit error rate (BER).

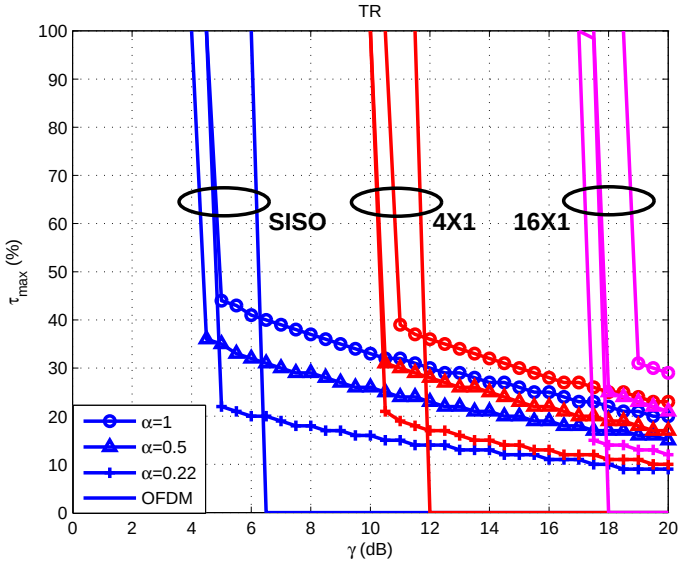

Figure 2.10: Optimal overlap ratio τ_{max} in function of γ for single carrier and multi-carrier systems using TR precoding

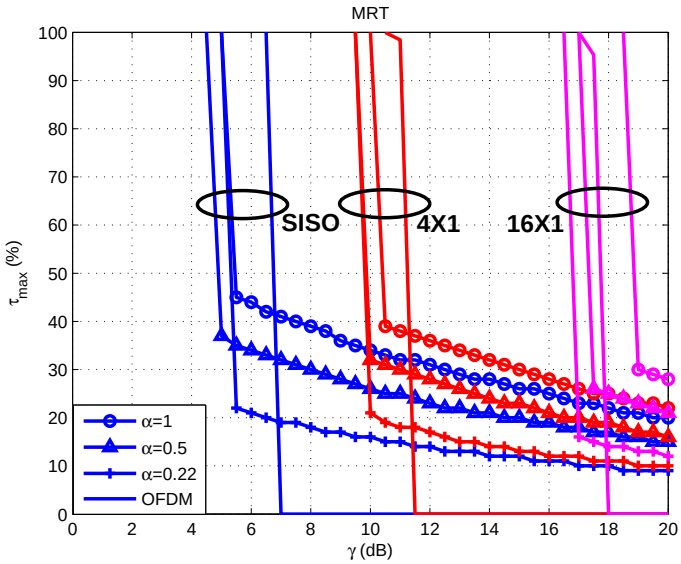

Figure 2.11: Optimal overlap ratio τ_{max} in function of γ for single carrier and multi-carrier systems using MRT precoding

2.3 Theoretical capacity derivation

In this part, we derive the theoretical capacity analysis using OFDM signals, for which the achievable rate is always higher than the single carrier case, and the signal expression is much more simple.

As seen in (2.20), the capacity equation can be separated into two parts with arguments SNR and SINR. We derive in the following the capacity of non-overlapped and overlapped subbands, respectively. The capacity of the non-overlapped subbands is equivalent to the capacity of a SU-MISO system. New capacity lower bounds are proposed for EGT and TR methods. Exact capacity equation is established using MRT method. On the other hand, the capacity of overlapped subbands is equivalent to a two-user MIMO system, which we study in a more general case by considering an arbitrary number of interfering users. New capacity lower bounds are proposed for EGT, TR and MRT methods. The accurate capacity approximations are also proposed for EGT and MRT methods at high SNR regime.

2.3.1 Capacity of the non-overlapped subbands

2.3.1.1 EGT SU-MISO capacity

With (2.20), the capacity of the non-overlapped sub-bands using EGT precoding is:

$$R_{EGT,avg,SNR} = \mathbb{E}_{\xi^{(1)}}\left[\log_2\left(1+\frac{1}{M}\left|\sum_{m=1}^{M}\left|\xi_m^{(1)}\right|\right|^2\gamma\right)\right]. \tag{2.27}$$

The CFR ξ_m is normalized as $\mathbb{E}\left[\frac{1}{M}\sum_{m=1}^{M}|\xi_m|^2\right] = \frac{1}{M}\sum_{m=1}^{M}\mathbb{E}\left[|\xi_m|^2\right] = 1$. For each antenna m, $|\xi_m|$ follows a Rayleigh distribution with $\sigma = \sqrt{\frac{1}{2}}$. The PDF of the equivalent channel coefficient is a sum of M i.i.d. Rayleigh distributed random variables. No closed-forme of this PDF has been found but it exists an interesting approximation [91] using small argument approximation (SAA):

$$f_{SAA}(x) = \frac{x^{2M-1}e^{-\frac{x^2}{2b}}}{2^{M-1}b^M(M-1)!}, \quad b = \frac{\sigma^2}{M}\left[(2M-1)!!\right]^{1/M}. \tag{2.28}$$

where σ is the Rayleigh parameter.

In fact, this approximation is a special case of Nakagami distribution by taking the parameters $m = M$ and $\omega = 2Mb$. The PDF of Nakagami distribution is:

$$f(x|m,\omega) = \frac{2m^m}{\Gamma(m)\omega^m}x^{2m-1}e^{-\frac{m}{\omega}x^2},\ x>0,\ m\geq 0.5,\ \omega>0. \tag{2.29}$$

where m is the shape parameter and ω is the scale parameter.

We have from [92], $\omega = \mathbb{E}\left[x^2\right]$. Hence, ω equals to the average channel gain $\phi_{Use,EGT} = \mathbb{E}\left[x_{EGT}\right] = \mathbb{E}\left[\frac{1}{M}\left(\sum_{m=1}^{M}|\xi_m|\right)^2\right]$. As each antenna is independent between each other, the average

channel gain $\phi_{Use,EGT}$ is:

$$\begin{aligned}\phi_{Use,EGT} &= \mathbb{E}\left[\frac{1}{M}\left(\sum_{m=1}^{M}|\xi_m|\right)^2\right] \\ &= \frac{1}{M}\sum_{m=1}^{M}E\left[|\xi_m|^2\right] + \frac{1}{M}\sum_{m=1}^{M}\sum_{\substack{m'=1\\m'\neq m}}^{M}E\left[|\xi_m|\right]E\left[|\xi_{m'}|\right] \\ &= 1 + \frac{M(M-1)}{M}\left(\sigma\sqrt{\frac{\pi}{2}}\right)^2 \\ &= 1 + \frac{\pi}{4}(M-1)\end{aligned} \tag{2.30}$$

As the square of Nakagami distribution follows gamma distribution, the channel gain $x_{EGT} = \frac{1}{M}\left(\sum_{m=1}^{M}|\xi_m|\right)^2$ can be approximated by a gamma distribution with parameters $(k = M, \theta = \frac{\omega}{M} = \frac{1+\frac{\pi}{4}(M-1)}{M})$. The PDF of gamma distribution is:

$$p(x_{EGT}; M) = \frac{x^{k-1}e^{-\frac{x}{\theta}}}{\Gamma(k)\theta^k} = \frac{M^M x^{M-1} e^{-\frac{Mx}{1+\frac{\pi}{4}(M-1)}}}{\Gamma(M)(1+\frac{\pi}{4}(M-1))^M} \tag{2.31}$$

from which the average capacity of the non-overlapped subbands is deduced:

$$\begin{aligned}R_{EGT,avg,SNR} &= \int_0^{+\infty}\ln_2(1+\frac{1}{M}\left(\sum_{m=1}^{M}|\xi_m|\right)^2\gamma)p(\xi_m)d\xi_m \\ &= \int_0^{+\infty}\ln_2(1+x_{EGT}\gamma)p(x_{EGT};k,\theta)dx \\ &= \frac{e^{1/\gamma\theta}}{\Gamma(k)\theta^k\gamma^k\ln(2)}\sum_{n=0}^{k-1}\binom{k-1}{n}(-1)^{k-1-n} \\ &\quad\left[(\theta\gamma)^{n+1}\Gamma(n+1)\left[\Psi(n+1)+ln(\theta\gamma)\right] + \frac{{}_2F_2(n+1,n+1;n+2,n+2;-1/\gamma\theta)}{(n+1)^2}\right]\end{aligned} \tag{2.32}$$

with $\psi(\cdot)$ is the Euler totient function, ${}_2F_2(\cdot)$ is the hypergeometric function. The computation is detailed in Appendix-A.

We propose also a simple lower capacity bound for $SNR >> 1$:

$$\begin{aligned}R_{EGT,avg,SNR} > \check{R}_{EGT,avg,SNR} &= \int_0^{+\infty}\log_2(x_{EGT}\gamma)p(x_{EGT};M)dx \\ &= \frac{\psi(M) + ln(\frac{1+\frac{\pi}{4}(M-1)}{M}) + ln(\gamma)}{ln(2)}\end{aligned} \tag{2.33}$$

The proposed capacity approximation and the lower bound are displayed in Fig. 2.12. We observe that the gamma approximation well fits the simulation results. Also, the lower bound become more and more accurate when the SNR or the antenna number M increase.

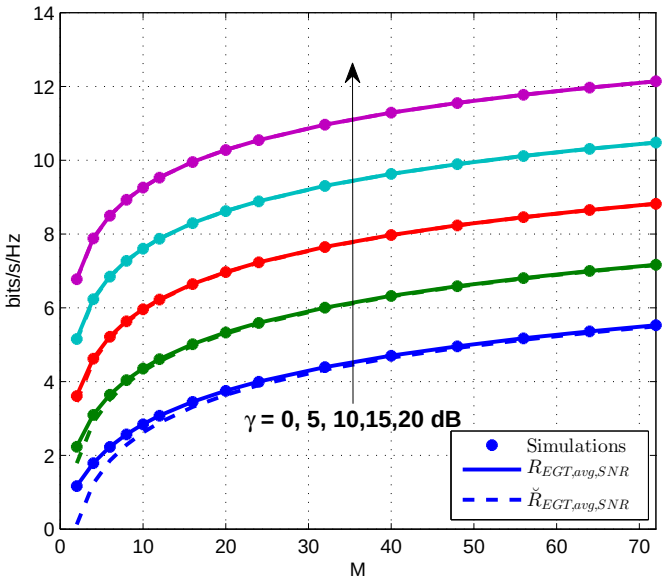

Figure 2.12: EGT SU-MISO capacity

2.3.1.2 TR SU-MISO capacity

For TR system, the average capacity of the non-overlapped subbands is:

$$\begin{aligned} R_{TR,avg,SNR} &= \mathbb{E}_{\xi^{(1)}}\left[\log_2\left(1+\frac{1}{M}\left|\sum_{m=1}^{M}|\xi_m^{(1)}|^2\right|^2\gamma\right)\right] \\ &= \int_0^{+\infty}\log_2(1+\frac{1}{M}\left|\sum_{m=1}^{M}|\xi_m|^2\right|^2\gamma)p(\xi_m)d\xi_m \\ &= \int_0^{+\infty}\log_2(1+x_{TR}^2\gamma)p(x_{TR};M)dx \end{aligned} \tag{2.34}$$

with $x_{TR}=\sum_{m=1}^{M}\frac{|\xi_m|^2}{\sqrt{M}}$ following the gamma distribution $\Gamma(M,\frac{1}{\sqrt{M}})$. A capacity lower bound can be deduced:

$$\begin{aligned} R_{TR,avg,SNR} > \check{R}_{TR,avg,SNR} &= \int_0^{+\infty}\log_2(x_{TR}^2\gamma)p(x_{TR};M)dx \\ &= \frac{2}{ln(2)}\int_0^{+\infty}\ln(x_{TR}\sqrt{\gamma})p(x_{TR};M)dx \\ &= \frac{2\psi(M)-ln(M)+ln(\gamma)}{ln(2)} \end{aligned} \tag{2.35}$$

The proposed capacity lower bounds are displayed in Fig. 2.13. We observe that, as in the EGT case, the capacity lower bounds become more and more accurate when the SNR or the number of antennas M increases.

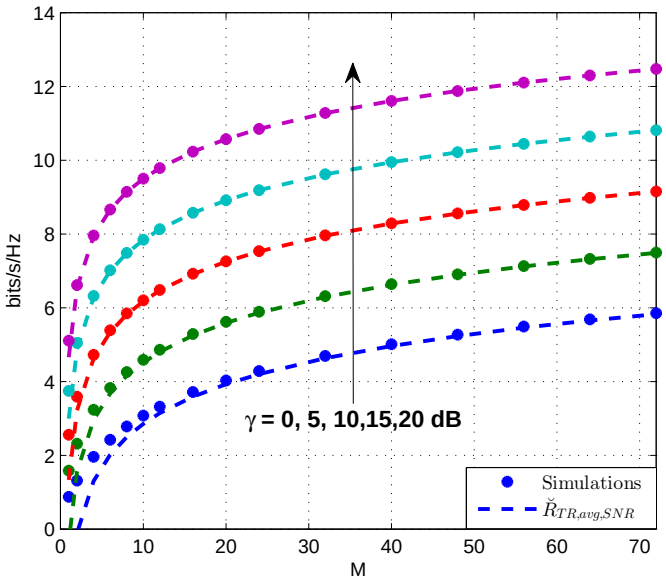

Figure 2.13: TR SU-MISO capacity

2.3.1.3 MRT SU-MISO capacity

For MRT system, the average capacity of the non-overlapped subbands is:

$$\begin{aligned} R_{MRT,avg,SNR} &= \mathbb{E}_{\xi^{(1)}}\left[\log_2\left(1+\sum_{m=1}^{M}\left|\xi_m^{(1)}\right|^2\gamma\right)\right] \\ &= \int_0^{+\infty}\log_2(1+\sum_{m=1}^{M}|\xi_m|^2\gamma)p(\xi_m)d\xi_m \\ &= \int_0^{+\infty}\log_2(1+x_{MRT}\gamma)p(x_{MRT};M)dx \end{aligned} \tag{2.36}$$

with $x_{MRT}=\sum_{m=1}^{M}|\xi_m|^2$ follows the gamma distribution $\Gamma(M,1)$. Using the computation of Appendix-A, the capacity is deduced:

$$\begin{aligned} R_{MRT,avg,SNR} = \frac{e^{1/\gamma\theta}}{\Gamma(k)\theta^k\gamma^k\ln(2)}\sum_{n=0}^{k-1}\binom{k-1}{n}(-1)^{k-1-n} \\ \left[(\theta\gamma)^{n+1}\Gamma(n+1)\left[\Psi(n+1)+ln(\theta\gamma)\right]+\frac{{}_2F_2(n+1,n+1;n+2,n+2;-1/\gamma\theta)}{(n+1)^2}\right] \end{aligned} \tag{2.37}$$

A simple capacity lower bound is given by:

$$\begin{aligned} R_{MRT,avg,SNR} > \check{R}_{MRT,avg,SNR} &= \int_0^{+\infty}\log_2(x_{MRT}\gamma)p(x_{MRT};M)dx \\ &= \frac{1}{ln(2)}\int_0^{+\infty}\ln(x_{MRT}\gamma)p(x_{MRT};M)dx \\ &= \frac{\psi(M)+ln(\gamma)}{ln(2)} \end{aligned} \tag{2.38}$$

The exact capacity expression and the capacity lower bound are displayed in Fig. 2.14.

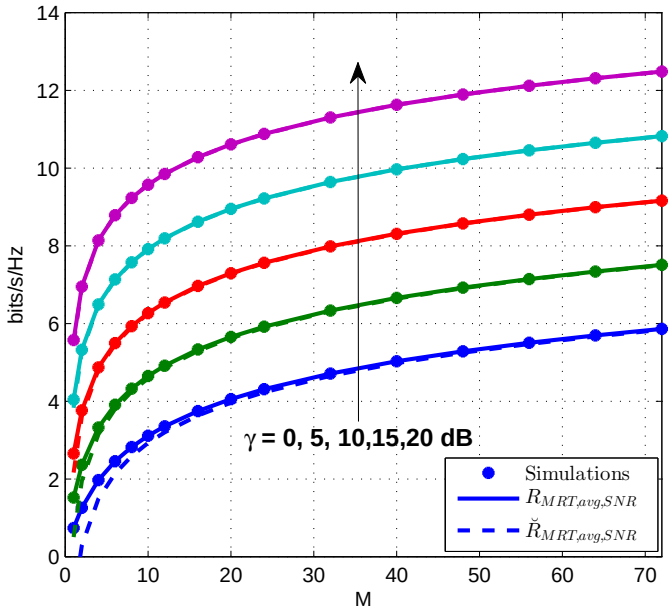

Figure 2.14: MRT SU-MISO capacity

2.3.2 Capacity of the overlapped subbands

2.3.2.1 EGT MU-MIMO capacity

For the overlapped subbands, the achievable rate using EGT is:

$$R_{EGT,avg,SINR} = \mathbb{E}_{\xi^{(1)}}\left[\log_2\left(1+\frac{\frac{1}{M}\left|\sum_{m=1}^{M}\left|\xi_m^{(1)}\right|\right|^2\gamma}{\frac{P_{Inf}}{P_{Use}}\gamma\frac{1}{M}\left|\sum_{m=1}^{M}\xi_m^{(1)}e^{-j\Phi_m^{(2)}}\right|^2+1}\right)\right]. \tag{2.39}$$

A capacity lower bound is proposed in [54] for massive MIMO context, which is based on the fact that the worst-case uncorrelated additive noise is independent Gaussian noise of same variance [93]. Applied to EGT precoding, the SINR lower bound is expressed as:

$$\check{SINR}_{EGT} = \frac{\frac{1}{M}\left|\mathbb{E}\left[\sum_{m=1}^{M}|\xi_m|\right]\right|^2\gamma}{\frac{1}{M}\mathbb{E}\left[\left|\sum_{m=1}^{M}\xi_m e^{-j\Phi_m}\right|^2\right]\frac{P_{Inf}}{P_{Use}}\gamma+var\{\frac{1}{\sqrt{M}}\sum_{m=1}^{M}|\xi_m|\}\gamma+1} \tag{2.40}$$

Therefore, the achievable rate lower bound is:

$$\check{R}_{EGT} = \log_2\left(1+\check{SINR}_{EGT}\right) \tag{2.41}$$

$\check{R}_{EGT}$ is displayed with the numerical results of $R_{EGT,avg,SINR}$ in Fig. 2.15. We observed that the lower bounds are much lower than the achievable rates, especially in high SNR regime where the inter-channel interference is dominant. In fact, the difference comes from two aspects:

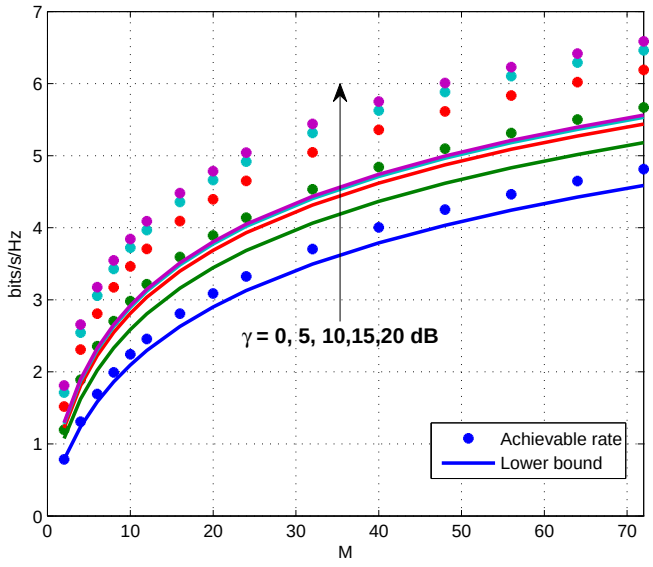

Figure 2.15: Achievable rate $R_{EGT,avg,SINR}$ and lower bound $\check{R}_{EGT}$ in function of the number of transmit antennas for different γ values

1) the distribution of the equivalent channel coefficient has not been considered. The influence is more visible in low SNR regime where the AWGN is dominant and the inter-channel interference presents less impact. 2) The distribution of the inter-channel interference has not been considered. Its influence is more visible in high SNR regime where interference is dominant.

For these reasons, we propose here another achievable rate lower bound to deal with the differences mentioned above. This lower bound better adapts the moderate-scale MU-MIMO systems.

The inter-channel interference term of EGT $J_{EGT} = \frac{1}{\sqrt{M}} \sum_{m=1}^{M} \xi_m e^{-j\Phi_m}$ is a Gaussian process of zero mean and variance $\phi_{Inf,EGT} = \mathbb{E}\left[\frac{1}{M}\left|\sum_{m=1}^{M} \xi_m e^{-j\Phi_m}\right|^2\right] = 1$. In fact, the CFR ξ_m is a complex Gaussian process, its real part and imaginary part are Gaussian distributed with zero mean and variance $\sigma^2 = \frac{1}{2}$ respectively. The phase $\Phi_m^{(2)}$ is uniformly distributed on $[0, 2\pi]$. According to the linearity propriety of Gaussian process, $J_{EGT} = \frac{1}{\sqrt{M}} \sum_{m=1}^{M} \xi_m e^{-j\Phi_m}$ is a Gaussian process. Therefore, the modulus square $|J_{EGT}|^2 = \frac{1}{M}\left|\sum_{m=1}^{M} \xi_m e^{-j\Phi_m}\right|^2$ follows a gamma distribution $\Gamma(1,1)$.

For any instantaneous realization of the channel, the channel gain $x_{EGT} = \frac{1}{M}\left|\sum_{m=1}^{M} |\xi_m|\right|^2$ and the interference power $|J_{EGT}|^2 = \frac{1}{M}\left|\sum_{m=1}^{M} \xi_m e^{-j\Phi_m}\right|^2$ both contain the same component ξ_m, hence their values are correlated. The correlation is measured by the correlation coefficient ρ. For two random variables x and y, ρ_{xy} is defined as [94]:

$$\rho_{xy} = \frac{\mathbb{E}\left[(x - \bar{x})(y - \bar{y})\right]}{\sigma_x \sigma_y} \tag{2.42}$$

The correlation coefficient equals to $+1$ in the case of a perfect direct (increasing) linear relationship (correlation), equals to -1 in the case of a perfect decreasing (inverse) linear relationship (anticorrelation) [95]. The other values between $]-1, +1[$ indicate the degree of linear depen-

dence between the variables. When it approaches zero, the relationship is closer to uncorrelated, the closer the coefficient is to either ±1, the stronger the correlation between the variables. The correlation between the channel gain x_{EGT} and the interference power $|J_{EGT}|^2$ is displayed in Fig. 2.16.

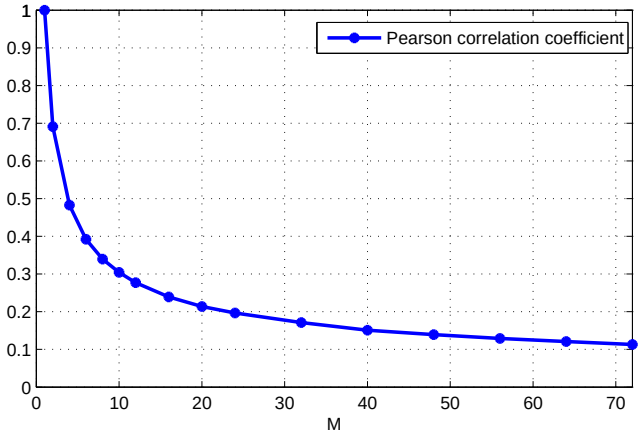

Figure 2.16: The correlation coefficient ρ between the channel gain x_{EGT} and the interference power $|J_{EGT}|^2$ in function of the number of transmit antennas M

For $M = 1$, we have $x_{EGT} = |J_{EGT}|^2 = |\xi_m|^2$, then $\rho = 1$. When M increases, the value of ρ rapidly decreases, which means that the correlation between the channel gain x_{EGT} and the interference power $|J_{EGT}|^2$ vanishes.

Therefore, we propose here an approximate model for achievable rate estimation. The inter-channel interference term $\tilde{J}_{EGT}$ is Gaussian distributed but assumed independent with the channel gain. Then $y_{EGT} = \left|\tilde{J}_{EGT}\right|^2$ follows a gamma distribution $\Gamma(1,1)$. The approximate achievable rate is:

$$\tilde{R}_{EGT,avg,SINR} = \mathbb{E}_{\xi_m^{(1)}}\left[\log_2\left(1 + \frac{x_{EGT}\gamma}{\frac{P_{Inf}}{P_{Use}} y_{EGT}\gamma + 1}\right)\right] \tag{2.43}$$

We display in Fig. 2.17 $\tilde{R}_{EGT,avg,SINR}$ and $R_{EGT,avg,SINR}$. We observed that the approximate model $\tilde{R}_{EGT,avg,SINR}$ is very close to the achievable rate $R_{EGT,avg,SINR}$ even with small number of antennas. These results prove that the correlation between the channel gain and the interference power can be neglected in achievable rate estimation.

$$\tilde{R}_{EGT,avg,SINR} = \int_0^{+\infty}\int_0^{+\infty} \log_2\left(1 + \frac{x_{EGT}\gamma}{\frac{P_{Inf}}{P_{Use}} y_{EGT}\gamma + 1}\right) p(x_{EGT})p(y_{EGT})dxdy \tag{2.44}$$

Let us study a more general case of multiple interfering users $N_u \geq 1$. Without loss of generality, we assume that all the users have the same power level. The channel gain of each user is Gamma distributed $x \sim \Gamma(k,\theta)$, as the MAI caused by different users is independent between each other, the interference term $J_{N_u} \sim \mathrm{CN}(0, N_u \cdot 2\sigma^2)$, and its power $\left|J_{N_u}\right|^2 \sim \Gamma(1, N_u \cdot 2\sigma^2)$. Then the PDF function of the sum of interference and noise power $v = \left|J_{N_u}\right|^2\gamma + 1$ writes:

$$p_{N_u}(v) = \frac{1}{N_u 2\sigma^2\gamma} e^{-\frac{v-1}{N_u 2\sigma^2\gamma}} \quad v \in]1, +\infty[\tag{2.45}$$

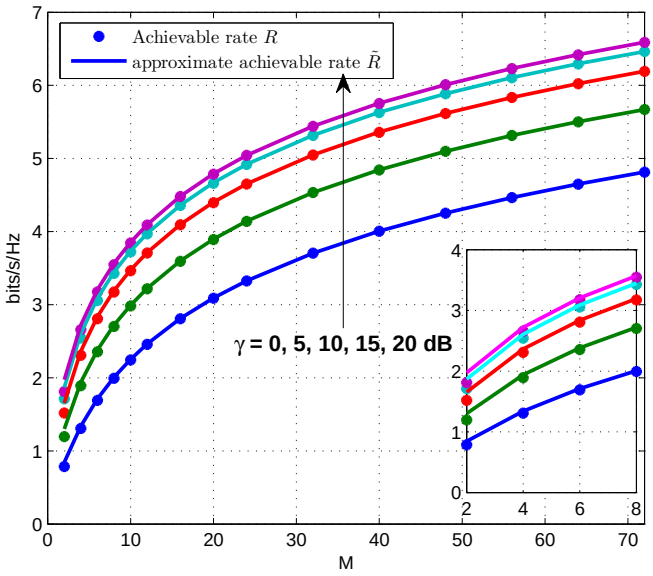

Figure 2.17: Achievable rate $R_{EGT,avg,SINR}$ and approximate model $\tilde{R}_{EGT,avg,SINR}$ in function of the number of transmit antennas M for different γ values

Then, the distribution of SINR $\Xi = \frac{x\gamma}{v}$ is:

$$\begin{aligned} p(\Xi) &= \frac{1}{\gamma}\int_1^{+\infty} p_x(\frac{\Xi v}{\gamma}) p_{N_u}(v) v dv \\ &= \frac{e^{\frac{1}{N_u 2\sigma^2\gamma}}}{N_u 2\sigma^2\Gamma(k)\theta^k}\Xi^{k-1}\int_1^{+\infty} v^k e^{-\left(\frac{\Xi}{\theta\gamma}+\frac{1}{N_u 2\sigma^2\gamma}\right)v} dv \\ &= \frac{e^{\frac{1}{N_u 2\sigma^2\gamma}}\theta}{N_u 2\sigma^2\Gamma(k)}\Xi^{k-1}\frac{\Gamma\left(k+1, \frac{\Xi}{\theta\gamma}+\frac{1}{N_u 2\sigma^2\gamma}\right)}{\left(\Xi+\frac{\theta}{N_u 2\sigma^2}\right)^{k+1}} \end{aligned} \tag{2.46}$$

Therefore, the approximated average achievable rate is:

$$\tilde{R}_{EGT,mu} = \int_0^{+\infty} \log_2(1+\Xi) p(\Xi) d\Xi \tag{2.47}$$

Noting $y = 1 + \Xi$,

$$\begin{aligned}
\tilde{R}_{EGT,mu} &= \frac{e^{\frac{1}{N_u 2\sigma^2 \gamma}}\theta}{N_u 2\sigma^2 \Gamma(k)\ln 2}\int_1^{+\infty} \ln(y)(y-1)^{k-1}\frac{\Gamma\left(k+1, \frac{y-1}{\gamma\theta}+\frac{1}{N_u 2\sigma^2\gamma}\right)}{\left(y-1+\frac{\theta}{N_u 2\sigma^2}\right)^{k+1}}dy \\
&= \frac{e^{\frac{1}{N_u 2\sigma^2 \gamma}}\theta}{N_u 2\sigma^2 \Gamma(k)\ln 2}\int_{\frac{1}{N_u 2\sigma^2}}^{+\infty} e^{-t}t^k \int_{t\theta\gamma+1-\frac{\theta}{N_u 2\sigma^2}}^{+\infty} \ln(y)\frac{(y-1)^{k-1}}{\left(y-1+\frac{\theta}{N_u 2\sigma^2}\right)^{k+1}}dydt \\
&= \frac{e^{\frac{1}{N_u 2\sigma^2 \gamma}}\theta}{N_u 2\sigma^2 \Gamma(k)\ln 2}\sum_{l=0}^{k-1}\binom{k-1}{l}\left(\frac{-\theta}{N_u 2\sigma^2}\right)^l \int_{\frac{1}{N_u 2\sigma^2}}^{+\infty} e^{-t}t^k \int_{t\theta\gamma+1-\frac{\theta}{N_u 2\sigma^2}}^{+\infty} \frac{\ln(y)}{\left(y-1+\frac{\theta}{N_u 2\sigma^2}\right)^{l+2}}dydt \\
&= \frac{e^{\frac{N_0}{N_u 2\sigma^2 \gamma}}\theta}{N_u 2\sigma^2 \Gamma(k)\ln 2}\sum_{l=0}^{k-1}\binom{k-1}{l}\left(\frac{-1}{N_u 2\sigma^2\gamma}\right)^l \int_{\frac{1}{N_u 2\sigma^2}}^{+\infty} e^{-t}t^{k-l}\frac{{}_2F_1(1,-l;1-l;-\frac{\theta t\gamma}{a})}{al(l+1)}dt \\
&\quad + \frac{e^{\frac{N_0}{N_u 2\sigma^2 \gamma}}}{N_u 2\sigma^2\gamma\Gamma(k)\ln 2}\sum_{l=0}^{k-1}\binom{k-1}{l}\left(\frac{-1}{N_u 2\sigma^2\gamma}\right)^l \int_{\frac{1}{N_u 2\sigma^2}}^{+\infty} e^{-t}t^{k-l-1}\frac{\log(t\theta\gamma+a)}{l+1}dt.
\end{aligned} \tag{2.48}$$

with $a = 1 - \frac{\theta}{N_u 2\sigma^2}$. The integration becomes too complex. For high SNR regime (SNR $\geq 20dB$), the power of the thermal noise is more than 100 times smaller then the transmitted power. Hence, ignoring the thermal noise for high SNR regime, the SINR $\dot{\Xi} = \frac{x\gamma}{\dot{\nu}\gamma} = \frac{x}{\dot{\nu}}$ with $\dot{\nu} = \left|J_{N_u}\right|^2$ and PDF writes:

$$p_{N_u}(\dot{\nu}) = \frac{1}{N_u 2\sigma^2}e^{-\frac{\dot{\nu}}{N_u 2\sigma^2}} \quad \dot{\nu} \in]0, +\infty[\tag{2.49}$$

The distribution of SINR $\dot{\Xi}$ is:

$$\begin{aligned}
p(\dot{\Xi}) &= \int_0^{+\infty} p_x(\dot{\Xi}\dot{\nu})p_{N_u}(\dot{\nu})\dot{\nu}d\dot{\nu} \\
&= \frac{1}{N_u 2\sigma^2\Gamma(k)\theta^k}\dot{\Xi}^{k-1}\int_0^{+\infty}\dot{\nu}^k e^{-\left(\frac{\dot{\Xi}}{\theta}+\frac{1}{N_u 2\sigma^2}\right)\dot{\nu}}d\dot{\nu} \\
&= \frac{k\theta}{N_u 2\sigma^2}\dot{\Xi}^{k-1}\frac{1}{\left(\dot{\Xi}+\frac{\theta}{N_u 2\sigma^2}\right)^{k+1}}
\end{aligned} \tag{2.50}$$

Therefore, the approximated average achievable rate is:

$$\dot{\tilde{R}}_{EGT,mu} = \int_0^{+\infty}\log_2(1+\dot{\Xi})p(\dot{\Xi})d\dot{\Xi} \tag{2.51}$$

Noting $y = 1 + \dot{\Xi}$,

$$\begin{aligned}
\dot{\tilde{R}}_{EGT,mu} &= \frac{k\theta}{N_u 2\sigma^2\ln 2}\int_1^{+\infty}\ln(y)(y-1)^{k-1}\frac{1}{\left(y-1+\frac{\theta}{N_u 2\sigma^2}\right)^{k+1}}dy \\
&= \frac{k\theta}{N_u 2\sigma^2\ln 2}\sum_{l=0}^{k-1}\binom{k-1}{l}\left(\frac{-\theta}{N_u 2\sigma^2}\right)^l\int_1^{+\infty}\frac{\ln(y)}{\left(y-1+\frac{\theta}{N_u 2\sigma^2}\right)^{l+2}}dy \\
&= \frac{k\theta}{N_u 2\sigma^2\ln 2}\sum_{l=1}^{k-1}\binom{k-1}{l}\frac{(-1)^l}{(l+1)^2}{}_2F_1(1,1;l+2;1-\frac{\theta}{N_u 2\sigma^2}) + \frac{k\theta\log(N_u 2\sigma^2/\theta)}{ln(2)(N_u 2\sigma^2-\theta)}
\end{aligned} \tag{2.52}$$

with $k = M$, $2\sigma^2 = 1$, $\theta = \frac{1+\frac{\pi}{4}(M-1)}{M}$.

Another approximated lower bound for high SINR regime writes:

$$\begin{aligned}\tilde{R}_{EGT,mu} > \tilde{\tilde{R}}_{EGT,mu} &= \int_0^{+\infty}\int_0^{+\infty} \log_2\left(\frac{x_{EGT}\gamma}{N_u y_{EGT}\gamma + 1}\right) p(x_{EGT})p(y_{EGT})dxdy \\ &= \int_0^{+\infty} \log_2\left(x_{EGT}\gamma\right) p(x_{EGT})dx - \int_0^{+\infty} \log_2\left(N_u y_{EGT}\gamma + 1\right) p(y_{EGT})dy\end{aligned} \tag{2.53}$$

The first part of the integration is directly obtained from (2.33). Then the second part of the integration becomes:

$$\begin{aligned}\int_0^{+\infty} \log_2\left(N_u y_{EGT}\gamma + 1\right) p(y_{EGT})dy &= \int_0^{+\infty} \log_2\left(N_u y_{EGT}\gamma + 1\right) e^{-y}dy \\ &= -e^{\frac{1}{N_u\gamma}} Ei(-\frac{1}{N_u\gamma})\end{aligned} \tag{2.54}$$

Therefore,

$$\tilde{\tilde{R}}_{EGT,mu} = \frac{\psi(M) + ln(\frac{1+\frac{\pi}{4}(M-1)}{M}) + e^{\frac{1}{N_u\gamma}} Ei(-\frac{1}{N_u\gamma}) + ln(\gamma)}{ln(2)} \tag{2.55}$$

where $Ei(\cdot)$ is the exponential integral function.

$\tilde{\tilde{R}}_{EGT,mu}$ is displayed in Fig. 2.18 with the achievable rates $R_{EGT,avg,SINR}$, $\tilde{R}_{EGT,avg,SINR}$ and $\dot{\tilde{R}}_{EGT,mu}$. When $SINR >> 1$, the lower bound approaches the achievable rate, otherwise, the precision of the lower bound decreases.

2.3.2.2 TR MU-MIMO capacity

For TR system, the correlation between the channel gain $x_{TR}^2 = \frac{1}{M}\left(\sum_{m=1}^{M}|\xi_m|^2\right)^2$ and the interference power $y_{TR} = \frac{1}{M}\left|\sum_{m=1}^{M}\xi_m^{(1)}\xi_m^{(2)*}\right|^2$ is weaker than in the EGT case, because that the amplitude of $\xi_m^{(2)}$ is also involved in the interference power term. The correlation coefficient is displayed in Fig. 2.19. Therefore, we derive similar approximate model of achievable rate as in the EGT case. The inter-channel interference term $\tilde{J}_{TR}$ is Gaussian distributed and assumed independent with the channel gain. The variance $\phi_{Inf,TR} = \mathbb{E}\left[\frac{1}{M}\left|\sum_{m=1}^{M}\xi_m^{(1)}\xi_m^{(2)*}\right|^2\right] = \frac{1}{M}\sum_{m=1}^{M}E\left[|\xi_m^{(1)}|^2\right]E\left[|\xi_m^{(2)}|^2\right] + \frac{1}{M}\sum_{m=1}^{M}\sum_{\substack{m'=1\\m'\neq m}}^{M}E\left[\xi_m^{(1)}\xi_m^{(2)*}\xi_{m'}^{(1)*}\xi_{m'}^{(2)}\right] = 1$. Then $y_{TR} = \left|\tilde{J}_{TR}\right|^2$ follows a gamma distribution $\Gamma(1,1)$. The approximate achievable rate is:

$$\tilde{R}_{TR,avg,SINR} = \mathbb{E}_{\xi_m^{(1)}}\left[\log_2\left(1 + \frac{x_{TR}^2\gamma}{\frac{P_{Inf}}{P_{Use}}y_{TR}\gamma + 1}\right)\right] \tag{2.56}$$

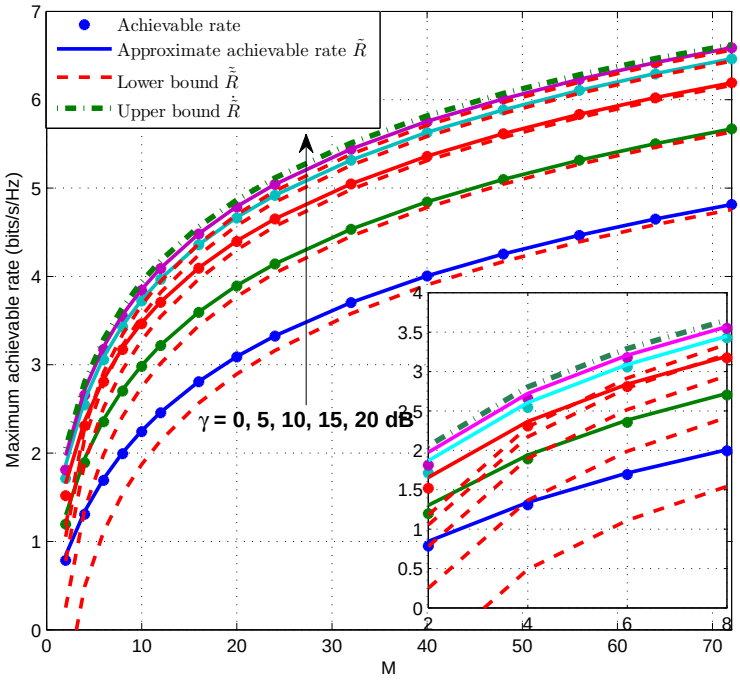

Figure 2.18: Achievable rate lower bound $\tilde{\tilde{R}}_{EGT,avg,SINR}$ in function of the number of transmit antennas M for different γ values

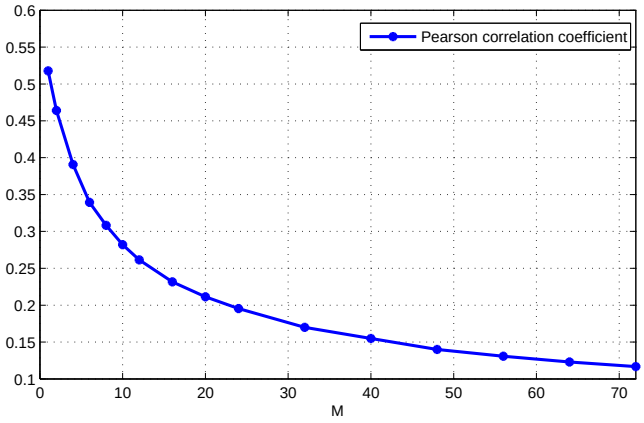

Figure 2.19: The correlation coefficient ρ between the channel gain x_{TR}^2 and the interference power y_{TR} in function of the number of transmit antennas M

Reuse the same derivation in 2.3.2.1, a closed-form capacity lower bound for high SINR and arbitrary interfering users is:

$$\begin{aligned}\tilde{\tilde{R}}_{TR,mu} &= \int_0^{+\infty}\int_0^{+\infty} \log_2\left(\frac{x_{TR}^2\gamma}{N_u y_{TR}\gamma+1}\right) p(x_{TR})p(y_{TR})dxdy \\ &= \int_0^{+\infty} \log_2\left(x_{TR}^2\gamma\right) p(x_{TR})dx - \int_0^{+\infty} \log_2\left(N_u y_{TR}\gamma+1\right) p(y_{TR})dy \\ &= \frac{2\psi(M) - ln(M) + e^{\frac{1}{N_u\gamma}} Ei(-\frac{1}{N_u\gamma}) + ln(\gamma)}{ln(2)}\end{aligned} \tag{2.57}$$

$R_{TR,avg,SINR}$, $\tilde{R}_{TR,avg,SINR}$ and $\tilde{\tilde{R}}_{TR,mu}$ are displayed in Fig. 2.20. The approximate model $\tilde{R}_{TR,avg,SINR}$ is validated because of the fact that its values are very closed to the real achievable rate $R_{TR,avg,SINR}$. However, the lower bound $\tilde{\tilde{R}}_{TR,mu}$ presents good accuracy only for high $SINR$ levels.

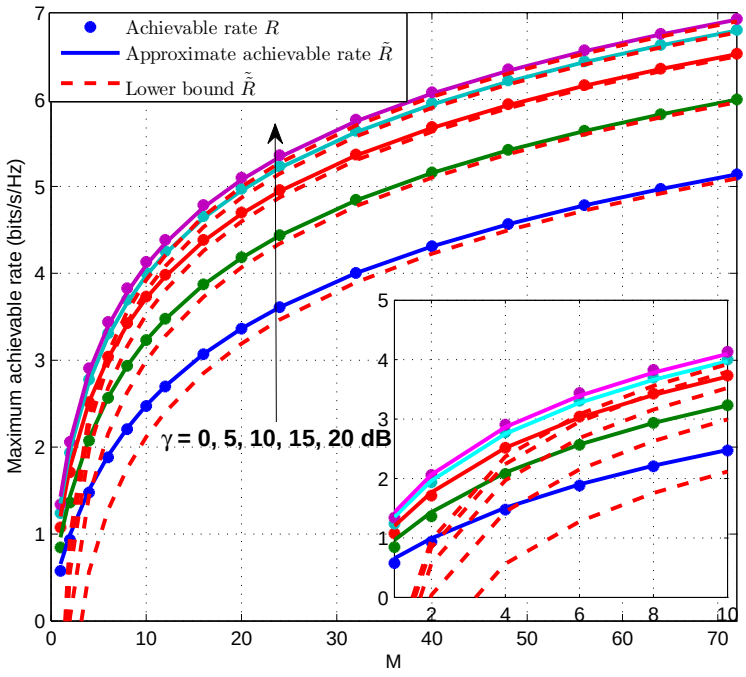

Figure 2.20: Achievable rate and its lower bounds in function of the number of transmit antennas M for different γ values

2.3.2.3 MRT MU-MIMO capacity

For MRT system, the channel gain $x_{MRT} = \sum_{m=1}^{M} |\xi_m^{(1)}|^2$ and the interference power $y_{MRT} = \frac{|\sum_{m=1}^{M} \xi_m^{(1)} \xi_m^{*(2)}|^2}{\sum_{m=1}^{M} |\xi_m^{(2)}|^2}$ are correlated as in EGT system as shown in Fig. 2.21. However, we assume the inter-channel interference term $\tilde{J}_{MRT}$ is Gaussian distributed and independent with the channel

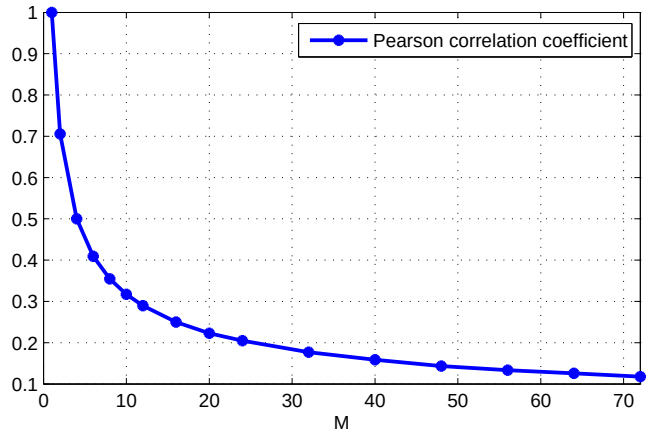

Figure 2.21: The correlation coefficient ρ between the channel gain x_{MRT} and the interference power y_{MRT} in function of the number of transmit antennas M

gain. The variance $\phi_{Inf,MRT} = \mathbb{E}\left[\frac{\left|\sum_{m=1}^{M}\xi_m^{(1)}\xi_m^{*(2)}\right|^2}{\sum_{m=1}^{M}\left|\xi_m^{(2)}\right|^2}\right] = 1$. Then $y_{MRT} = \left|\tilde{J}_{MRT}\right|^2$ follows a gamma distribution $\Gamma(1,1)$. The approximate achievable rate is:

$$\tilde{R}_{MRT,avg,SINR} = \mathbb{E}_{\xi_m^{(1)}}\left[\log_2\left(1+\frac{x_{MRT}\gamma}{\frac{P_{Inf}}{P_{Use}}y_{MRT}\gamma+1}\right)\right] \tag{2.58}$$

We use the same derivation as in 2.3.2.1, an achievable rate upper bound by ignoring the thermal noise is:

$$\dot{\tilde{R}}_{MRT,mu} = \frac{k\theta}{N_u 2\sigma^2 \ln 2}\sum_{l=1}^{k-1}\binom{k-1}{l}\frac{(-1)^l}{(l+1)^2}\,{}_2F_1(1,1;l+2;1-\frac{\theta}{N_u 2\sigma^2}) + \frac{k\theta\log(N_u 2\sigma^2/\theta)}{ln(2)(N_u 2\sigma^2-\theta)} \tag{2.59}$$

with $k = M$, $\theta = 1$ and $N_u > 1$ is the number of interfering users.

When $N_u = \theta = 2\sigma^2 = 1$,

$$\dot{\tilde{R}}_{MRT,mu} = \frac{k}{\ln 2}\sum_{l=0}^{k-1}\binom{k-1}{l}(-1)^l\frac{1}{(l+1)^2} \tag{2.60}$$

A more simple capacity lower bound is:

$$\begin{aligned}\tilde{\tilde{R}}_{MRT,mu} &= \int_0^{+\infty}\int_0^{+\infty}\log_2\left(\frac{x_{MRT}\gamma}{N_u y_{MRT}\gamma+1}\right)p(x_{MRT})p(y_{MRT})dxdy \\ &= \int_0^{+\infty}\log_2\left(x_{MRT}\gamma\right)p(x_{MRT})dx - \int_0^{+\infty}\log_2\left(N_u y_{MRT}\gamma+1\right)p(y_{MRT})dy \\ &= \frac{\psi(M)+e^{\frac{1}{N_u\gamma}}Ei(-\frac{1}{N_u\gamma})+ln(\gamma)}{ln(2)}\end{aligned} \tag{2.61}$$

$R_{MRT,avg,SINR}$, $\tilde{R}_{MRT,avg,SINR}$, $\dot{\tilde{R}}_{MRT,mu}$ and $\tilde{\tilde{R}}_{MRT,mu}$ are displayed in Fig. 2.22. The approximate model $\tilde{R}_{MRT,mu}$ and the upper bound $\dot{\tilde{R}}_{MRT,mu}$ are validated.

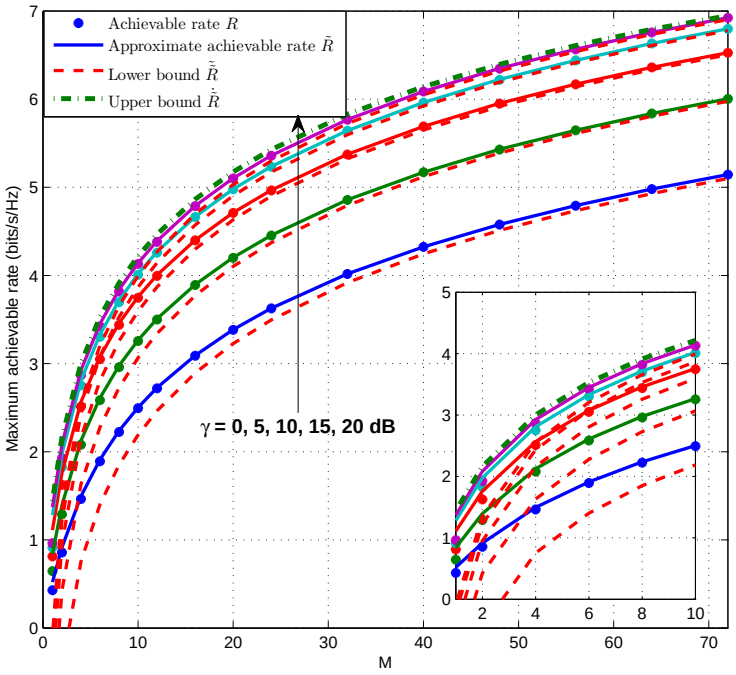

Figure 2.22: Achievable rate and its lower bounds in function of the number of transmit antennas M for different γ values

Through the analysis derived above, the approximate models that we proposed for achievable sum rate of general MU-MIMO systems present a good accuracy for arbitrary number of transmit antennas. The precision of lower bounds $\tilde{\tilde{R}}_{EGT,mu}$, $\tilde{\tilde{R}}_{TR,mu}$ and $\tilde{\tilde{R}}_{MRT,mu}$ increase with the number of transmit antennas and the SNR level. The upper bounds $\tilde{R}_{EGT,mu}$ and $\tilde{R}_{MRT,mu}$ are available for SNR $\geq 20dB$. We present in Fig. 2.23 an evaluation of $\tilde{R}_{MRT,(Nu+1)}$ for the total capacity of the system. Noting that all the users have the same power level.

We observe that the capacity increase monotonously with the transmit antenna number M and the co-exist user number N_u. This results is coherent with the capacity lower bound derived in [46]. However, the capacity can not grow to infinite since $(N_u + 1) \leq \tau_r$ with τ_r is the number of UL pilots [46]. Moreover, when the antenna number M is fixed, the capacity of each user decrease with the augmentation of $(N_u + 1)$ as shown in Fig. 2.24. Hence, once a minimum capacity bound is fixed for each user, our model helps to determinate the maximum $(N_u + 1)$ can be served. Moreover, our model can be easily adapted to the other circumstances by adding other interference components such as channel estimation error [96], inter-cellular interference [97] and pilot contamination [54].

2.4 Conclusion

In this chapter, we analyzed the system capacity of the PFBO scheme. It is shown that the PFBO scheme can improve the system capacity in a range of SNR depending on the transmit signal waveforms and the multi-antenna focusing gains. Both single carrier and multicarrier wave-

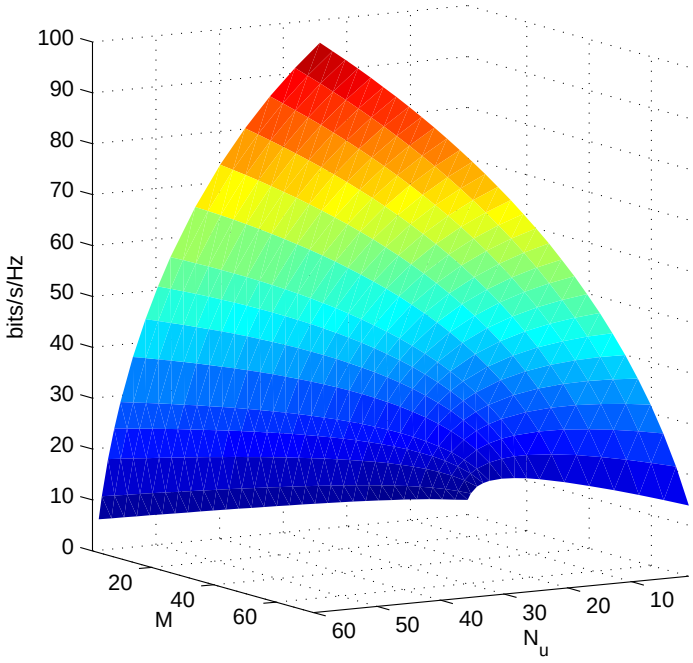

Figure 2.23: Achievable sum rate of a MU-MIMO system with $N_u + 1$ users

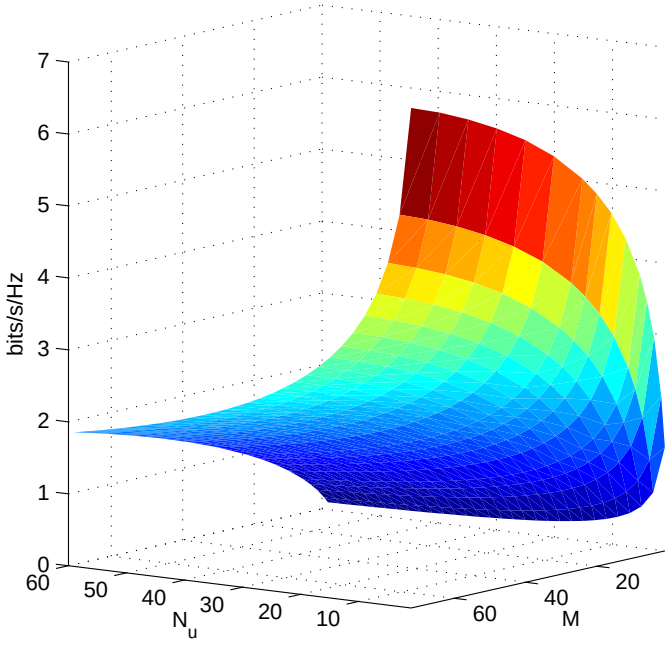

Figure 2.24: Average achievable rate per user in a MU-MIMO system with $N_u + 1$ users

forms are studied through simulations. The optimal overlap ratios, which provide the maximal achievable sum rate of the two-user PFBO systems have be originally identified as a function of the SNR level and the number of transmit antennas.

Particularly, based on OFDM systems, we proposed new closed-form capacity lower bounds for general MU-MIMO systems using EGT, TR and MRT precoding techniques. These capacity bounds were derived based on a statistical analysis of the channel behavior. Thus they turn out to be more accurate than the capacity lower bounds proposed in the literature for general massive MIMO systems.

The results of sections 2.1 and 2.2 for optimal overlap ratio identification with single carrier and multicarrier waveforms have been published in:

H. Fu, M. Crussière and M. Hélard, "Spectral Efficiency Optimization in Overlapping Channels using TR-MISO Systems", in *Proc. IEEE Wireless Communications and Networking Conference (WCNC 2013)*, pp. 3770-3775, Shanghai, China, Apr. 2013.

CHAPTER 3

BER ANALYSIS FOR BANDWIDTH OVERLAY OFDM SYSTEMS

As we saw in the previous chapter, the spectral efficiency of a multi-user system can be improved by overlapping a part of frequency bandwidth among the users. The inter-channel is overcome thanks to the spatial division multiplexing gain of precoded MIMO systems. In chapters 3 and 4, we investigate the BER performance, which measures the quality of transmission, for PFBO systems. We study in chapter 3, the impact of MAI for OFDM systems, then the performance of SS-OFDM is derived in chapter 4.

In this chapter, we begin the BER analysis using AWGN channels, then extend the study to precoded MU-MIMO systems using Rayleigh channels. Closed-form BER expressions are obtained for non-overlapped and overlapped cases, respectively. The multiuser case is also discussed. The analytical BER equations are confirmed through Monte-Carlo simulations.

3.1 BER analysis for AWGN channel

We begin the BER analysis using AWGN channels, which helps to clarify the impact of channel overlay to the system performance.

3.1.1 Signals equations

Taking the OFDM channel overlay system model introduced in 2.1.2, where, two users, namely u_1 and u_2, are allocated to a common subset of subcarriers as remained in Fig. 3.1. u_1 is assumed to be the user of interest while u_2 is the interfering one. The channel overlapping is proceeded progressively subcarrier by subcarrier, such that the bandwidth overlap can be expressed as:

$$\Delta_f = N_R \times \delta_f \tag{3.1}$$

where N_R is the number of overlapped subcarriers, δ_f is the intercarrier spacing of the OFDM signals, assumed to be identical for u_1 and u_2. Due to the orthogonality among the subcarriers,

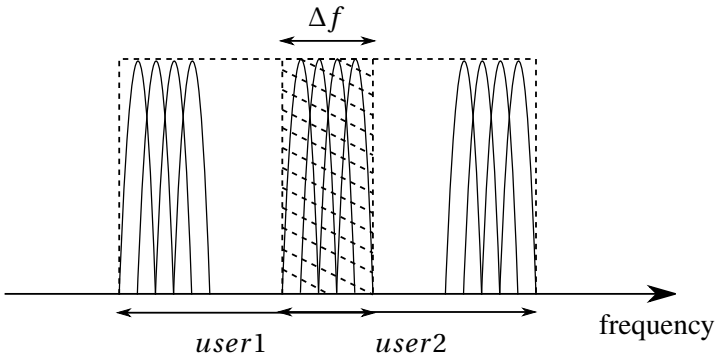

Figure 3.1: OFDM overlapped system

the impact of the overlap process can be studied independently at each subcarrier. Hence, it is straightforward to state that the receive symbol on subcarrier p writes:

$$\begin{cases} Y_p^{(1)} = H_p^{(1)} a_p^{(1)} + N_p, & \forall p \in \{1, \cdots, N_f - N_R\} \\ Y_p^{(1)} = H_p^{(1)} a_p^{(1)} + H_{p'}^{(2)} a_{p'}^{(2)} + N_p, & \text{otherwise} \end{cases} \tag{3.2}$$

where $H_p^{(1)}$ and N_p are CFR coefficients and noise term samples affecting subcarrier p respectively, and where p' defines the subcarrier index for the interfering user such that $p' = p - N_f + N_R$, N_f is the total number of OFDM subcarriers. As usual in OFDM, equalization factors are applied subcarrier by subcarrier before demapping.

3.1.2 BER analysis

In this section, we propose to derive the theoretical BER equation for the proposed PFBO-OFDM system, which will give some insight into the system performance and help us to analyze the simulation results. For simplicity, we consider that both $user1$ and $user2$ adopt the binary phase-shift keying (BPSK) modulation and that the channel is AWGN. Hence $H_p^{(1)} = 1$ and $H_{p'}^{(2)} = 1$.

With BPSK modulation, the symbols transmitted to $user1$ $a_p^{(1)} = \pm 1$, the received symbols on the subcarriers experiencing adjacent channel overlay take three possible values depending on the symbols transmitted to the interfering user. More precisely, we have $y_p^{(1)} \in \{-2, 0, 2\}$ with probability $\{0.25, 0.5, 0.25\}$ respectively as illustrated in Fig. 3.2.

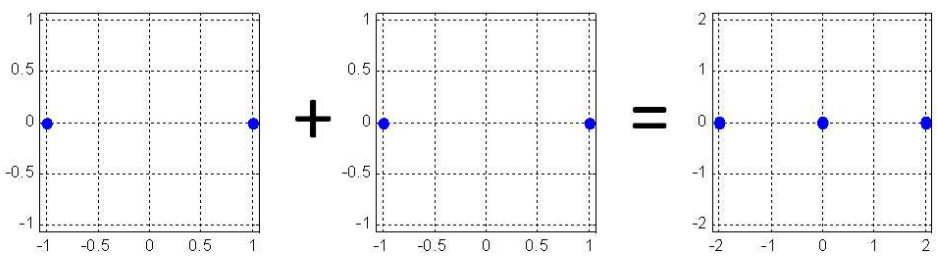

Figure 3.2: Resulting signal constellation pattern with BPSK signal overlap.

As evident from these considerations, the inter-channel interference resulting from the channel overlapping can not be reduced to a Gaussian stochastic process, which would otherwise have led to a straightforward BER computation using Gaussian error functions evaluated at adequate SINR values (Signal to Interference and Noise Ratio). In contrast to that, we need here to make an exhaustive summation of the Gaussian error functions associated to each possible receive symbol. The probability density function (PDF) of the received overlapped BPSK symbols is depicted in Fig. 3.3. Accordingly, the BER for any interfered subcarriers can easily be calculated as:

$$\begin{aligned} \mathrm{BER}_{OFDM,\Delta f} &= P_{(\hat{a}_p^{(1)}=0|a_p^{(1)}=1)}\frac{1}{2}erfc(0) + P_{(\hat{a}_p^{(1)}=2|a_p^{(1)}=1)}\frac{1}{2}erfc(\frac{2\sqrt{E_b}}{N_0}) \\ &= \frac{1}{4}(1+erfc(\frac{2\sqrt{E_b}}{N_0})) \end{aligned} \tag{3.3}$$

where E_b is the energy per bit in the transmission signal, N_0 is the noise power spectral density of the AWGN channel and $erfc(\cdot)$ is the complementary error function.

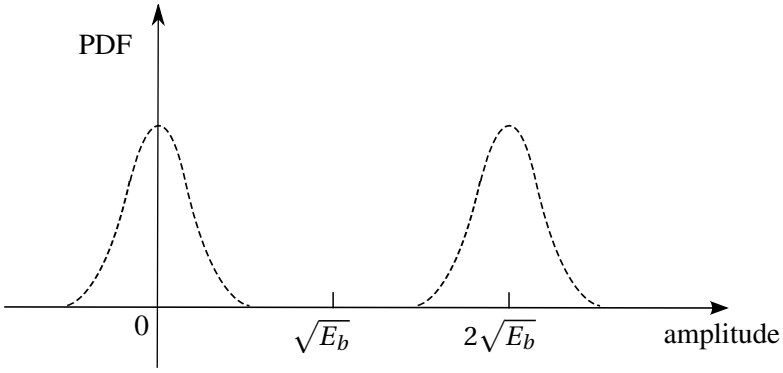

Figure 3.3: PDF of overlapped BPSK symbol of two users, where the symbol transmitted to the first user is $a_k^{(1)} = 1$.

The BER over the entire signal band can be computed as the average BER across all the subcarriers, such as:

$$\mathrm{BER}_{\mathrm{OFDM}} = \frac{N_R}{4N_f}\Big(1+erfc\big(2\sqrt{\frac{E_b}{N_0}}\big)\Big) + \big(1-\frac{N_R}{N_f}\big)\frac{1}{2}erfc\Big(\sqrt{\frac{E_b}{N_0}}\Big) \tag{3.4}$$

As depicted in Fig. 3.4, (3.4) is verified through simulations with $N_f = 64$ and $N_R \in \{1, 7\}$.

At this stage, it can be already concluded that the BER dramatically degrades when the number N_R of interfering subcarriers increases. In fact, the first term in the equation (3.4), namely $\frac{N_R}{4N}$, is dominant at high SNR regime and creates an error floor.

We note that this BER derivation can be extended to higher order modulations by exhaustively analyzing the possible receive symbols.

3.2 When the MISO channels can be considered as flat fading?

As shown in [18, 32], with a large scale transmit antenna arrays, the equivalent channel response can be considered as flat fading. So we ask the question: how many antennas are needed to consider the channel as flat fading? To answer this question, we study in this part the coherence bandwidth of the equivalent precoded MISO channel.

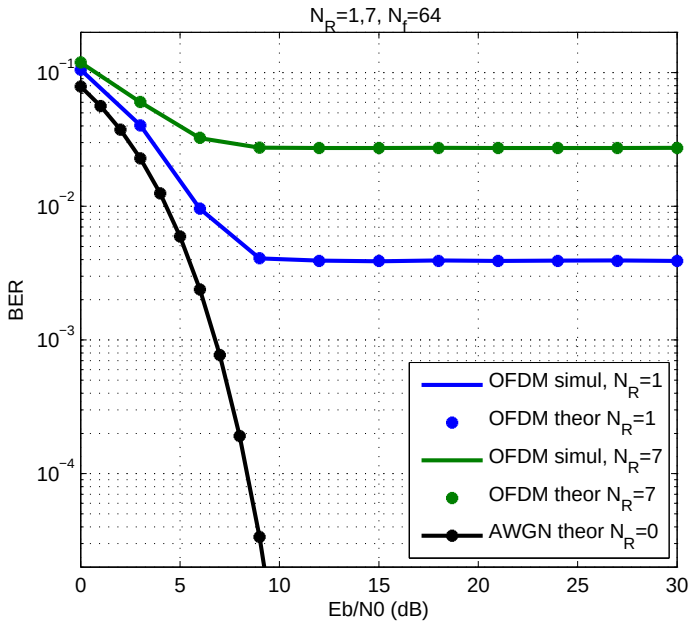

Figure 3.4: Performance of PFBO OFDM systems with $N_R \in \{1, 7\}$ in AWGN channels

3.2.1 For Rayleigh channel model

Recall the Rayleigh channel model presented in 1.4.3.2 with the number of coherence bandwidths $N_{coh} = N_f = 64$, which means that all the OFDM subcarriers fade independently with each others. The equivalent CFR of EGT precoded MISO channel is:

$$H_{p,EGT} = \frac{1}{\sqrt{M}} \sum_{m=1}^{M} \left| H_{p,m} \right| \tag{3.5}$$

With TR precoding technique, the equivalent channel response is:

$$H_{p,TR} = \frac{1}{\sqrt{M}} \sum_{m=1}^{M} \left| H_{p,m} \right|^2 \tag{3.6}$$

With MRT precoding technique, the equivalent channel response is:

$$H_{p,MRT}(f) = \sqrt{\sum_{m=1}^{M} \left| H_{p,m} \right|^2} \tag{3.7}$$

Let us focus on the example of EGT-MISO system. We present in Fig. 3.5 the normalized CFR $\bar{H}_{p,EGT}$ for 1×1, 4×1, 16×1 EGT-MISO channel. The power normalization, denoted by $\bar{(\cdot)}$, is for the purpose of better illustrating the difference on fluctuations.

We observe that when the antenna number M increases, the equivalent CFR becomes more and more flat, due to the superposition of the CFR of different antenna pairs. It has been mentioned in [32], as M increases, the equivalent MISO channel tends to an almost Gaussian channel.

The coherence bandwidth B_C refers to a statistical range of frequencies over which the channel frequency response is considered to hold the same gain and linear phase. Hence a signal transmitted within the coherence bandwidth can be viewed as experiencing flat fading. In this thesis,

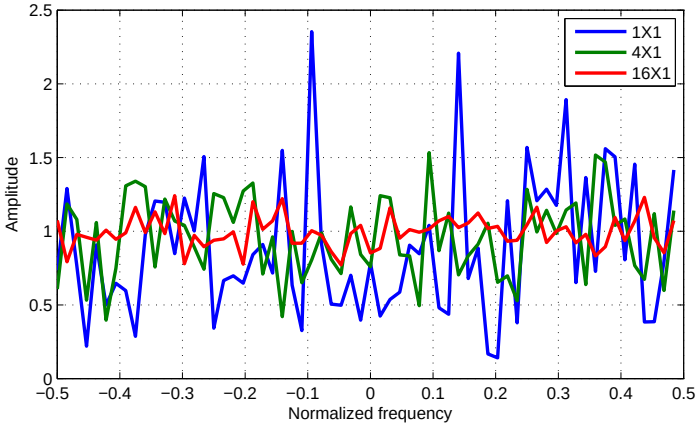

Figure 3.5: Normalized equivalent CFR for 1×1, 4×1, 16×1 EGT-MISO systems

the coherence bandwidth is defined as the frequency range over which the CFR has a correlation function of at least 0.9 [85]. The correlation function of the CFR of EGT-MISO and AWGN channels are displayed in Fig. 3.6.

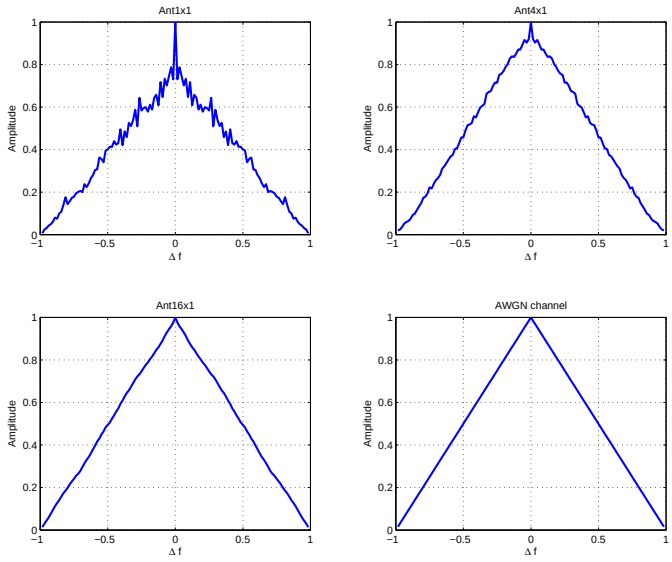

Figure 3.6: Correlation function of CFR of Rayleigh channel response for 1×1, 4×1, 16×1 EGT-MISO channel and AWGN channel

As the AWGN channel is perfectly flat fading, we take its coherence bandwidth $B_{c,AWGN}$ as a reference, for which the correlation function of CFR of AWGN channel on $\left[-\frac{B_{c,AWGN}}{2}, \frac{B_{c,AWGN}}{2}\right]$ is ≥ 0.9. Hence, we can evaluate the ratio of the coherence bandwidth of EGT, TR and MRT MISO channel to $B_{c,AWGN}$ to reflect the flatness of these channels, as shown in Fig. 3.7. When the ratio is close to 0, it means that the coherence bandwidth of the channel is narrow and the channel is very frequency selective. When the ratio is close to 1, it means that the channel is almost flat

fading. We note that the all three precoded channels approach AWGN channel when the number of antennas increases. More precisely, the curve of MRT rises with the fastest rate. The curve of EGT is very close to that of MRT. The curve of TR rises slower because that its CFR is of order 2, which makes the channel more fluctuate. However, as shown in the figure, around 30 antennas are needed to make the ratio exceeds 0.9, i.e. the coherence bandwidth of the MISO channel attains $0.9 \times B_{c,AWGN}$. These results show that for the range of $4 \sim 30$ antennas, the effect of channel frequency selectivity can not be neglected. This character of channel encourages us to study the system performance in this antenna range.

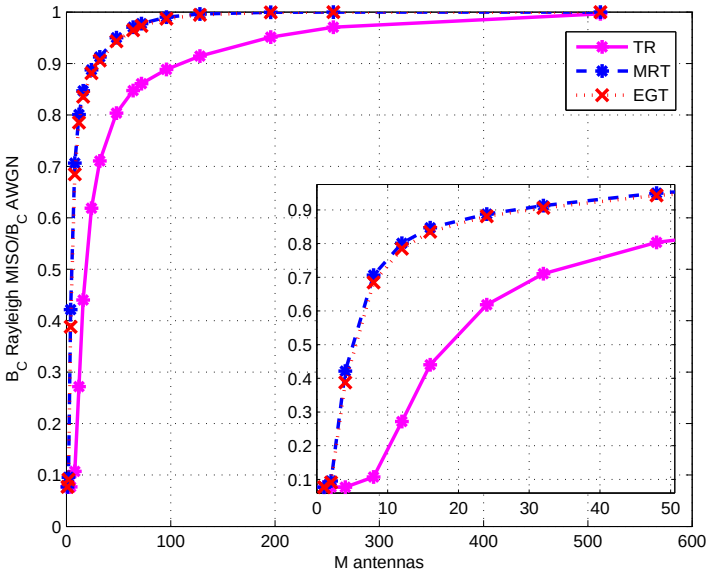

Figure 3.7: The ratio of the coherence bandwidth of EGT, TR, MRT MISO channel to the coherence bandwidth of AWGN channel

3.2.2 For BRAN-A channel model

In order to study a practical channel case, we use the Broadband Radio Access Network (BRAN) channel models 1.4.3.3. BRAN-A model represents a typical office environment.

An example of normalized CFR of BRAN-A channel in 1×1, 4×1, 16×1 EGT-MISO system is presented in Fig. 3.8.

In SISO case, we observe the correlation between the subbands adjacent (the CFR is less fluctuate than Rayleigh model). The BRAN-A channel model is closer to the real propagation environment than the theoretical Rayleigh model. However, similar to the Rayleigh model, with the increase of the antenna number M, the equivalent CFR tends to be flat. We then display the correlation function of the CFR in Fig. 3.9.

The ratios of the coherence bandwidth between the precoded MISO BRAN-A channels and $B_{c,AWGN}$ are also presented in Fig. 3.10. We note that the coherence bandwidth of BRAN-A channel is larger than that of the Rayleigh channel when the antenna number is small ($M \leq 12$ for MRT and EGT system, $M \leq 4$ for TR system) because of the correlation within the subbands.

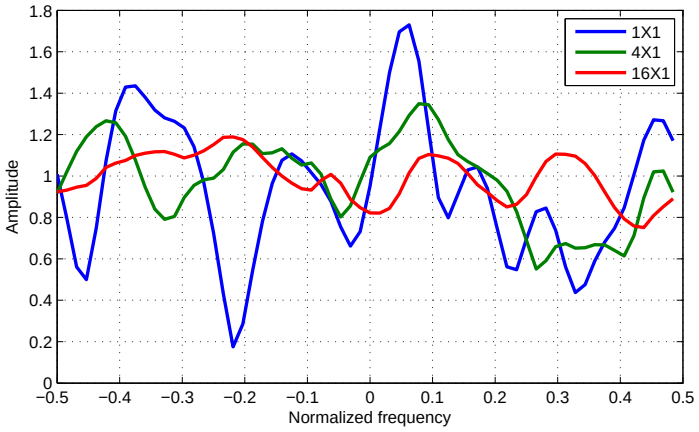

Figure 3.8: Normalized equivalent CFR for 1×1, 4×1, 16×1 EGT-MISO systems

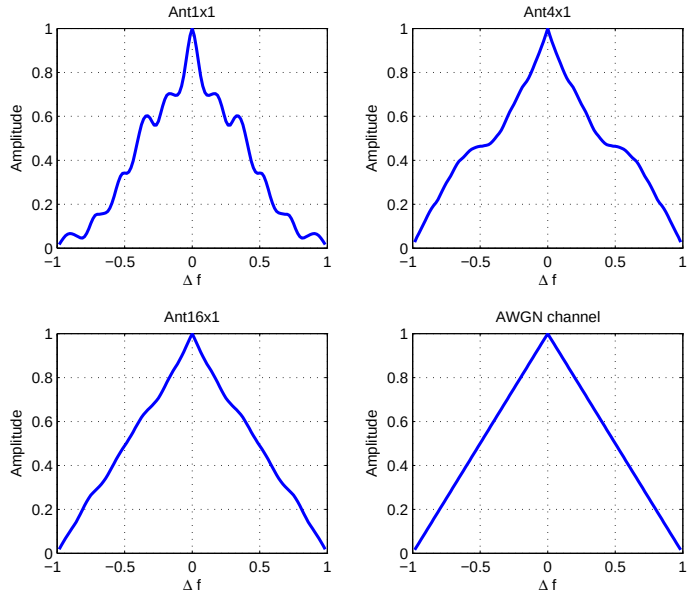

Figure 3.9: Correlation function of BRAN-A frequency channel response for 1×1, 4×1, 16×1 EGT-MISO channel and AWGN channel

However, as the BRAN-A channel exhibits the similar fading effect, its coherence bandwidth does not tend to that of AWGN channel even with very large number of transmit antennas.

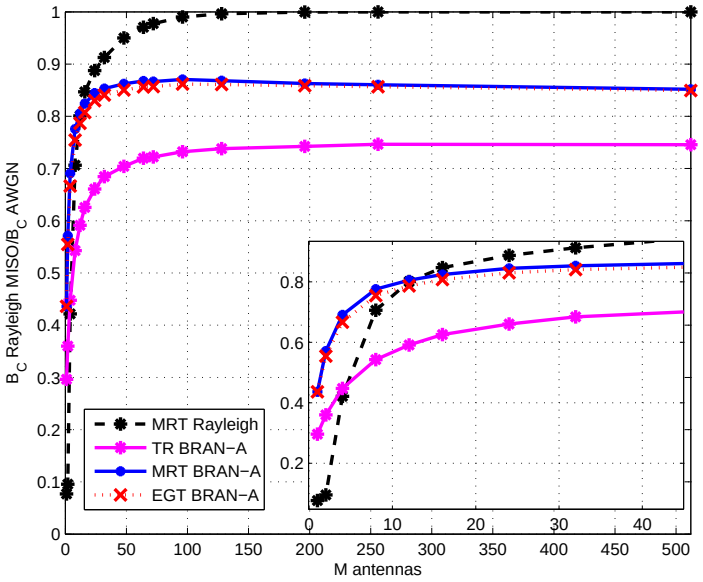

Figure 3.10: The ratio of the coherence bandwidth of EGT, TR, MRT MISO channel to the coherence bandwidth of AWGN channel, BRAN-A channel

In the simulations, both the Rayleigh and the BRAN-A channel models are used to analyze the performance of bandwidth overlay systems.

3.3 BER analysis for Rayleigh channel

As the propagation channels are not always flat fading, we study in this section the BER performance using theoretical Rayleigh channel model to clarify the impact of the frequency selectivity of the channel to the BER performance of the bandwidth overlay systems.

3.3.1 Signal equations

Taking the signal equations of 3.1, for precoded MU-MIMO systems, the equivalent CFR at the receiver is $H_p^{(1)} = \sum_{m=1}^{M} H_{p,m}^{(1)} V_{p,m}^{(1)}$ and $H_{p'}^{(2)} = \sum_{m=1}^{M} H_{p,m}^{(1)} V_{p',m}^{(2)}$. Recalling that $H_{p,m}$ is the CFR of the p^{th} subcarrier on the m^{th} antenna, $V_{p,m}$ is the corresponding precoding factor. p' defines the subcarrier index for the interfering user such that $p' = p - N_f + N_R$, N_f is the total number of OFDM subcarriers while N_R is the number of reused subcarriers. Hence the received signal on subcarrier p writes:

$$\begin{cases} Y_p^{(1)} = \sum_{m=1}^{M} H_{p,m}^{(1)} V_{p,m}^{(1)} a_p^{(1)} + N_p, & \forall p \in \{1, \cdots, N_f - N_R\} \\ Y_p^{(1)} = \sum_{m=1}^{M} H_{p,m}^{(1)} V_{p,m}^{(1)} a_p^{(1)} + \sum_{m=1}^{M} H_{p,m}^{(1)} V_{p',m}^{(2)} a_{p'}^{(2)} + N_p, & \text{otherwise.} \end{cases} \tag{3.8}$$

Using EGT precoding technique, the received symbol writes:

$$\begin{cases} Y^{(1)}_{p,EGT,nr} = \frac{1}{\sqrt{M}} \sum_{m=1}^{M} \left| H^{(1)}_{p,m} \right| a^{(1)}_{p} + N_p, \quad \forall p \in \{1, \cdots, N_f - N_R\} \\ Y^{(1)}_{p,EGT,r} = \frac{1}{\sqrt{M}} \sum_{m=1}^{M} \left| H^{(1)}_{p,m} \right| a^{(1)}_{p} + \frac{1}{\sqrt{M}} \sum_{m=1}^{M} H^{(1)}_{p,m} e^{-j\Phi^{(2)}_{p',m}} a^{(2)}_{p'} + N_p, \quad \text{otherwise.} \end{cases} \tag{3.9}$$

Using TR precoding technique, the received symbol writes:

$$\begin{cases} Y^{(1)}_{p,TR,nr} = \frac{1}{\sqrt{M}} \sum_{m=1}^{M} \left| H^{(1)}_{p,m} \right|^2 a^{(1)}_{p} + N_p, \quad \forall p \in \{1, \cdots, N_f - N_R\} \\ Y^{(1)}_{p,TR,r} = \frac{1}{\sqrt{M}} \sum_{m=1}^{M} \left| H^{(1)}_{p,m} \right|^2 a^{(1)}_{p} + \frac{1}{\sqrt{M}} \sum_{m=1}^{M} H^{(1)}_{p,m} H^{(2)*}_{p',m} a^{(2)}_{p'} + N_p, \quad \text{otherwise.} \end{cases} \tag{3.10}$$

Using MRT precoding technique, the received symbol writes:

$$\begin{cases} Y^{(1)}_{p,MRT,nr} = \sqrt{\sum_{m=1}^{M} \left| H^{(1)}_{p,m} \right|^2} a^{(1)}_{p} + N_p, \quad \forall p \in \{1, \cdots, N_f - N_R\} \\ Y^{(1)}_{p,MRT,r} = \sqrt{\sum_{m=1}^{M} \left| H^{(1)}_{p,m} \right|^2} a^{(1)}_{p} + \frac{\sum_{m=1}^{M} H^{(1)}_{p,m} H^{(2)*}_{p',m}}{\sqrt{\sum_{m=1}^{M} \left| H^{(1)}_{p,m} \right|^2}} a^{(2)}_{p'} + N_p, \quad \text{otherwise.} \end{cases} \tag{3.11}$$

3.3.2 Single user BER derivation

We begin by analyzing the BER performance of the subchannels without overlapping. A closed-form BER approximation is proposed for EGT method. Then the exact closed-form BER expressions are derived for TR and MRT methods.

3.3.2.1 Single user BER derivation using EGT

In the case of EGT, the PDF of equivalent CFR is a sum of M i.i.d. random variables following a Rayleigh distribution with $\sigma = \sqrt{\frac{1}{2}}$. We use the Nakagami approximation presented in 2.2.3. For the purpose of highlighting the diversity evolution while increasing the number of transmit antennas M, without loss of generality, the average channel power gain is normalized as $E\left[\left(\frac{1}{\sqrt{M}} \sum_{m=1}^{M} \left| H^{(1)}_{k,m} \right|\right)^2\right] = 1$. The normalization factor is $\frac{1}{\Phi_{Use,EGT}} = \frac{1}{\frac{\pi}{4} M + 1 - \frac{\pi}{4}}$. In this way, the SNR at the receiver side is always the same for arbitrary M value. The channel coefficient of EGT $r_{EGT} = \frac{1}{\sqrt{M}} \sum_{m=1}^{M} \left| H^{(1)}_{k,m} \right|$ can be approximated by a Nakagami$(M, 1)$ process which PDF function is:

$$f(r|M) = \frac{2M^M}{(M-1)!} r^{2M-1} e^{-Mr^2}, r > 0 \tag{3.12}$$

Therefore, the average BER is [98, p118 - Eq (B.6)]:

$$\begin{aligned} P_{eEGT,nr}\left(\frac{Eb}{N0}, M\right) &= \int_0^{\infty} f(r|M) Q(r\sqrt{\frac{2Eb}{N0}}) dr \\ &= \frac{\Gamma\left(M + \frac{1}{2}\right)}{2\sqrt{\pi}\Gamma(M+1)} \cdot \frac{\left[M \frac{N_0}{E_b}\right]^M}{\left[1 + M \frac{N_0}{E_b}\right]^{M+\frac{1}{2}}} \times {}_2F_1\left(1, M + \frac{1}{2}, M+1, \frac{M}{M + \frac{Eb}{N0}}\right) \end{aligned} \tag{3.13}$$

This formula is available for arbitrary $M > 0.5$ and $\frac{Eb}{N0} > 0$.

3.3.2.2 Single user BER derivation using TR

In the case of TR, the equivalent channel coefficient is a sum of M i.i.d. random variables following a gamma distribution which is also a gamma distribution as presented in 2.2.3. The average channel power gain is normalized as $\Phi_{Use,TR} = E\left[\left(\frac{1}{\sqrt{M}}\sum_{m=1}^{M}\left|H_{k,m}^{(1)}\right|^2\right)^2\right] = 1$ with the power normalization factor $\frac{1}{\Phi_{Use,TR}} = \frac{1}{M+1}$. Therefore, the channel coefficient $r_{TR} \sim \Gamma(M, \frac{1}{\sqrt{M^2+M}})$. The PDF function of r_{TR} is:

$$f(r|M) = \frac{\left(M^2+M\right)^{M/2}}{\Gamma(M)} r^{M-1} e^{-\sqrt{M^2+M}r},\ r > 0,\ M > 0 \tag{3.14}$$

Therefore, the average BER is [99, p7 - Eq (4.3.14)]:

$$\begin{aligned} P_{eTR,nr}\left(\frac{Eb}{N0}, M\right) &= \int_0^\infty f(r|M) Q(r\sqrt{\frac{2Eb}{N0}}) dr \\ &= \frac{1}{2} - \sqrt{\frac{1}{2\pi}} \sum_{k=0}^{M-1} \left(\frac{\left(M^2+M\right)N_0}{2Eb}\right)^{M/2-(k+1)/2} e^{\frac{\left(M^2+M\right)N_0}{8Eb}} D_{k-M}\left(\sqrt{\frac{\left(M^2+M\right)N_0}{2Eb}}\right). \end{aligned} \tag{3.15}$$

With $D_v(\cdot)$ is the parabolic cylinder function. This formula is available for arbitrary $M > 0$ and $\frac{Eb}{N0} > 0$.

3.3.2.3 Single user BER derivation using MRT

In the case of MRT, the equivalent channel coefficient is the root of a sum of M i.i.d. random variables following a gamma distribution which follows a Nakagami distribution. The average channel power gain is normalized as $\Phi_{Use,MRT} = E\left[\left(\sum_{m=1}^{M}\left|H_{k,m}^{(1)}\right|^2\right)^2\right] = 1$ with the power normalization factor $\frac{1}{\Phi_{Use,MRT}} = \frac{1}{M}$. Therefore, the channel coefficient $r_{MRT} \sim \text{Nakagami}(M, 1)$. The PDF function of r_{MRT} is the same as that of r_{EGT} approximation Eq. (3.12). It is reasonable because that the channels with EGT and MRT have the same diversity but not the same power gain [59]. Therefore, the exact average BER of MRT equals to the EGT BER approximation Eq. (3.13) when the channel power gains are for both cases normalized to 1.

3.3.3 Two-user MIMO BER derivation

In this part, the BER performance of the overlapped bandwidth, which is equivalent to a two-user MIMO system, is analyzed. We studied in detail the BER using EGT precoding technique, which is more complex than the MRT and TR cases because the correlation between the useful signal and the inter-channel interference is the highest (c.f. Fig. 2.16). To model the effect of correlation, the inter-channel interference is considered as a distortion factor of the useful signal. The Nakagami distribution is used to model both the channel fading and the impact of interference. At the end, we show that the Nakagami approximation provides a satisfactory accuracy for BER estimation with the Nakagami parameters linearly depend on the antenna number M.

3.3.3.1 Interference term for EGT technique

Defining $\theta_{p,m} = \Phi^{(1)}_{p,m} - \Phi^{(2)}_{p,m}$ as the phase difference between $H^{(1)}_{p,m}$ and $H^{(2)}_{p,m}$, the inter-channel interference term identified in Eq. (3.9) can be re-expressed as:

$$I = \frac{1}{\sqrt{M}} \sum_{m=1}^{M} \left| H^{(1)}_{p,m} \right| e^{j\theta_{p,m}} a^{(2)}_p. \tag{3.16}$$

As such, the equivalent channel seen by the interfering symbols is a random variable (RV) defined as $\nu = \frac{1}{\sqrt{M}} \sum_{m=1}^{M} \left| H^{(1)}_{p,m} \right| e^{j\theta_{p,m}}$. According to the property of normal distribution, $\nu \sim \mathscr{CN}(0, 2\sigma^2)$ with $\sigma^2 = \frac{1}{\frac{\pi}{2}M + 2 - \frac{\pi}{2}}$. However, ν is correlated with the channel equivalent coefficient r_{EGT}. In this case, the common interference models based on the classical Gaussian approximation or on other RV assumed independent from the useful term are likely to yield poor BER estimates [54], which is further verified through our simulation results. At this stage then, a joint p.d.f. for RVs r_{EGT} and ν is needed to pursue the investigations. To circumvent such a hard task, we rather propose in the sequel to treat the inter-channel interference term as an additional distortion factor applied to the useful term.

3.3.3.2 Interference as a distortion factor of the useful term

Without loss of generality, we omit the OFDM subcarrier index p, the following analysis is available for all the overlapped subcarriers. we note $a^{(2)} = \rho \cdot e^{J\phi \cdot a^{(1)}}$, with ρ and ϕ being some amplitude and phase terms depending on the constellation point coordinates. Then, ignoring noise, we may write the received useful symbols as,

$$Y^{(1)} = \frac{1}{\sqrt{M}} \sum_{m=1}^{M} \left| H^{(1)}_{m} \right| (1 + \rho e^{J\psi_m}) a^{(1)} \tag{3.17}$$

where $\psi_m = \theta + \phi$ such that $\psi_m \sim \text{Unif}(0, 2\pi)$. We treat at first the BER performance using the BPSK modulation for its simplicity and robustness in low SNR regime. With the BPSK modulation, we have $\rho = 1$. The behavior of the resulting EGT-MIMO equivalent channel can thus be described through the following complex RV $z = \frac{1}{\sqrt{M}} \sum_{m=1}^{M} \left| H^{(1)}_{m} \right| (1 + e^{J\psi_m})$. Supposing the user of interest transmits a symbols $a^{(1)} = 1$, the point cloud without noise term is displayed in Fig. 3.11, where we observe the impact of the inter-channel interference with different M values.

The next step in our study is then to determine the p.d.f. of z. To that perspective, Proposition 1 hereafter gives a useful intermediate result for $M = 1$.

Proposition 1: For Rayleigh fading with parameter σ, the equivalent fading model of a two-user BPSK EGT-SISO transmission is such that,

$$y = \underbrace{\xi\, e^{J\varphi}}_{z} \cdot x \quad \text{where} \quad \begin{cases} \xi \sim \text{Nakagami}(1/2, 4\sigma^2) \\ \varphi \sim \text{Unif}(-\pi/2, \pi/2) \end{cases} \tag{3.18}$$

with x, y the transmitted and received symbols respectively.

Proof: In the single antenna case, i.e. $M = 1$, from the definition of z, we have $\xi = |z| = |H|\sqrt{(1+\cos\psi)^2 + \sin^2\psi} = 2|H||\cos(\psi/2)|$ and $\varphi = \arctan[(\sin\psi)/(1+\cos\psi)] = \psi/2$. First, as $\psi \sim \text{Unif}(0, 2\pi)$, therefore $\varphi \sim \text{Unif}(-\pi/2, \pi/2)$. Then, as far as ξ is concerned, one may notice that its p.d.f. $p(\xi)$ is such that $p(\xi) = 2p(\underline{\xi})$, where $\underline{\xi} = 2|H|\cos\psi/2$ is a even function, $\underline{\xi} \in]-\infty, +\infty[$.

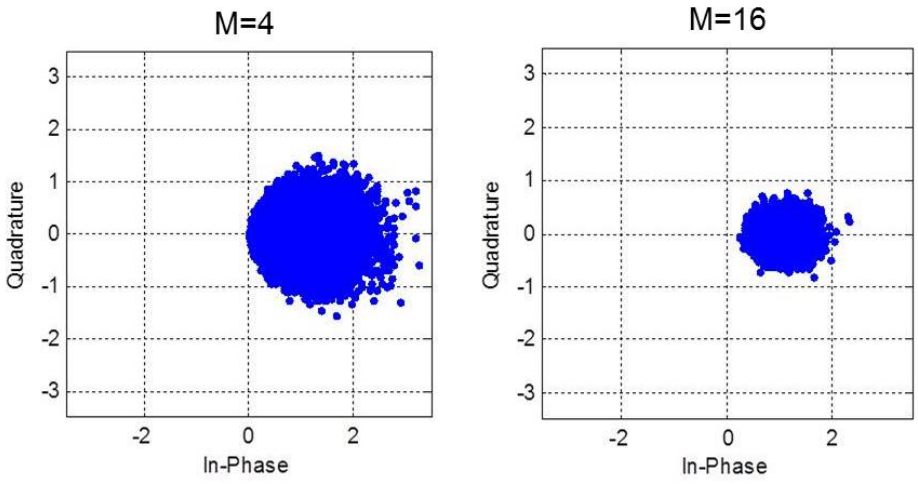

Figure 3.11: BPSK point cloud without noise for $4X1$ and $16X1$

The proof goes thus on with the computation of the characteristic function of $\underline{\xi}$. Using similar manipulations as in [80, Appendix A], we obtain:

$$\Phi_{\underline{\xi}}(t) = \mathbb{E}\left[e^{it\underline{\xi}}\right] = \int_0^{+\infty} \frac{r}{\sigma^2} e^{-\frac{r^2}{2\sigma^2}} J_0(2tr)\, dr = e^{-2\sigma^2 t^2}$$

where $J_0(x)$ is the zeroth-order Bessel function of the first kind, and in which the involved integral is evaluated with the help of [100, p706, Eq. (6.631.4)]. Then the p.d.f. of ξ is computed as,

$$p(\xi) = 2 \cdot \frac{1}{2\pi} \int_{-\infty}^{+\infty} e^{-2\sigma^2 t^2 - \jmath t\underline{\xi}} dt = \frac{1}{\sigma\sqrt{2\pi}} e^{-\frac{\xi^2}{8\sigma^2}}$$

solving the integral using [100, p337, Eq. (3.323.2)]. One may finally recognize a particular form of the Nakagami-m p.d.f.. The proof concludes by identifying parameters m and w in $p(\xi)$. ■

From the above result then, z can be expressed in the MIMO case as a combination of M independent Nakagami-m RVs ξ_m affected by M independent random phases φ_m, i.e. $z = \frac{1}{\sqrt{M}} \sum_{m=1}^{M} \xi_m \cdot e^{\jmath\varphi_m}$. As we are interested in BPSK symbols, we have only to study the real part of z, $z_R = \frac{1}{\sqrt{M}} \sum_{m=1}^{M} \xi_m \cdot \cos(\varphi_m)$. It follows that z_R can be viewed as an equivalent RV consisting of M weighted Nakagami-m RVs, with random weighting factors $0 \leq \cos(\varphi_m) \leq 1$. Exploiting the conclusions of [92], z_R is thus likely to be adequately approximated by a single Nakagami-m RV whose parameters can be set using the following Proposition 2.

Proposition 2: For Rayleigh fading, the power normalized fading model of a two-user BPSK EGT-MIMO transmission ($M \geq 2$) can be approximated by:

$$y_R = \Xi \cdot x_R \quad \text{where} \quad \Xi \sim \text{Nakagami}(\tilde{m}, \tilde{w}) \tag{3.19}$$

with x_R, y_R the real part of the symbols, and with:

$$\begin{cases} \tilde{m} \cdot \left[\frac{\Gamma(\tilde{m})}{\Gamma(\tilde{m}+\frac{1}{2})}\right]^2 = 1 + \frac{\frac{6}{\pi}-1}{M} \\ \tilde{w} = \frac{\pi M + 6 - \pi}{\pi M + 4 - \pi} \end{cases} \tag{3.20}$$

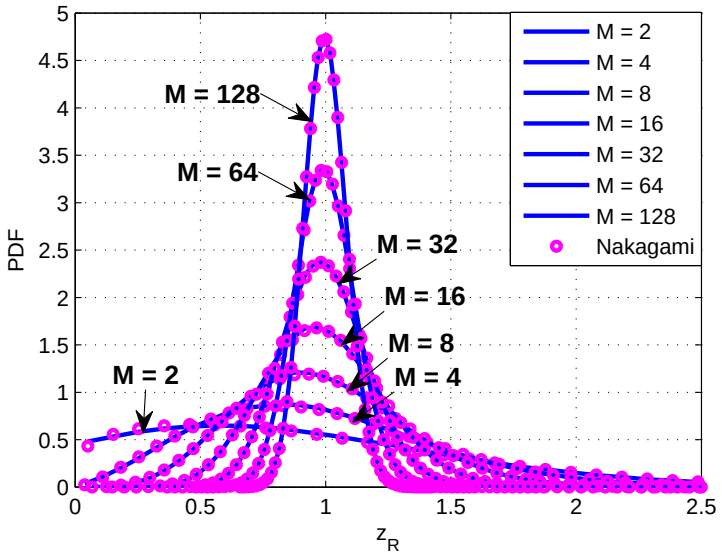

Figure 3.12: PDF of the In-phase component z_R for different number M of transmit antennas. Comparison with the Nakagami-m approximation.

Proof: The proof simply relies on the estimation of the parameters of the Nakagami-m law using moment based method. From the considerations in [101], accurate fitting is obtained by estimating the first and second order moments of the RV. Since z_R can be written as $z_R = \frac{1}{\sqrt{M}} \sum_{m=1}^{M} |h_{1,m}| (1 + \cos(\psi_m))$, we have,

$$\mathbb{E}[z_R] = \sqrt{\frac{\pi}{2} M\sigma^2}, \qquad \mathbb{E}[z_R^2] = \frac{\pi}{2}\sigma^2 M + (3 - \frac{\pi}{2})\sigma^2. \tag{3.21}$$

with $\sigma^2 = \frac{1}{\frac{\pi}{2}M + 2 - \frac{\pi}{2}}$ after the power normalization.

On the other hand we have from [92]:

$$\mathbb{E}[\Xi] = \frac{\Gamma(\tilde{m} + \frac{1}{2})}{\Gamma(\tilde{m})} \sqrt{\frac{\tilde{\omega}}{\tilde{m}}}, \qquad \mathbb{E}[\Xi^2] = \tilde{\omega}. \tag{3.22}$$

The proof then concludes by combining Eq. (3.22) and Eq. (3.21). Since $m \geq 0.5$ in the Nakagami-m p.d.f., it can be verified that $\tilde{m}$ is defined for $M \geq 2$ only. ■

Note that the proposition is not available for $M = 1$ because $\tilde{m}_{M=1} < 0.5$ which exceeds the limit of the shape parameter as defined in the Nakagami model (c.f. Eq. (2.29)).

The proposed model in Proposition 2 can be viewed as an extension of that of single user case 3.3.2.1. When an interfering user is considered, the impact of the interference term being reflected by the new definition of the shape and scale parameters $\tilde{m}$ and $\tilde{w}$. In Fig. 3.12, we show a good match between the approximated (circle) and exact (solid line) p.d.f. of z_R, even if slight differences occur for small M and small x. This lack of accuracy is due to the Nakagami p.d.f. which strictly zeroed at $r = 0$ (c.f. Eq. (2.29)). Then its tail in that region remains thinner than that of the true channel distribution. This defect is no longer visible when M increases. The variations of $\tilde{m}$ and $\tilde{w}$ against M are plotted in Fig. 3.13. Clearly, the larger M, the lower $\tilde{w}$ and larger $\tilde{m}$. More precisely, from Eq. (3.37) and Fig. 3.13, we have that $\tilde{w} \to 1$ for $M \to \infty$.

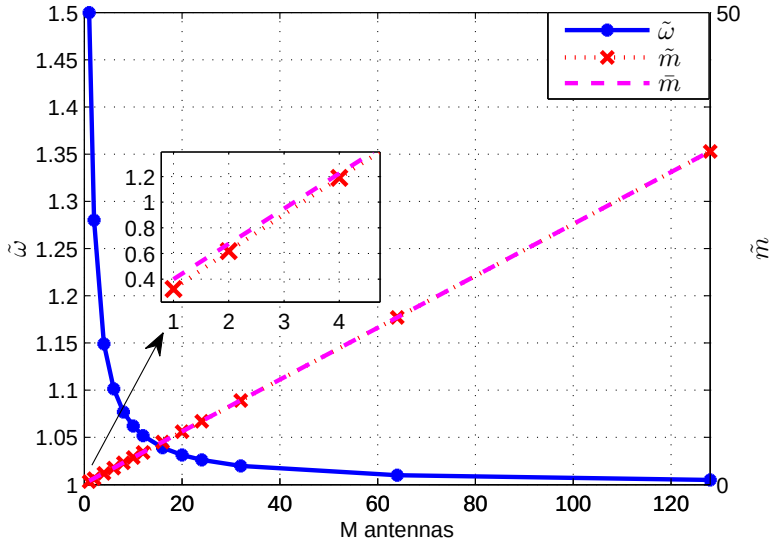

Figure 3.13: Variations of the parameters of the Nakagami-m equivalent channel against the number M of transmit antennas.

Noting that $\tilde{w} = \mathbb{E}[z_R^2]$ represents the received average signal power, $\tilde{w}$ can be seen as a kind of "overfading" effect coming from the additional interference term and tends to vanish in the large antenna regime. Also, it appears from Fig. 3.13 that $\tilde{m}$ almost follows a linear progression with M, some gap being observed with small M. Asymptotically, this tells us that the fading amplitude is linearly decreasing with M and thus converges to 0 for $M \to \infty$. Essentially, we hereby verify that the two-user EGT-MIMO channel becomes equivalent to a non-interfering and non-fading channel, which is a well-known result of Massive MIMO systems. However, by our analysis of the equivalent EGT-MIMO channel in the asymptotic regime, we bring a new result that is summarized in the following Theorem 1.

Theorem 1: For Rayleigh fading, the in-phase component of a two-user BPSK EGT-MIMO system with a sufficiently large M experiences the Nakagami-m fading with parameters

$$\begin{cases} \bar{m} = \frac{\pi}{24-4\pi} M + \frac{1}{8} \\ \\ \bar{w} = 1 \end{cases} \tag{3.23}$$

Proof: The proof directly relies on Proposition 2 in which we evaluate parameters $\tilde{m}$ and $\tilde{w}$ for $M \to \infty$. Then, getting $\bar{w}$ is straightforward, while getting $\bar{m}$ is obtained using the approximation of [102, p257, Eq. (6.1.47)] for $\frac{\Gamma(\tilde{m}+\frac{1}{2})}{\Gamma(\tilde{m})}$, i.e.

$$\frac{\tilde{m}}{M} = \frac{\pi}{24-4\pi} - \frac{\pi}{192-32\pi}\frac{1}{\tilde{m}} + \frac{1}{4M} + \mathcal{O}\left(\frac{1}{\tilde{m}}\right) \tag{3.24}$$

Evaluating $\lim_{M\to\infty} \tilde{m}$ at order $\mathcal{O}(1)$ concludes the proof. ■

3.3.3.3 Simulation results

From the previous p.d.f. expressions, it is now possible to derive the theoretical BER of the two-user EGT-MIMO system, i.e. to compute Eq. (3.25). In this equation, $Q(.)$ is the Marcum

function and ${}_2F_1(.)$ is the Gauss hypergeometric function which convergence within the unit circle is compatible with $\forall \frac{E_b}{N_0} > 0$, $\frac{\frac{\tilde{m}}{\tilde{\omega}}}{\frac{\tilde{m}}{\tilde{\omega}} + \frac{E_b}{N_0}} < 1$. The integral is computed using [98, p118 - Eq. (B.6)].

$$
\begin{aligned}
P_e\left(\frac{E_b}{N_0}\right) &= \int_0^{\infty} Q\left(\Xi\sqrt{\frac{2E_b}{N_0}}\right) f(\Xi)\, d\Xi \\
&= \frac{\Gamma\left(\tilde{m}+\frac{1}{2}\right)}{2\sqrt{\pi}\Gamma(\tilde{m}+1)} \cdot \frac{\left[\frac{\tilde{m}}{\tilde{\omega}}\frac{N_0}{E_b}\right]^{\tilde{m}}}{\left[1+\frac{\tilde{m}}{\tilde{\omega}}\frac{N_0}{E_b}\right]^{\tilde{m}+\frac{1}{2}}} \times {}_2F_1\left(1, \tilde{m}+\frac{1}{2}, \tilde{m}+1, \frac{\frac{\tilde{m}}{\tilde{\omega}}}{\frac{\tilde{m}}{\tilde{\omega}}+\frac{Eb}{N0}}\right)
\end{aligned}
\tag{3.25}
$$

Fig. 3.14 shows the BER curves obtained for various M. Monte-Carlo simulations are compared with the analytical results of Eq. (3.25) when applying Proposition 2, i.e. using $(\tilde{m}, \tilde{\omega})$, or Theorem 1, i.e. using $(\bar{m}, \bar{\omega})$. In addition, BER curves for the commonly used Gaussian approximation of the inter-channel interference term are given for comparison purpose. In that case, the Gaussian process is calibrated with variance $\sigma_I^2 = 2\sigma^2$. The match between theoretical and simulated results is very satisfactory with our Nakagami-m model compared to the Gaussian model, the latter turning out to be very poor. With $M = 2$, however, we observe a gap at high SNR region between the Nakagami-based models and the simulated system. This lack of accuracy is due to the defect of the Nakagami approximation with small M as explained in the comments of Fig. 3.12. On the other hand, using Theorem 1 for small M leads to a slight underestimation of the fading amplitude ($\bar{m} > \tilde{m}$) when M is too small, which is translated into an higher slope of the related BER curves at low SNR regime. Moreover, as $\bar{w} < \tilde{w}$, we observe a lower slope at high SNR regime. Nonetheless, as long as $M \geq 8$, the accuracy of our model becomes excellent, which makes it worthy of interest for many configurations of the number of antennas.

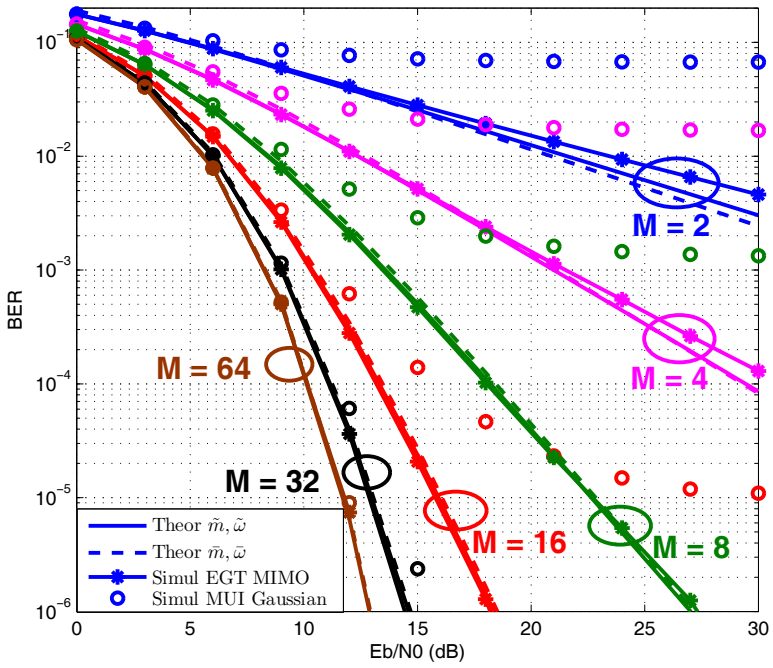

Figure 3.14: Average BER for the 2 users EGT-MIMO OFDM system with OFDM size $N_f = 64$ and various M. Comparison between simulation, theoretical and Gaussian approximation results.

3.3.3.4 Optimal overlap ratio based on BER performance

With the BER expressions for the single user MISO system and two-user MIMO system, it is easy to deduce the BER performance of PFBO system with different overlap ratio as shown in Fig. 3.15 for $M = 4$ and Fig. 3.16 for $M = 8$.

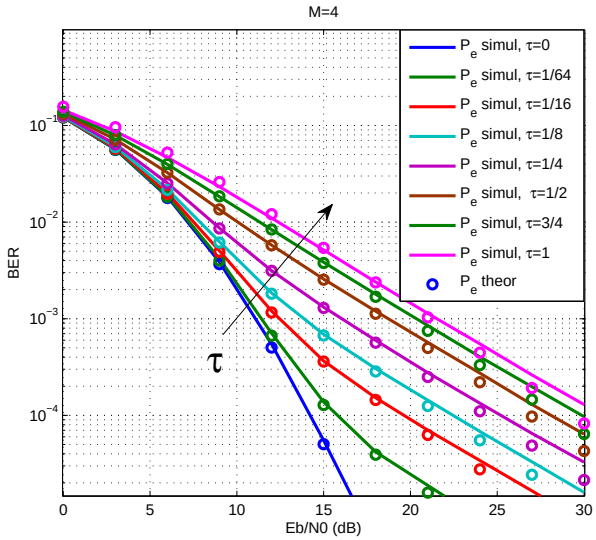

Figure 3.15: Average BER for PFBO OFDM systems with OFDM size $N_f = 64$ and number of transmit antennas $M = 4$. The overlap ratio τ within 2 users varies from 0 to 1.

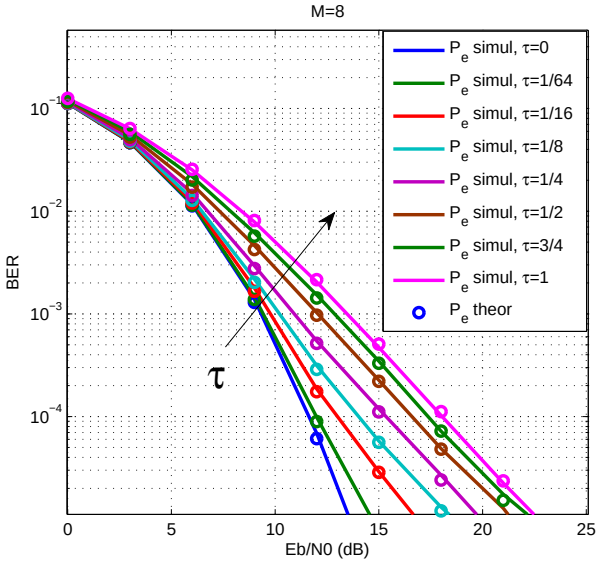

Figure 3.16: Average BER for PFBO OFDM systems with OFDM size $N_f = 64$ and number of transmit antennas $M = 8$. The overlap ratio τ within 2 users varies from 0 to 1.

In practical transmission cases, the systems normally work with a target BER depending on the technique of channel coding. Here for PFBO systems, with a fixed target BER, we can obtain the maximal overlap ratio that the system is able to support, denoted as τ_{opt}. Assuming a target BER of 5×10^{-3}, we present in Fig. 3.17 the τ_{opt} in systems with different number of transmit antennas M. We observe that, with the increase of M, the system can support a higher τ_{opt}. With 4 antennas, the two users can have a 100% overlapping since SNR $\gamma = 16dB$. And with 16 antennas, the two users can have a 100% overlapping since SNR $\gamma = 8dB$, then more users can be supported for higher SNR regime.

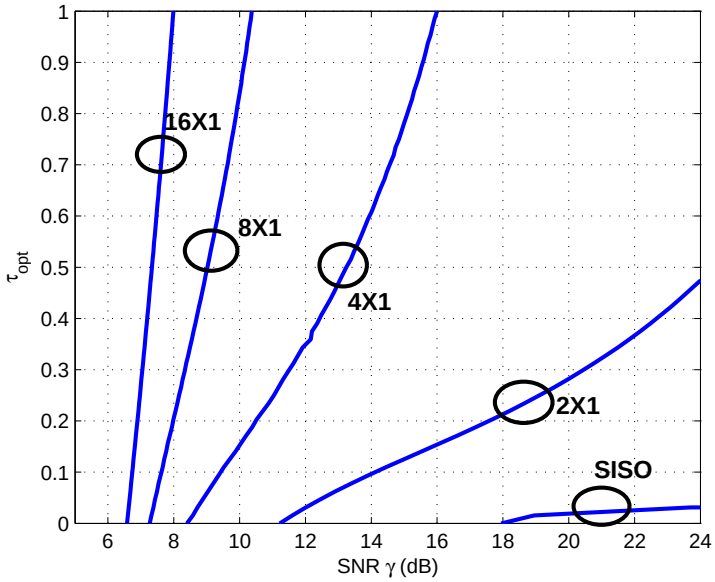

Figure 3.17: Maximal overlap ratio for a target BER of 5×10^{-3}.

Here the optimal overlap ratio analysis based on BER performance can be considered as a complement of the capacity analysis in 2.2.4, under a fixed throughput and constellation scheme.

3.3.4 Extension to more general MU-MIMO cases

3.3.4.1 Two-user QPSK case

For the QPSK modulation, the BER estimation is more complicated, because the point cloud exceeds the decision threshold $Re\{Y^{(1)}\} > 0$, $Im\{Y^{(1)}\} > 0$ as shown in Fig. 3.18.

In fact, the symbol received on the real axis is:

$$Y_Q^{(1)} = \frac{1}{\sqrt{M}} \sum_{m=1}^{M} \left|H_m^{(1)}\right| \left(\frac{1}{\sqrt{2}} + \cos(\psi_m)\right) a^{(1)} \tag{3.26}$$

For each term $\xi_{QPSK,m} = \frac{1}{\sqrt{2}} + \cos(\psi_m)$, $\psi_m \sim \text{Unif}(0, 2\pi)$. $\xi_{QPSK,m} \leq 0$ when $\psi_m \in \left[\frac{3}{4}\pi, \frac{5}{4}\pi\right]$, otherwise, $\xi_{QPSK,m} > 0$. The p.d.f function of $\xi_{QPSK,m}$ can be computed using the p.d.f. of $\cos(\cdot)$ function given in [83]:

$$f_{\cos}(x) = \begin{cases} \frac{1}{\pi} \frac{1}{\sqrt{1-x^2}}, & \forall x \in (-1, 1) \\ 0, & \text{otherwise} \end{cases} \tag{3.27}$$

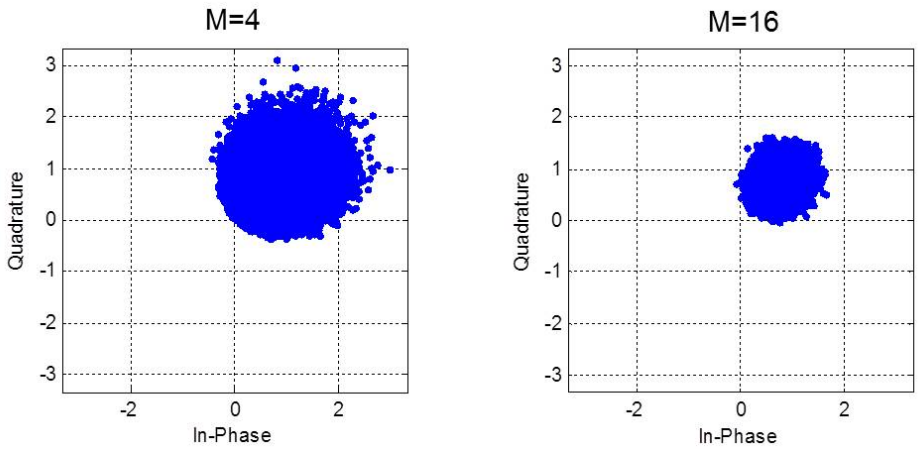

Figure 3.18: QPSK point cloud without noise for 4×1 and 16×1

Hence, the p.d.f. of $\xi_{QPSK,m}$ can be obtained by changing variable $\xi = x + \frac{1}{\sqrt{2}}$:

$$f_{\xi_{QPSK}}(\xi) = \begin{cases} \frac{1}{\pi} \frac{1}{\sqrt{1-(y-1/\sqrt{2})^2}}, & \forall y \in (-1+\frac{1}{\sqrt{2}}, 1+\frac{1}{\sqrt{2}}) \\ 0, \quad \text{otherwise} \end{cases} \tag{3.28}$$

The p.d.f. of $\xi_{QPSK,m}$ is quite complex to be derived. We evaluate numerically the possibility of $\frac{1}{\sqrt{M}} \sum_{m=1}^{M} \left| H_m^{(1)} \right| \xi_{QPSK,m} \leq 0$ in function of M as shown in Fig. 3.19.

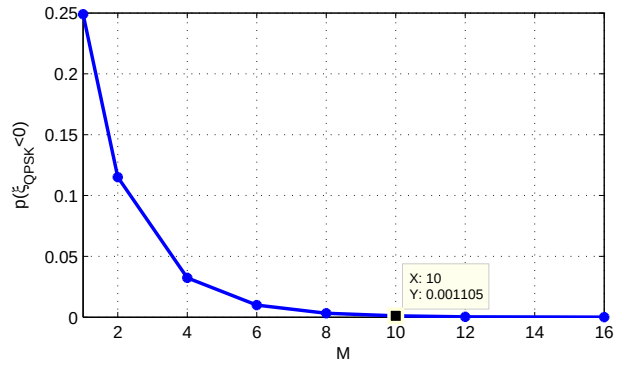

Figure 3.19: The possibility of $\frac{1}{\sqrt{M}} \sum_{m=1}^{M} \left| H_m^{(1)} \right| \xi_{QPSK,m} \leq 0$ in function of M

The distribution of $\frac{1}{\sqrt{M}} \sum_{m=1}^{M} \left| H_m^{(1)} \right| \xi_{QPSK,m}$ is displayed in Fig. 3.20.

We observe that when the received symbol exceeds the decision threshold, the classical Nakagami model can not approximate the channel distribution. To deal with this problem, we use a translated Nakagami distribution which means that geometrically translate the Nakagami distribution to the negative part.

To achieve the translation, we note at first L_t as the translation length. The translated signal sample is:

$$Y_{Q,L} = \frac{1}{\sqrt{M}} \sum_{m=1}^{M} |H_m| (\frac{1}{\sqrt{2}} + \cos(\psi_m)) a + L_t \tag{3.29}$$

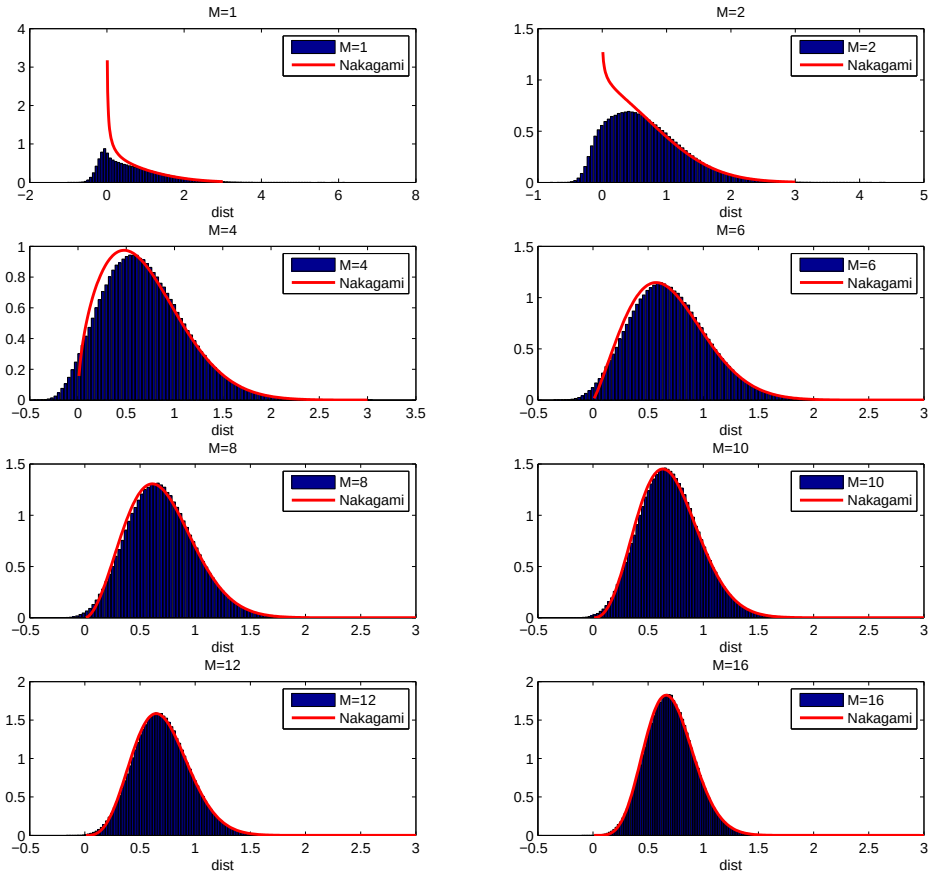

Figure 3.20: The distribution of $\frac{1}{\sqrt{M}}\sum_{m=1}^{M}\left|H_m^{(1)}\right|\xi_{QPSK,m}$ with different M values

Thus the mean and moment of order 2 of $Y_{Q,L}$ is:

$$\mathbb{E}\left[Y_{Q,L}\right]=\mathbb{E}\left[Y_Q\right]+L_t=\sigma\frac{\sqrt{\pi M}}{2}+L_t \tag{3.30}$$

$$\begin{aligned}\mathbb{E}\left[\left|Y_{Q,L}\right|^2\right]&=\mathbb{E}\left[\left|Y_Q\right|^2\right]+L_t^2+2L_t\mathbb{E}\left[Y_Q\right]\\&=\frac{\pi}{4}M\sigma^2+2\sigma^2-\frac{\pi}{4}\sigma^2+L_t^2+L_t\sigma\sqrt{\pi M}\end{aligned} \tag{3.31}$$

Remain that $\sigma^2=\frac{1}{\frac{\pi}{2}M+2-\frac{\pi}{2}}$ to assume $\mathbb{E}\left[\frac{1}{M}\left|\sum_{m=1}^{M}|H_m|\right|^2\right]=1$.

Assuming Y_L follows Nakagami distribution, using the same method as *Proposition 2*, the parameters of Nakagami fading model are:

$$\begin{cases}\tilde{m}_{Q,L}=\frac{\alpha\pi}{32-4\pi}M+\frac{L_t^2(8-2\pi)}{32-4\pi}+\frac{1}{8}, \quad \alpha=2L_t^2+1+2L_t\sqrt{2+\frac{8-2\pi}{\pi M}}\\ \tilde{w}_{Q,L}=\frac{\pi M+8-\pi}{2\pi M+8-2\pi}+L_t^2+L_t\sqrt{\frac{2}{1+\frac{4-\pi}{\pi M}}}\end{cases} \tag{3.32}$$

The prescion of translated Nakagami distribution is verified in Fig. 3.21.

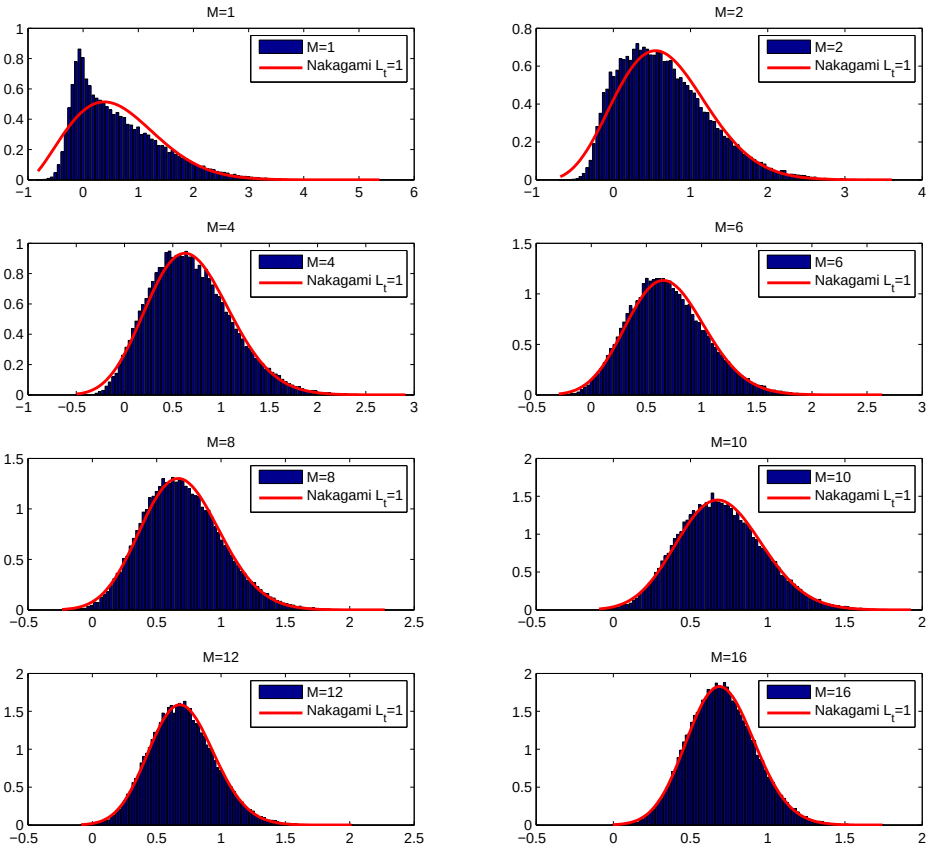

Figure 3.21: The distribution of $\frac{1}{\sqrt{M}}\sum_{m=1}^{M}\left|H_m^{(1)}\right|\xi_{QPSK,m}$ and $Nakagami(x-1|\tilde{m}_{Q,L},\tilde{w}_{Q,L})$

It is easy to estimate the ratio of symbols exceed the decision threshold using the cumulative distribution function (CDF) of Nakagami distribution:

$$F_X(x)=\frac{\gamma(\tilde{m_{Q,L}},\frac{\tilde{m_{Q,L}}}{\tilde{w_{Q,L}}}x^2)}{\Gamma(\tilde{m_{Q,L}})} \tag{3.33}$$

The CDF is displayed in Fig. 3.22.

The BER performance is presented in Fig. 3.23. We observe that the Nakagami approximation is more accurate than the Gaussian approximation. However, the Nakagami approximation do not well fit the simulation results for $M \leq 16$. This mismatch is because that the received symbols on real or image axises have a small power comparing to that of interference. Many terms of $\xi_{QPSK,m}$ become negative and change the distribution of the equivalent channel. Indeed, the Nakagami equation is designed to approximate the addition of positive only terms, hence it do not well fit our channel distribution. An extension of Nakagami equation including negative terms is an interesting subject for future works.

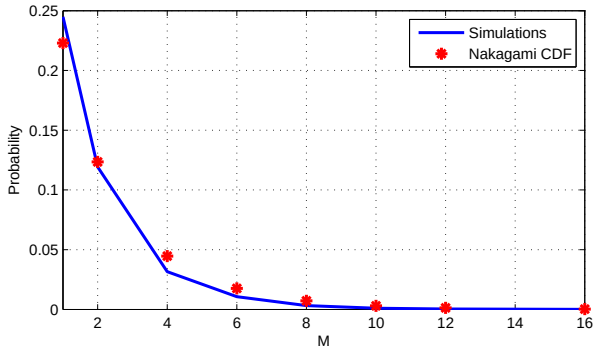

Figure 3.22: The CDF of $Nakagami(x-1|\tilde{m}_{Q,L},\tilde{w}_{Q,L}) \leq 0$ and the simulation results of $\frac{1}{\sqrt{M}}\sum_{m=1}^{M}\left|H_m^{(1)}\right|\xi_{QPSK,m} \leq 0$ in function of M

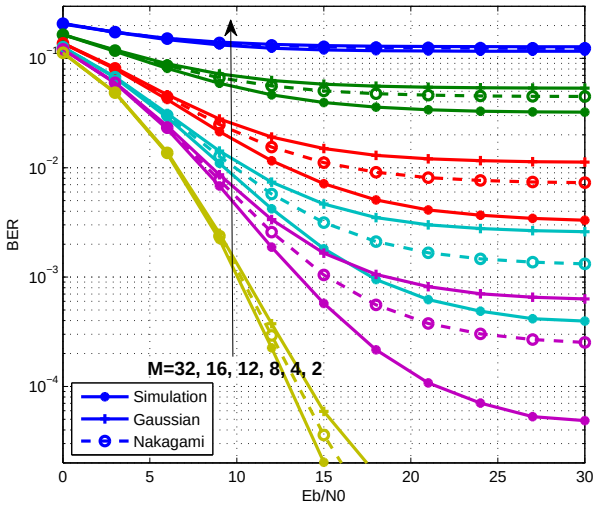

Figure 3.23: Two-user MIMO OFDM performance with QPSK

However, as the order of constellation increases, the impact of the inter-channel interference tends to that of Gaussian interference as shown in Fig. 3.24 for systems using 8PSK constellation. In fact, due to the central limit theorem, the more symbols of different power levels are involved, the more the interference tends to Gauss distribution.

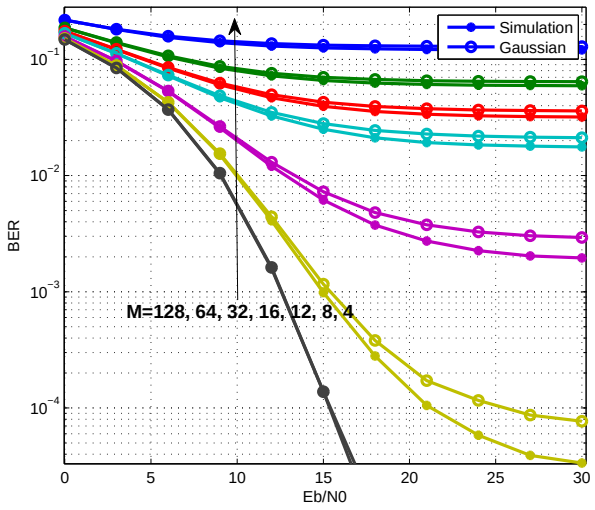

Figure 3.24: Two-user MIMO OFDM performance with 8PSK

3.3.4.2 Multiuser BPSK case

For MU-MIMO system of K user using BPSK constellation, the received symbol writes:

$$Y^{(1)} = \frac{1}{\sqrt{M}} \sum_{m=1}^{M} \left| H_m^{(1)} \right| (1 + \sum_{k=2}^{K} \cos(\psi_m^{(k)})) a^{(1)} \tag{3.34}$$

Hence the average and the signal power can be computed as:

$$E\left[Y^{(1)}\right] = E\left[\frac{1}{\sqrt{M}} \sum_{m=1}^{M} \left| H_m^{(1)} \right|\right] = \sigma \sqrt{\frac{\pi M}{2}} \tag{3.35}$$

and

$$E\left[\left|Y^{(1)}\right|^2\right] = 2\sigma^2(1 + (K-1)/2) + (M-1)\frac{\pi}{2}\sigma^2 \tag{3.36}$$

Using the same translated Nakagami distribution as in QPSK case 3.3.4.1, the Nakagami parameters for MU-MIMO systems are obtained as:

$$\begin{cases} \tilde{m}_{K,L} = \frac{\alpha\pi}{8(K+1)-4\pi} M + \frac{L_t^2(4-\pi)}{8(K+1)-4\pi} + \frac{1}{8}, \quad \alpha = L_t^2 + 1 + 2L_t\sqrt{1+\frac{4-\pi}{\pi M}} \\ \tilde{w}_{K,L} = \frac{\pi M + 2(K+1) - \pi}{\pi M + 4 - \pi} + L_t^2 + 2L_t\sqrt{\frac{1}{1+\frac{4-\pi}{\pi M}}} \end{cases} \tag{3.37}$$

The ratio of symbols exceeds the decision threshold (the equivalent channel response becomes negative) is displayed in Fig. 3.25 for three users case, where we obtained similar ratio as in two-users QPSK case. However, the useful signal power is equal to 1, while in QPSK case, the useful power on real or imaginary axis is only $\frac{1}{2}$. The useful signal in MU-MIMO BPSK case is less affected by the MAI interference. Therefore, the Nakagami equation better fits the channel distribution as shown in Fig. 3.26, where the Nakagami approximation well fits the channel distribution for antenna number $M \geq 8$.

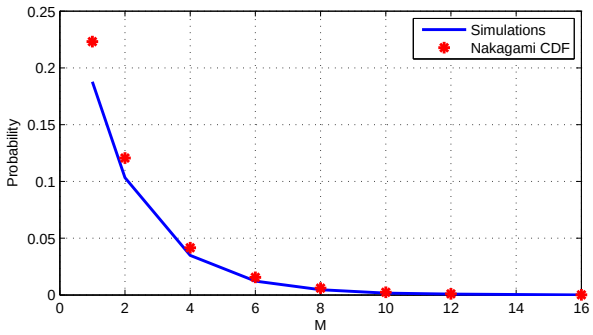

Figure 3.25: The CDF of $Nakagami(x-1|\tilde{m}_{K,L}, \tilde{w}_{K,L}) \leq 0$ and the simulation results of probability of $\frac{1}{\sqrt{M}}\sum_{m=1}^{M}\left|H_m^{(1)}\right|(1+\sum_{k=2}^{3}\cos(\psi_m^{(k)})) \leq 0$ in function of M

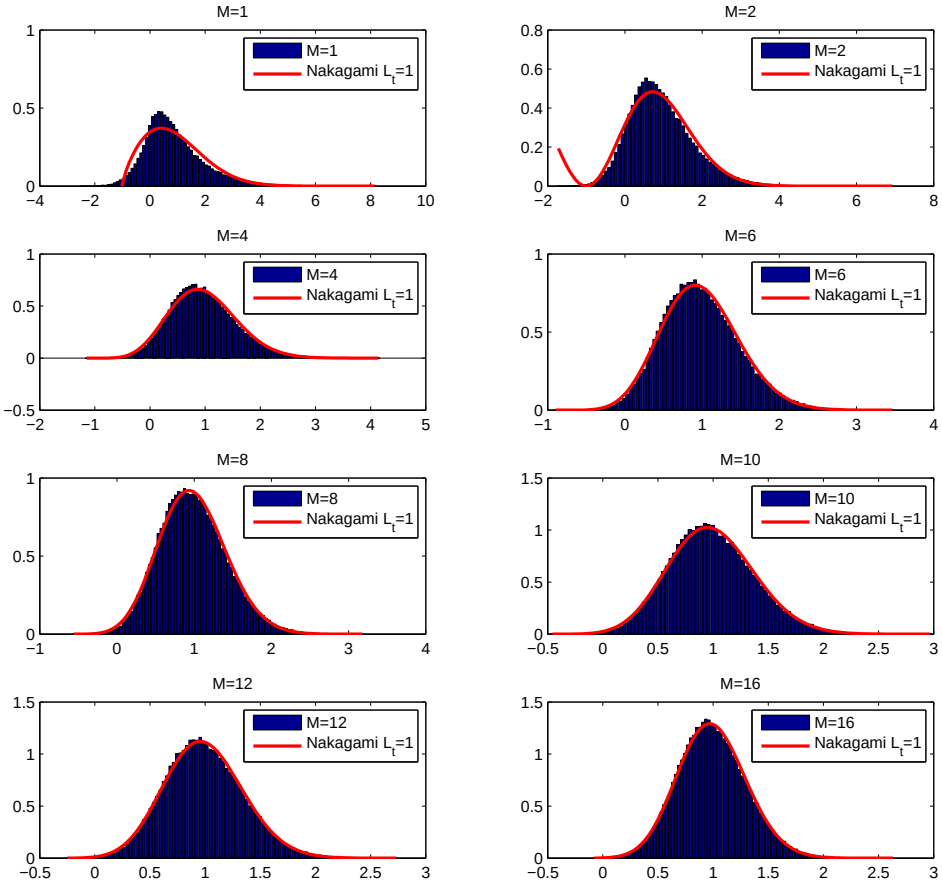

Figure 3.26: The distribution of $\frac{1}{\sqrt{M}}\sum_{m=1}^{M}\left|H_m^{(1)}\right|(1+\sum_{k=2}^{3}\cos(\psi_m^{(k)}))$ and $Nakagami(x-1|\tilde{m}_{K,L}, \tilde{w}_{K,L})$

The BER performance of three-user MIMO OFDM BPSK systems is displayed in Fig. 3.27. We observe that the Nakagami approximation well follows the simulation results, the gradient is similar. The gap comes from the mismatch between the Nakagami equation and the real channel distribution which once again due to the negative terms caused by the MAI. However, as shown in Fig. 3.28 for 8 users case, the Gaussian approximation becomes available when more users are considered for the system.

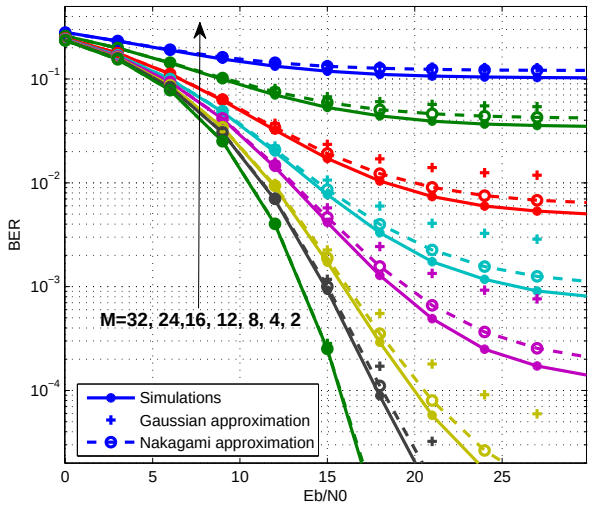

Figure 3.27: MU-MIMO OFDM system performance with 3 users

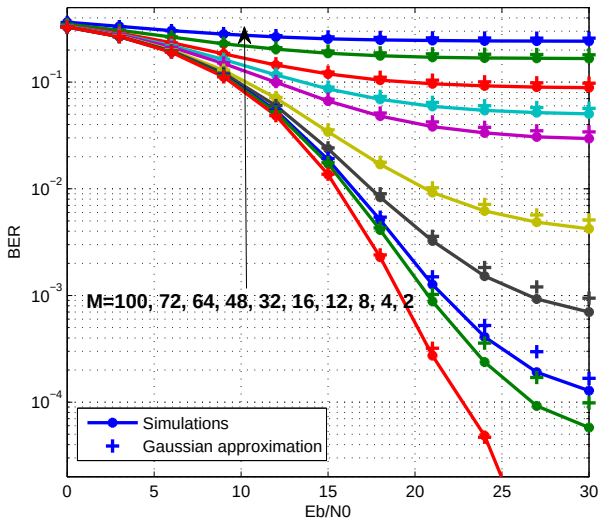

Figure 3.28: MU-MIMO OFDM system performance with 8 users

3.4 Conclusion

In this chapter, we studied the BER performance of the PFBO scheme applied to OFDM systems. The BER expressions were established for both AWGN channels and Rayleigh fading channels. Particularly, for Rayleigh fading channels, we proposed to use the stochastic Nakagami process to model the correlation between the useful signal and the multi-user interference for EGT two-user MIMO systems using BPSK modulation. The choice of the statistical model was justified and the linear relation between the Nakagami parameters and the number of transmit antennas was demonstrated. The model was shown to be also available when multiple interfering users were considered.

The BER analysis of MU-MIMO system in Rayleigh channel was derived using EGT precoding technique. However, the Nakagami approximation is also available for MRT case. While for TR case, the gamma distribution can be used through similar analysis.

The results of section 3.1 for BER analysis of SISO PFBO OFDM system in AWGN channel have be published in:

H. Fu, M. Crussière and M. Hélard, "Partial channel overlay in moderate-scale MIMO systems using WH precoded OFDM", in *Proc. 21st International Conference on Telecommunications (ICT 2014)*, pp. 16-21, Lisbon, Portugal, May 2014.

The results of section 3.3 for BER analysis of two-user EGT MIMO system in Rayleigh channel will be published in:

H. Fu, M. Crussière and M. Hélard, "BER Analysis for Downlink Multiuser MIMO-OFDM System using Equal Gain Transmission", accepted for publication in *IEEE wireless communications Letters*.

CHAPTER 4

BER ANALYSIS FOR BANDWIDTH OVERLAY SS-OFDM SYSTEMS

In the previous chapter, we analyzed the BER performance of the PFBO scheme when applied to classical OFDM waveform. In this chapter, we intend to assess how this performance are going to evolve when adding a spread spectrum (SS) component to the OFDM waveform, namely using the SS-OFDM system. As SS-OFDM is known to be robust to narrow-band interference, the PFBO SS-OFDM system is expected to outperform the PFBO-OFDM one, at least in some situations that have to be identified. Following the same approach as in the previous chapter, we analyze the BER performance of the PFBO SS-OFDM system over AWGN first and then over frequency Rayleigh channels. A Closed-form BER approximation is derived for AWGN channels. While with Rayleigh channels, the impact of the inter-channel interference is precisely analyzed for each signal component.

4.1 SS-OFDM systems

The SS techniques appeared in 1940s and were dedicated for military applications. These techniques increase the resistance to the interference and jamming, and provide secure and low-power transmissions. Now for wireless communications systems, SS is widely used for multi-user multiple access, known as CDMA, or be combined with OFDM systems, such as multi-carrier CDMA (MC-CDMA) and linear-precoded OFDM (LP-OFDM) [103].

The SS techniques offer an additional multipath diversity gain to conventional OFDM systems by spreading each data symbol on the whole frequency bandwidth [104, 105]. This multipath diversity gain also can be used to combat the narrow band interference. Therefore, in this thesis, we use the SS techniques to mitigate the MAI of MU-MIMO systems.

4.1.1 SS-OFDM transmission chain

The SS techniques can easily be associated with OFDM systems by applying spreading sequences to the symbols conveyed by every OFDM subcarrier as shown in Fig. 4.1. Where

$\{c_1,\ldots,c_{N_f}\}$ present the codewords correspond to data symbols $\{a_1,\ldots,a_{N_f}\}$, each codeword contain L_c chips with L_c is equal to the subcarrier number N_f.

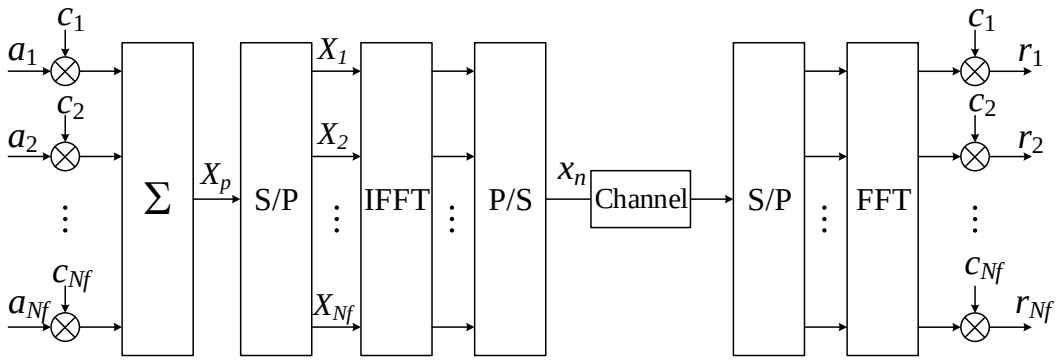

Figure 4.1: SS-OFDM chain

The SS-OFDM symbols before IFFT bloc are presented in Fig. 4.2. The symbol transmitted on the p^{th} subcarrier is:

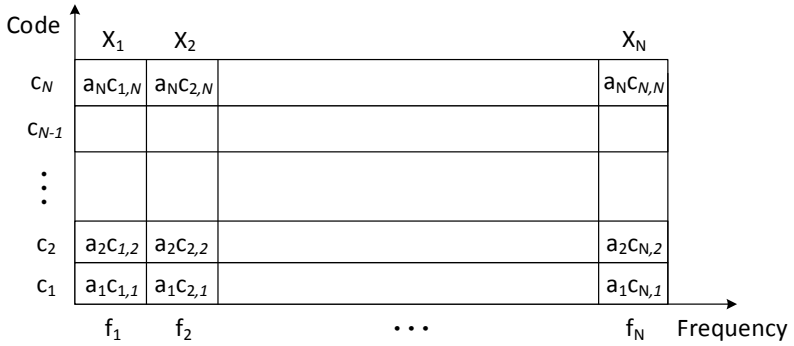

Figure 4.2: SS-OFDM frequency symbols

$$X_p = \sum_{i=1}^{N_f} a_i c_{p,i} \tag{4.1}$$

In this way, SS can be viewed as a particular frequency domain precoding technique. Each data symbol is spread on all the OFDM subcarriers, which allows each data symbol benefits the full frequency diversity gain of the channel. Moreover, the damage of certain subcarriers will not leads to a entire lost of the data symbols.

4.1.2 Spreading codes

To accommodate divers transmission requests, many spreading codes have been proposed [106, 107]. In general, these codes can be separated in two classes: orthogonal codes and non-orthogonal codes. In the synchronous communications systems, orthogonal codes are often used

to avoid the inter-code interference (ICI). The Walsh-Hadamard codes are the most used codes in this case, for its simplicity and good orthogonality property. While in asynchronous systems, the situation is more complicated, there exist pseudo-noise (PN) sequences, Gold codes [108], Kasami codes, etc.

4.1.2.1 Walsh-Hadamard codes

The Walsh-Hadamard (WH) codes are orthogonal between each other. They are commonly used in synchronous CDMA systems (DL transmission) for IS-95, 3G etc. The WH codes is based on the Hadamard matrix which, of size $L_c \times L_c$, is constructed recursively as:

$$WH_1 = 1,\ WH_{L_c} = \begin{bmatrix} WH_{\frac{L_c}{2}} & WH_{\frac{L_c}{2}} \\ WH_{\frac{L_c}{2}} & -WH_{\frac{L_c}{2}} \end{bmatrix}, \tag{4.2}$$

Each WH codeword is a column of Hadamard matrix. A rescaling by $1/\sqrt{L_c}$ is required to make the matrix unitary.

We also present an example of WH codes with $L_c = 64$ in Fig. 4.3. We can clearly observe the periodicity by block within the codes. The matrix is regular and symmetric.

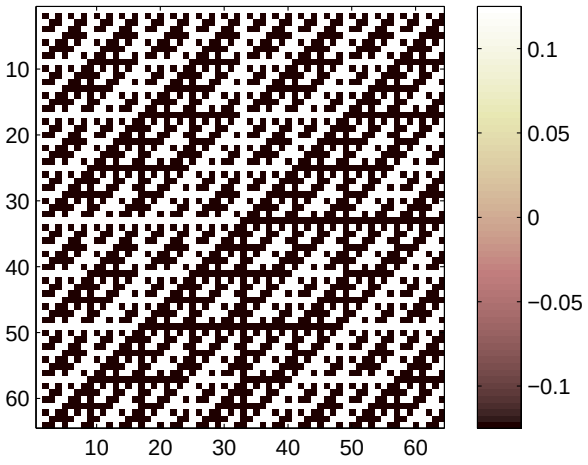

Figure 4.3: WH codes

The auto-correlation and cross-correlation values for WH codes are displayed in Fig. 4.4. We obtain 1 on diagonal for the auto-correlation functions and 0 for all the cross-correlation functions. This confirms that the WH codes are orthogonal between each other.

The WH codes can be extended to the complex values. One example is unified complex Hadamard transform (UCHT) as:

$$UCHT_2 = \begin{bmatrix} 1 & j \\ 1 & -j \end{bmatrix},\ UCHT_{L_c} = UCHT_2 \otimes UCHT_{L_c-1}, \tag{4.3}$$

An overview of complex Hadamard matrix with basic properties is presented in [109].

Golay complementary series [110] are also orthogonal codes. The advantage of Golay code is that, the FFT of Golay codes has an envelope little fluctuate, contrary to that of the WH codes.

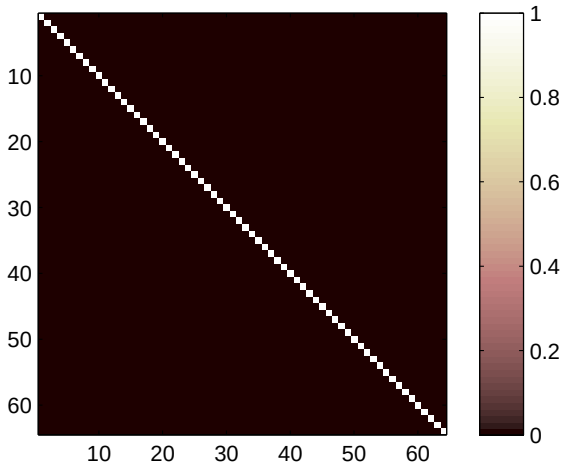

Figure 4.4: WH codes auto-correlation and cross-correlation values

This property is particularly useful in OFDM system which suffers from high PAPR of the signal. However, this thesis will not discuss the PAPR problem, hence we choose the WH codes for its simplicity.

4.1.2.2 PN codes

The pseudo noise (PN) sequences, also called maximal-length sequences or m-sequences, are based on a pseudo random binary sequence of length $2^m - 1$. This random sequence is generated from a binary primitive polynomial of degree m [111]. Then each PN codeword is obtained by shift circularly the sequence to the right by one chip. An example for PN codes of degree 6, which means length $L_{PN} = 63$, is presented in Fig. 4.5.

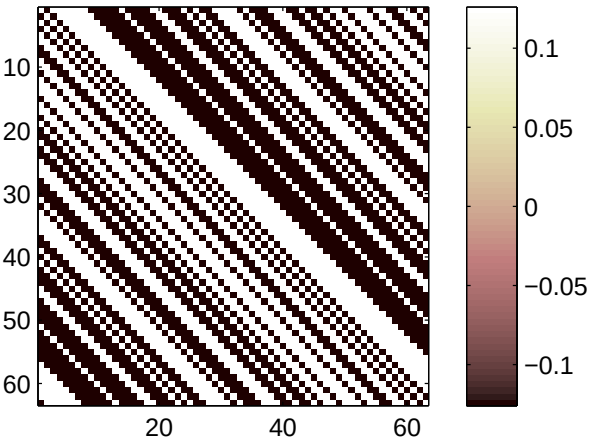

Figure 4.5: PN codes

The auto-correlation and cross-correlation values for PN codes are displayed in Fig. 4.6. We also obtain 1 for the auto-correlation functions but the cross-correlation functions are equal to $-\frac{1}{L_{PN}}$. As the poor cross-correlation character, PN sequences are rather used for system synchronization or channel estimation [112].

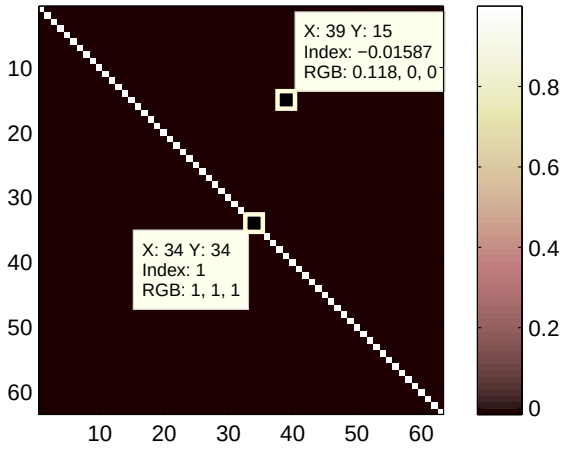

Figure 4.6: PN codes auto-correlation and cross-correlation values

The Gold codes are constructed by combining two PN sequences. The specialty of Gold codes is that a codebook of length L_{Gold} contains $L_{Gold}+2$ codewords. The large number of codewords allows to serve more users.

We test through simulations the performance of WH and PN codes in SISO SS-OFDM PFBO system as shown in Fig. 4.7. AWGN channel is used. The performance of SISO OFDM PFBO system is also presented as reference. WH codes of length $L_c = 64$ and PN codes of length $L_{PN} = 63$ are used. We observe that for non overlapping case, i.e. $N_R = 0$, WH SS-OFDM has the same performance as the OFDM system, because no multipath diversity gain present in AWGN channel. The performance of PN codes is worse because the codes are non-orthogonal. The WH codes outperform the PN codes for $N_R \leq 12$. Then for larger N_R, the interference becomes too strong and the performances of WH codes and PN codes become similar. However, the SS-OFDM system is shown more robust to the narrow band interference than the OFDM system.

In the following, we analyze the BER performance of SS-OFDM system in AWGN and Rayleigh channel. The WH codes will be used as spreading codes for the orthogonality property.

4.2 BER analysis for two-user SISO PFBO system in AWGN channel

4.2.1 System description

Taking basis on an OFDM signal consisting of N_f subcarriers, we use WH sequences of length $L_c = N_f$, which means that the precoding function affects all the subcarriers of each user. $user1$ and $user2$ utilize the same sequences. To have equivalent bit rate as with non-precoded OFDM, we will consider a full loaded SS-OFDM system, meaning that the number of precoding

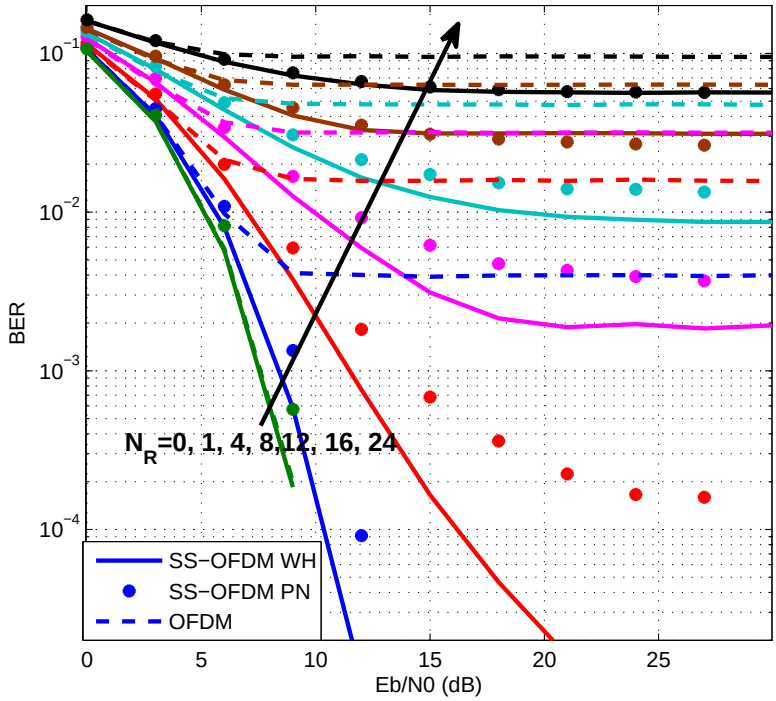

Figure 4.7: Performance of WH and PN codes in SISO PFBO SS-OFDM systems with AWGN channel, modulation QPSK

sequences is $N_c = L_c = N_f$. In such a case, each user is assigned N_f precoding sequences and can then transmit N_f constellation symbols as in the non-precoding OFDM case.

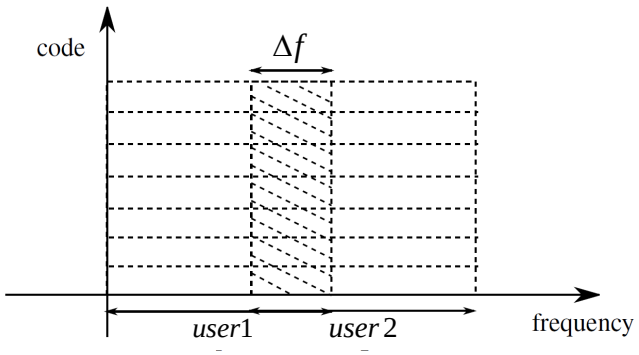

Figure 4.8: SS-OFDM overlapping model.

The signal spectrum of the SS-OFDM system with PFBO is shown in Fig. 4.8 highlighting that N_R subcarriers of $user2$'s signal falls into the $user1$'s signal band. Assuming perfect syn-

chronization, the signal received by $user1$ on subcarrier p is:

$$\begin{cases} Y_p^{(1)} = H_p^{(1)} \sum_{i=1}^{N_c=N_f} c_{p,i} a_i^{(1)} + N_p, & \forall k \in \{1, \cdots, N - N_R\} \\ Y_p^{(1)} = H_p^{(1)} \sum_{i=1}^{N_c=N_f} c_{p,i} a_i^{(1)} + H_{p'}^{(2)} \sum_{i=1}^{N_c=N_f} c_{p',i} a_i^{(2)} + N_p, & \text{otherwise} \end{cases} \tag{4.4}$$

As in OFDM, equalization factors can be applied to SS-OFDM signals to compensate the channel attenuation. For the simplicity of the implementation, equalization is often processed before the despreading function. Denoting the equalization factor as G_p, the ith received symbol after despreading then expresses:

$$r_i^{(1)} = \sum_{p=1}^{N} |c_{p,i}|^2 G_p^{(1)} H_p^{(1)} a_i^{(1)} + I_i + J_{i,N_R} + \hat{N}_p, \tag{4.5}$$

where I_i represents the ICI obtained from the symbols $j \neq i$ of u_1 and J_{i,N_R} is the inter-channel interference term due to the bandwidth overlap. Note that contrary to the OFDM case, the interfering signal is spread over all the OFDM spectrum. As a consequence, the impact on the received symbols is equivalent whatever the symbol. The ICI term writes:

$$I_i = \sum_{j \neq i} \sum_{p=1}^{N_f} c_{p,i} c_{p,j} G_p^{(1)} H_p^{(1)} a_l^{(1)}, \tag{4.6}$$

The ICI term strongly depends on the equalization technique used, namely zero-forcing (ZF) or minimum mean square error (MMSE) [105]. The inter-channel interference term can be expressed as:

$$J_{i,N_R} = \sum_{l=1}^{N_f} \sum_{p'=1}^{N_R} c_{N_f - N_R + p',i} c_{p',l} G_{N_f - N_R + p'}^{(1)} H_{p'}^{(2)} a_l^{(2)} \tag{4.7}$$

and depends on the number of overlapped subcarriers N_R.

4.2.2 BER analysis

As in the OFDM case, we consider at first the case of AWGN channel. Hence, $H_p = G_p = 1$ and the ICI term I_i given in (4.24) is zero because of the orthogonality of WH sequences. The BER analysis then reduces to the study of the impact of the inter-channel interference term J of Eq. (4.7). Fig. 4.9 gives the interfering patterns that occur around a useful constellation symbol (with $a_i^{(1)} = 1$ here) after despreading and for two values of N_R. It appears that the interfering signals can follow different distribution laws. Whereas the distribution seems to be almost continuous for $N_R = 7$, it is clearly discrete for $N_R = 32$. In the following, we will then give the BER expressions for the two cases.

4.2.2.1 Channel overlapping yielding a normally distributed interference

According to the central limit theorem and assuming that interfering symbols $a_u^{(2)}$ in Eq. (4.7) are independent, the distribution of the inter-channel interference is close to a normal distribution for a sufficiently high number N_f of subcarriers. Fig. 4.10 presents one example of the measured

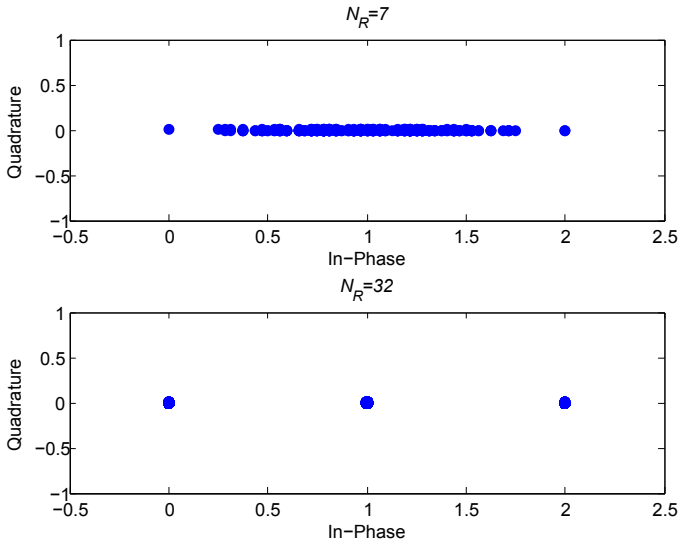

Figure 4.9: Received overlapped symbols with $N_R = 7$ and $N_R = 32$.

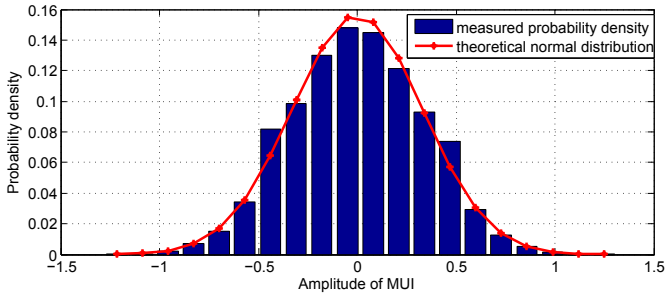

Figure 4.10: Distribution of MUI with $N_R = 7$, $N_f = L_c = 64$.

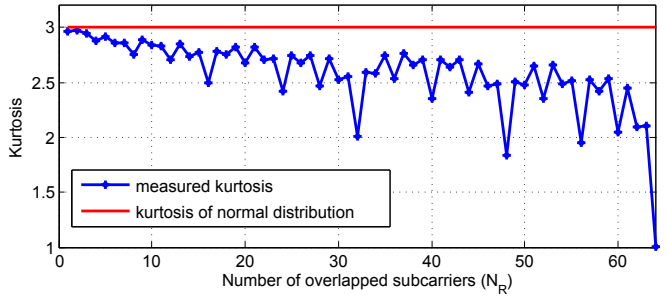

Figure 4.11: Measured kurtosis of the inter-channel interference with respect to different levels of signal bandwidth overlapping.

distribution of the inter-channel interference with $N_f = 64$ and an overlap of $N_R = 7$. The red curve highlights the fact that the interference component could eventually be approximated by a normal distribution.

To go further, it is interesting to evaluate the normality of the inter-channel interference term and measure the kurtosis of J_{i,N_R} with respect to different levels of bandwidth overlap as shown in Fig. 4.11. It can be seen from the measurements that the interference is approximately normally distributed, namely for small values of N_R, whereas the normal approximation no more holds in some cases, e.g. $N_R \in \{32, 48, 56, 60, 62, 63, 64\}$. This bias is caused by the structure of the WH codebook for which the continuous distribution is not a convenient model.

When the interference distribution is close to a normal distribution, the BER can be calculated as:

$$\mathrm{BER}_{\mathrm{SS-OFDM}} = \int_0^{+\infty} p(x)\left(\frac{1}{2}erfc\left(\frac{x}{\sqrt{N_0}}\right)\right)dx + \int_{-\infty}^{0} p(x)\left(1 - \frac{1}{2}erfc\left(\frac{-x}{\sqrt{N_0}}\right)\right)dx, \tag{4.8}$$

where $\mathrm{erfc}(\cdot)$ is the complementary error function, $p(x)$ is the p.d.f function of the normal law:

$$p(x) = \frac{1}{\sigma\sqrt{2\pi}} e^{\frac{(x-\mu)^2}{2\sigma^2}}, \tag{4.9}$$

with parameter μ and σ defined as the mean and standard deviation, respectively. These parameters can easily be obtained from Eq. (4.7):

$$\mathbb{E}[J_{i,N_R}] = \sum_{l=1}^{N_f} \sum_{k'=1}^{N_R} c_{N_f - N_R + k',i}\; c_{k',l}\; \mathbb{E}[a_l^{(2)}] = 0, \tag{4.10}$$

and

$$\sigma^2_{J_{i,N_R}} = \mathbb{E}\left[\sum_{l=1}^{N} \sum_{k'=1}^{N_R} c^2_{N_f - N_R + k',i} c^2_{k',l} |a_l^{(2)}|^2\right] = \frac{N_R}{N_f}. \tag{4.11}$$

Where $\mathbb{E}[\cdot]$ is the expectation operation. It is then deduced that $\mu = \sqrt{E_b}$ and $\sigma = \sqrt{\frac{N_R}{N_f}}$.

To make the analytical derivation feasible, it is convenient to use the following approximation [113]:

$$erfc(x) \approx \frac{1}{6} e^{-x^2} + \frac{1}{2} e^{-\frac{4x^2}{3}}. \tag{4.12}$$

Integrating this approximation in Eq. (4.8) and after some computations we get:

$$\begin{aligned} \mathrm{BER}_{\text{SS-OFDM}} = &\frac{1}{2} erfc\left(\sqrt{\frac{E_b}{2\sigma^2}}\right) + \frac{1}{12\sqrt{1 + \frac{2\sigma^2}{N_0}}}\; e^{-\frac{E_b}{2\sigma^2 + N_0}}\; erf\left(\sqrt{\frac{E_b}{2\sigma^2(1 + \frac{2\sigma^2}{N_0})}}\right) \\ &+ \frac{1}{4\sqrt{1 + \frac{8\sigma^2}{3N_0}}}\; e^{-\frac{E_b}{2\sigma^2 + \frac{3}{4}N_0}}\; erf\left(\sqrt{\frac{E_b}{2\sigma^2(1 + \frac{8\sigma^2}{3N_0})}}\right) \end{aligned} \tag{4.13}$$

where $erf(\cdot)$ is the error function and reminding that $\sigma^2 = \frac{N_R}{N_f}$ corresponds to the interference power level. From this results, we conclude that the effect of the bandwidth overlap has a progressive impact on the performance degradation depending on the relative levels of noise and interference. More precisely, the second and third terms in the equation are balanced by ratio σ^2/N_0 that compares the noise and interference levels. In particular, at high SNR, i.e. $N_0 \to 0$, these two terms becomes null and the BER is only driven by the first term of the equation which depends on the overlap ratio N_R/N_f and will cause an error floor.

4.2.2.2 Channel overlapping yielding interference terms with discrete distribution

When the interference distribution is discrete, the BER is obtained by separately computing the p.d.f of each possible received symbol value. For instance, in the case of $N_R = 32$ as shown in Fig. 4.9, the possible received signal values (without noise) are $\{0,1,2\}$ according to probabilities $\{0.25, 0.5, 0.25\}$. In a more general case, the BER expression can be given knowing that the received signal can contain $R_L = \{r_1, r_2, \ldots, r_L\}$ discrete possible values. The probability of receiving the l^{th} value can be expressed as:

$$p_l = \binom{L-1}{l-1} \frac{1}{2^{L-1}}, \tag{4.14}$$

this is verified by another example for $N_R = 8$:

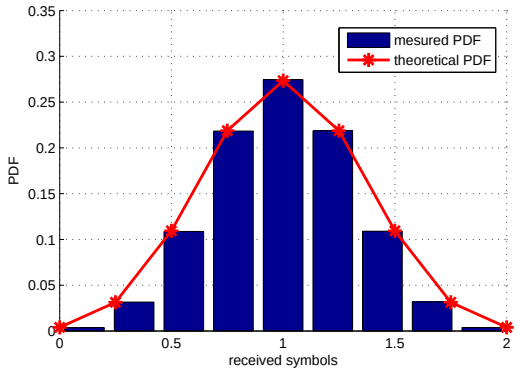

Figure 4.12: Overlapped BPSK symbols distribution for $N_R = 8$, $N_f = 64$

The BER then writes:

$$\mathrm{BER}_{\mathrm{SS-OFDM}} = \sum_{l=1}^{L} p_l \, \frac{1}{2} erfc(r_l \sqrt{\frac{E_b}{N_0}}). \tag{4.15}$$

4.3 BER analysis for two-user MIMO PFBO system in Rayleigh channel

4.3.1 Signals equations

For two-user MIMO PFBO systems, with Rayleigh channel described in 1.4.3.2 (1.29), the signal received by $user1$ on subcarrier p writes:

$$\begin{cases} Y_p^{(1)} = \sum_{m=1}^{M} H_{p,m}^{(1)} V_{p,m}^{(1)} \sum_{i=1}^{N_c=N_f} c_{p,i} a_i^{(1)} + N_p, & \forall k \in \{1, \cdots, N_f - N_R\} \\ Y_p^{(1)} = \sum_{m=1}^{M} H_{p,m}^{(1)} V_{p,m}^{(1)} \sum_{i=1}^{N_c=N_f} c_{p,i} a_i^{(1)} + \sum_{m=1}^{M} H_{p,m}^{(1)} V_{p',m}^{(2)} \sum_{i=1}^{N_c=N_f} c_{p',i} a_i^{(2)} + N_p, & \text{otherwise} \end{cases} \tag{4.16}$$

In common SISO MC-CDMA systems, MMSE receivers outperforms ZF receivers [114, 115, 104]. For PFBO MIMO SS-OFDM systems, the simulation results of system performance are

presented in Fig. 4.13 for $M = 4$ and in Fig. 4.14 for $M = 8$. In Fig. 4.13, we observe that the performance gap between the MMSE and ZF receivers, in the beginning increases with N_R (as shown for $N_R = 4, 8, 16$) then decreases to null (as shown for $N_R = 16, 32, 48$). This because that, the MMSE receiver minimizes the average symbol error, thus less error is bring to the despreading step and the SS codes help to mitigate the interference. However, when N_R becomes too large, most code chips are erroneous, the SS codes can no more mitigate the interference. In this case, the performances of MMSE and ZF receivers tend to be the same. Similar performance is shown in Fig. 4.14 for $M = 8$ antennas. With the increase of antenna number, the interference reduces and the performance gap becomes less visible.

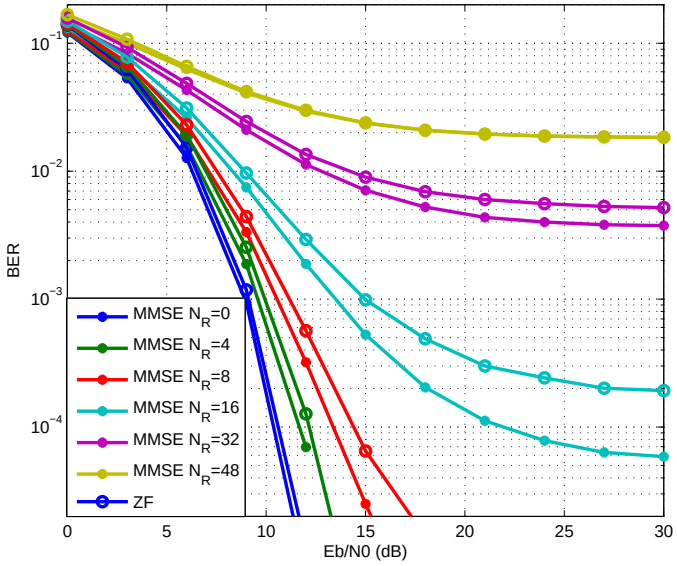

Figure 4.13: SS-OFDM system with MMSE and ZF receiver, $M = 4$, QPSK

To keep the generality of our analysis, we use the MMSE receiver for the following BER derivation.

4.3.2 MMSE reception

Since the subbands with overlapping and without overlapping do not have same level of interference, the MMSE equalizer is different in these subbands. For the subbands without overlapping, the MMSE equalizer writes:

$$G_p = \frac{\sum_{m=1}^{M} H_{p,m}^{(1)*} V_{p,m}^{(1)*}}{\left|\sum_{m=1}^{M} H_{p,m}^{(1)} V_{p,m}^{(1)}\right|^2 + N0}, \quad \forall p \in \{1, \cdots, N_f - N_R\} \tag{4.17}$$

For the subbands with overlapping, the MMSE equalizer writes:

$$G_{p,R} = \frac{\sum_{m=1}^{M} H_{p,m}^{(1)*} V_{p,m}^{(1)*}}{\left|\sum_{m=1}^{M} H_{p,m}^{(1)} V_{p,m}^{(1)}\right|^2 + \left|\sum_{m=1}^{M} H_{p,m}^{(1)} V_{p,m}^{(1)}\right|^2 + N0}, \ \forall p \in \{N_f - N_R + 1, \cdots, N_f\} \tag{4.18}$$

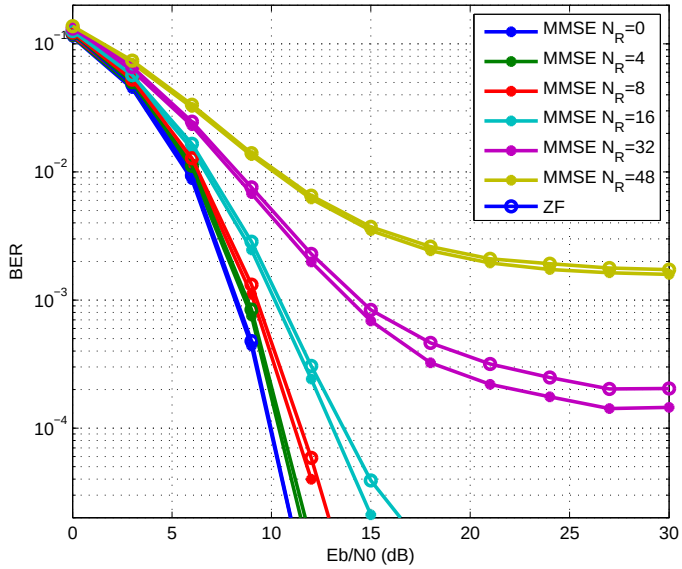

Figure 4.14: SS-OFDM system with MMSE and ZF receiver, $M = 8$, QPSK

We use in the following analysis EGT precoding technique. Hence the received signal writes:

$$\begin{cases} Y^{(1)}_{p,EGT} = \dfrac{1}{\sqrt{M}} \displaystyle\sum_{m=1}^{M} \left| H^{(1)}_{p,m} \right| \sum_{i=1}^{N_c=N_f} c_{p,i}\, a^{(1)}_i + N_p, \ \forall k \in \{1, \cdots, N_f - N_R\} \\ Y^{(1)}_{p,EGT} = \dfrac{1}{\sqrt{M}} \displaystyle\sum_{m=1}^{M} \left| H^{(1)}_{p,m} \right| \sum_{i=1}^{N_c=N_f} c_{p,i}\, a^{(1)}_i + \dfrac{1}{\sqrt{M}} \sum_{m=1}^{M} H^{(1)}_{p,m} \Phi^{(2)}_{p',m} \sum_{i=1}^{N_c=N_f} c_{p',i}\, a^{(2)}_i + N_p, \text{ otherwise} \end{cases} \tag{4.19}$$

The EGT MMSE equalizers write:

$$G_p = \frac{\frac{1}{\sqrt{M}} \sum_{m=1}^{M} \left| H^{(1)}_{p,m} \right|}{\frac{1}{M} \left(\sum_{m=1}^{M} \left| H^{(1)}_{p,m} \right| \right)^2 + N0}, \quad \forall p \in \{1, \cdots, N_f - N_R\} \tag{4.20}$$

$$\begin{aligned} G_{p,R} &= \frac{\frac{1}{\sqrt{M}} \sum_{m=1}^{M} \left| H^{(1)}_{p,m} \right|}{\frac{1}{M} \left(\sum_{m=1}^{M} \left| H^{(1)}_{p,m} \right| \right)^2 + \frac{1}{M} \sum_{m=1}^{M} \left| H^{(1)}_{p,m} \Phi^{(2)*}_{p,m} \right|^2 + N0} \\ &= \frac{\frac{1}{\sqrt{M}} \sum_{m=1}^{M} \left| H^{(1)}_{p,m} \right|}{\frac{1}{M} \left(\sum_{m=1}^{M} \left| H^{(1)}_{p,m} \right| \right)^2 + \frac{1}{M} \sum_{m=1}^{M} \left| H^{(1)}_{p,m} \right|^2 + \frac{1}{M} \sum_{m=1}^{M} \sum_{m' \neq m}^{M} H^{(1)}_{p,m} \Phi^{(2)*}_{p,m} H^{(1)*}_{p,m'} \Phi^{(2)}_{p,m} + N0} \\ &\approx \frac{\frac{1}{\sqrt{M}} \sum_{m=1}^{M} \left| H^{(1)}_{p,m} \right|}{\frac{1}{M} \left(\sum_{m=1}^{M} \left| H^{(1)}_{p,m} \right| \right)^2 + \frac{1}{M} \sum_{m=1}^{M} \left| H^{(1)}_{p,m} \right|^2 + N0}, \quad \forall p \in \{N_f - N_R + 1, \cdots, N_f\} \end{aligned} \tag{4.21}$$

Hence the ith received symbol after equalization and despreading writes:

$$\begin{aligned} r_i^{(1)} &= \sum_{p=1}^{N_f} c_{p,i} G_p^{(1)} Y_p^{(1)} \\ &= Z_i a_i^{(1)} + I_i + J_{i,N_R} + \hat{N}_i \end{aligned} \tag{4.22}$$

With

$$\begin{aligned} Z_i &= \sum_{p=1}^{N_f} \frac{G_p^{(1)}}{\sqrt{M}} \sum_{m=1}^{M} \left| H_{p,m}^{(1)} \right| \left| c_{p,i} \right|^2 \\ &= \sum_{p=1}^{N_f - N_R} \frac{\frac{1}{M}\left(\sum_{m=1}^{M} \left| H_{p,m}^{(1)} \right|\right)^2}{\frac{1}{M}\left(\sum_{m=1}^{M} \left| H_{p,m}^{(1)} \right|\right)^2 + N_0} \left| c_{p,i} \right|^2 \\ &\quad + \sum_{p'=N_f-N_R+1}^{N_f} \frac{\frac{1}{M}\left(\sum_{m=1}^{M} \left| H_{p',m}^{(1)} \right|\right)^2}{\frac{1}{M}\left(\sum_{m=1}^{M} \left| H_{p',m}^{(1)} \right|\right)^2 + \frac{1}{M}\sum_{m=1}^{M} \left| H_{p,m}^{(1)} \right|^2 + N_0} \left| c_{p',i} \right|^2 \\ &= 1 - \sum_{p=1}^{N_f - N_R} \frac{N_0}{\frac{1}{M}\left(\sum_{m=1}^{M} \left| H_{p,m}^{(1)} \right|\right)^2 + N_0} \left| c_{p,i} \right|^2 \\ &\quad - \sum_{p'=N_f-N_R+1}^{N_f} \frac{\frac{1}{M}\sum_{m=1}^{M} \left| H_{p',m}^{(1)} \right|^2 + N_0}{\frac{1}{M}\left(\sum_{m=1}^{M} \left| H_{p',m}^{(1)} \right|\right)^2 + \frac{1}{M}\sum_{m=1}^{M} \left| H_{p',m}^{(1)} \right|^2 + N_0} \left| c_{p',i} \right|^2 \end{aligned} \tag{4.23}$$

As the equivalent channel after equalization in not flat, the orthogonality within the WH codes is degraded, i.e. $Z_i \neq 1$.

The ICI term writes:

$$\begin{aligned} I_i = \sum_{j \neq i} \Bigg(& \sum_{p=1}^{N_f - N_R} c_{p,i} c_{p,j} \frac{\frac{1}{M}\left(\sum_{m=1}^{M} \left| H_{p,m}^{(1)} \right|\right)^2}{\frac{1}{M}\left(\sum_{m=1}^{M} \left| H_{p,m}^{(1)} \right|\right)^2 + N_0} \\ & + \sum_{p'=N_f-N_R+1}^{N_f} c_{p',i} c_{p',j} \frac{\frac{1}{M}\left(\sum_{m=1}^{M} \left| H_{p',m}^{(1)} \right|\right)^2}{\frac{1}{M}\left(\sum_{m=1}^{M} \left| H_{p',m}^{(1)} \right|\right)^2 + \frac{1}{M}\sum_{m=1}^{M} \left| H_{p',m}^{(1)} \right|^2 + N_0} \Bigg) a_j^{(1)} \end{aligned} \tag{4.24}$$

And the inter-channel interference term writes:

$$J_{i,N_R} = \sum_{j=1}^{N_f} \sum_{p'=1}^{N_R} c_{N_f-N_R+p',i} c_{p',j} \frac{\frac{1}{M}\sum_{m=1}^{M} H_{N_f-N_R+p',m}^{(1)} \Phi_{p',m}^{(2)*} \sum_{m=1}^{M} \left| H_{N_f-N_R+p',m}^{(1)} \right|}{\frac{1}{M}\left(\sum_{m=1}^{M} \left| H_{N_f-N_R+p',m}^{(1)} \right|\right)^2 + \frac{1}{M}\sum_{m=1}^{M} \left| H_{N_f-N_R+p',m}^{(1)} \right|^2 + N_0} a_j^{(2)} \tag{4.25}$$

The noise term writes:

$$\hat{N}_i = \left(\sum_{p=1}^{N_f - N_R} c_{p,i} \frac{\frac{1}{\sqrt{M}} \sum_{m=1}^{M} \left| H_{p,m}^{(1)} \right|}{\frac{1}{M} \left(\sum_{m=1}^{M} \left| H_{p,m}^{(1)} \right| \right)^2 + N0} + \sum_{p'=N_f - N_R + 1}^{N_f} c_{p',i} \frac{\frac{1}{\sqrt{M}} \sum_{m=1}^{M} \left| H_{p',m}^{(1)} \right|}{\frac{1}{M} \left(\sum_{m=1}^{M} \left| H_{p',m}^{(1)} \right| \right)^2 + \frac{1}{M} \sum_{m=1}^{M} \left| H_{p',m}^{(1)} \right|^2 + N_0} \right) N_p^{(1)} \tag{4.26}$$

4.3.3 BER derivation

Thanks to the spreading code, each signal component results from an averaging over all the subcarriers. In this way, the colored narrow band interference is transformed into a white noise over the whole bandwidth. To study the system BER, it is then sufficient to find the expected value of each signal component, such as:

$$BER = \frac{1}{2} \operatorname{erfc} \left(\frac{\mathbb{E}[Z_i] \sqrt{Eb}}{\sqrt{\mathbb{E}\left[|I_i|^2\right] + \mathbb{E}\left[\left|J_{i,N_R}\right|^2\right] + \mathbb{E}\left[\left|\hat{N}_i\right|^2\right]}} \right) \tag{4.27}$$

This BER expression is validated through simulations in 4.4.2. Hence we study in the following the expected value of each term.

4.3.3.1 Channel diversity

First, let us compute the term $\mathbb{E}[Z_i]$. This will reveal the channel diversity experienced by the symbol. Without loss of generality, as the OFDM subcarriers independently fade with each other, we omit the subcarrier index p, the CFR $H_{p,m}^{(1)}$ is noted as ξ_m which follows independent Gaussian distribution.

Hence,

$$\mathbb{E}[Z_i] = 1 - \frac{N_f - N_R}{N_f} \mathbb{E}\left[\frac{N_0}{\frac{1}{M} \left(\sum_{m=1}^{M} |\xi_m| \right)^2 + N_0} \right] - \frac{N_R}{N_f} \mathbb{E}\left[\frac{\frac{1}{M} \sum_{m=1}^{M} |\xi_m|^2 + N_0}{\frac{1}{M} \left(\sum_{m=1}^{M} |\xi_m| \right)^2 + \frac{1}{M} \sum_{m=1}^{M} |\xi_m|^2 + N_0} \right] \tag{4.28}$$

The expected value of $\mathbb{E}\left[\frac{1}{x+N_0}\right]$ with $x \sim \Gamma(k,\theta)$, noted as $\alpha(x)$, is derived in Appendix-B, from which we then have:

$$\alpha(x) = \mathbb{E}\left[\frac{1}{x+N_0}\right] = \frac{e^{\frac{N_0}{\theta}} (-N_0)^{k-1} \left(-Ei\left(-\frac{N_0}{\theta}\right) \right)}{\theta^k \Gamma(k)} + \frac{e^{\frac{N_0}{\theta}}}{\Gamma(k)} \sum_{n=0}^{k-2} \binom{k-1}{n} (-N_0)^n \frac{\Gamma(k-1-n, \frac{N_0}{\theta})}{\theta^{n+1}} \tag{4.29}$$

with $x \sim \Gamma(k,\theta)$.

The expected value of $\mathbb{E}\left[\frac{\frac{1}{M}\sum_{m=1}^{M}|\xi_m|^2+N_0}{\frac{1}{M}\left(\sum_{m=1}^{M}|\xi_m|\right)^2+\frac{1}{M}\sum_{m=1}^{M}|\xi_m|^2+N_0}\right]$ is quite difficult to compute. However, through simulation results shown in Fig. 4.15, at high SNR regime or for $M \geq 10$, we have:

$$\mathbb{E}\left[\frac{\frac{1}{M}\sum_{m=1}^{M}|\xi_m|^2+N_0}{\frac{1}{M}\left(\sum_{m=1}^{M}|\xi_m|\right)^2+\frac{1}{M}\sum_{m=1}^{M}|\xi_m|^2+N_0}\right] \approx \frac{\mathbb{E}\left[\frac{1}{M}\sum_{m=1}^{M}|\xi_m|^2+N_0\right]}{\mathbb{E}\left[\frac{1}{M}\left(\sum_{m=1}^{M}|\xi_m|\right)^2\right]+\mathbb{E}\left[\frac{1}{M}\sum_{m=1}^{M}|\xi_m|^2\right]+N_0} = \frac{\frac{1}{\frac{\pi}{4}M+1-\frac{\pi}{4}}+N_0}{1+\frac{1}{\frac{\pi}{4}M+1-\frac{\pi}{4}}+N_0} \tag{4.30}$$

We observe in Fig. 4.15 that for high SNR level ($\frac{Eb}{N_0} \geq 9dB$) or large number of transmit antenna $M \geq 10$, the approximations well fit the simulation results of $\mathbb{E}\left[\frac{\frac{1}{M}\sum_{m=1}^{M}|\xi_m|^2+N_0}{\frac{1}{M}\left(\sum_{m=1}^{M}|\xi_m|\right)^2+\frac{1}{M}\sum_{m=1}^{M}|\xi_m|^2+N_0}\right]$.

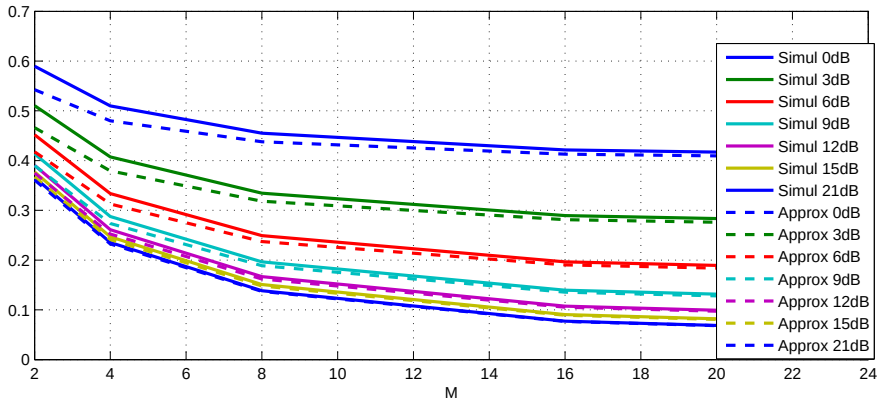

Figure 4.15: Channel diversity coefficient and approximation for different $\frac{Eb}{N_0}$ values

Hence, as a conclusion, for systems of $\frac{Eb}{N_0} \geq 9dB$ or $M \geq 10$:

$$\mathbb{E}[Z_i] = 1 - \frac{N_f - N_R}{N_f}\alpha(x) - \frac{N_R}{N_f}\frac{\frac{1}{\frac{\pi}{4}M+1-\frac{\pi}{4}}+N_0}{1+\frac{1}{\frac{\pi}{4}M+1-\frac{\pi}{4}}+N_0} \tag{4.31}$$

4.3.3.2 ICI term

This interference widely depends on the overlap ratio. It approaches to the Gaussian distribution except with some particular N_R. We display in Fig. 4.16 the kurtosis of ICI terms. We observe that most kurtosis values are closed to 3 except when $N_R = 32$. Hence, we assume that the ICI term is Gaussian distributed. Moreover, $\mathbb{E}[I_i] = 0$. As the $\mathbb{E}\left[|I_i|^2\right]$ is difficult to compute, we compute in the following $\mathbb{E}[|I_i|]$. Then with the Gaussian assumption, $\mathbb{E}\left[|I_i|^2\right] = \frac{\pi}{2}\mathbb{E}[|I_i|]^2$.

The expected values of ICI term $\mathbb{E}[|I_i|]$ are displayed in Fig. 4.17 for $M = 4$ and Fig. 4.18 for $M = 16$.

It is observed that except the cases where the SNR is too small ($\frac{Eb}{N0} \leq 9dB$), the expected value of ICI presents a parabolic form. This actually means that with a half part of codes that are overlapped, the orthogonality among the codes is degraded at most.

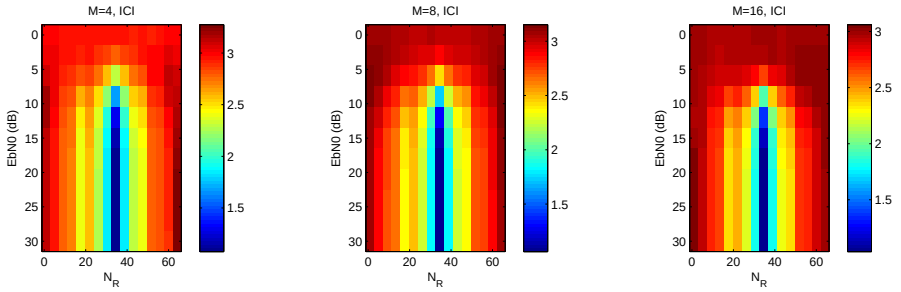

Figure 4.16: Kurtosis, ICI

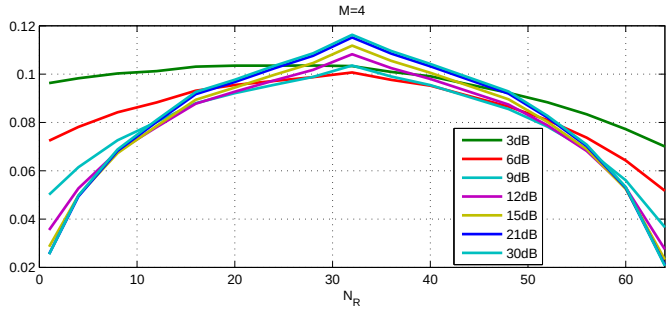

Figure 4.17: Expected value of ICI in absolute value, $M = 4$, $N_f = L_c = 64$

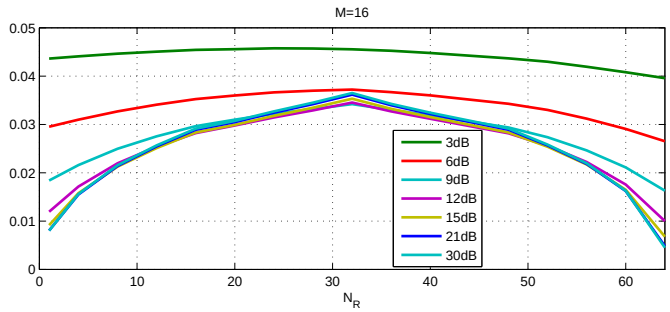

Figure 4.18: Expected value of ICI in absolute value, $M = 16$, $N_f = L_c = 64$

In fact, due to the orthogonality among the codes, we have:

$$\sum_{j \neq i} \left(\sum_{p=1}^{N-N_R} c_{p,i} c_{p,j} + \sum_{p'=N-N_R+1}^{N} c_{p',i} c_{p',j} \right) a_j^{(1)} = 0 \tag{4.32}$$

However, with an equalization different in each subcarrier, the orthogonality is destroyed.

With the expression of I_i in eq. 4.24, we have:

$$\begin{aligned}\mathbb{E}\left[|I_i|\right] &= \mathbb{E}\left[\left|\sum_{j\neq i}\left(\sum_{p=1}^{N_f-N_R} c_{p,i}c_{p,j}\frac{\frac{1}{M}\left(\sum_{m=1}^{M}|\xi_m|\right)^2}{\frac{1}{M}\left(\sum_{m=1}^{M}|\xi_m|\right)^2+N_0}\right.\right.\\ &\quad\left.\left.+\sum_{p'=N_f-N_R+1}^{N_f} c_{p',i}c_{p',j}\frac{\frac{1}{M}\left(\sum_{m=1}^{M}|\xi_m|\right)^2}{\frac{1}{M}\left(\sum_{m=1}^{M}|\xi_m|\right)^2+\frac{1}{M}\sum_{m=1}^{M}|\xi_m|^2+N_0}\right)a_j^{(1)}\right|\right]\\ &= \mathbb{E}\left[\left|\sum_{p=1}^{N_f-N_R}\sum_{j\neq i} c_{p,i}c_{p,j}a_j^{(1)}\frac{\frac{1}{M}\left(\sum_{m=1}^{M}|\xi_m|\right)^2}{\frac{1}{M}\left(\sum_{m=1}^{M}|\xi_m|\right)^2+N_0}\right.\right.\\ &\quad\left.\left.+\sum_{p'=N_f-N_R+1}^{N_f}\sum_{j\neq i} c_{p',i}c_{p',j}a_j^{(1)}\frac{\frac{1}{M}\left(\sum_{m=1}^{M}|\xi_m|\right)^2}{\frac{1}{M}\left(\sum_{m=1}^{M}|\xi_m|\right)^2+\frac{1}{M}\sum_{m=1}^{M}|\xi_m|^2+N_0}\right|\right]\end{aligned} \tag{4.33}$$

With (4.32), we can deduce that:

$$\sum_{p=1}^{N_f-N_R}\sum_{j\neq i} c_{p,i}c_{p,j}a_j^{(1)} = -\sum_{p'=N_f-N_R+1}^{N_f}\sum_{j\neq i} c_{p',i}c_{p',j}a_j^{(1)} = \Lambda \tag{4.34}$$

Hence,

$$\mathbb{E}\left[|I_i|\right] \approx \pm\mathbb{E}\left[|\Lambda|\right]\mathbb{E}\left[\left|\frac{\frac{1}{M}\left(\sum_{m=1}^{M}|\xi_m|\right)^2}{\frac{1}{M}\left(\sum_{m=1}^{M}|\xi_m|\right)^2+N_0}\right|\right] \mp \mathbb{E}\left[|\Lambda|\right]\mathbb{E}\left[\left|\frac{\frac{1}{M}\left(\sum_{m=1}^{M}|\xi_m|\right)^2}{\frac{1}{M}\left(\sum_{m=1}^{M}|\xi_m|\right)^2+\frac{1}{M}\sum_{m=1}^{M}|\xi_m|^2+N_0}\right|\right] \tag{4.35}$$

Noting $\kappa(N_R) = \mathbb{E}\left[|\Lambda|\right]$, then we have:

$$\mathbb{E}\left[|I_i(N_R)|\right] = \kappa(N_R) * \left(\mathbb{E}\left[\left|\frac{\frac{1}{M}\left(\sum_{m=1}^{M}|\xi_m|\right)^2}{\frac{1}{M}\left(\sum_{m=1}^{M}|\xi_m|\right)^2+N_0}\right|\right] - \mathbb{E}\left[\left|\frac{\frac{1}{M}\left(\sum_{m=1}^{M}|\xi_m|\right)^2}{\frac{1}{M}\left(\sum_{m=1}^{M}|\xi_m|\right)^2+\frac{1}{M}\sum_{m=1}^{M}|\xi_m|^2+N_0}\right|\right]\right) \tag{4.36}$$

At high SNR regime, using the approximation of (4.30), we have:

$$\mathbb{E}\left[\left|\frac{\frac{1}{M}\left(\sum_{m=1}^{M}|\xi_m|\right)^2}{\frac{1}{M}\left(\sum_{m=1}^{M}|\xi_m|\right)^2+N_0}\right|\right] \approx \frac{1}{1+N_0} \tag{4.37}$$

and

$$\mathbb{E}\left[\left|\frac{\frac{1}{M}\left(\sum_{m=1}^{M}|\xi_m|\right)^2}{\frac{1}{M}\left(\sum_{m=1}^{M}|\xi_m|\right)^2+\frac{1}{M}\sum_{m=1}^{M}|\xi_m|^2+N_0}\right|\right] \approx \frac{1}{1+\frac{1}{\frac{\pi}{4}M+1-\frac{\pi}{4}}+N_0} \tag{4.38}$$

$\kappa(N_R)$ is displayed in Fig. 4.19, from which we find the same parabolic form as in Fig. 4.17 and Fig. 4.18.

$\mathbb{E}\left[\left|\frac{\frac{1}{M}\left(\sum_{m=1}^{M}|\xi_m|\right)^2}{\frac{1}{M}\left(\sum_{m=1}^{M}|\xi_m|\right)^2+N_0}\right|\right] - \mathbb{E}\left[\left|\frac{\frac{1}{M}\left(\sum_{m=1}^{M}|\xi_m|\right)^2}{\frac{1}{M}\left(\sum_{m=1}^{M}|\xi_m|\right)^2+\frac{1}{M}\sum_{m=1}^{M}|\xi_m|^2+N_0}\right|\right]$ and the approximation $\frac{1}{1+N_0} - \frac{1}{1+\frac{1}{\frac{\pi}{4}M+1-\frac{\pi}{4}}+N_0}$ with $\frac{Eb}{N_0} = 20dB$ are displayed in Fig. 4.20. We observe that the approximation values well fit the simulation results. Moreover, the curves decrease with the number of antennas M, this is reasonable because the term $\frac{1}{\frac{\pi}{4}M+1-\frac{\pi}{4}}$ reduces when M increases.

Hence, for $\frac{Eb}{N0} \geq 9dB$, $\mathbb{E}\left[|I_i(N_R)|\right] = \kappa(N_R)\left(\frac{1}{1+N_0} - \frac{1}{1+\frac{1}{\frac{\pi}{4}M+1-\frac{\pi}{4}}+N_0}\right)$. Accordingly, $\mathbb{E}\left[|I_i(N_R)|^2\right] = \frac{\pi}{2}\kappa(N_R)^2\left(\frac{1}{1+N_0} - \frac{1}{1+\frac{1}{\frac{\pi}{4}M+1-\frac{\pi}{4}}+N_0}\right)^2$.

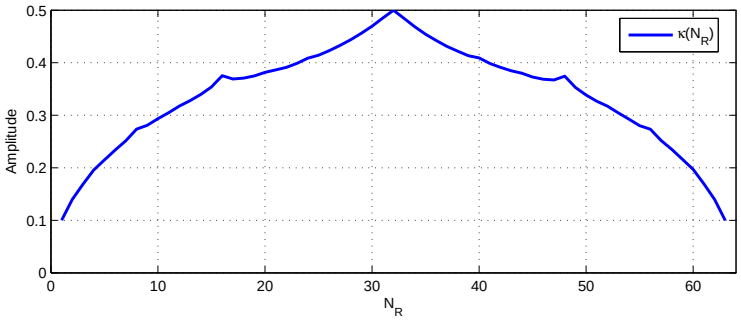

Figure 4.19: $\kappa(N_R)$

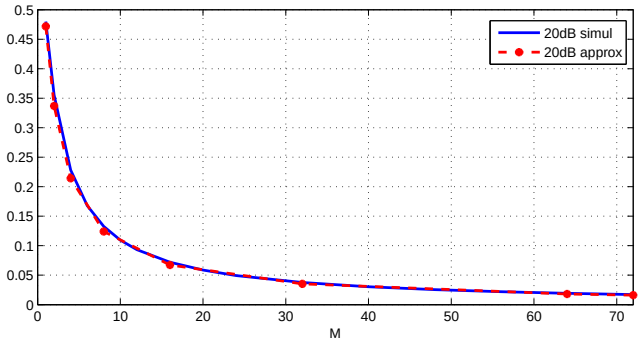

Figure 4.20: $\mathbb{E}\left[\left|\frac{\frac{1}{M}\left(\sum_{m=1}^{M}|\xi_m|\right)^2}{\frac{1}{M}\left(\sum_{m=1}^{M}|\xi_m|\right)^2+N_0}\right|\right]-\mathbb{E}\left[\left|\frac{\frac{1}{M}\left(\sum_{m=1}^{M}|\xi_m|\right)^2}{\frac{1}{M}\left(\sum_{m=1}^{M}|\xi_m|\right)^2+\frac{1}{M}\sum_{m=1}^{M}|\xi_m|^2+N_0}\right|\right]$ and the approximation

4.3.3.3 Inter-channel Interference

The inter-channel interference can be considered as a Gaussian process with zero mean and variance linearly dependent on N_R as shown in Fig. 4.21.

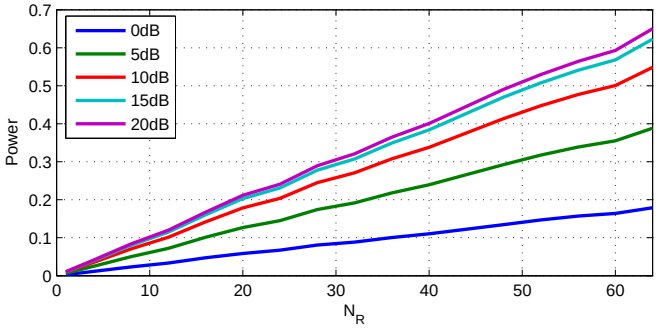

Figure 4.21: Power of inter-channel interference, $M = 4$

The power of the inter-channel interference term is computed as:

$$\begin{aligned}\mathbb{E}\left[\left|J_{i,N_R}\right|^2\right] &= \mathbb{E}\left[\left|\sum_{j=1}^{N_f}\sum_{p'=1}^{N_R} c_{N_f-N_R+p',i}c_{p',j}\ \frac{\frac{1}{M}\sum_{m=1}^{M}\xi_m\Phi_m^{(2)*}\ \sum_{m=1}^{M}|\xi_m|}{\frac{1}{M}\left(\sum_{m=1}^{M}|\xi_m|\right)^2+\frac{1}{M}\sum_{m=1}^{M}|\xi_m|^2+N_0}a_j^{(2)}\right|^2\right] \\ &= \frac{N_R}{N_f}\mathbb{E}\left[\frac{\frac{1}{M}\left(\sum_{m=1}^{M}|\xi_m|^2\right)\ \frac{1}{M}\left(\sum_{m=1}^{M}|\xi_m|\right)^2}{\left(\frac{1}{M}\left(\sum_{m=1}^{M}|\xi_m|\right)^2+\frac{1}{M}\sum_{m=1}^{M}|\xi_m|^2+N_0\right)^2}\right] \\ &\approx \frac{N_R}{N_f}\frac{\frac{1}{\frac{\pi}{4}M+1-\frac{\pi}{4}}}{\left(1+\frac{1}{\frac{\pi}{4}M+1-\frac{\pi}{4}}+N_0\right)^2}\end{aligned} \tag{4.39}$$

The simulation results of $\mathbb{E}\left[\left|J_{i,N_R}\right|^2\right]$ and the approximations are displayed in Fig. 4.22 with $N_R = 1$, $N_f = 64$:

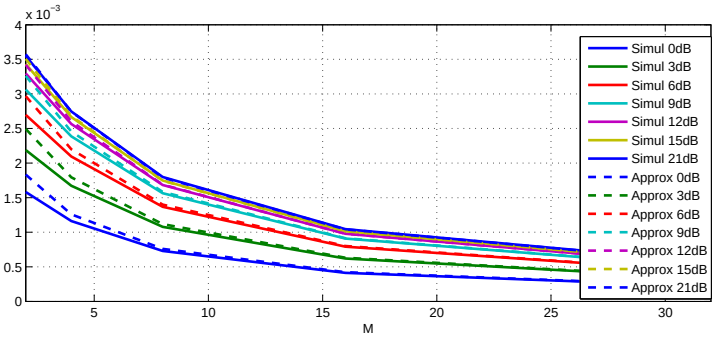

Figure 4.22: Simulations results and approximations of $\mathbb{E}\left[\left|J_{i,N_R}\right|^2\right]$ with $N_R = 1$, $N_f = 64$

We observe that the approximation well fit the simulation results as soon as $M \geq 8$ for whole SNR regime. Hence the approximation is validated.

4.3.3.4 Noise term

The power of the received noise after equalization and despreading writes:

$$\begin{aligned}
\mathbb{E}\left[\left|\hat{N}_i\right|^2\right] &= \mathbb{E}\left[\left|\left(\sum_{p=1}^{N_f-N_R} c_{p,i}\frac{\frac{1}{\sqrt{M}}\sum_{m=1}^{M}|\xi_m|}{\frac{1}{M}\left(\sum_{m=1}^{M}|\xi_m|\right)^2+N0}\right.\right.\right. \\
&\quad \left.\left.\left. + \sum_{p'=N_f-N_R+1}^{N_f} c_{p',i}\frac{\frac{1}{\sqrt{M}}\sum_{m=1}^{M}|\xi_m|}{\frac{1}{M}\left(\sum_{m=1}^{M}|\xi_m|\right)^2+\frac{1}{M}\sum_{m=1}^{M}|\xi_m|^2+N0}\right) N_p^{(1)}\right|^2\right] \\
&= \frac{N_f-N_R}{N_f}\mathbb{E}\left[\frac{\frac{1}{M}\left(\sum_{m=1}^{M}|\xi_m|\right)^2}{\left(\frac{1}{M}\left(\sum_{m=1}^{M}|\xi_m|\right)^2+N0\right)^2}\right]N_0 \\
&\quad + \frac{N_R}{N_f}\mathbb{E}\left[\frac{\frac{1}{M}\left(\sum_{m=1}^{M}|\xi_m|\right)^2}{\left(\frac{1}{M}\left(\sum_{m=1}^{M}|\xi_m|\right)^2+\frac{1}{M}\sum_{m=1}^{M}|\xi_m|^2+N0\right)^2}\right]N_0 \\
&\approx \frac{N_f-N_R}{N_f}\frac{N_0}{(1+N_0)^2}+\frac{N_R}{N_f}\frac{N_0}{\left(1+\frac{1}{\frac{\pi}{4}M+1-\frac{\pi}{4}}+N_0\right)^2}
\end{aligned} \tag{4.40}$$

As a conclusion, we find that for $\frac{Eb}{N0} \geq 9dB$ or with in general $M \geq 10$, simple approximation can be obtained for each signal component. From which we can deduce the BER approximation. However, with small number of antennas ($M < 10$), more precise analysis on statistic is required.

4.4 Simulation results

4.4.1 SS-OFDM systems over SISO AWGN channels

As a first step, the BER expressions derived in the previous sections for the PFBO SS-OFDM system are confronted to simulation results. Monte-Carlo simulations are run on AWGN channels using an SS-OFDM system of size $L_C = N = 64$ subcarriers and mapped with QPSK constellation. The subcarrier overlapping is performed with $N_R = 1$ and $N_R = 7$. Simulation results are given in Fig. 4.23, where solid lines represent the simulation results and markers correspond to theoretical performance given by Eq. (4.13). The performance of PFBO-OFDM system is also presented as a reference. From a system comparison point of view, it can be concluded that, as expected, the SS-OFDM system better resists to the bandwidth overlap process than the classical OFDM system, due to its natural robustness against narrow-band interferers.

We find that the simulation results satisfactory fit the BER theoretical values. In particular, the error floor that was expected from the analytical equations are easily observed. The small gap between the simulation results and the theoretical estimation for the SS-OFDM system with $N_R = 7$ comes from the error of the PDF approximation (c.f. Fig. 4.10). With longer spreading sequence, for instance, $L_C = N = 512$, the normal distribution approximation becomes more reliable as shown in Fig. 4.24.

Finally, the BER expression for the case where the inter-channel interference is following a discrete distribution, i.e. Eq. (4.15), is also verified for $N_R = 8$ and $N_f = 64$ in Fig. 4.25:

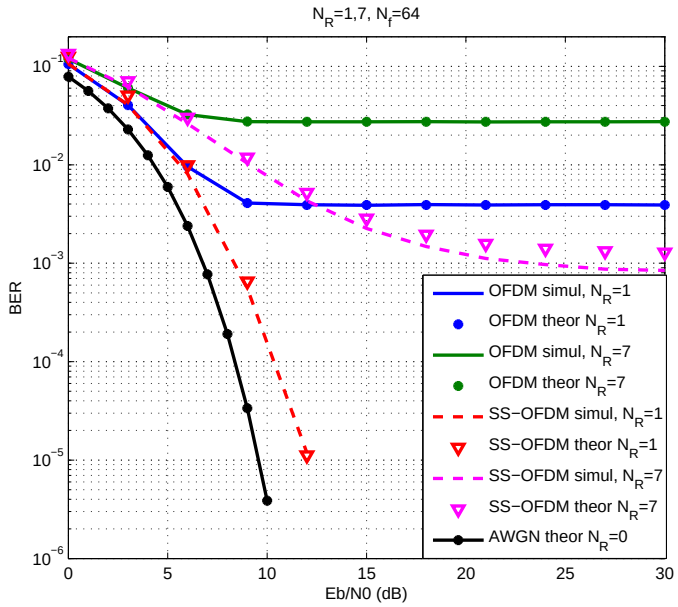

Figure 4.23: Performance comparison of OFDM and SS-OFDM systems with $N_f = 64$ and partial bandwidth overlay of $N_R = 1,7$ and over AWGN channels

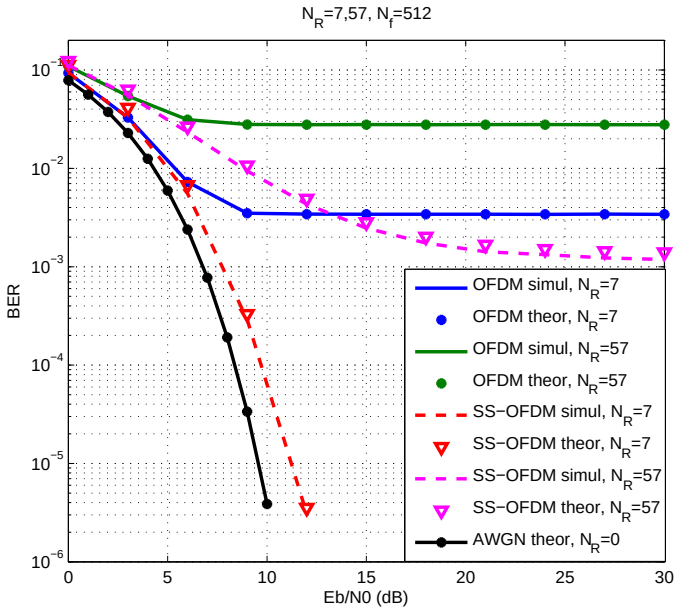

Figure 4.24: Performance comparison of OFDM and SS-OFDM systems with $N_f = 512$ and partial bandwidth overlay of $N_R = 7,57$ and over AWGN channels

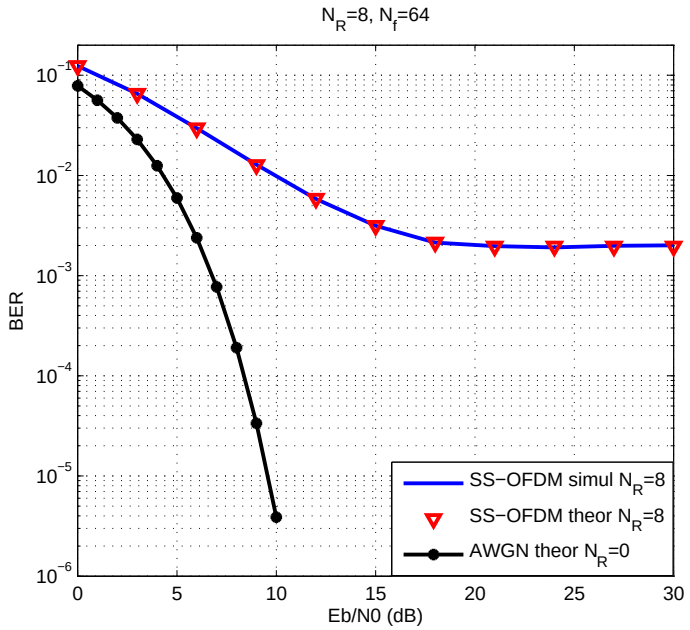

Figure 4.25: Performance of SS-OFDM system with partial bandwidth overlay of $N_R = 8$ and over AWGN channels

4.4.2 SS-OFDM systems over MU-MIMO Rayleigh channels

We now extend the study to the case of MU-MIMO systems adopting the EGT precoding technique. The BER approximation of (4.27) is verified with simulations in Fig. 4.26 for $M = 4$ and in Fig. 4.26 for $M = 8$. The BER approximation well fits the simulation results, which validates the Gaussian assumption of the signal components and thereby, proves that the SS technique can "whiten" the narrow band interference. For a system comparison point of view, we present also the simulation results of partial band jamming (PBJ) system [82, 83] where the inter-channel interference is considered as an independent narrow band Gaussian noise. We observe that the performance of PFBO and PBJ systems get close when the antenna number increases. As soon as $M \geq 12$ are used, both systems provide the same performance which means that the inter-channel interference becomes equivalent to the PBJ approach. This can be understood because the correlation between the inter-channel interference and the useful signal becomes negligible. However, for a smaller number of antennas, e.g. M=4, our approach outperforms the PBJ model.

4.4.3 OFDM and SS-OFDM performance comparison

In this part, we use the BRAN-A channel to show that the performance analysis is available for more realistic channels. The simulations are first performed with $M = 1$ as indicated in Fig. 4.28 and with an incremental bandwidth overlap factor $N_R \in \{1, 2, 4, 8\}$. It can first be concluded that, as in the AWGN case, SS-OFDM exhibits higher robustness than OFDM to the overlap process, as evident from the error floor levels. This is once again interpreted as being due to the high frequency diversity exploitation obtained from the WH spreading process.

When we increase the number of antennas, as shown in Fig. 4.29 for $M = 4$ and Fig. 4.29 for $M = 10$, the SS-OFDM curves approach the AWGN reference curve. This tends to prove

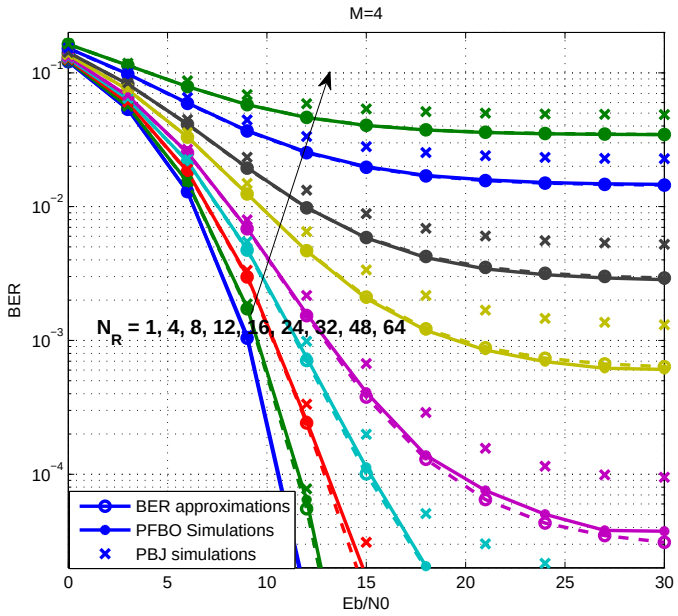

Figure 4.26: Performance of SS-OFDM with antenna number $M = 4$ and $N_f = 64$, QPSK constellation

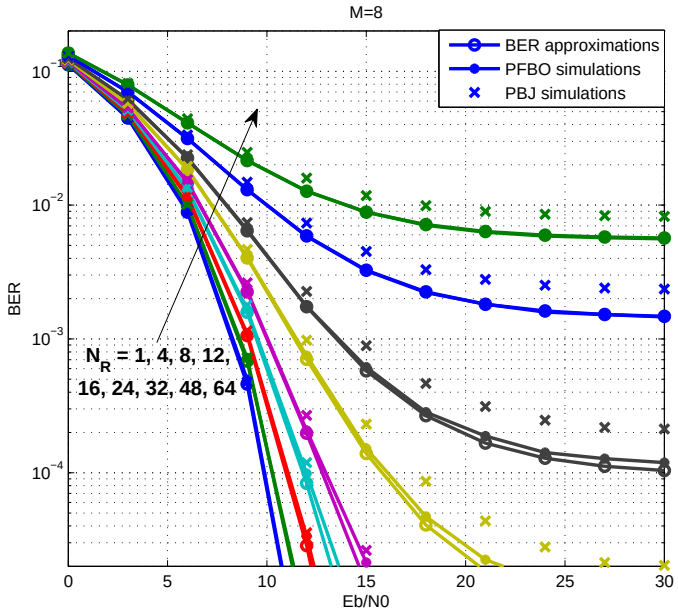

Figure 4.27: Performance of SS-OFDM with antenna number $M = 8$ and $N_f = 64$, QPSK constellation

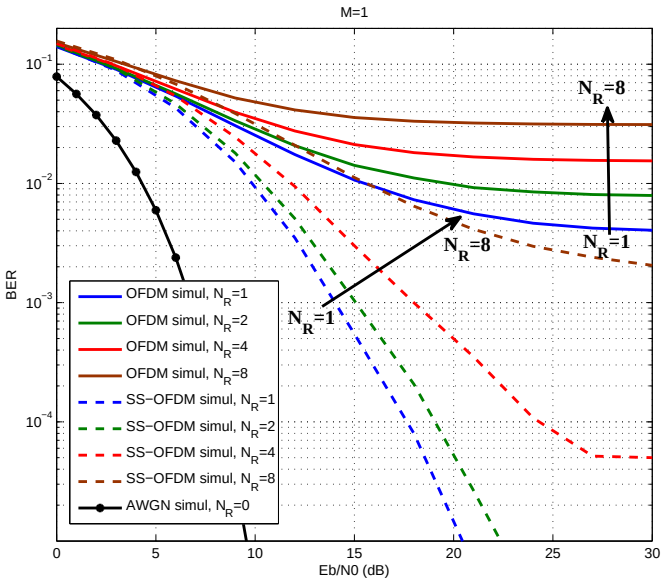

Figure 4.28: Performance of OFDM and SS-OFDM EGT-SISO transmission with PFBO

that the MISO equivalent channel becomes flat and Gaussian, even with $M = 4$ antennas. The global trend then, is that the OFDM curves tend to approach the SS-OFDM curves due to a substantial reduction of the error floor. Such reduction means that the MUI is better mitigated as M increases, which has to be directly related to the improvement of the focusing effect of precoded MU-MIMO systems. Going on in the increase of the number of transmit antennas would lead to the massive MIMO situation for which the error floor would completely disappear. In the intermediate situation here, for a moderate number of antennas, the SS-OFDM solution turns out to be of high interest.

To highlight the benefit of the SS-OFDM strategy when the number of antennas remains reasonable, we plot in Fig. 4.31 the overlap ratio (in %) that each system is able to support under a target BER of 10^{-3} and for an increasing number of M. We observe that with a small scale antenna system, WH precoder can improve the achievable capacity of the OFDM system with subcarrier reuse. For example, in the SISO case, subcarrier reuse is not beneficial in the OFDM system whereas 18.75% ($N_R = 12$) overlapping can be achieved in the WH precoded SS-OFDM system. Moreover, in a 6×1 TR-MISO system, WH precoded system allows nearly 53% overlapping while traditional OFDM permits only 11% frequency reuse.

In general, the SS-OFDM system is able to resist to higher ratios of bandwidth reuse than the OFDM system for $M \leq 9$. However, when $M \geq 10$, the OFDM system can afford 100% of bandwidth overlap, whereas the SS-OFDM system has to use at least $M = 12$ antennas to reach that situation. With 100% overlap in fact, the inter-channel interference term is equivalent for both systems while the ICI that occurs for the SS-OFDM system has still a significant impact since the channel is not sufficient flat. Indeed, further increasing the number of antennas would yield equivalent results for both systems at 100% overlap.

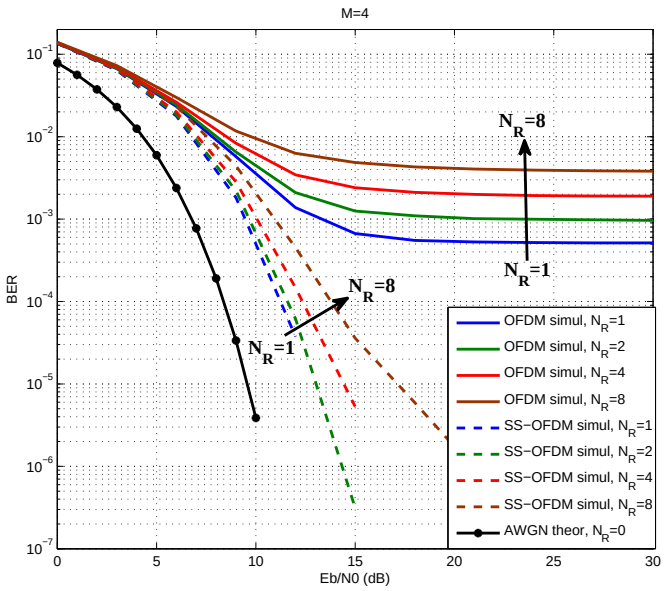

Figure 4.29: Performance of OFDM and SS-OFDM EGT-MIMO transmission with $M = 4$ and PFBO

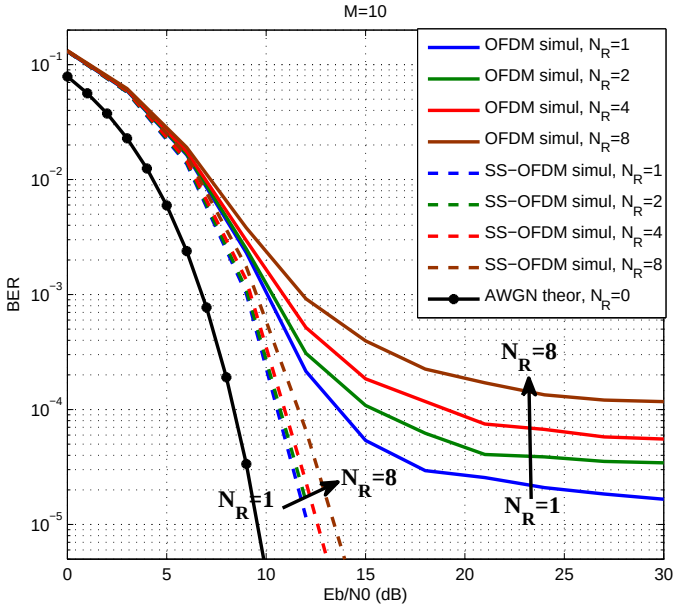

Figure 4.30: Performance of OFDM and SS-OFDM EGC-MIMO transmission with $M = 10$ and PFBO

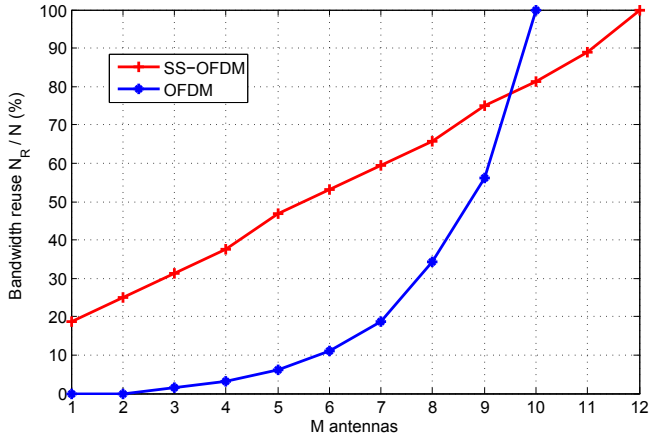

Figure 4.31: Achievable bandwidth reuse rate versus the number of antennas M at target BER=10^{-3}

4.5 Conclusion

In this chapter, we studied the BER performance of the PFBO scheme applied to SS-OFDM systems. The BER expressions were established for both AWGN channels and Rayleigh fading channels. It was proved that the SS techniques are able to whiten the narrow band interference. Hence, in a small-scale MIMO system, SS-OFDM systems outperform the OFDM systems with the use of PFBO scheme.

The original results of section 4.2 for BER analysis of SISO PFBO SS-OFDM system in AWGN channel have been published in:

H. Fu, M. Crussière and M. Hélard, "Partial channel overlay in moderate-scale MIMO systems using WH precoded OFDM", in *Proc. 21st International Conference on Telecommunications (ICT 2014)*, pp. 16-21, Lisbon, Portugal, May 2014.

CONCLUSION AND PERSPECTIVES

In this thesis, we studied the theoretical performance of MU-MIMO systems with a moderate-scale antenna array.

In the beginning, we presented the traditional MU-MIMO systems and the emerging massive MIMO systems. On this basis we proposed the moderate-scale MIMO as an intermediate of these systems which could take advantage of the multi-antenna multiplexing gain and would remain not too costly for practical implementation. However, the small number of antennas results in a relatively low multiplexing gain. The inter-user interference can no more be neglected and the channel can not be considered as flat fading.

Hence, a PFBO scheme, which consists in partial spectrum overlapping between two users, was proposed to limit the inter-channel interference for the case where the number of transmit antennas is not sufficient to assume a perfect SDMA among the users.

In this way, we analyzed in chapter 2 the system capacity of the PFBO scheme. It was shown that using single carrier modulation, slight spectral efficiency gain could be expected even with SISO systems. Also, this gain could be further amplified in MU-MIMO systems by increasing the number of transmit antennas. With multi-carrier modulation, the PFBO scheme was proved to improve the system capacity at low SNR regime. The optimal overlap ratio was identified and shown dependent to the roll-off factor, the SNR and the antenna numbers.

Moreover, we proposed in chapter 2 new closed-form capacity lower bounds for MU-MIMO systems using EGT, TR and MRT precoding techniques. These capacity bounds were based on a statistical analysis of the channel behavior, thus more accurate than the capacity lower bounds proposed in the literature for general massive MIMO systems.

Then we focused on the BER performance analysis of the PFBO scheme in chapter 3 and 4. In OFDM systems, the BER expressions were established for both AWGN channel and Rayleigh fading channel. Particularly, for Rayleigh fading channels, we proposed to use the Nakagami equation to model the correlation between the useful signal and the multi-user interference for EGT and MRT. The choice of the statistical model was justified and the linear relation between the Nakagami parameters and the number of transmit antenna was demonstrated. Initially derived for BPSK and 2 users, the model was shown to be valid when multiple interfering users were considered.

We introduced in chapter 4 the SS technique to further mitigate the impact of the inter-channel interference. For SS-OFDM systems, the BER expressions were also established for both AWGN channels and Rayleigh fading channels. In fact, due to the SS techniques, the expected value of the channel response was sufficient to provide accurate BER approximations. The BER approximations were confirmed with the simulation results. It was shown that the SS techniques widely improve the performance of the PFBO scheme especially with small overlap ratio.

For perspectives, at first, the closed-form expressions of the achievable sum rate approximation proposed in chapter 2 is derived without considering the thermal noise. Hence it is available

only for $SNR \geq 20dB$. Also, the capacity lower bounds are not accurate with small scale antenna arrays and low SNR. More general closed-form expressions including the low SNR regime are expected to be derived in future works.

Moreover, the BER analysis derived in chapter 3 for two-user MIMO OFDM system using QPSK constellation is considered can be improved in precision. The classical Nakagami equation can not properly approximate the impact of the multi-user interference in this case because some interference terms can be stronger than the useful signal terms and thus change the distribution of the equivalent channel. The solution can be searching another distribution which is able to approximate the addition of both positive and negative terms. Otherwise, an extension of Nakagami equation by adding supplementary arguments also can be considered.

For a system level point of view, the applications of PFBO MU-MIMO systems need to be considered. For a multiuser transmission scenario, the organization of users and the strategy of performing the PFBO need to be more specifically studied. The power allocation issue is also important to enhance the transmission quality and to optimize the system capacity.

At the end, the PAPR value of the precoded MU-MIMO OFDM systems also is an interesting issue. In literature, the PAPR value of EGT in SU-MIMO OFDM system is shown to be $1dB$ smaller than that of MRT techniques. However, for MU-MIMO systems, the channel behaviors are different from that of SU-MIMO systems. Moreover, the PAPR value of TR techniques has not been evaluated in neither systems. It will be interesting to compare the PAPR values of EGT, MRT and TR techniques in MU-MIMO systems.

Appendix

APPENDIX-A

Integration $\int_0^{+\infty} \log_2(1+x\gamma)\Gamma(x;k,\theta)dx$

The p.d.f. function of gamma distribution is:

$$f(x;k,\theta) = \frac{x^{k-1}e^{-\frac{x}{\theta}}}{\theta^k \Gamma(k)}$$

Then,

$$\int_0^{+\infty} \log_2(1+x\gamma)\Gamma(x;k,\theta)dx = \frac{1}{\Gamma(k)\theta^k \log(2)} \int_0^{+\infty} \log(1+x\gamma)x^{k-1}e^{-\frac{x}{\theta}}dx$$

$$= \frac{e^{1/\gamma\theta}}{\Gamma(k)\theta^k\gamma^k \log(2)} \int_1^{+\infty} \log(y)(y-1)^{k-1}e^{-\frac{y}{\theta\gamma}}dy$$

$$= \frac{e^{1/\gamma\theta}}{\Gamma(k)\theta^k\gamma^k \log(2)} \sum_{n=0}^{k-1} \binom{k-1}{n} (-1)^{k-1-n} \int_1^{+\infty} \log(y) y^n e^{-\frac{y}{\theta\gamma}}dy$$

$$= \frac{e^{1/\gamma\theta}}{\Gamma(k)\theta^k\gamma^k \log(2)} \sum_{n=0}^{k-1} \binom{k-1}{n} (-1)^{k-1-n} \left[\int_0^{+\infty} \log(y) y^n e^{-\frac{y}{\theta\gamma}}dy - \int_0^{1} \log(y) y^n e^{-\frac{y}{\theta\gamma}}dy\right]$$

$$= \frac{e^{1/\gamma\theta}}{\Gamma(k)\theta^k\gamma^k \log(2)} \sum_{n=0}^{k-1} \binom{k-1}{n} (-1)^{k-1-n}$$

$$\left[(\theta\gamma)^{n+1}\Gamma(n+1)\left[\Psi(n+1) + log(\theta\gamma)\right] + \frac{{}_2F_2(n+1,n+1;n+2,n+2;-1/\gamma\theta)}{(n+1)^2}\right]$$

with $\psi(\cdot)$ is the Euler totient function, ${}_2F_2(\cdot)$ is the hypergeometric function.

APPENDIX-B

Expected value $\mathbb{E}\left[\frac{1}{\Gamma(k,\theta)+N_0}\right]$

The p.d.f. function of gamma distribution is:

$$f(x;k,\theta)=\frac{x^{k-1}e^{-\frac{x}{\theta}}}{\theta^k\Gamma(k)}$$

Then,

$$\begin{aligned}
\mathbb{E}\left[\frac{1}{x+N_0}\right] &= \int_0^{+\infty}\frac{1}{x+N_0}\frac{x^{k-1}e^{-\frac{x}{\theta}}}{\theta^k\Gamma(k)}dx \\
&= \frac{1}{\theta^k\Gamma(k)}\int_0^{+\infty}\frac{1}{x+N_0}x^{k-1}e^{-\frac{x}{\theta}}dx \\
&= \frac{1}{\theta^k\Gamma(k)}\int_{N_0}^{+\infty}\frac{1}{y}(y-N_0)^{k-1}e^{-\frac{y-N_0}{\theta}}dy \\
&= \frac{e^{\frac{N_0}{\theta}}}{\theta^k\Gamma(k)}\int_{N_0}^{+\infty}\frac{1}{y}\sum_{n=0}^{k-1}\binom{k-1}{n}y^{k-1-n}(-N_0)^n e^{-\frac{y}{\theta}}dy \\
&= \frac{e^{\frac{N_0}{\theta}}}{\theta^k\Gamma(k)}\sum_{n=0}^{k-1}\binom{k-1}{n}(-N_0)^n\int_{N_0}^{+\infty}y^{k-2-n}e^{-\frac{y}{\theta}}dy \\
&= \frac{e^{\frac{N_0}{\theta}}}{\theta^k\Gamma(k)}(-N_0)^{k-1}\int_{N_0}^{+\infty}\frac{e^{-\frac{y}{\theta}}}{y}dy+\frac{e^{\frac{N_0}{\theta}}}{\theta^k\Gamma(k)}\sum_{n=0}^{k-2}\binom{k-1}{n}(-N_0)^n\int_{N_0}^{+\infty}y^{k-2-n}e^{-\frac{y}{\theta}}dy \\
&= \frac{e^{\frac{N_0}{\theta}}(-N_0)^{k-1}\left(-Ei\left(-\frac{N_0}{\theta}\right)\right)}{\theta^k\Gamma(k)}+\frac{e^{\frac{N_0}{\theta}}}{\Gamma(k)}\sum_{n=0}^{k-2}\binom{k-1}{n}(-N_0)^n\frac{\Gamma(k-1-n,\frac{N_0}{\theta})}{\theta^{n+1}}.
\end{aligned}$$

List of Figures

BIBLIOGRAPHY

[1] Gerard J Foschini. Layered space-time architecture for wireless communication in a fading environment when using multi-element antennas. *Bell labs technical journal*, 1(2):41–59, 1996.

[2] Armin Wittneben. A new bandwidth efficient transmit antenna modulation diversity scheme for linear digital modulation. In *Communications, 1993. ICC'93 Geneva. Technical Program, Conference Record, IEEE International Conference on*, volume 3, pages 1630–1634. IEEE, 1993.

[3] Nambi Seshadri and Jack H Winters. Two signaling schemes for improving the error performance of frequency-division-duplex (fdd) transmission systems using transmitter antenna diversity. In *Vehicular Technology Conference, 1993., 43rd IEEE*, pages 508–511. IEEE, 1993.

[4] Vahid Tarokh, N. Seshadri, and A.R. Calderbank. Space-time codes for high data rate wireless communication: performance criterion and code construction. *Information Theory, IEEE Transactions on*, 44(2):744–765, Mar 1998.

[5] AJ. Paulraj and C.B. Papadias. Space-time processing for wireless communications. *Signal Processing Magazine, IEEE*, 14(6):49–83, Nov 1997.

[6] Vahid Tarokh, Hamid Jafarkhani, and A.R. Calderbank. Space-time block codes from orthogonal designs. *Information Theory, IEEE Transactions on*, 45(5):1456–1467, Jul 1999.

[7] Siavash Alamouti. A simple transmit diversity technique for wireless communications. *Selected Areas in Communications, IEEE Journal on*, 16(8):1451–1458, 1998.

[8] A Narula, M.D. Trott, and Gregory W. Wornell. Performance limits of coded diversity methods for transmitter antenna arrays. *Information Theory, IEEE Transactions on*, 45(7):2418–2433, Nov 1999.

[9] Vahid Tarokh, S. Alamouti, and P. Poon. New detection schemes for transmit diversity with no channel estimation. In *Universal Personal Communications, 1998. ICUPC '98. IEEE 1998 International Conference on*, volume 2, pages 917–920 vol.2, Oct 1998.

[10] J.H. Winters. On the capacity of radio communication systems with diversity in a rayleigh fading environment. *Selected Areas in Communications, IEEE Journal on*, 5(5):871–878, Jun 1987.

[11] Emre Telatar. Capacity of multi-antenna gaussian channels. *European transactions on telecommunications*, 10(6):585–595, 1999.

[12] P.W. Wolniansky, G.J. Foschini, G.D. Golden, and R. Valenzuela. V-blast: an architecture for realizing very high data rates over the rich-scattering wireless channel. In *Signals, Systems, and Electronics, 1998. ISSSE 98. 1998 URSI International Symposium on*, pages 295–300, Sep 1998.

[13] M. Skoglund and G. Jöngren. On the capacity of a multiple-antenna communication link with channel side information. *Selected Areas in Communications, IEEE Journal on*, 21(3):395–405, Apr 2003.

[14] Jerry R Hampton. *Introduction to MIMO Communications*. Cambridge University Press, 2013.

[15] Quentin H Spencer, Christian B Peel, A Lee Swindlehurst, and Martin Haardt. An introduction to the multi-user mimo downlink. *Communications Magazine, IEEE*, 42(10):60–67, 2004.

[16] Max HM Costa. Writing on dirty paper (corresp.). *Information Theory, IEEE Transactions on*, 29(3):439–441, 1983.

[17] Giuseppe Caire and Shlomo Shamai. On the achievable throughput of a multiantenna gaussian broadcast channel. *Information Theory, IEEE Transactions on*, 49(7):1691–1706, 2003.

[18] Thomas L Marzetta. Noncooperative cellular wireless with unlimited numbers of base station antennas. *Wireless Communications, IEEE Transactions on*, 9(11):3590–3600, 2010.

[19] David Tse and Pramod Viswanath. *Fundamentals of wireless communication*. Cambridge university press, 2005.

[20] Andrea Goldsmith. *Wireless communications*. Cambridge university press, 2005.

[21] Sayantan Choudhury and Jerry D Gibson. Ergodic capacity, outage capacity, and information transmission over rayleigh fading channels. In *Proceedings of the Information Theory and Applications Workshop*, 2007.

[22] Lizhong Zheng and D.N.C. Tse. Diversity and multiplexing: a fundamental tradeoff in multiple-antenna channels. *Information Theory, IEEE Transactions on*, 49(5):1073–1096, May 2003.

[23] D.J. Love and R.W. Heath. Equal gain transmission in multiple-input multiple-output wireless systems. *Communications, IEEE Transactions on*, 51(7):1102–1110, July 2003.

[24] William C Jakes. Mobile microwave communication, 1974.

[25] Titus KY Lo. Maximum ratio transmission. In *Communications, 1999. ICC'99. 1999 IEEE International Conference on*, volume 2, pages 1310–1314. IEEE, 1999.

[26] M.-A. Khalighi, J. Brossier, G.V. Jourdain, and K. Raoof. Water filling capacity of rayleigh mimo channels. In *Personal, Indoor and Mobile Radio Communications, 2001 12th IEEE International Symposium on*, volume 1, pages A–155–A–158 vol.1, Sep 2001.

[27] Lu Lu, G.Y. Li, A.L. Swindlehurst, A. Ashikhmin, and Rui Zhang. An overview of massive mimo: Benefits and challenges. *Selected Topics in Signal Processing, IEEE Journal of*, 8(5):742–758, Oct 2014.

[28] Richard P Martin, Amin M Vahdat, David E Culler, and Thomas E Anderson. *Effects of communication latency, overhead, and bandwidth in a cluster architecture*, volume 25. ACM, 1997.

[29] Hanan Weingarten, Yossef Steinberg, and Shlomo Shamai. The capacity region of the gaussian mimo broadcast channel. In *IEEE International Symposium on Information Theory*, pages 174–174, 2004.

[30] Quentin H Spencer, A Lee Swindlehurst, and Martin Haardt. Zero-forcing methods for downlink spatial multiplexing in multiuser mimo channels. *Signal Processing, IEEE Transactions on*, 52(2):461–471, 2004.

[31] Christian B Peel, Bertrand M Hochwald, and A Lee Swindlehurst. A vector-perturbation technique for near-capacity multiantenna multiuser communication-part i: channel inversion and regularization. *Communications, IEEE Transactions on*, 53(1):195–202, 2005.

[32] Fredrik Rusek, Daniel Persson, Buon Kiong Lau, Erik G Larsson, Thomas L Marzetta, Ove Edfors, and Fredrik Tufvesson. Scaling up mimo: Opportunities and challenges with very large arrays. *Signal Processing Magazine, IEEE*, 30(1):40–60, 2013.

[33] Erik G Larsson, Ove Edfors, Fredrik Tufvesson, and Thomas L Marzetta. Massive mimo for next generation wireless systems. *arXiv preprint arXiv:1304.6690*, 2013.

[34] Hien Quoc Ngo, Erik G Larsson, and Thomas L Marzetta. Energy and spectral efficiency of very large multiuser mimo systems. *Communications, IEEE Transactions on*, 61(4):1436–1449, 2013.

[35] Junyoung Nam, Jae-Young Ahn, Ansuman Adhikary, and Giuseppe Caire. Joint spatial division and multiplexing: Realizing massive mimo gains with limited channel state information. In *Information Sciences and Systems (CISS), 2012 46th Annual Conference on*, pages 1–6. IEEE, 2012.

[36] Yantao Han, Jiqing Ni, and GaoKe Du. The potential approaches to achieve channel reciprocity in fdd system with frequency correction algorithms. In *Communications and Networking in China (CHINACOM), 2010 5th International ICST Conference on*, pages 1–5. IEEE, 2010.

[37] Thomas L Marzetta. How much training is required for multiuser mimo? In *Signals, Systems and Computers, 2006. ACSSC'06. Fortieth Asilomar Conference on*, pages 359–363. IEEE, 2006.

[38] Clayton Shepard, Hang Yu, Narendra Anand, Erran Li, Thomas Marzetta, Richard Yang, and Lin Zhong. Argos: Practical many-antenna base stations. In *Proceedings of the 18th annual international conference on Mobile computing and networking*, pages 53–64. ACM, 2012.

[39] Florian Kaltenberger, Haiyong Jiang, Maxime Guillaud, and Raymond Knopp. Relative channel reciprocity calibration in mimo/tdd systems. In *Future Network and Mobile Summit, 2010*, pages 1–10. IEEE, 2010.

[40] Haifan Yin, D. Gesbert, M. Filippou, and Yingzhuang Liu. A coordinated approach to channel estimation in large-scale multiple-antenna systems. *Selected Areas in Communications, IEEE Journal on*, 31(2):264–273, February 2013.

[41] Alexei Ashikhmin and Thomas Marzetta. Pilot contamination precoding in multi-cell large scale antenna systems. In *Information Theory Proceedings (ISIT), 2012 IEEE International Symposium on*, pages 1137–1141. IEEE, 2012.

[42] Hien Quoc Ngo and E.G. Larsson. Evd-based channel estimation in multicell multiuser mimo systems with very large antenna arrays. In *Acoustics, Speech and Signal Processing (ICASSP), 2012 IEEE International Conference on*, pages 3249–3252, March 2012.

[43] M. L. Doelz, E. T. Heald, and D. L. Martin. Binary data transmission techniques for linear systems. *Proceedings of the IRE*, 45(5):656–661, May 1957.

[44] L.J. Cimini. Analysis and simulation of a digital mobile channel using orthogonal frequency division multiplexing. *Communications, IEEE Transactions on*, 33(7):665–675, Jul 1985.

[45] G.L. Stuber, J.R. Barry, S.W. McLaughlin, Ye Li, M.-A Ingram, and T.G. Pratt. Broadband mimo-ofdm wireless communications. *Proceedings of the IEEE*, 92(2):271–294, Feb 2004.

[46] Hong Yang and Thomas L Marzetta. Performance of conjugate and zero-forcing beamforming in large-scale antenna systems. *IEEE Journal on Selected Areas in Communications*, (31):172–179, 2013.

[47] Shengli Zhou and Georgios B Giannakis. Optimal transmitter eigen-beamforming and space-time block coding based on channel mean feedback. *Signal Processing, IEEE Transactions on*, 50(10):2599–2613, 2002.

[48] Mai Vu and A Paulraj. Mimo wireless linear precoding. *Signal Processing Magazine, IEEE*, 24(5):86–105, Sept 2007.

[49] Lloyd N Trefethen and David Bau III. *Numerical linear algebra*, volume 50. Siam, 1997.

[50] Arogyaswami Paulraj, Rohit Nabar, and Dhananjay Gore. *Introduction to space-time wireless communications*. Cambridge university press, 2003.

[51] Haralabos C Papadopoulos, Giuseppe Caire, and Sean A Ramprashad. Achieving large spectral efficiencies from mu-mimo with tens of antennas: Location-adaptive tdd mu-mimo design and user scheduling. In *Signals, Systems and Computers (ASILOMAR), 2010 Conference Record of the Forty Fourth Asilomar Conference on*, pages 636–643. IEEE, 2010.

[52] Emil Björnson, Luca Sanguinetti, Jakob Hoydis, and Mérouane Debbah. Designing multiuser mimo for energy efficiency: When is massive mimo the answer? *arXiv preprint arXiv:1310.3843*, 2013.

[53] Jingon Joung, Yeow Khiang Chia, and Sumei Sun. Energy-efficient, large-scale distributed-antenna system (l-das) for multiple users. *Selected Topics in Signal Processing, IEEE Journal of*, 8(5):954–965, Oct 2014.

[54] Jubin Jose, Alexei Ashikhmin, Thomas L Marzetta, and Sriram Vishwanath. Pilot contamination and precoding in multi-cell tdd systems. *Wireless Communications, IEEE Transactions on*, 10(8):2640–2651, 2011.

[55] Jakob Hoydis, Stephan Ten Brink, Mérouane Debbah, et al. Massive mimo in the ul/dl of cellular networks: How many antennas do we need? *IEEE Journal on selected Areas in Communications*, 31(2):160–171, 2013.

[56] Xiayu Zheng, Yao Xie, Jian Li, and Petre Stoica. Mimo transmit beamforming under uniform elemental power constraint. *Signal Processing, IEEE Transactions on*, 55(11):5395–5406, Nov 2007.

[57] Shang-Ho Tsai. Transmit equal gain precoding in rayleigh fading channels. *Signal Processing, IEEE Transactions on*, 57(9):3717–3721, Sept 2009.

[58] Shang-Ho Tsai. Equal gain transmission with antenna selection in mimo communications. *Wireless Communications, IEEE Transactions on*, 10(5):1470–1479, May 2011.

[59] Thierry Dubois, Maryline Hélard, Matthieu Crussière, and Cécile Germond. Performance of time reversal precoding technique for miso-ofdm systems. *EURASIP Journal on Wireless Communications and Networking*, 2013(1):1–16, 2013.

[60] Chi-Liang Chao, Shang-Ho Tsai, and Terng-Yin Hsu. Bit allocation schemes for mimo equal gain precoding. *Wireless Communications, IEEE Transactions on*, 10(5):1345–1350, 2011.

[61] Mathias Fink. Time reversal of ultrasonic fields. i. basic principles. *Ultrasonics, Ferroelectrics and Frequency Control, IEEE Transactions on*, 39(5):555–566, 1992.

[62] G Lerosey, J De Rosny, A Tourin, A Derode, G Montaldo, and M Fink. Time reversal of electromagnetic waves. *Physical review letters*, 92(19):193904, 2004.

[63] Persefoni Kyritsi, George Papanicolaou, Patrick Eggers, and Alex Oprea. Miso time reversal and delay-spread compression for fwa channels at 5 ghz. *Antennas and Wireless Propagation Letters, IEEE*, 3(1):96–99, 2004.

[64] Ali Khaleghi, Ghaïs El Zein, and Ijaz Haider Naqvi. Demonstration of time-reversal in indoor ultra-wideband communication: time domain measurement. In *Wireless Communication Systems, 2007. ISWCS 2007. 4th International Symposium on*, pages 465–468. IEEE, 2007.

[65] Beibei Wang, Yongle Wu, Feng Han, Yu-Han Yang, and KJ Ray Liu. Green wireless communications: a time-reversal paradigm. *Selected Areas in Communications, IEEE Journal on*, 29(8):1698–1710, 2011.

[66] Claude Oestges, Arnold D Kim, George Papanicolaou, and Arogyaswami J Paulraj. Characterization of space-time focusing in time-reversed random fields. *Antennas and Propagation, IEEE Transactions on*, 53(1):283–293, 2005.

[67] Shao-Qiu Xiao, Jian Chen, Bing-Zhong Wang, and Xiao-Fei Liu. A numerical study on time-reversal electromagnetic wave for indoor ultra-wideband signal transmission. *Progress In Electromagnetics Research*, 77:329–342, 2007.

[68] Ijaz Haider Naqvi, Ali Khaleghi, and Ghaïs El Zein. Time reversal uwb communication system: a novel modulation scheme with experimental validation. *EURASIP Journal on Wireless Communications and Networking*, 2010:33, 2010.

[69] Majid Emami, Mai Vu, Jan Hansen, Arogyaswami J Paulraj, and George Papanicolaou. Matched filtering with rate back-off for low complexity communications in very large delay spread channels. In *Signals, Systems and Computers, 2004. Conference Record of the Thirty-Eighth Asilomar Conference on*, volume 1, pages 218–222. IEEE, 2004.

[70] Thierry Dubois, Matthieu Crussiere, and Maryline Helard. On the use of time reversal for digital communications with non-impulsive waveforms. In *Signal Processing and Communication Systems (ICSPCS), 2010 4th International Conference on*, pages 1–6. IEEE, 2010.

[71] Feng Han, Yu-Han Yang, Beibei Wang, Yongle Wu, and K.J.R. Liu. Time-reversal division multiple access over multi-path channels. *Communications, IEEE Transactions on*, 60(7):1953–1965, July 2012.

[72] Thierry Dubois, Maryline Hélard, Matthieu Crussière, et al. Time reversal in a miso ofdm system: Guard interval design, dimensioning and synchronisation aspects. In *WWRF29*, 2012.

[73] Yue Wang and Justin Coon. Full rate orthogonal space-time block coding in ofdm transmission using time reversal. In *Wireless Communications and Networking Conference, 2009. WCNC 2009. IEEE*, pages 1–6. IEEE, 2009.

[74] Hoon Huh, Giuseppe Caire, Haralabos C Papadopoulos, and Sean A Ramprashad. Achieving" massive mimo" spectral efficiency with a not-so-large number of antennas. *Wireless Communications, IEEE Transactions on*, 11(9):3226–3239, 2012.

[75] Agisilaos Papadogiannis, David Gesbert, and Eric Hardouin. A dynamic clustering approach in wireless networks with multi-cell cooperative processing. In *Communications, 2008. ICC'08. IEEE International Conference on*, pages 4033–4037. IEEE, 2008.

[76] Paul Bender, Peter Black, Matthew Grob, Roberto Padovani, Nagabhushana Sindhushyana, and Andrew Viterbi. Cdma/hdr: a bandwidth efficient high speed wireless data service for nomadic users. *Communications Magazine, IEEE*, 38(7):70–77, 2000.

[77] Utra high speed downlink packet access, Mar. 2001.

[78] Caijun Zhong, Shi Jin, Kai-Kit Wong, M-S Alouini, and Tharmalingam Ratnarajah. Low snr capacity for mimo rician and rayleigh-product fading channels with single co-channel interferer and noise. *Communications, IEEE Transactions on*, 58(9):2549–2560, 2010.

[79] Valentine A Aalo and Jingjun Zhang. Performance analysis of maximal ratio combining in the presence of multiple equal-power cochannel interferers in a nakagami fading channel. *Vehicular Technology, IEEE Transactions on*, 50(2):497–503, 2001.

[80] N.C. Beaulieu and J. Cheng. Precise error-rate analysis of bandwidth-efficient bpsk in nakagami fading and cochannel interference. *Communications, IEEE Transactions on*, 52(1):149–158, Jan 2004.

[81] K. Sivanesan and N.C. Beaulieu. Outage and ber of mrc diversity in bandlimited microcellular systems with cci. *Communications Letters, IEEE*, 9(3):207–209, March 2005.

[82] Jeongho Park, Changeon Kang, Daesik Hong, et al. Effect of partial band jamming on ofdm-based wlan in 802.11 g. In *Acoustics, Speech, and Signal Processing, 2003. Proceedings.(ICASSP'03). 2003 IEEE International Conference on*, volume 4, pages IV–560. IEEE, 2003.

[83] Jun Luo, J.H. Andrian, and Chi Zhou. Bit error rate analysis of jamming for ofdm systems. In *Wireless Telecommunications Symposium, 2007. WTS 2007*, pages 1–8, April 2007.

[84] Marvin K Simon and Mohamed-Slim Alouini. *Digital communication over fading channels*, volume 95. John Wiley & Sons, 2005.

[85] William CY Lee. *Mobile cellular telecommunications: analog and digital systems*. McGraw-Hill Professional, 1995.

[86] Broadband radio access networks (bran); hiperlan type2; physical layer, december 2001.

[87] Jonas Medbo. Radio wave propagation characteristics at 5 ghz with modeling suggestions for hiperlan/2. *ETSI BRAN 3ERI074A*, 1998.

[88] T. van Waterschoot, V. Le Nir, J. Duplicy, and M. Moonen. Analytical expressions for the power spectral density of cp-ofdm and zp-ofdm signals. *Signal Processing Letters, IEEE*, 17(4):371–374, April 2010.

[89] SM Emami, J Hansen, AD Kim, G Papanicolaou, AJ Paulraj, D Cheung, and C Prettie. Predicted time reversal performance in wireless communications using channel measurements. *IEEE Communications Letters*, 2004.

[90] Claude Elwood Shannon. Communication in the presence of noise. *Proceedings of the IRE*, 37(1):10–21, 1949.

[91] Seymour Stein Mischa Schwartz, William R. Bennett. *Communication systemes and techniques*. McGraw-Hill, 1966.

[92] Minoru Nakagami. The m-distribution-a general formula of intensity distribution of rapid fading. *Statistical Method of Radio Propagation*, 1960.

[93] Babak Hassibi and Bertrand M Hochwald. How much training is needed in multiple-antenna wireless links? *Information Theory, IEEE Transactions on*, 49(4):951–963, 2003.

[94] Athanasios Papoulis and S Unnikrishna Pillai. *Probability, random variables, and stochastic processes*. Tata McGraw-Hill Education, 2002.

[95] Shirley Dowdy, Stanley Wearden, and Daniel Chilko. *Statistics for research*, volume 512. John Wiley & Sons, 2011.

[96] Lingzhi Cao and Norman C Beaulieu. Closed-form ber results for mrc diversity with channel estimation errors in ricean fading channels. *Wireless Communications, IEEE Transactions on*, 4(4):1440–1447, 2005.

[97] Hien Quoc Ngo, Michail Matthaiou, Trung Q Duong, and Erik G Larsson. Uplink performance analysis of multicell mu-simo systems with zf receivers. *Vehicular Technology, IEEE Transactions on*, 62(9):4471–4483, 2013.

[98] Marvin K Simon. *Probability distributions involving Gaussian random variables: A handbook for engineers and scientists*. Springer, 2007.

[99] Edward W Ng and Murray Geller. A table of integrals of the error functions. *Journal of Research of the National Bureau of Standards B*, 73:1–20, 1969.

[100] Izrail Solomonovich Gradshteyn, Iosif Moiseevich Ryzhik, Alan Jeffrey, Daniel Zwillinger, and Scripta Technica. *Table of integrals, series, and products*, volume 6. Academic press New York, 1965.

[101] Ali Abdi and Mostafa Kaveh. Performance comparison of three different estimators for the nakagami m parameter using monte carlo simulation. 4(4):119–121, 2000.

[102] Milton Abramowitz, Irene A Stegun, et al. *Handbook of mathematical functions*, volume 1. Dover New York, 1972.

[103] Vincent Le Nir. *Etude et optimisation des systĺĺme multi-antennas associĺęs ĺd' des modulations multiporteuses*. PhD thesis, INSA de Rennes, 2004.

[104] Maryline Hélard, Rodolphe Le Gouable, Jean-Francois Hélard, and Jean-Yves Baudais. Multicarrier cdma techniques for future wideband wireless networks. In *Annales des télécommunications*, volume 56, pages 260–274. Springer, 2001.

[105] S. Kaiser. Ofdm code-division multiplexing in fading channels. *Communications, IEEE Transactions on*, 50(8):1266–1273, Aug 2002.

[106] Esmael H Dinan and Bijan Jabbari. Spreading codes for direct sequence cdma and wideband cdma cellular networks. *Communications Magazine, IEEE*, 36(9):48–54, 1998.

[107] B.M. Popovic. Spreading sequences for multicarrier cdma systems. *Communications, IEEE Transactions on*, 47(6):918–926, Jun 1999.

[108] Robert Gold. Optimal binary sequences for spread multiplexing (corresp.). *Information Theory, IEEE Transactions on*, 13(4):619–621, 1967.

[109] Wojciech Tadej and Karol Życzkowski. A concise guide to complex hadamard matrices. *Open Systems & Information Dynamics*, 13(02):133–177, 2006.

[110] Marcel JE Golay. Complementary series. *Information Theory, IRE Transactions on*, 7(2):82–87, 1961.

[111] Andrew J Viterbi. *CDMA: principles of spread communication*. Addison Wesley Longman Publishing Co., Inc., 1995.

[112] Ming Liu, Matthieu Crussiere, and J Helard. A novel data-aided channel estimation with reduced complexity for tds-ofdm systems. *Broadcasting, IEEE Transactions on*, 58(2):247–260, 2012.

[113] Marco Chiani, Davide Dardari, and Marvin K Simon. New exponential bounds and approximations for the computation of error probability in fading channels. *Wireless Communications, IEEE Transactions on*, 2(4):840–845, 2003.

[114] Jean-Yves Baudais. *Etude des modulations à porteuses multiples et à spectre étalé: analyse et optimisation*. PhD thesis, l'INSA de Rennes, may 2001.

[115] Rodolphe Le Gouable. *Association de modulations multiporteuses et de techniques d'accès multiple: applications aux transmissions sans fil haut débit*. PhD thesis, l'INSA de Rennes, mars 2001.

INSA de RENNES
Service des Formations

AVIS DU JURY SUR LA REPRODUCTION DE LA THESE SOUTENUE

Titre de la thèse:
Optimisation de la ressource spectrale pour les systèmes MU-MIMO avec recouvrement fréquentiel partiel

Nom Prénom de l'auteur : FU HUA

Membres du jury :
- Madame HELARD Maryline
- Monsieur CRUSSIERE Matthieu
- Monsieur LE RUYET Didier
- Madame BOUCHERET Marie-Laure
- Monsieur RADOI Emanuel
- Monsieur FERRE Guillaume

Président du jury : ML Boucheret

Date de la soutenance : 22 Mai 2015

Reproduction de la these soutenue

Thèse pouvant être reproduite en l'état
~~Thèse pouvant être reproduite après corrections suggérées~~

Fait à Rennes, le 22 Mai 2015

Signature du président de jury

Le Directeur,

M'hamed DRISSI

Résumé

Pour les prochaines générations de systèmes de communications sans fil, un défi majeur est de poursuivre l'augmentation de l' efficacité spectrale de ces systèmes pour satisfaire la montée croissante des demandes en débit, tout en revoyant à la baisse la consommation énergétique des équipements et répondre ainsi aux objectifs des "communications vertes''. L'une des stratégies permettant de traiter ce problème sont les communications multi-antennes multi-utilisateurs (MU-MIMO), notamment lorsque le nombre d'antennes devient très grand (Massive MIMO). Il est alors possible d'adresser de multiples utilisateurs simultanément grâce à une opération linéaire de précodage spatial.

Le but de cette thèse consiste à optimiser l'efficacité spectrale des systèmes MU-MIMO dans le cas d'un nombre d'antennes qui reste modéré, et une consommation énergétique faible. Nous avons donc étudié les techniques de précodage à haute efficacité énergétique basées sur la notion de filtre adapté au canal, tels que la technique MRT (maximum ratio transmission), EGT (equal gain transmission) et TR (time reversal). Notre travail s'est concentré sur l'analyse théorique des performances de ces techniques. Nous avons de plus introduit un nouveau schéma de transmission, nommé PFBO (partial frequency bandwidth overlay), visant à améliorer l'efficacité spectrale des systèmes MU-MIMO à faible nombre d'antennes et pour de faibles niveaux de rapports signal à bruit (SNR).

Dans une première partie, nous avons étudié l'efficacité spectrale du schéma PFBO dans le cas de transmissions mono-porteuses et multi-porteuses. Les taux de recouvrement optimaux fournissant une capacité système maximale dans le cas de transmissions MISO et MIMO à deux utilisateurs ont été identifiés. Puis l'étude a été étendue aux cas MU-MIMO avec un nombre arbitraire d'utilisateurs. Nous avons modélisé précisément le comportement du canal équivalent après précodage, en utilisant respectivement les techniques EGT, TR et MRT. De nouvelles bornes de capacité non disponibles dans la littérature ont alors été obtenues et ont montré une précision satisfaisante.

Dans la deuxième partie, le taux d'erreur binaire pour le schéma PFBO a été étudié sur canal plat et canal de Rayleigh. Les expressions du taux d'erreurs binaires ont été obtenues. En particulier, nous avons proposé un modèle statistique pour rendre compte du comportement du canal après précodage ainsi que de l'interférence inter-utilisateur. Une première proposition de modèle a été introduite pour les systèmes EGT-MIMO à deux utilisateurs utilisant une modulation BPSK. Ce modèle a été également validé dans le cas d'une modulation QPSK ou pour de multiples utilisateurs.

Dans la dernière partie, nous avons combiné le principe du schéma PFBO aux systèmes OFDM à spectre étalé (SS-OFDM). Nous avons analysé les performances théoriques de ce système sur canal plat et canal de Rayleigh. Les expressions de taux d'erreurs binaires ont été établies et validées par simulations. Nous avons alors pu montrer que la composante SS permettait d'améliorer les performances du schéma PFBO lorsque le taux de recouvrement restait modéré.

Abstract

For the next generations of wireless communication systems, getting higher spectral efficiencies is remaining a big challenge to answer the explosively increasing demand of throughput. Meanwhile, the energy consumption of equipments and the transmitting power density have to be reduced to achieve the objective of ''green communications''. One of the most promising strategies to deal with such issues is using multi-user multiple-input multiple-output (MU-MIMO) schemes, namely for large-scale antenna systems. It becomes then possible to simultaneously serve multiple simple device users using linear spatial precoding techniques.

The objective of this thesis is to optimize the spectral efficiency of MU-MIMO systems in the context of moderate-scale antenna arrays and low energy consumption. Hence, we studied different high-energy efficiency precoding techniques based on matched filtering approach, such as maximum ratio transmission (MRT), equal gain transmission (EGT) and time reversal (TR). We were interested in the theoretical performance analysis of these techniques. In addition, we introduced a scheme based on partial frequency bandwidth overlay (PFBO) to improve and adapt the spectral efficiency of a MU-MIMO system at low signal to noise ratio (SNR) regime.

In a first part, we studied the spectral efficiency of the proposed PFBO scheme with both single-carrier and multi-carrier modulations. We identified the optimal bandwidth overlap ratios that provide the maximum achievable rate for two-user SIMO and MIMO systems. Then the study was extended to a more general MU-MIMO case with an arbitrary number of users. We precisely modeled the channel behavior after precoding when using EGT, TR and MRT techniques. New closed-form capacity lower bounds not available in the literature were then obtained and shown to be satisfactory accurate.

In the second part, the bit error rate (BER) performance of PFBO scheme was studied for both flat fading channels and theoretical Rayleigh channels. Closed-form BER equations were obtained. Particularly, we proposed a statistical model to reflect the behavior of the non-flat fading channel after precoding and to take into account the correlated interference terms that occur in a two-user EGT-MIMO system using BPSK modulation. This model was also validated in case of QPSK modulation and with more users.

In the last part, we proposed to combine our PFBO principle with spread-spectrum OFDM techniques (SS-OFDM). We analyzed the theoretical BER performance of such a scheme using flat fading channels and theoretical Rayleigh channels. New closed-form BER approximation equations were then established and compared through simulations. Eventually, we showed that the SS component of the proposed system provides performance gains that depend on the overlap ratio used in the PFBO scheme.

N° d'ordre : 15ISAR 15 / D15 - 15

Institut National des Sciences Appliquées de Rennes
20, Avenue des Buttes de Coëmes • CS 70839 • F-35708 Rennes Cedex
Tel : 02 23 23 82 00 - Fax : 02 23 23 83 96